NUREG/CR-4420
SAND85-0707
R5, R7
Printed January 1986

TURC1: Large Scale Metallic Melt-Concrete Interaction Experiments and Analysis

J. E. Gronager, A. J. Suo-Anttila, D. R. Bradley,
J. E. Brockmann

Prepared by
Sandia National Laboratories
Albuquerque, New Mexico 87185 and Livermore, California 94550
for the United States Department of Energy
under Contract DE-AC04-76DP00789

8603100099 ;60131
PDR NUREG
CR-4420 R PDR

Prepared for
U. S. NUCLEAR REGULATORY COMMISSION

SF 2900Q(8-81)

NOTICE

This report was prepared as an account of work sponsored by an agency of the United States Government. Neither the United States Government nor any agency thereof, or any of their employees, makes any warranty, expressed or implied, or assumes any legal liability or responsibility for any third party's use, or the results of such use, of any information, apparatus product or process disclosed in this report, or represents that its use by such third party would not infringe privately owned rights.

Available from

Superintendent of Documents
U.S. Government Printing Office
Post Office Box 37082
Washington, D.C. 20013-7982

and

National Technical Information Service
Springfield, VA 22161

NUREG/CR-4420
SAND85-0707
R5, R7

TURC1: LARGE SCALE METALLIC MELT-CONCRETE INTERACTION EXPERIMENTS AND ANALYSIS

J. E. Gronager
A. J. Suo-Antilla*
D. R. Bradley
J. E. Brockmann

January 1986

Sandia National Laboratories
Albuquerque, NM 87185
Operated by
Sandia Corporation
for the
U.S. Department of Energy

Prepared for
Containment Systems Branch
Division of Accident Evaluation
Office of Nuclear Regulatory Research
U.S. Nuclear Regulatory Commission
Washington, DC 20555
Under Memorandum of Understanding DOE 40-550-75
NRC FIN No. A1218

*Science Applications International Corporation
Albuquerque, New Mexico 87102

ABSTRACT

Two large scale molten debris-concrete experiments, TURC1T, a thermite-concrete interaction experiment, and TURC1SS, a stainless steel-concrete experiment, are reported here. The experiments consisted of teeming molten debris (>100 kg) onto limestone/common sand concrete. The molten debris was allowed to cool naturally. The concrete ablation rate, composition of evolved gases, and aerosol data are presented.

The experimental results have been compared to CORCON calculations in order to validate the code. This comparison showed that while some parts of the code performed well (chemical equilibrium model), other sections required further model development (melt-concrete heat transfer model).

An analysis of the two experiments was performed using a new analysis model. The results of the analysis seem to suggest that the heat transfer mechanism of concrete ablation is similar to nucleate boiling heat transfer, rather than gas film heat transfer.

TABLE OF CONTENTS

FIGURES

Tables

Acknowledgments

The successful completion of the TURC series of experiments required the assistance of many individuals. The authors are particularly grateful for the assistance of J. H. Bentz and K. Fleming, who provided much of the effort in design, assembly, and conduct of the experiments. Additionally, significant contributions were made by F. E. Arellano (Gas Sampling and Analysis), D. A. Lucero (Aerosol Instrumentation), T. Y. Chu (Thermal Analysis), A. J. Grimley (Thermodynamics), D. A. Powers (Chemistry), and E. R. Copus (Design). Thanks to R. U. Acton and T. M. Kerley for their assistance and support during the experiment assembly and conduct. Also thanks to T. Lee (NRC) for his helpful comments during the preparation of this document.

Lastly, the efforts of B. Lucero and M. Leyva in the preparation of this document is much appreciated.

1 INTRODUCTION

The interaction of molten fuel, fuel cladding, and core structures with a concrete basemat has been recognized since the Reactor Safety Study, WASH-1400, as important aspects of severe reactor accidents.[1] An assessment of the physical source term resulting from these interactions is desirable if a comprehensive evaluation of the risks posed to reactor containments and engineered safety systems are to be made. Consequently, if the pressure load applied by the molten core debris-concrete interactions (possibly coupled with other physical events) should fail containment, a source of radioactive release to the environment would be realized. Over the past several years, an intensive study of these core debris-concrete interactions has been sponsored at Sandia National Laboratories by the Containment Systems Research Branch of the NRC's Office of Nuclear Regulatory Research.[2,3,4,5]

A brief review of past experimental investigations of molten debris-concrete interactions shows two major categories:

1. those experiments[6,7,8] conducted with simulant material such as dry ice, plexiglass, or water and

2. experiments[2,3,4,5] conducted principally with high-temperature metallic materials and concrete.

The advantage of the first group of experiments is the possibility of observing the interaction zone between the simulant concrete and molten debris. However, the fundamental physical processes of high-temperature heat transfer with an ill-defined ablating material, such as concrete, cannot be realized because it is not possible to match the relevant thermophysical properties and the interactions they produce. On the other hand, experiments within the second category provide actual data of the physical mechanisms of heat transfer and the physical source terms, such as combustible gas generation, aerosol generation rates, and fission-product transport from the molten debris.

Past category two experiments were principally investigating the global effects of molten-debris concrete interactions. The principal thrust of the experiments was the broad quantification of the physical processes which may impact containment integrity. These initial experiments provided investigators with an understanding of the principal phenomena and led to the development of two important severe accident analysis codes:

1. The CORCON[9,13] model of core debris-concrete interaction

2. the VANESA[10] model of radionuclide release and aerosol generation.

At the present stage of our understanding of core debris-concrete interaction, primarily steel melts and their global behavior had been investigated. Since the expected core debris composition ejected from the reactor vessel will certainly contain UO_2, ZrO_2, and Zr metal (as well as steel), it is imperative to investigate the interaction of these prototypic materials with concrete.

The Transient Urania-Concrete Test (TURC) program had been initiated to provide preliminary observations of large scale $UO_2/ZrO_2/Zr$ melt-concrete interactions. The TURC test matrix, shown in Table 1.1, consisted of four experiments: two metallic melt-concrete tests (TURC1T and TURC1SS), a molten UO_2/ZrO_2-concrete test and a $UO_2/ZrO_2/Zr$ metal test (TURC3). In this report the results of the two initial experiments, TURC1T and TURC1SS, will be presented.

The purpose of these experiments was to provide a comparison metallic data base for the oxide laden experiments TURC2 and TURC3, such that possible geometry or experiment design considerations were minimized. In addition, these experiments would provide a vehicle for including the previous extensive data base with the TURC experiments.

This report has the following outline

Chapter 1 is an introduction and overview of the TURC series experiments.

Chapter 2 is a description of the experimental apparatus and procedure.

Chapter 3 presents the results of the TURC1 series experiments.

Chapter 4 provides CORCON comparison with the experiments.

Chapter 5 presents an analysis of the experimental results.

Chapter 6 presents a summary and the conclusions of the experiments and analysis.

Table 1.1

TURC Test Matrix

Experiment	Molten Debris	Initial Debris Temperature °K	Initial Debris Mass Kg	Concrete
TURC1T	Fe-Al_2O_3	~2700	200	LCS
TURC1SS	S.S.304	2350	200	LCS
TURC2	UO_2/ZrO_2	2800	200	LCS
TURC3	$UO_2/ZrO_2/Zr$	2600	200	LCS

2 EXPERIMENT DESCRIPTION

2.1 OVERVIEW OF EXPERIMENTAL FACILITIES

The experimental facility for conducting TURC1T and TURC1SS is shown schematically in Figures 2.1 and 2.2. The facility consists of two major components: (1) the melt generator in which the melts were produced; and (2) the interaction chamber where the molten debris-concrete interaction occurs.

The melt generators for the experiments differ significantly due to the method of producing the molten debris. The molten debris used in TURC1T is the reaction product of an iron oxide-aluminum thermite reaction, whereas the TURC1SS experiment utilized molten stainless steel produced by standard induction heating techniques. Details of the melt generators design and melt parameters are discussed in Section 2.2.

Once the melt has been produced, the molten debris is teemed down into the experiment crucible, located within a 13 m^3 interaction chamber.

After the teeming process is completed, the top orifice of the crucible is sealed with a sliding portcullis. Reaction products generated during the interaction are vented through an exit port and piped out of the interaction chamber into the gravel filter.

The crucible utilized in these experiments is of a new design and purpose. The crucible consists of an instrumented concrete slug cast at the base of a MgO annulus. The crucible design permits only axial ablation of the concrete slug. Thus, reaction products of the melt-concrete interaction will pass upward through the melt pool and be released, providing data consistent with conditions found at a horizontal surface in a reactor cavity. Details of the crucible fabrication and materials are discussed in Section 2.3.

The instrumentation of the experiment consisted of embedded thermocouples within the interaction crucible, discrete sampling of evolved gases, and aerosol instrumentation.

In order to evaluate the transport of fission products during melt-concrete interaction, various chemical species, listed in Table 2.1, were added to the melts; and samples of aerosols evolving from the melt pool were taken. The instrumentation utilized during the experiments is described in further detail in Section 2.4.

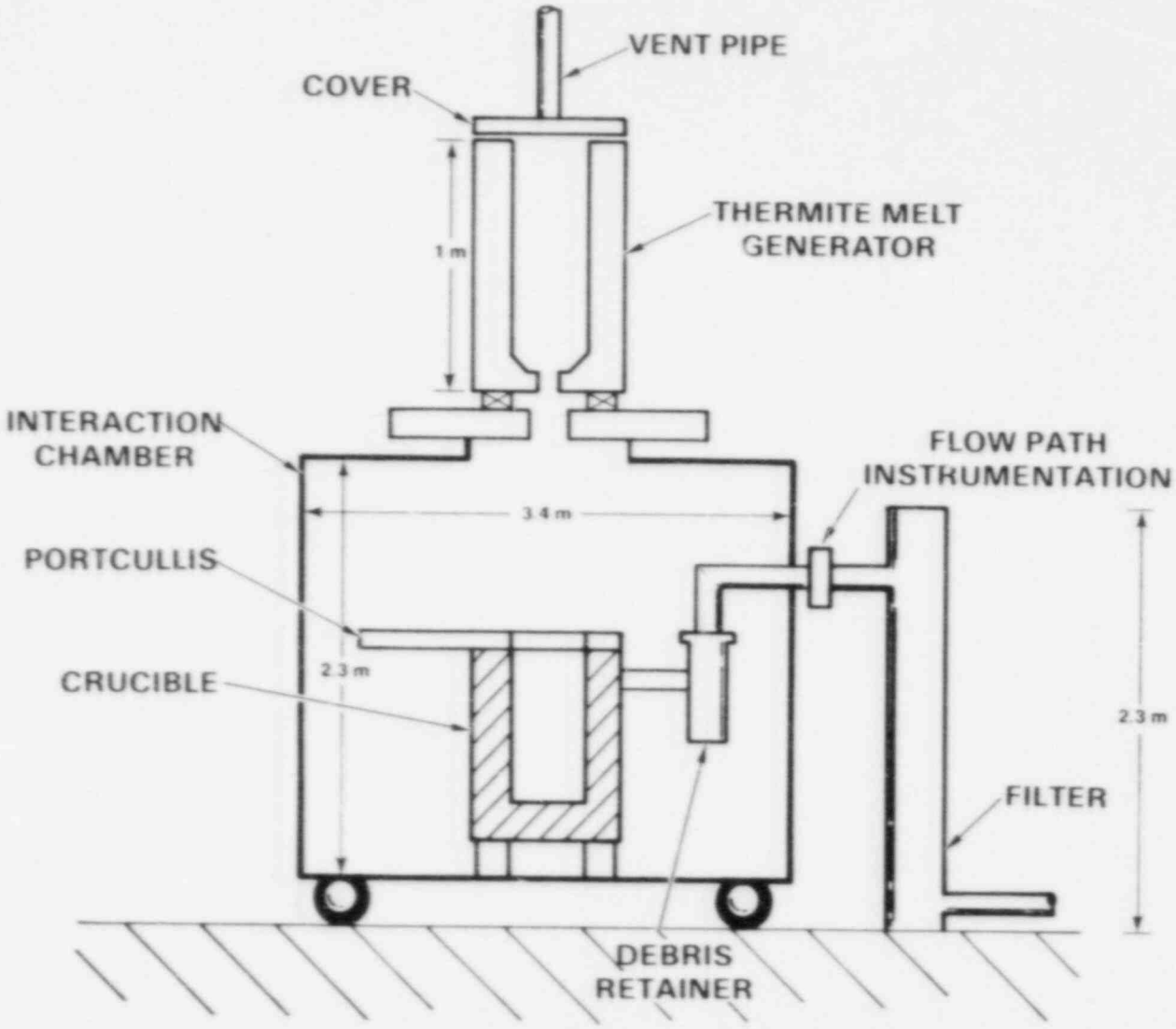

Figure 2.1 TURC1T Experimental Facility

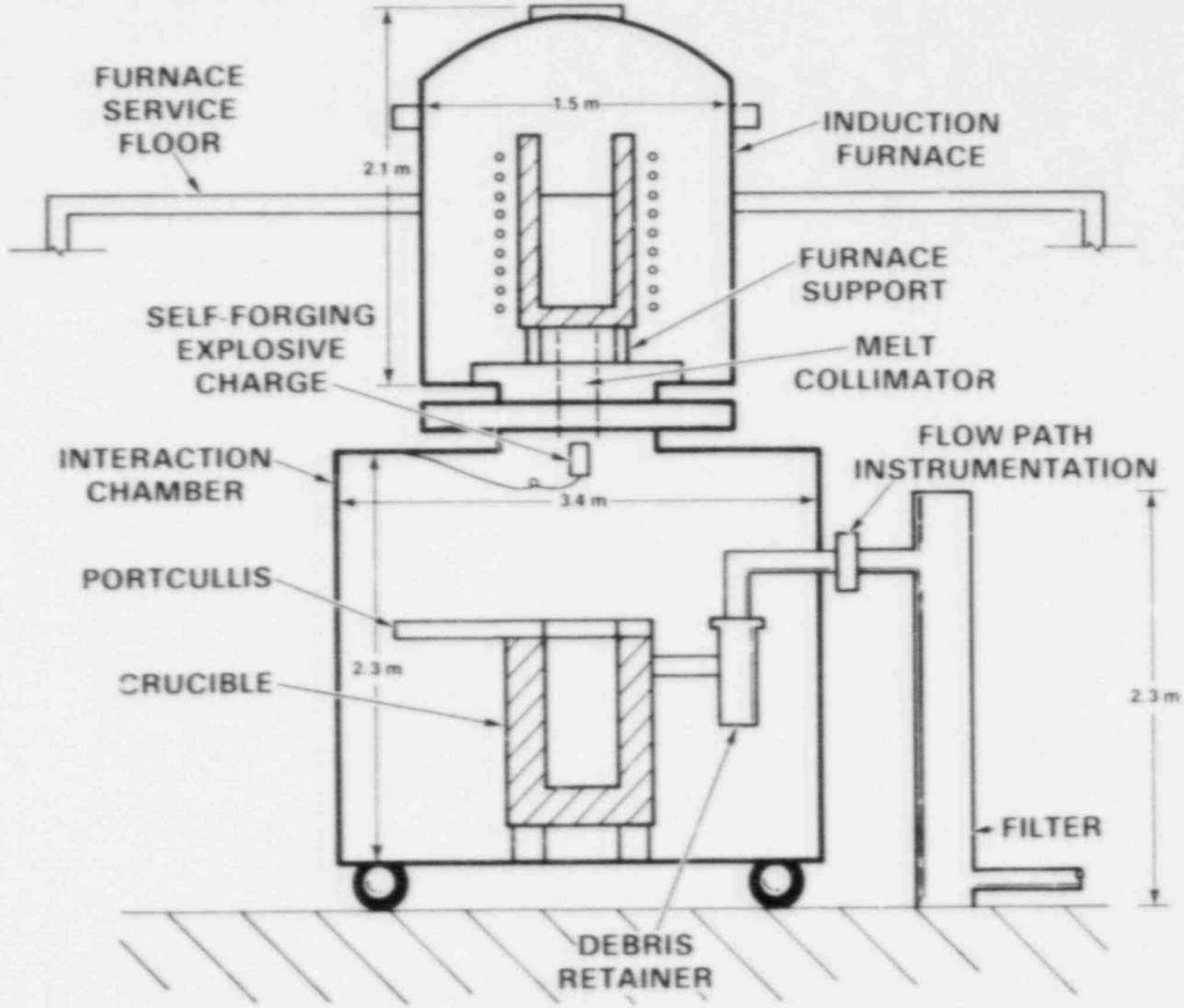

Figure 2.2 TURCISS Experimental Facility

Table 2.1

TURC1T and TURC1SS Fission-Product Mocks

Fission Product	Quantity	Category
Te	1 kg*	Chaleogens
Mn	1 kg**	Early Transition Elements
Mo	1 kg**	Early Transition Elements
CsI	1 kg*	Alkali Metals/Halogens
BaO	1 kg**	Alkaline Earths
ZrO_2	1 kg**	Tetravalents
CeO_2	1 kg**	Tetravalents
La_2O_3	1 kg**	Trivalents
Ni	1 kg**	Platinoids

*Loaded into experimental crucible
**Loaded into melt generator

2.2 EXPERIMENT MOLTEN DEBRIS

2.2.1 TURC1T Melt Generator

The melt generator utilized in the TURC1T experiment is shown in Figure 2.3. The vessel was fabricated from K/R-cast 98* castable MgO material. A cover plate contained a debris shield and vent stack in order to minimize the ejection of molten debris during the thermite burn.

The melt generator was assembled as follows:

1. A 1.3-cm-thick aluminum melt plug was installed at the base of the MgO conical cavity of the melt generator.

2. 200 kg of the Fe_2O_3-Al thermite was loaded and tamped.

3. Pyro-fuse(s) ignitor wire was installed at 5 locations, 1 cm below the top surface of the thermite.

4. The debris shield, cover plate, gasket, and vent stack were installed.

A test of the melt generator was conducted to assure the integrity of the melt generator and cover plate. The thermite was ignited and burned for approximately 30 seconds, followed by a 1- to 2-second delay as the molten thermite attacked the melt plug at the base. The debris flowed out of the generator in approximately 3 seconds. The test indicated that the debris shield and vent stack performed adequately to minimize ejection of debris. An improved gasket at the cover plate would probably eliminate most of the ejected material (estimated to be less than 5% of the molten mass). Note: This test did not contain fission-product mocks.

Posttest examination showed minor cracking of the melt generator's exterior. An examination of the interior cavity showed no evidence of gross quantities of unburned thermite powder. A crust on the wall, 1-cm thick, consisting mostly of oxidic material was uniformly deposited on the interior surfaces. The debris shield was completely destroyed. The cover plate copper gasket had partially failed.

For the TURC1T experiment a new melt generator was fabricated and the copper cover plate gasket was replaced with a graphite foil material.

*Product of the Kaiser Refractory Corp.

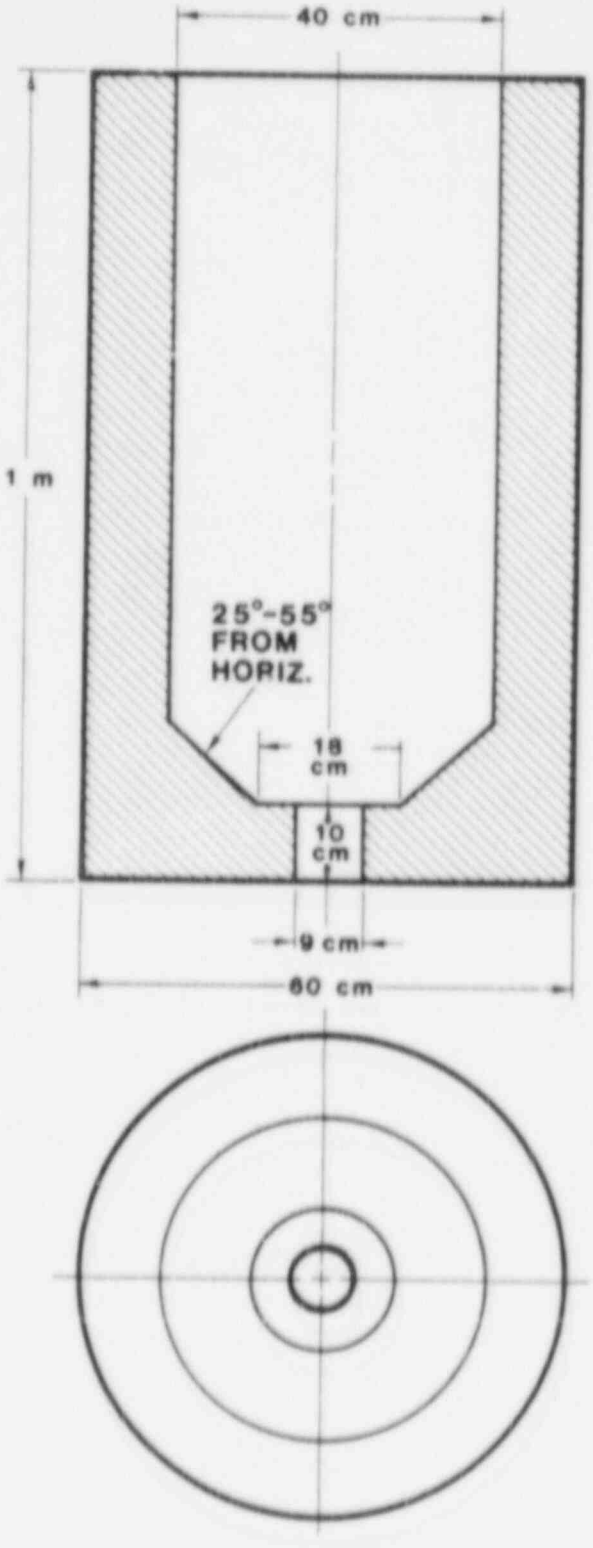

Figure 2.3 TURC1T Melt Generator

2.2.2 TURC1T Melt Composition and Temperature

The melt utilized in the TURC1T experiment consisted of 200 kg of iron-alumina melt and 9 kg of fission-product mocks (listed in Table 2.1).

The estimated initial melt composition of the TURC1T is listed in Table 2.2. The melt was produced by the metallothermitic reaction of iron oxide and aluminum:

$$3\ Fe_3O_4 + 8\ Al \longrightarrow 9\ Fe + 4\ Al_2O_3 + \text{heat} \qquad (2.1)$$

If the reaction is assumed to be stoichiometric, then the energy release is approximately 3624 kJ/kg.

The melt charge is prepared by thoroughly mixing the iron oxide, aluminum, and fission-product mock powders. The iron oxide powder is pretreated by baking the powder at 1000 K for 8 hours. This process has been found to reduce the organic contaminants usually found in the iron oxide powder.

The final composition of the melt after the metallothermitic reaction is only approximately known. In order to determine the composition of the melt delivered to the interaction crucible, a simulation of the thermite reaction with the fission-product mock present was performed.[11]

The VCS algorithm[12] was used to determine the equilibrium mole fractions of forty-eight chemical species at 2700 K. The species chosen were those contained in the original sample augmented by all likely reaction products. These species are listed in Table 2.3 along with their free energies of formation.

The results of the simulation are shown in Table 2.4. The primary driving reaction, Equation 2.1, is found to go nearly to completion (~ 99% of Al is found as Al_2O_3). An examination of the original fission product mock-species shows Ni, Mo, ZrO_2, and La_2O_3 are essentially unchanged (<~1%). BaO and CeO_2 are found to react to a small extent (2.5% and 3.4%, respectively). The largest change comes in the Mn, which is calculated to consume most of the oxygen not reacted in the Fe-Al-O system. It was found that 22% of the Mn reacts to form MnO in the final composition, which in turn may have been vaporized and removed from the melt.

As noted above the iron oxide powder was pretreated by baking the powder at 1000 K for 8 hours. It has been suggested that the pretreat process may have modified the initial composition of Fe_3O_4 to Fe_2O_3 if sufficient oxygen were present.

Table 2.2

TURC1T Initial Chemical Composition

Species	Initial Moles
Fe_3O_4	659.00
La_2O_3	3.07
BaO	6.52
CeO_2	5.81
ZrO_2	8.12
Ni	17.03
Mn	18.20
Mo	10.42
Al	1757.32
O_2	0.15

Table 2.3

TURC1T Melt Chemical Species Examined

Species*	Free Energy of Formation K cal/mole	Species	Free Energy of Formation K cal/mole
O_2(g)	0.	Mn(1)	5.868E0
La(s)	2.737E1	MnO(1)	-3.735E1
La(1)	0.	MnO(s)	-2.938E1
La_2O_3(1)	-2.480E2	Mn_3O_4(1)	-8.170E1
La_2O_3(s)	-2.469E2	Mn_3O_4(s)	-8.120E1
Ce(s)	2.674E1	Mo(s)	0.
Ce(1)	0.	Mo(1)	0.607E0
CeO_2(1)	-1.180E2	MoO(s)	3.147E1
CeO_2(s)	-1.294E2	MoO_2(s)	-3.492E1
BaO(s)	-4.659E1	MoO_2(s)	-2.443E1
BaO(1)	-6.085E1	MoO_3(s)	-4.723E1
BaO(s)	-5.832E1	Fe(s)	1.504E0
Ba(s)	0.	Fe(1)	0.
Ba(1)	8.995E0	Fe(s)	1.178E1
ZrO_2(s)	-7.664E1	FeO(1)	-2.656E1
ZrO_2(1)	-1.401E2	FeO(s)	-2.017E1
ZrO_2(g)	-1.418E2	Fe_3O_4(s)	-6.054E1
Zr(1)	0.	Fe_3O_4(1)	-7.567E1
Zr(s)	1.346	Al(s)	1.684E0
Ni(1)	0.	Al(1)	0.
Ni(s)	8.902E0	AlO(s)	-2.716E1
NiO(1)	-2.132E0	AlO_2(s)	-4.385E1
NiO(s)	-2.134E0	Al_2O_3(1)	-1.980E2
Mn(s)	0.	Al_2O_3(s)	-1.943E2

*S: solid
1: liquid
g: gas

Table 2.4

Calculated TURC1T Melt Chemical Species at 2700 K

Species*	Equilibrium Moles	Mole Fraction
Fe(1)	1.95E+03	6.65E-01
Al_2O_3(1)	8.69E+02	2.96E-01
FeO(1)	2.46E+01	8.37E-03
Ni(1)	1.70E+01	5.80E-03
Mn(1)	1.42E+01	4.84E-03
Mo(1)	1.04E+01	3.55E-03
ZrO_2(1)	8.11E+00	2.76E-03
BaO(1)	6.36E+00	2.17E-03
CeO_2(1)	5.61E+00	1.91E-03
La_2O_3(1)	3.06E+00	1.04E-03
Al(1)	1.84E+01	6.28E-03
MnO(1)	3.99E+00	1.36E-03
Ce(1)	1.98E-01	6.77E-05
Ba(1)	1.59E-01	5.40E-05
La(1)	1.04E-02	3.53E-06
Zr(1)	4.68E-03	1.59E-06
NiO(1)	2.26E-03	7.68E-07
Fe_3O_4	0.0	0.0
Mn_3O_4(1)	0.0	0.0

*l = liquid

A comparison of the iron oxide before and after the pretreat process was not performed, but recent experiments performed by Marshall[32] demonstrated the formation of Fe_2O_3 during a similar baking pretreat process.

Since Fe_2O_3 is unstable above 1700 K its decomposition is a source of oxygen to the system. As shown in Table 2.2, the initial chemical composition utilized in the simulation includes excess oxygen which in part was consumed by the Mn. Thus with the exception of Mn, the effect of Fe_2O_3 on the final melt composition is probably minimal.

The temperature of the thermite melt delivered to the interaction crucible is dependent on several factors:

1. The completeness of the metallothermitic reaction.

2. Heat losses to the melt generator during the metallothermitic reaction.

3. Heat losses during the melt teem.

The extent to which the metallothermitic reaction goes to completion will determine the initial (adiabatic) temperature of the melt. Figure 2.4 shows the calculated melt temperature versus extent of reaction under adiabatic conditions. Powers[5] concluded that the temperature of the melt is limited by the vaporization of one or more of the reaction products. As shown in Figure 2.4, the boiling of excess aluminum at ~2700 K holds the extent of reaction between 84 and 90 percent. Measurements of the thermite temperature are quite difficult. Wartenbury and Wehner[15] determined the melt temperature by optical pyrometry to be 2673 $\pm$ 50 K. Bogolyubov[16] used shielded thermocouples to obtain a value of 2693 K, thus supporting Powers suggestion of a temperature of 2700 K.

The thermite burn in TURC1T took 23 seconds to complete. During this time, the melt was in contact with the MgO wall of the melt generator, heating the wall and thus cooling the melt. To ascertain the effect of this contact, a two-dimensional finite difference heat transfer model was utilized to calculate heat transfer into the MgO wall. The model assumed that the melt temperature was uniform and that the properties of the melt were constant over the temperature range 2500 to 3000 K. The MgO wall was heated by convection from the melt. Using the correlation by Seban and Shimazaki:[7]

$$Nu = 5.0 + 0.025\ Pe^{0.8} \qquad (2.2)$$

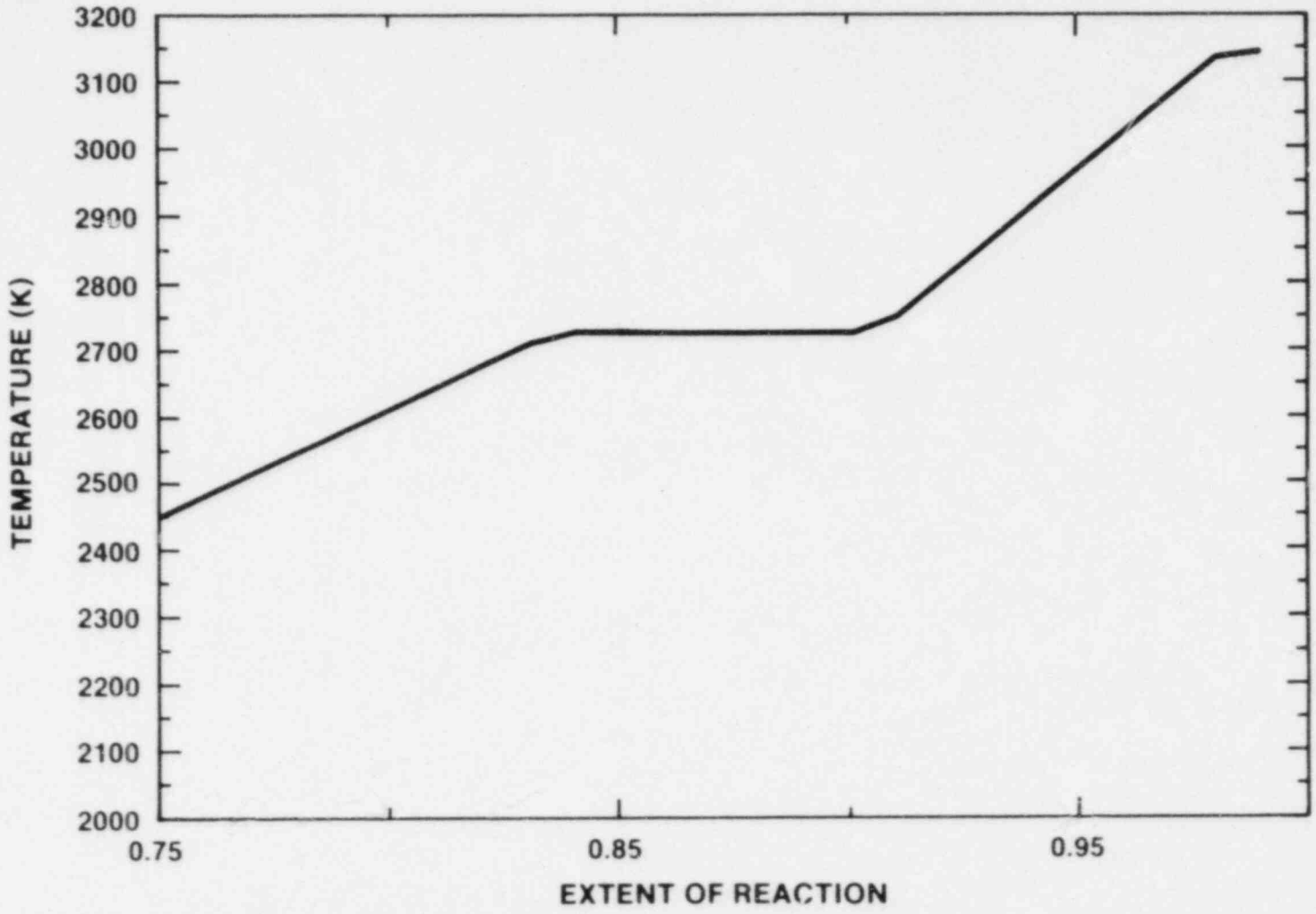

Figure 2.4 Thermite Temperature vs Extent of Reaction

for liquid metals where Nu and Pe are the Nussett and Peclet numbers respectively, a heat transfer coefficient of 7000 W/m^2-K was determined. Due to the cover plate, upward radiation heat transfer was assumed negligible. With an initial temperature of 2700 K, the melt was found to cool to 2560 K in 23 seconds.

The transfer of the melt from the generator to the interaction crucible took ~ 3 seconds, radiative heat transfer to the surrounding structure was calculated to cool the melt 40 K more, resulting in an initial melt temperature of 2520 K. This value may represent a lower bound of the melt pool temperature.

2.2.3 TURC1SS Melt Generator

The TURC1SS molten debris was produced by melting 200 kg of type 304 stainless steel within an induction melting furnace shown schematically in Figure 2.2.

The induction furnace, at the Large Melt Facility, is approximately 1.5 meters in diameter and 2.1 meters tall. During normal operation, the furnace pressure was approximately 0.114 MPa. The furnace is purged continuously with argon at a nominal rate of 14.1 m^3/hr (equivalent to four change-overs of the furnace atmosphere per hour). A vacuum pump and regulating valve are used to keep the furnace at the operating pressure.

The stainless steel for this melt experiment was contained in an alumina crucible. The crucible was 0.66 m high with an internal depth of 0.64 m. The crucible inside and outside diameters were 40 cm and 46 cm, respectively.

The induction coil for the nominal 1 kHz, 280 kW power supply had two electrical sections with six turns in each section. The coil was 0.56 m in length and 0.53 m in diameter. All coil surfaces had a flexible insulating coating applied by the manufacturer (Inductotherm Corp.) to minimize arcing between coil turns. The spacing between the coil and the crucible was filled with a dry magnesium oxide powder.

The teeming process of the melt from the crucible is accomplished by firing an explosive self-forging projectile into the base of the alumina crucible. The explosive is mounted on a support tube just below the transfer section between the furnace chamber and the interaction chamber (see Figure 2.2). The explosive charge is remotely armed and fired. The explosive is approximately 3.8 cm in diameter and 7.5 cm tall. Alignment of the explosive is aided by a neon laser placed between two "sights" mounted on the explosive.

The explosive projectile impacts the alumina crucible forming a uniform 7.0-cm diameter hole. The melt then teems out

under its own head and the slight overpressure of the furnace. The teeming is complete in approximately 3 seconds.

2.2.4 TURC1SS Initial Melt Composition and Temperature

As described above, the melt charge utilized in the TURC1SS experiment consisted of 202 kg of stainless steel type 304 plus several chemical species representing possible fission-product species. The chemical composition of the melt loaded into the melt generator is shown in Table 2.5. At the melt temperature of 2350 K and the inert furnace atmosphere, no change in the melt composition is expected to occur.

A posttest examination of the Al_2O_3 melt crucible within the furnace shows considerable side wall erosion or melting. The eroded material apparently floated to the top of the molten metallic phase. Due to upward heat losses, the Al_2O_3 formed a thin crust. A mass balance was attempted to determine the quantity of Al_2O_3 material that may have been teemed into the interaction crucible. The measurement was difficult due to the physical condition of the crucible and support hardware. An upper limit of 2.5 w/o Al_2O_3 may have been teemed along with the metallic phase into the interaction crucible.

Temperature measurements of the molten steel prior to teeming were attempted by standard pyrometer techniques as well as with Al_2O_3 sheath W-Re thermocouples. Temperature measurements above 2000 K were unsuccessful. The thermocouple sheath had ruptured due to physical loads of the shifting mass during melting. The pyrometer sight tube used also shifted during the melting of the metallic mass resulting in poor optical alignment. Pyrometer measurements of the top surface of the molten pool were then made; but due to upward heat losses, the surface temperature was apparently below the range of the pyrometer (1500 K).

The melt temperature was estimated to be 2346 K due to the melting and thermal equilibrium with the Al_2O_3 crucible sidewalls during the heating. From the erosion pattern of the Al_2O_3 melt crucible it was apparent that the metallic phase was well stirred during heating. Due to radiative cooling during melt teem, the initial melt pool temperature was estimated to be 2300 K.

2.3 EXPERIMENT INTERACTION CRUCIBLE

2.3.1 Interaction Crucible Description and Fabrication

The crucible used in the TURC test was of a new design and purpose. The crucible, shown schematically in Figure 2.5, consisted of an instrumented concrete slug 41 cm in diameter and 30 cm in height, cast at the base of a MgO annulus, 70 cm outside diameter and 1.2 meters in height.

Table 2.5 TURC1SS Initial Melt Composition

Species	Gram-Moles
Fe	2517.5
Cr	692.4
Ni	289.6
Si	142.4
Mn	72.8
Mo	10.4
ZrO_2	8.12
BaO	6.5
CeO_2	5.8
La_2O_3	3.1
P	2.6
S	2.5
Te*	7.8
Cs/I*	3.85

* These species were placed within the interaction crucible cavity.

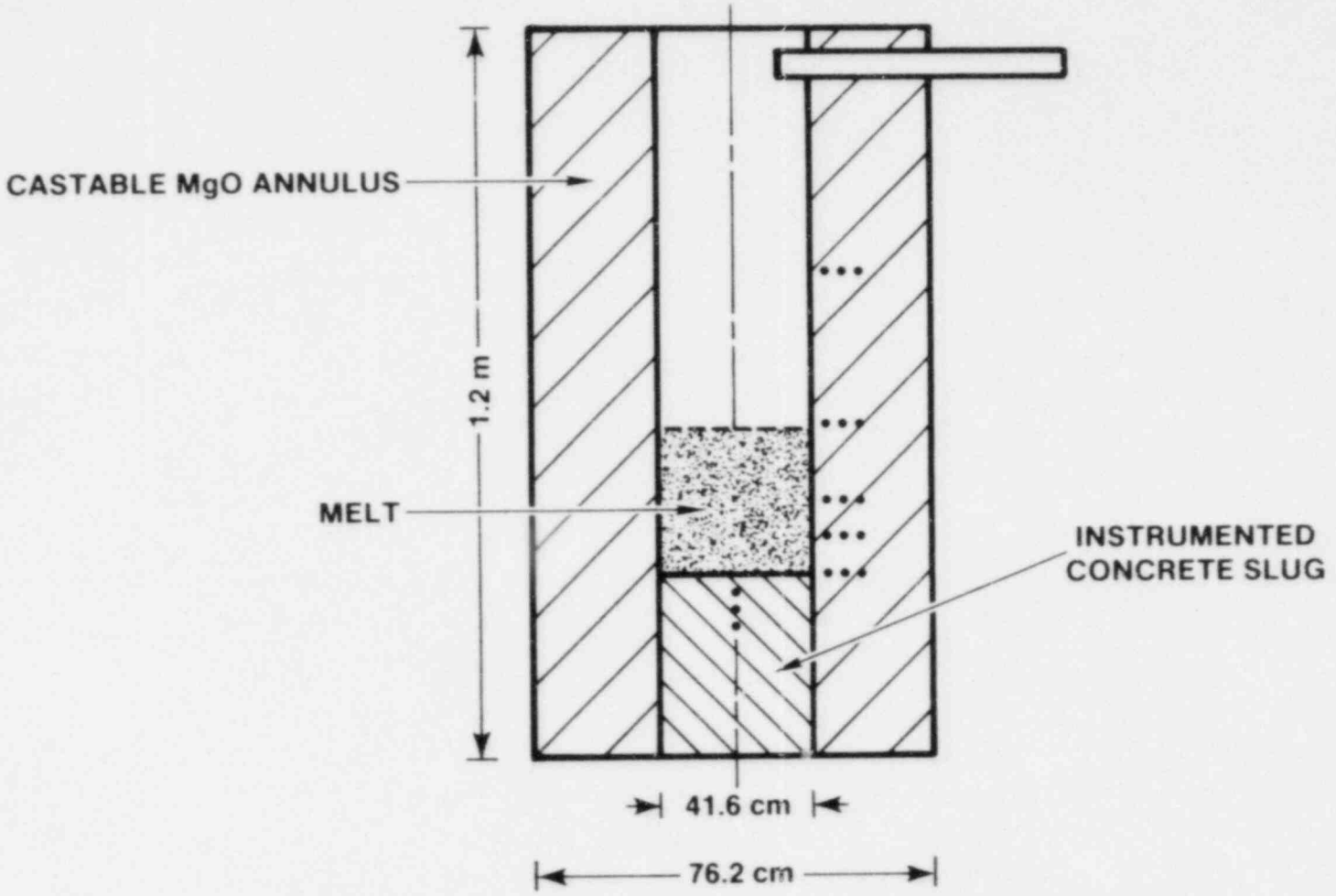

Figure 2.5 Interaction Crucible

The purpose of the design is to provide only axial or one-dimensional ablation of the concrete slug, hence the reaction products evolved during the interaction phase of the experiment must pass upward through the melt to be released. These conditions would be consistent with conditions found at a horizontal surface in the reactor cavity.

By eliminating a concrete ablative sidewall, reaction products generated at the core debris-concrete interaction can be quantified, without the influence of reaction products generated at different thermophysical conditions found at the sidewalls. The crucible design has been labeled as the "1-D" crucible.

The 1-D crucible is fabricated in two major steps: first the construction of the MgO annulus and second the casting of the concrete slug.

The MgO annulus was constructed using SONOTUBE* forms. The forms are right circular cylinders manufactured from paper. The MgO annulus, shown in Figure 2.6, was fabricated by arranging two sonotube forms in a concentric array in which a plywood base was installed. This was followed by the installation of the 7.5-cm diameter exhaust tube and the thermocouple arrays.

The thermocouple arrays, shown in Figures 2.7 and 2.8, consisted of a 5-cm-diameter cylinder of the MgO castable material, in which four holes were drilled at 1-cm intervals. K-type, 1.5 mm diameter, thermocouples were installed in this fixture. The fixture was then installed at predetermined locations (see Table 2.12) within the annulus form. In the region where the concrete slug would be cast, a wire wrap 1.5-mm diameter, by 2-cm pitch, was installed in order to improve the bonding between the concrete slug and the MgO annulus.

Once the form was prepared, the MgO castable, described in the following section, was mixed in a clean paddle-type mixer. Once a homogeneous mixture was obtained, the material was hand-loaded into the forms. A high-speed vibrator was utilized to densify the mass. The procedure was repeated until the form was full.

After casting, the annulus was cured at ambient air temperature for three days. Further curing was accomplished by placing a heating element within the central cavity and maintaining a temperature of 473 K for 24 hours, followed by a cooling period of 24 hours.

Once the annulus was cooled to room temperature, the inner SONOTUBE form and wire wrap were removed, and a plywood platform

---

*SONOTUBE forms trademark of the SONOCO Products.

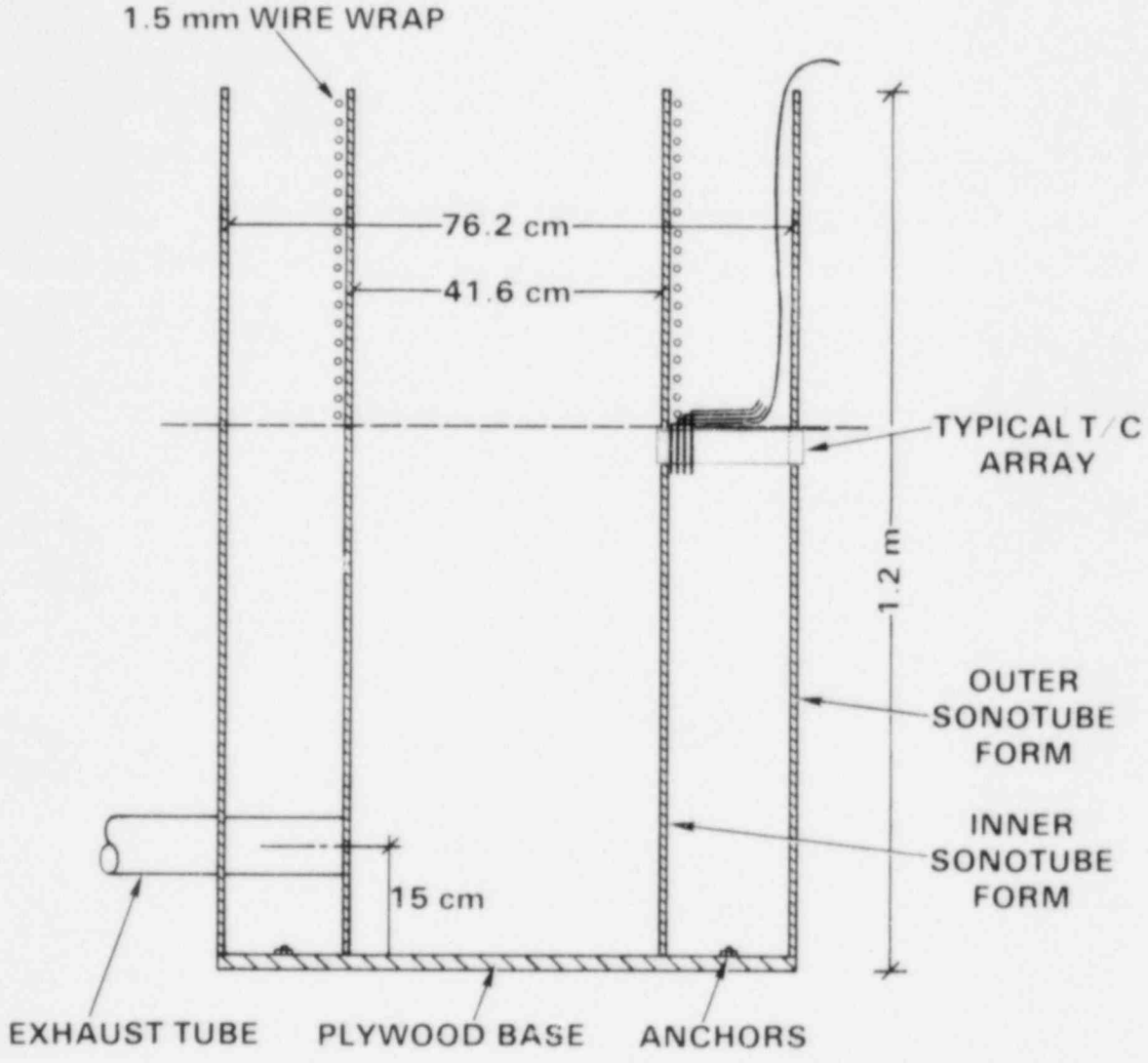

Figure 2.6. Fabrication Details of MgO Annulus

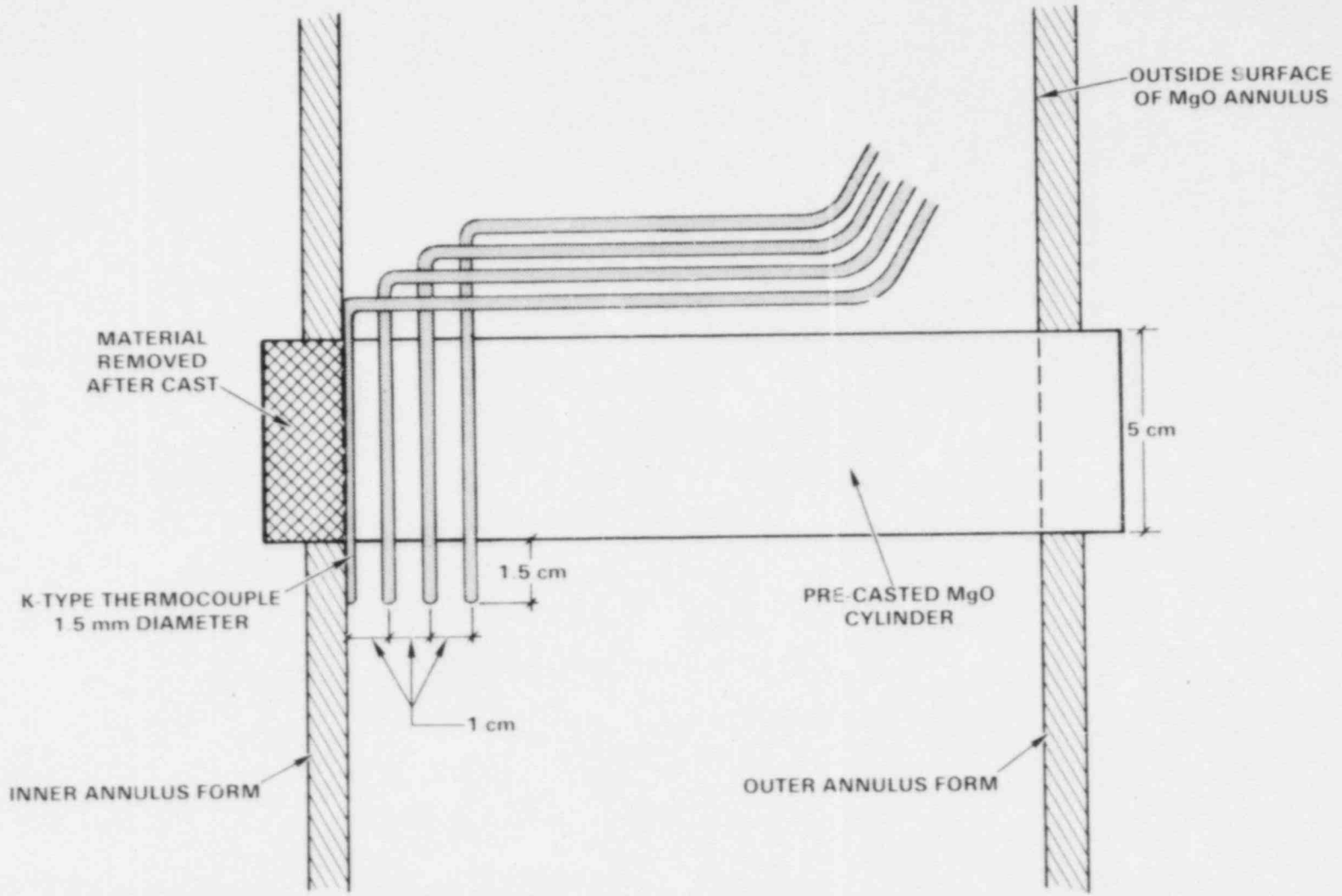

Figure 2.7 MgO Annulus Thermocouple Arrays

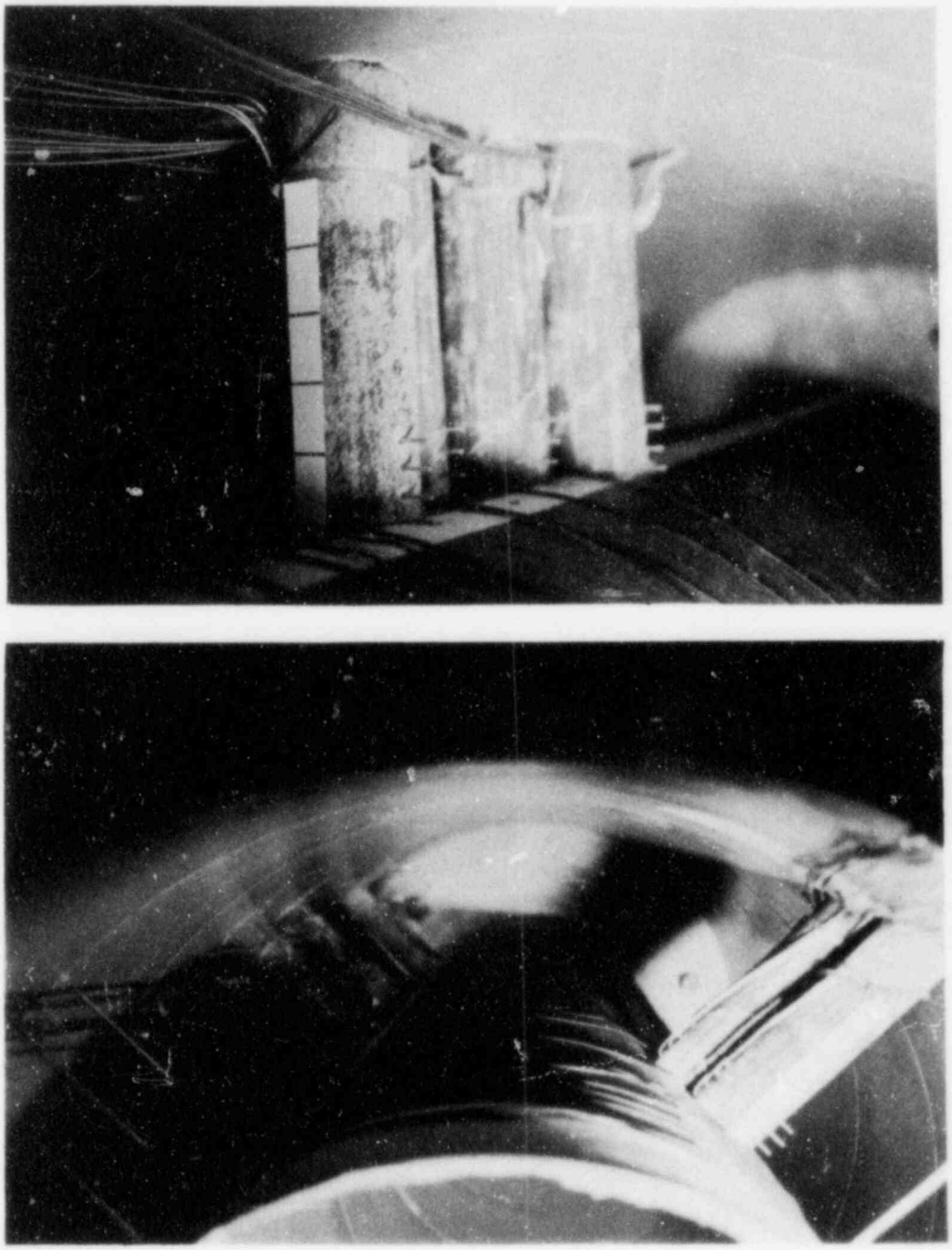

Figure 2.8 MgO Annulus Thermocouple Arrays Installed in Form

was constructed 30 cm from the base of the MgO annulus (this is the same region where the wire wrap was installed). Carefully prepared thermocouple arrays, shown in Figure 2.9, held rigidly in place by a framework of 0.5 mm stainless steel wires, were installed on the platform and structural support was provided from outside the annulus. Careful measurements of the thermocouple locations were documented (Tables 2.12 - 2.14).

The casting of the limestone/common sand concrete (LCS) was performed by mixing the concrete constituents listed in Table 2.6 in a paddle mixer. Once a homogeneous mixture was achieved, three test cylinders were cast and slump measurements made. Details of the measurements and other physical data will be discussed in the next sections. Approximately 0.021 m^3 of concrete was required per crucible. The concrete was allowed to cure for a minimum of 60 days before use. Curing was performed at ambient conditions. No special environmental chamber was utilized.

2.3.2 Crucible Materials

The two major components of the 1-D crucible were limestone/common sand concrete and Kaiser K/R-CAST98** castable MgO refractory. In this section details of the physical and thermal properties of these materials will be presented.

The concrete used in the TURC series of experiments, limestone/common sand, was chosen due to its composition and physical characteristics between that of basaltic (siliceous) and limestone (calcareous) concretes.[3]

Due to the transient nature of the TURC experiments, one becomes acutely aware of the fact that the initial energy in the molten debris is the driving potential behind the debris-concrete interaction. It is also apparent that one of the largest losses of energy from the molten debris occurs during the decomposition and melting of the concrete. Thus, a concrete with a low enthalpy of decomposition and melting is desirable to achieve a prolonged interaction time for a given energy inventory within the melt.

A comparison of the three principal concrete types found in American reactors shows that the basaltic concrete has the lowest enthalpy of decomposition and melting (824 J/g), followed by limestone/common sand (1666 J/g), and limestone (2500 J/g).[3] Thus, based on thermal characteristics, basaltic concrete would be the most desirable concrete for the TURC experiments.

** Product of the Kaiser Refractory Corp.

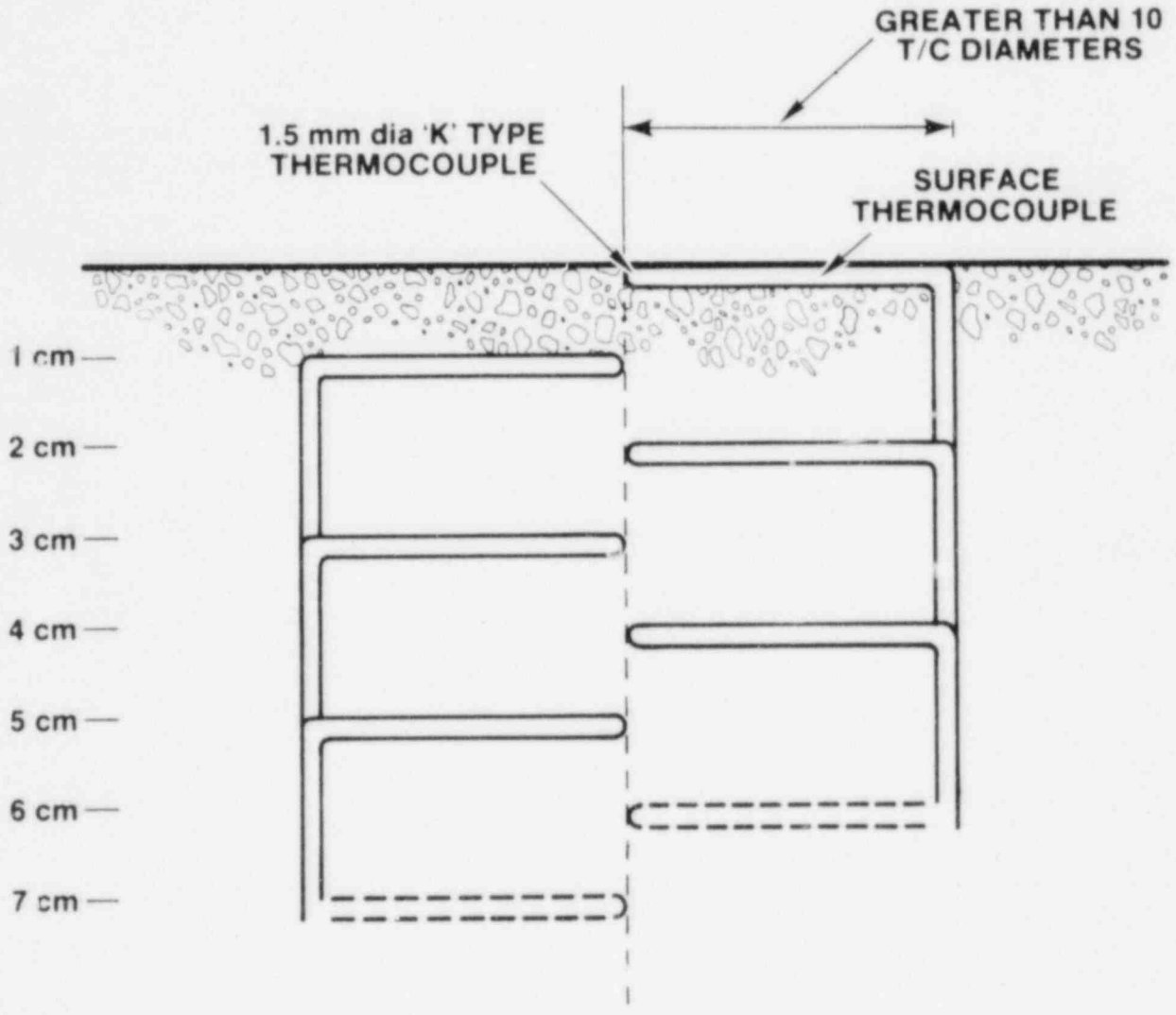

Figure 2.9 Concrete Thermocouple Array Details

Table 2.6

Composition of Limestone/Common Sand Concrete

Item	Proportion	Fraction
Cement, type I & II	42.7 kg	0.15
Water	19.1	0.07
Concrete Sand (common)	93.2	0.33
Aggregate, Limestone 1.9 cm max.	85	0.031
Limestone Sand	42.3	0.14
Air Entrainment Agent (AE)	0.021	
TOTAL	282.3 kg	1.00

Another characteristic most desirable to investigate in these preliminary large-scale molten debris-concrete interaction experiments is the physical source terms of combustible gas production (H_2 and CO) and the transport of fission products from the molten debris. In order to provide an experimental environment in which these source terms could be observed, a significant source of gas release from the decomposing concrete was desirable.

The two major gases released from decomposing concrete are water vapor and carbon dioxide. The water released from all three types of concrete is approximately the same, but the carbon dioxide release is significantly different. Limestone concrete contains the highest CO_2 content of concretes at 35.7 w/o followed by limestone/common sand at 22.0 w/o, and basaltic containing only 1.5 w/o. Based on an experimental gas-release criteria, limestone concrete is the most desirable.

Thus, in order to address both experimental thermal and physical considerations the Limestone Common Sand (LCS) concrete was chosen.

A summary of the concrete casting data for the two experiments is shown in Table 2.7.

A fairly complete description of the chemical, physical, and thermal characteristics of limestone/common sand concrete was presented by Powers.[3] Portions of the Powers data are presented in Tables 2.8 and 2.9 and Figures 2.10 and 2.11.

The mixing, forming, and casting of the concrete follow established procedures for the industry.[18] An air entrainment agent (AE) was added to the concrete mix per ASTM C-494-71 specifications. Additionally, a curing compound was applied to the concrete surfaces. The curing compound, BURKE Res-X,* was applied at the recommended rate of coverage. It forms a thin film that inhibits the evaporation of water from the concrete, thus assuring a constant supply of water for hydration of the Portland cement. The thin film oxidizes and dissipates after exposure to air for 45 to 60 days.

The MgO material used to fabricate the MgO annulus is a commercially available product from Kaiser Refractories. The product identity is K/R-Cast 98. The chemical analysis of the MgO castable is shown in Table 2.10. As one will notice, the main constituent is MgO (~97%). The presence of small quantities

Table 2.7 Concrete Casting Data

Test	Concrete Type	Cure (days)	Cold Compressive Strength, Pcc	
			28 Days	90 Days
TURC1T	LCS	110	282	295
TURC1SS	LCS	80	290	314

*Burke Res-X is a product of Burke Concrete Accessories, Inc.

Table 2.8 Chemical Compositions of the Limestone/Common Sand Concrete and the Concrete Constituents

Oxide	Cement w/o	Limestone/ Common Sand Concrete w/o	Expected Error w/o
Fe_2O_3	4.11	1.44	0.3
Cr_2O_3	0.011	0.014	0.01
MnO	0.08	0.03	0.02
TiO_2	0.2	0.18	0.04
K_2O	0.54	1.22	0.4
Na_2O	0.27	0.82	0.2
CaO	63.5	31.2	1.0
MgO	1.53	0.48	0.5
SiO_2	20.1	35.7	1.5
Al_2O_3	4.2	3.6	0.2
CO_2	ND	22	1.0
H_2O	ND	4.8	0.5
SO_2	1.0	<0.2	0.2

Table 2.9 Stoichiometry of Thermal Events in the Decomposition of Limestone/Common Sand Concrete (Cured 90 Days)

Thermal Events	Limestone/ Common Sand Concrete
Free water (weight %)	2.7 ± 0.3
Enthalpy of free water loss* (KJ/kg)	81.6 ± 9.0
Bound water (weight %)	2.0 ± 0.3
Enthalpy of bound water loss (KJ/kg)	120 ± 20
Carbon dioxide (weight %)	22.0 ± 0.7
Enthalpy of carbon dioxide loss (KJ/kg)	962 ± 50
Free SiO_2 (weight %)	30 ± 2
Enthalpy of SiO_2 phase change (KJ/kg)	3.1 ± 0.5
Melting temperature range (K)	1423 to 1673
Enthalpy of melting (KJ/kg)	500 ± 75

*All enthalpic values are reported as KJ/kg virgin concrete

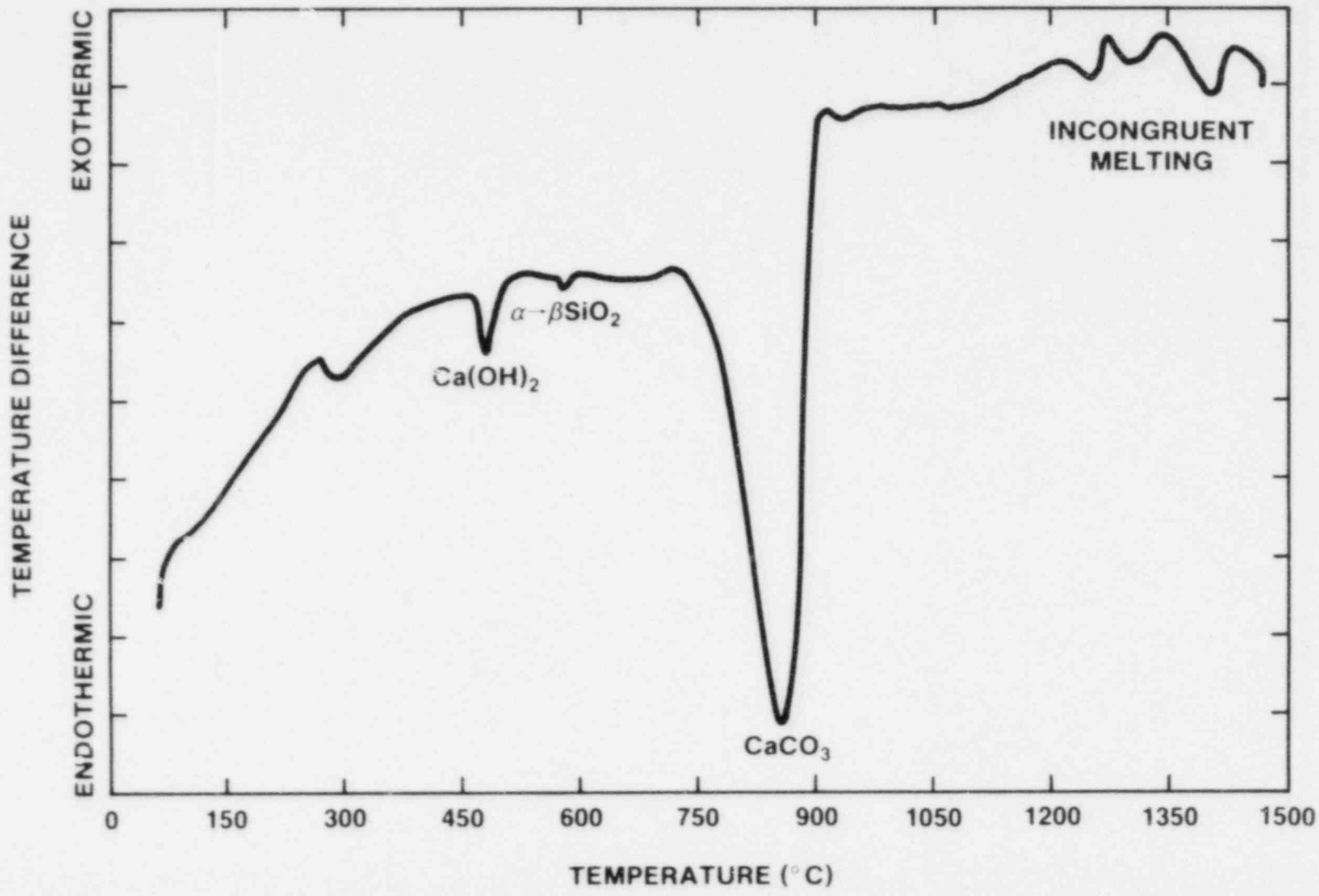

Figure 2.10 Differential Thermogram of Limestone/Common Sand Concrete

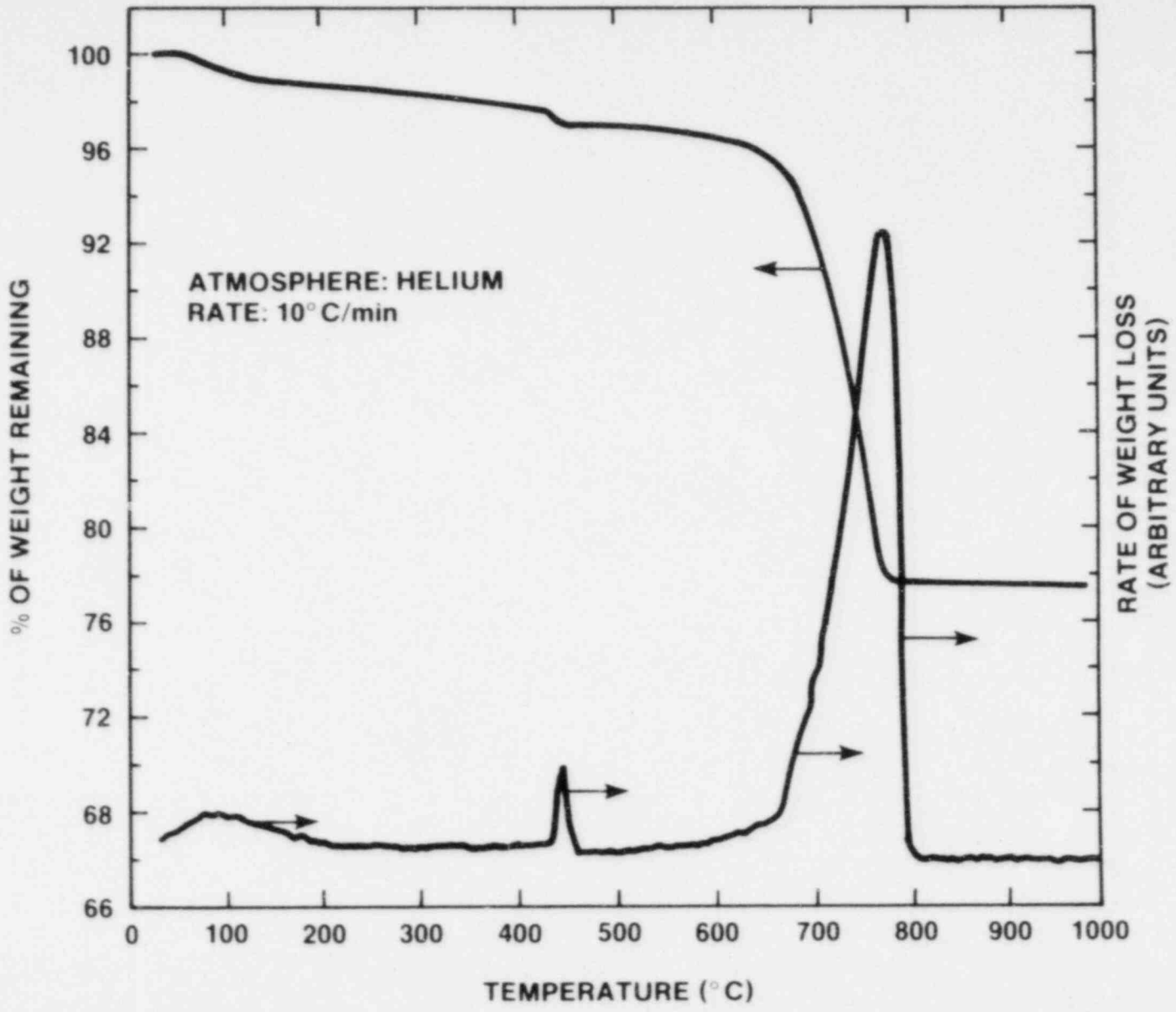

Figure 2.11 Thermogram (TGA) of Limestone/Common Sand Concrete

Table 2.10 Chemical Analysis of MgO K/R-Cast 98

Material	w/o
MgO	97.1
SiO_2	0.4
Al_2O_3	0.1
Fe_2O_3	0.3
CaO	1.0
Cr_2O_3	1.1

of SiO_2, Al_2O_3, Fe_2O_3, CaO, and Cr_2O_3 are believed to have no significant impact on the experiment environment. The density of the cured MgO castable is 2950 kg/m^3, with a cold crushing strength of 33 MPa.

The thermal characteristics of the MgO K/R-Cast 98 material were analyzed using thermogravimetric analysis (TGA). This analysis was performed with a Dupont 790 thermal analysis apparatus with a 1870 K DTA cell and Model 950 TGA attachment. The TGA was performed in dry air with a flow rate of 50 cc/min. The heating rate was 10 K/min from ambient room temperature to 1400 K.

Three MgO K/R-Cast 98 samples were analyzed. Sample 1 (TGA #1) was taken directly from the shipping sack; sample 2 (TGA #2) was cast with 5 w/o water, air cured 3 days, followed by baking at 470 K for 24 hours, then allowed to air-cool for an additional 24 hours. This sample follows the recommended fabrication process of the TURC MgO annulus. The third sample (TGA #3) was cast with 5 w/o water, air-cured for 6 days, but no oven drying was performed. The thermograms produced for the three samples are shown in Figures 2.12 - 2.14. Weight losses correlated with release of free and bounded water were found in all three samples. TGA of sample 1 showed a 4.5% weight loss at ~373 K, indicating that the material may be quite hygroscopic. The apparent increase in weight from 950 K and above may be due to instrument drift or chemical oxidation of Fe_2O_3 within the sample.

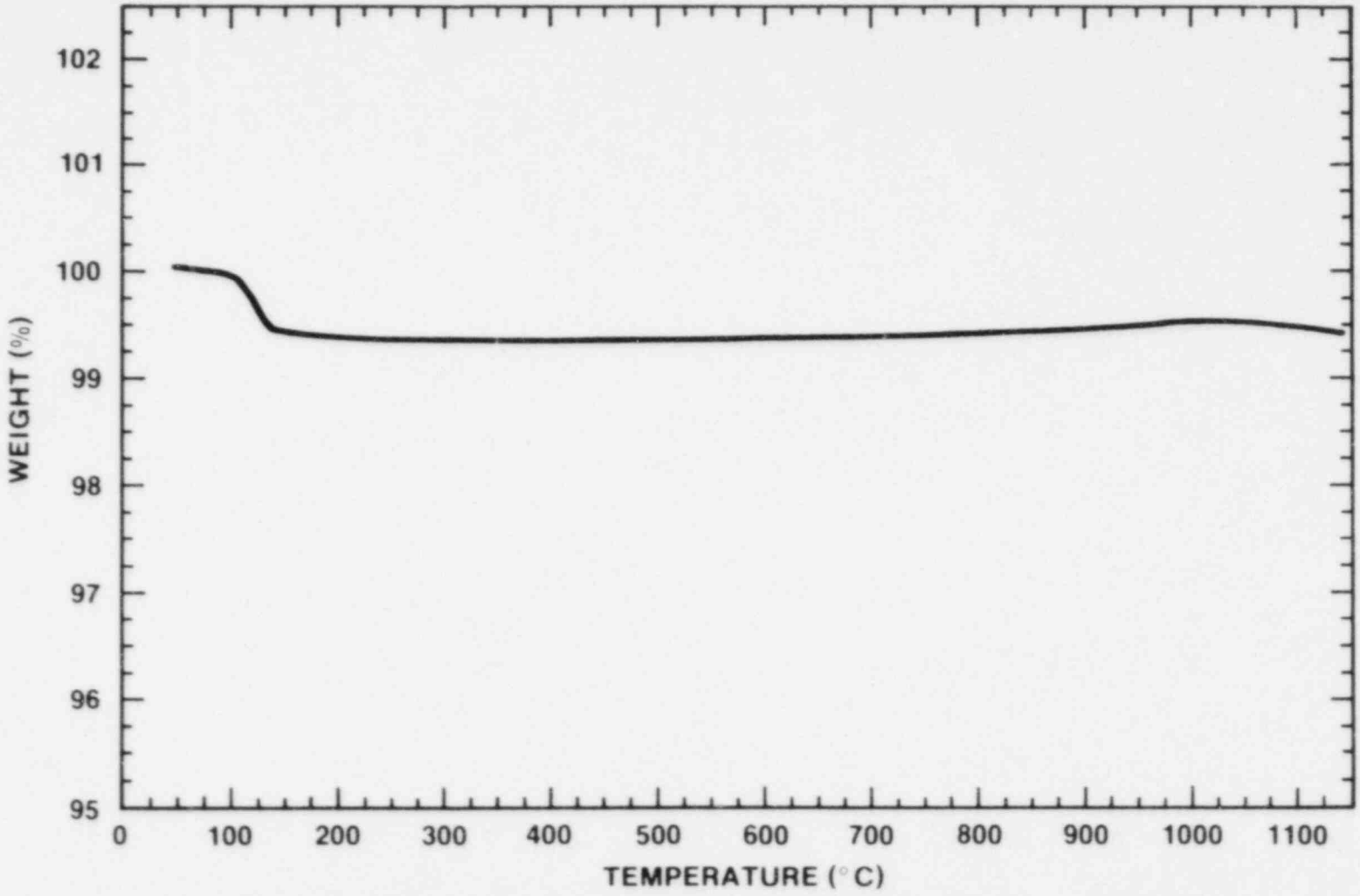

Figure 2.12 Thermograph of MgO K/R Cast 98; Sample 1: As Received Material

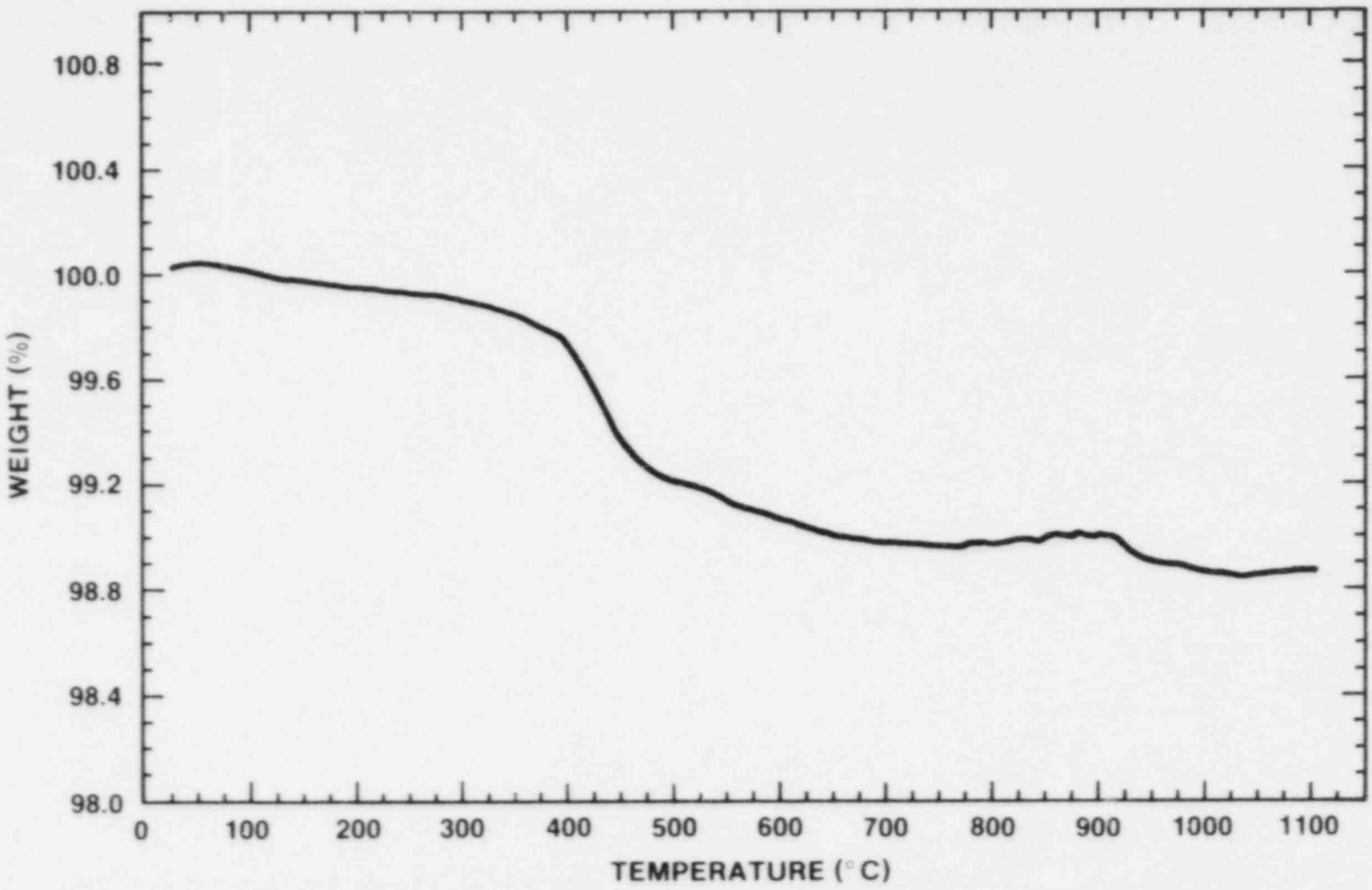

Figure 2.13 Thermograph of MgO K/R Cast 98; Sample 2: Air-Cure 24 Hours, Baked at 470 K for 24 Hours

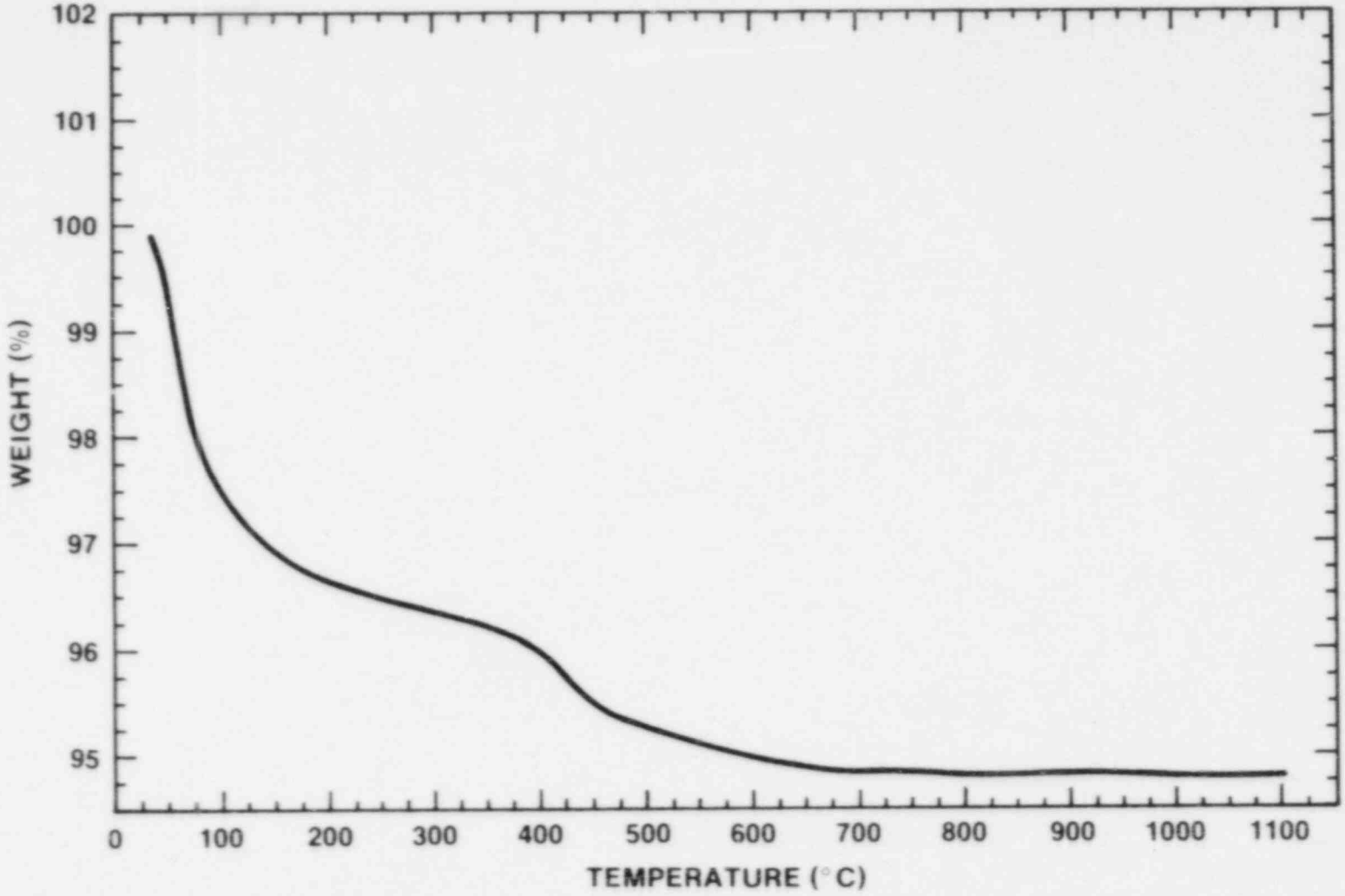

Figure 2.14 Thermograph of MgO K/R Cast 98; Sample 3: Air Cure Only

TGA of sample 2 shows a 0.2 w/o loss due to release of water between ambient temperature and 700 K. From 700 K and 1000 K, an additional 0.8 w/o loss was observed, probably due to the decomposition of brucite.

TGA of sample 3 released approximately 4 w/o water between 323 K and 700 K, followed by approximately a 1 w/o loss between 700 K and 1000 K, once again due to the decomposition of brucite.

The thermal properties of the castable K/R-Cast 98 were investigated. Experiments were conducted to study the thermal response of the MgO to intense heating conditions similar to those expected during an experiment.

Experiments[19] were carried out at the Sandia Solar Tower where MgO specimens were subjected to incident solar fluxes in the range of 6.5×10^5 W/m^2 to 1.4×10^6 W/m^2. A test specimen 45 cm x 45 cm x 8 cm was cast of the K/R-Cast 98 material. The test specimen was well instrumented with 17 1.5 mm diameter type K thermocouples, located from 0.3 cm to 6.3 cm below the exposed surface. The test specimen was mounted in a frame compatible with the Solar Tower assemblies. The incident flux was monitored by heat flux gauges deployed along the top and side of the test specimen. The back of the test specimen was well insulated in order to approach an adiabatic boundary condition.

The data was analyzed by the "PROPTY" code developed by J. V. Beck.[20] The code determines the thermal conductivity of a material that fits a set of temperature response curves for specific spacial interval and boundary conditions.

A typical thermal history is shown in Figure 2.15. As one can see, the temperature rise is interrupted at 373 K. This is due to the release of the free water in the castable material. The material continued to be heated until approximately 1673 K, then the solar heat flux was removed and the test specimen was allowed to cool.

The presence of the free water within the castable material causes some problems in the analysis of the experimental data. As shown in Figure 2.16 the predicted thermal history utilizing the determined material properties from "PROPTY" poorly predicts this region.

The PROPTY prediction of the thermal conductivity of the MgO is shown in Figure 2.17. A cneck on the relative accuracy of the values of the conductivity is demonstrated by comparing the predicted thermal response with the actual experimental data. As shown in Figure 2.16, excellent agreement is achieved. The absolute values of thermal conductivity (k) are dependent on the initial value chosen for k at a fixed temperature. Within the

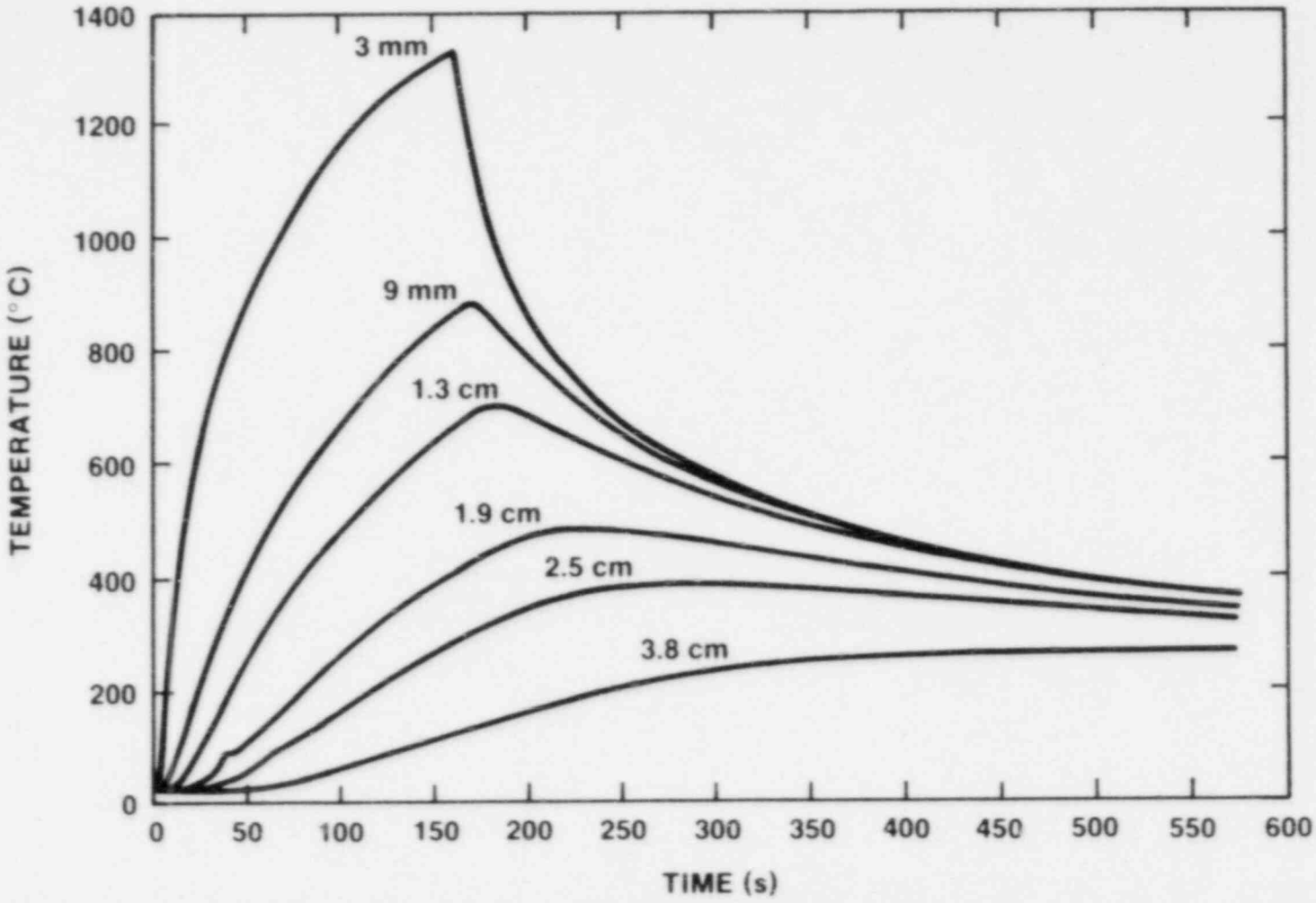

Figure 2.15 Representative Temperature History of MgO Sample Exposed to Solar Heat Flux 1.4 x 10^6 w/m^2

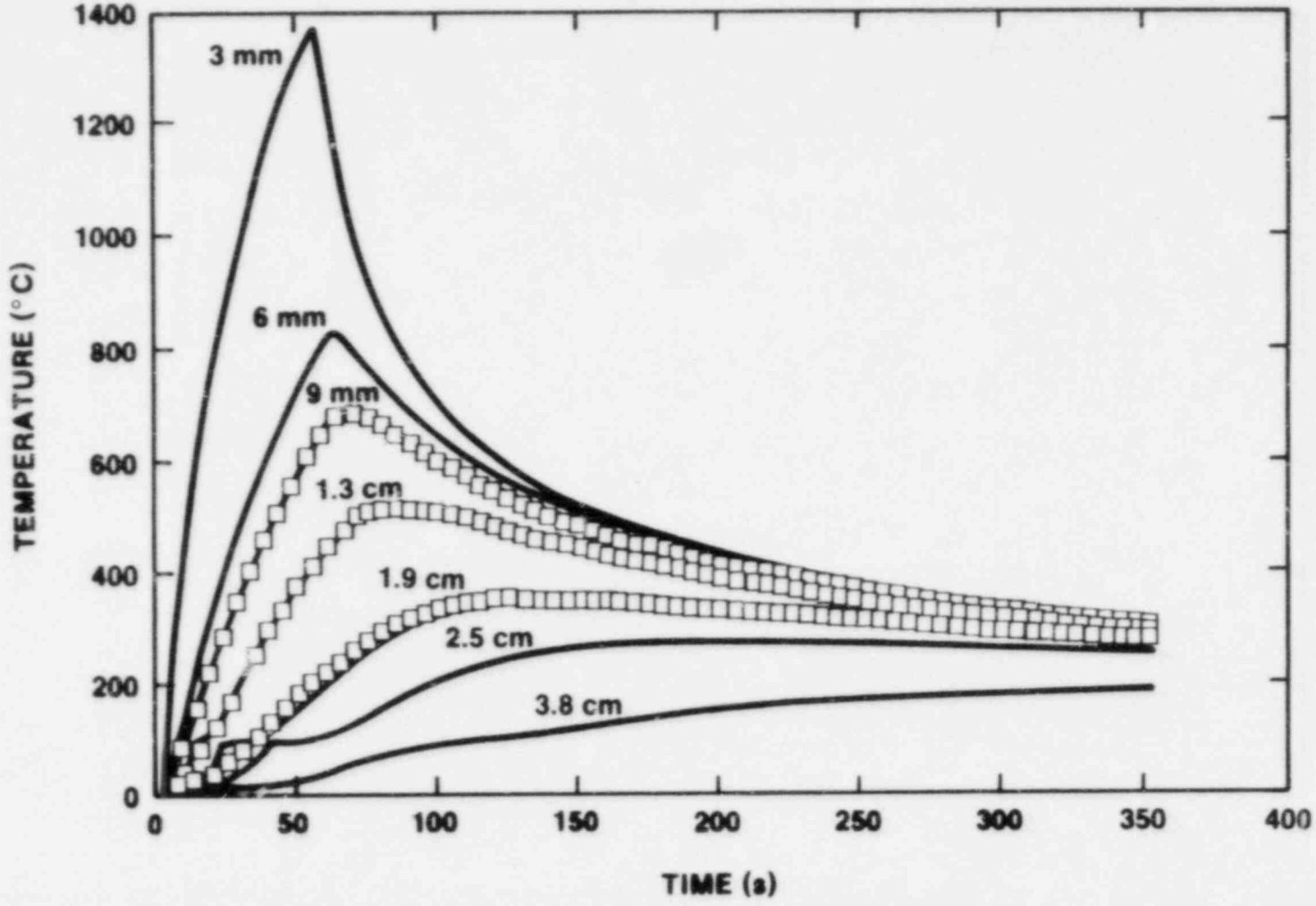

Figure 2.16 Comparison of Experiment Thermal History and Predictions of the "PROPTY" Code

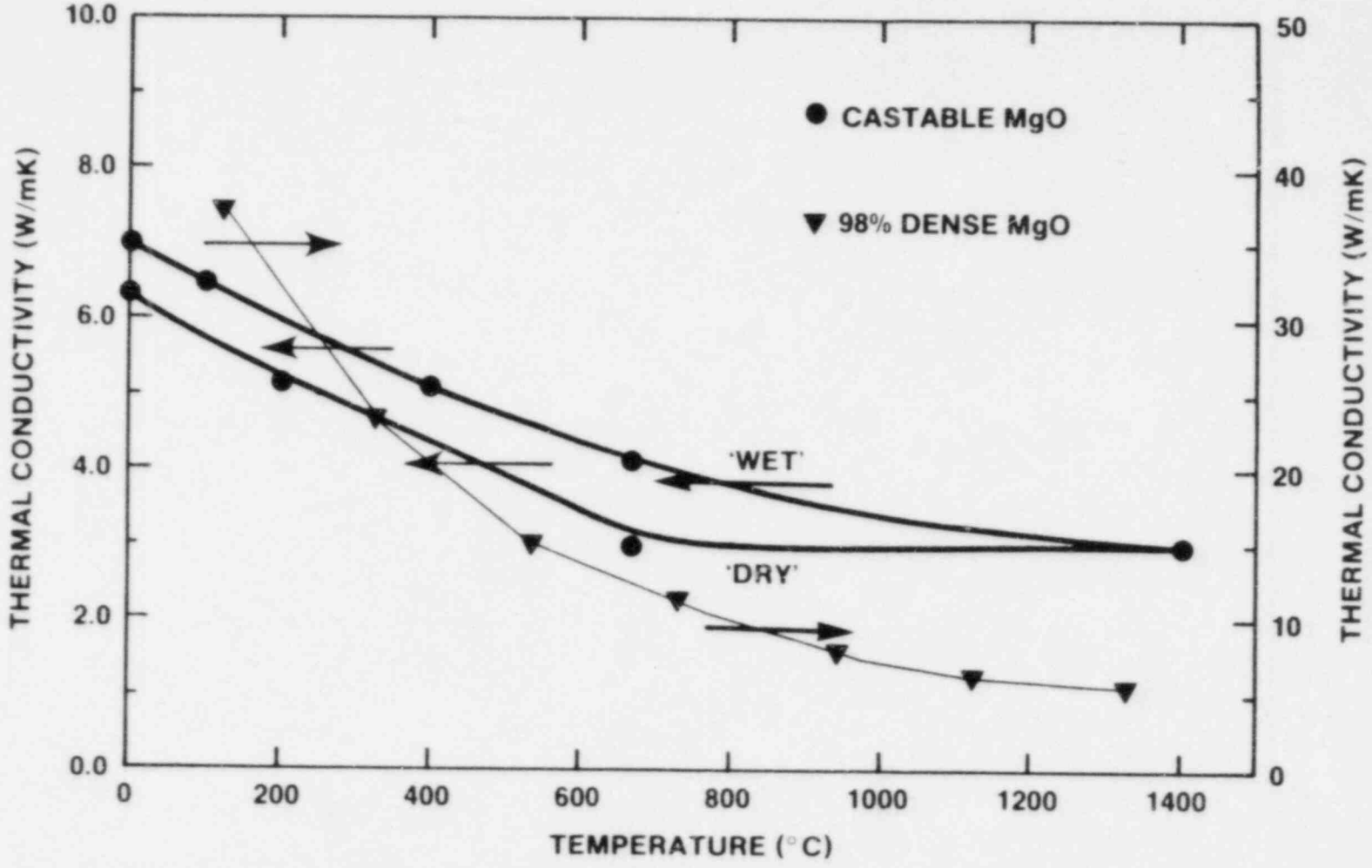

Figure 2.17 "PROPTY" Thermal Conductivity Prediction for Castable MgO Material

PROPTY code this value is fixed, and the values of k at other fixed temperature points are allowed to vary in order to minimize the RMS difference value. A study was conducted to determine the best value for the k at 277 K. The results show the initial value of k for the minimum RMS error to be 6.5 W/m K. Comparison with published data[21] is also shown in Figure 2.17. The discrepancy is quite apparent, and basically due to the physical nature of different material: preparation, water content, and density.

The physical properties of the K/R-Cast 98 material were also investigated. The bulk density of the material was found to be 2680 kg/m^3. By comparing the theoretical density for MgO of 3,570-3,590 kg/m^3 and the K/R-Cast 98, we found the cured material to have a 25% porosity.

Cold compressive strength measurements were made of the K/R-Cast 98. Three samples of each process were examined. The samples were 15.25 cm in diameter by 30.5 cm in height. The results of the test are summarized in Table 2.11. As one can see, the oven bake cure produces a relative strength twice that of concrete.

2.4 EXPERIMENT INSTRUMENTATION

The instrumentation utilized in the TURC1T and TURC1SS experiments consisted of embedded thermocouples within the interaction crucible, grab sampling of evolved gas, and aerosol measurements. The following sections will describe the instrumentation as well as the data acquisition system.

2.4.1 Crucible Instrumentation

Instrumentation within the crucible consisted of K-type thermocouples located within the concrete slug and MgO annulus. The thermocouples were utilized to determine concrete erosion rates, location of the physical isotherms (such as the concrete dehydration front interface), and for the determination of heat fluxes into the concrete and MgO sidewalls.

Axial temperature profiles within the concrete slug were measured at three radial locations (0, 3, 18 cm from centerline). Overall thermocouple axial separation resulted in a spatial resolution of 0.5 cm. Additional thermocouple arrays located within the MgO annulus measured radial temperature profiles at several axial locations. Table 2.12 through Table 2.14 and Figure 2.18 summarize the thermocouple locations.

Table 2.11 Cold Compressive Strength of MgO K/R-Cast 98

Test	Size Cm	Load kg	kg/cm^2	Cure
KR1	15.25 cm diameter 30.50 cm height	72,500	397	Air cure - 3 days Oven bake 473K-24 hrs
KR2	15.25 cm diameter 30.50 cm height	68,409	374	Air cure - 3 days Oven bake 473K-24 hrs
KR3	15.25 cm diameter 30.50 cm height	74,318	406	Air cure - 3 days Oven bake 473K-24 hrs
KR4	15.25 cm diameter 30.50 cm height	682	3.7	Air cure - 3 days - No oven bake
KR5	15.25 cm diameter 30.50 cm height	1,091	6.0	Air cure - 3 days - No oven bake
KR6	15.25 cm diameter 30.50 cm height	2,045	11.1	Air cure - 3 days - No oven bake

Table 2.12 Location of Thermocouples within MgO Sidewall TURC1T, TURC1SS (see Figure 2.18)

Thermocouple No.	r	θ	z
MG1	0 cm	0 deg.	0 cm
MG2	1	0	0
MG3	2	0	0
MG4	3	0	0
MG5	0	0	+5.2
MG6	1	0	+5.2
MG7	2	0	+5.2
MG8	3	0	+5.2
MG9	0	90	+15.0
MG10	1	90	+15.0
MG11	2	90	+15.0
MG12	3	90	+15.0
MG13	0	90	+30.0
MG14	1	90	+30.0
MG15	2	90	+30.0
MG16	3	90	+30.0
MG17	0	90	+60.0
MG18	1	90	+60.0
MG19	2	90	+60.0
MG20	3	90	+60.0
MG21	0	0	-5.1
MG22	1	0	-5.1
MG23	2	0	-5.1
MG24	3	0	-5.1
MG25	0	0	-10.0
MG26	1	0	-10.0
MG27	2	0	-10.0
MG28	3	0	-10.0

Table 2.13 Location of Thermocouples Within Concrete Slug

TURC1T

Thermocouple No.	r	θ	z
C1	0 cm	0 deg.	0 cm
C2	0	0	-1.0
C3	0	0	-2.1
C4	0	0	-3.2
C5	0	0	-4.0
C6	0	0	-5.0
C7	0	0	-6.0
C8	0	0	-7.0
C9	0	0	-8.0
C10	0	0	-9.0
C11	0	0	-10.0
C12	0	0	-12.0
C13	0	0	-14.0
C14	0	0	-16.2
C15	0	0	-18.0
C16	3	0	0
C17	3	0	-0.5
C18	3	0	-1.5
C19	3	0	-2.5
C20	3	0	-3.4
C21	3	0	-4.5
C22	3	0	-5.5
C23	3	0	-6.5
C24	3	0	-7.6
C25	3	0	-8.5
C26	3	0	-9.5
C27	3	0	-10.5
C28	3	0	-11.6
C29	18	0	0
C30	18	0	-1.0
C31	18	0	-2.0
C32	18	0	-3.0
C33	18	0	-4.0
C34	18	0	-5.0
C35	18	0	-6.1
C36	18	0	-7.0
C37	18	0	-8.0
C38	18	0	-9.0
C39	18	0	-10.0
C40	18	0	-10.9
C41	18	0	-12.0
C42	18	0	-14.0
C43	18	0	-16.0
C44	18	0	-18.0

Table 2.14 Location of Thermocouples Within Concrete Slug

TURC1SS

Thermocouple No.	r	θ	z
C1	0 cm	0 deg.	0 cm
C2	0	0	-1.0
C3	0	0	-2.1
C4	0	0	-3.0
C5	0	0	-4.0
C6	0	0	-5.0
C7	0	0	-6.0
C8	0	0	-7.0
C9	0	0	-8.0
C10	0	0	-8.9
C11	0	0	-10.0
C12	0	0	-12.0
C13	0	0	-14.0
C14	0	0	-16.2
C15	0	0	-18.0
C16	3	0	0
C17	3	0	-0.4
C18	3	0	-1.5
C19	3	0	-2.5
C20	3	0	-3.4
C21	3	0	-4.5
C22	3	0	-5.5
C23	3	0	-6.5
C24	3	0	-7.4
C25	3	0	-8.5
C26	3	0	-9.5
C27	3	0	-10.5
C28	3	0	-11.6
C29	18	0	0
C30	18	0	-1.0
C31	18	0	-2.0
C32	18	0	-3.0
C33	18	0	-4.0
C34	18	0	-5.0
C35	18	0	-6.1
C36	18	0	-7.0
C37	18	0	-8.0
C38	18	0	-9.0
C39	18	0	-10.0
C40	18	0	-10.9
C41	18	0	-12.0
C42	18	0	-14.0
C43	18	0	-16.0
C44	18	0	-18.0

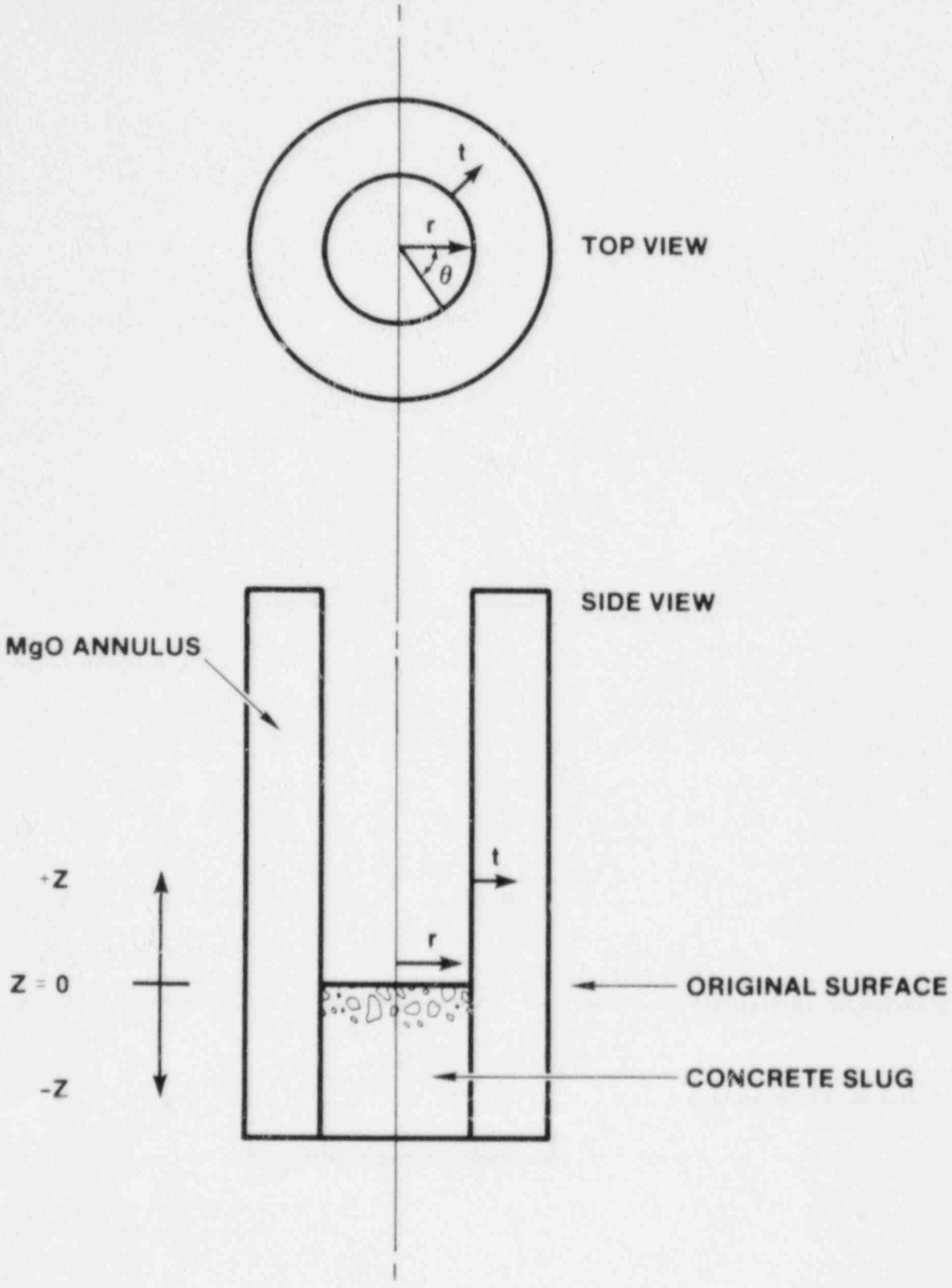

Figure 2.18 Thermocouple Placement Map (see Table 2.12)

2.4.2 Gas Measurements

The composition of the gases generated during the test was determined from grab samples. The gases were sampled at the exit port of the interaction crucible.

The gas sampling scheme is shown in Figure 2.19. It consisted of a 2-m long sampling line which fed a remotely controlled valve network. A total of 30, 150-cm^3 gas samples can be taken with this equipment. The dead volume within the sample line and valve network was estimated at 50-cm^3, or one-third the sample volume. The sampling rate varied from 5 to 10 seconds between samples early in the experiment to 15 to 30 seconds between samples near the end of the experiment. Since the rate of sampling was quasi-continuous, the gases sampled were considered a reasonably close representation of the evolved gases.

The gas samples collected were analyzed with an H.P. 5836 Gas Chromatograph. Samples were injected directly from grab sample bottles into a Porapak Q, 80/100 mesh column which was time-temperature programmed from 223 K to 473 K (- 50°C to 200°C). The porous polymer beads in the column provide sharp symmetrical peaks and low retention volumes for polar materials such as alcohols, acids, and glycols.

Detection was accomplished by using a thermal conductivity detector that was tuned to the primary standard gas mixture made up of the following constituents: H_2, N_2, Ar, CO, CH_4, CO_2, C_2H_4, C_2H_6, and O_2. The above gas species were used to calibrate the gas chromatograph. Only peaks that were assignable to the calibration standard were detected.

The sample introduction loop into the gas chromatograph was preceded by an activated charcoal trap that served the purpose of trapping out condensables such as water. This was a necessary step taken, since previous experiments[5] indicated H_2O was generated in excess of 5% of total pressure. Also, this procedure served the purpose of preventing saturation or loading of the gas separation columns so as not to mask the quantitative analysis of the compositions.

2.4.3 Aerosol Measurements

The aerosol instrumentation on the experiments consisted of filters for bulk aerosol concentration determination, cascade impactors and cascade cyclones for aerosol size distribution measurement, and an opacity meter to monitor aerosol mass loading in the exhaust pipe. The filters, impactors, and cyclones operate by having an aerosol sample drawn through them. These devices were plumbed into the sampling train, and flow was regulated by critical orifices and remotely controlled valves. The

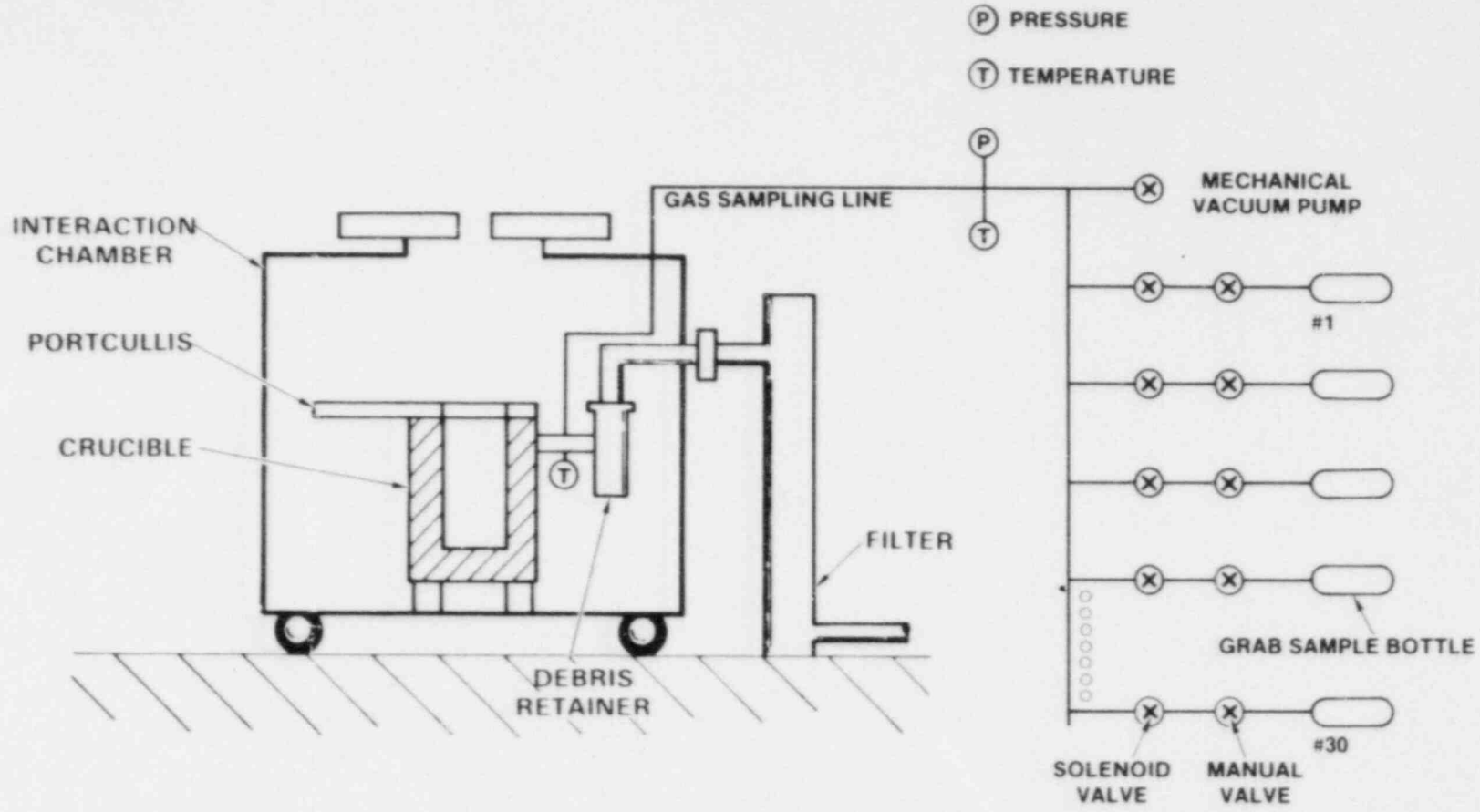

Figure 2.19 Gas Sample Technique for TURC Series of Experiments

instrumentation for TURC1T and TURC1SS is given in Table 2.15. A description of the instrumentation follows.

Anderson MkIII cascade impactor: This device inertially classifies aerosol particles into nine size bins. It consists of eight stages and an after filter and employs glass fiber collection substrates. It yields a mass distribution of aerosol with respect to aerodynamic equivalent particle diameter. The Anderson MkIII cascade impactor is 8.2 cm in diameter and 18 cm long and is constructed of stainless steel.

A preseparator which removes particles nominally larger than 15 micrometers aerodynamic diameter was used to avoid overloading (more than 15 mg of material on any one stage) of the impactor with large particles. It effectively collects material which would otherwise be collected on the first two stages of the impactor. The preseparator collects material in an impaction cup, which is brushed out to retrieve the collected sample. The preseparator is of stainless steel construction, 8.2 cm in diameter and 12.8-cm long. It threads into the front of the impactor. The assembled preseparator-impactor is 8.2 cm in diameter and 29.8-cm long.

Flow through the impactor is controlled by a Millipore critical flow orifice connected directly at the back of the impactor. The impactor is operated for a short (10-sec to 60-sec) period of time during the test.

Sierra cascade cyclone: This device also inertially classifies aerosol particles and yields a mass distribution with respect to aerodynamic equivalent particle diameter. A cyclone is capable of collecting much more material than an impactor and can

Table 2.15

Aerosol Instrumentation for TURC1T and TURC1SS

	TURC1T	TURC1SS
Anderson MkIII Cascade Impactors	8	10
Sierra Cascade Cyclones	2	2
Gelman High Pressure Filters	6	7
Dynatron Opacity Meter	-	1

be used to collect material for bulk analysis. The Sierra cascade cyclone is a series of six cyclones (of increasing capability to collect smaller particles) followed by a glass fiber back-up filter. The aerosol sample is brushed out of the collection cup of each cyclone for weighing. The cascade cyclone is of stainless steel construction and when assembled is 12.7 cm in diameter at the widest point and about 60 cm in length.

Flow through the cyclone is controlled by Millipore critical orifices connected directly to the back. Because of the large collection capacity, this device is operated for long periods of time in order to collect larger quantities of size classified material for later analysis.

Gelman in-line stainless steel filter holder: This stainless steel 5.9-cm diameter 5.7-cm long filter holder (Gelman catalog number 2220) is designed for pressure applications of up to 200 psig. It uses 47-mm diameter Durapore Membrane filtration media from Millipore (catalog designation HVLP 047). The effective filtration area is 9.6 cm^2. Flow is controlled by a Millipore critical flow orifice.

Dynatron model 301 opacity meter: This device measures the attenuation of a light beam as it travels through an aerosol. Light attenuation correlates with mass loading. Correlation of the opacity meter output with the mass measured by the filter samples provides a continuous record of mass concentration in the 3-inch pipe exhausting gas and aerosol from the interaction crucible in the TURC tests. The windows allowing light transmission are kept clean and free of aerosol deposition by a purge gas flow.

The aerosol sampling devices are all attached to a vacuum through a system of remotely controlled valves. Flow is controlled by Millipore critical flow orifices which have been calibrated in the Sandia primary standards laboratory. Remote control of the valves is performed by Modicon Micro 80 programmable controller manufactured by Gould. The controller executes a preprogrammed sampling sequence.

The samplers require heating to 125°C to avoid condensation of water. This is accomplished with electrical heating tape and insulation and is controlled by an Omega model 920 temperature controller with a Type K thermocouple.

Temperature and pressure measurements are required to characterize the flow conditions. Temperature measurements are obtained with Type K thermocouples. The pressure transducers employed are a mix of Kulite and Microswitch and have been calibrated in Sandia's standards laboratory.

Figure 2.20 is a schematic of the filter sample sampling train. Figure 2.21 is a schematic of the impactor sampling train. Two impactors are ganged together and run simultaneously in parallel at different flow conditions. This increases the information about the aerosol distribution for use in a data reduction scheme currently under development. Figure 2.22 is a schematic of the cyclone sampling train. Figure 2.23 is a schematic of the opacity meter. Figure 2.24 is a schematic of the TURC-1T test showing the location of the sampling trains. Figure 2.25 is a schematic of the TURC-1SS test.

2.4.4 Data Acquisition System

The data acquisition system for the experiment facility is shown schematically in Figure 2.26. One hundred twenty-eight channels of data may be acquired during an experiment. For the TURC experiments, 122 channels were used: 96 channels for type K thermocouples (chromel-alumel), 16 channels for type C thermocouples (tungsten-tungsten rhenium) and 10 channels for voltages up to 10 volts for other types of sensors.

Data are taken in a sample and hold mode in which four channels are measured in a 50 microsecond window. All 122 channels are thus acquired in 1.6 milliseconds. An analog-to-digital converter sequentially converts each channel and sends the data to the computer. At the computer, calibration, correction, and conversion factors are applied to the data which are then stored on magnetic tape. In addition, the data may be printed or plotted. The data sampling rate is set by the computer. The fastest mode is one scan of all channels every second. The thermocouples are connected to the acquisition system through a reference junction. The junction is set to 65.5°C.

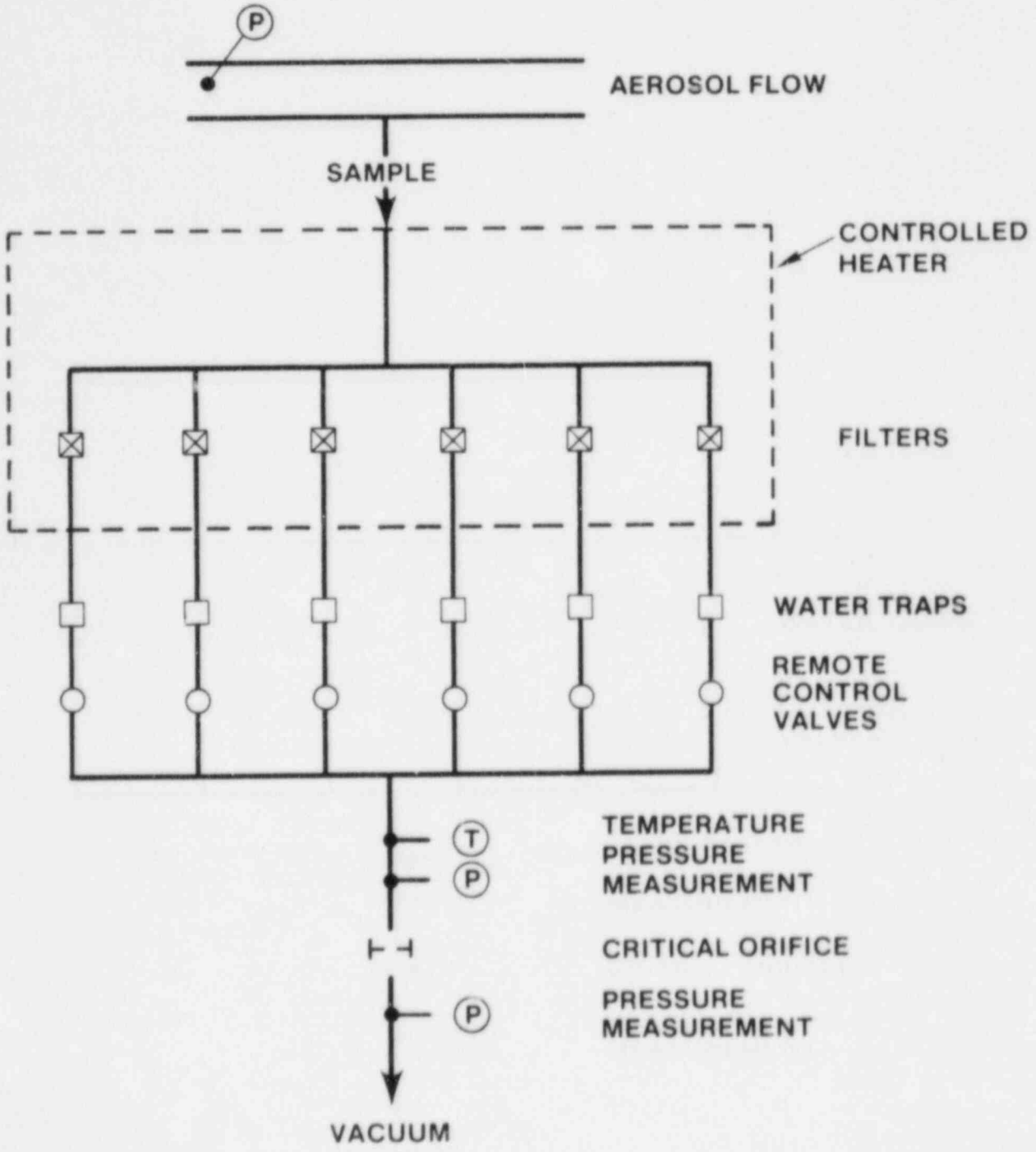

Figure 2.20 Filter Sampling Train

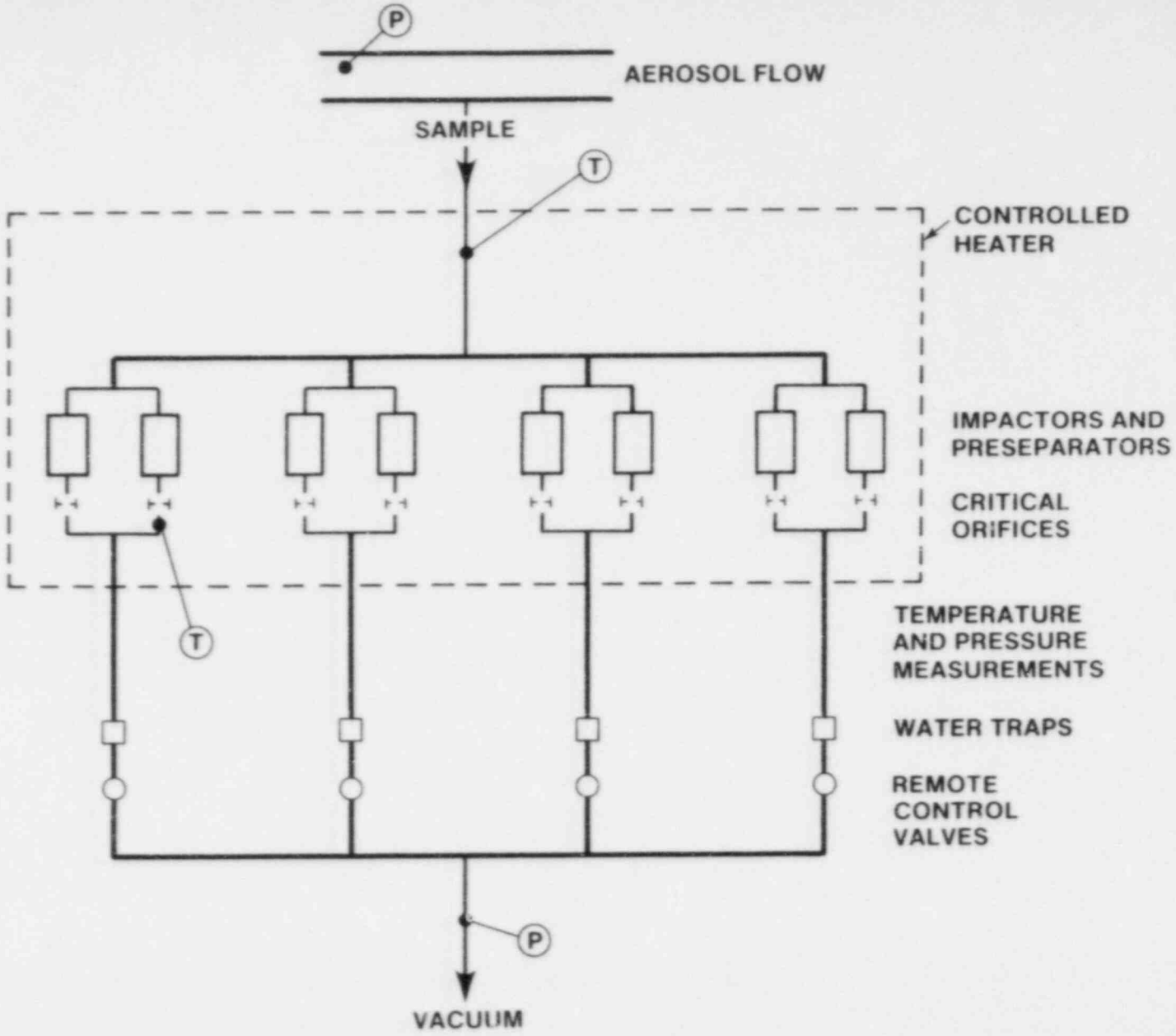

Figure 2.21 Impactor Sampling Train

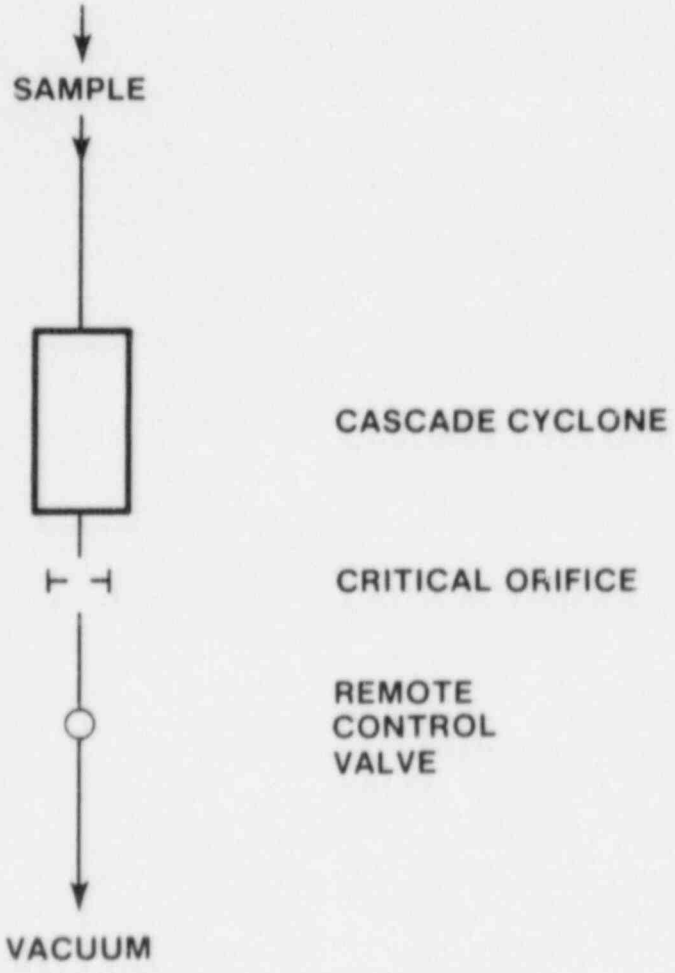

Figure 2.22 Cyclone Sampling Train

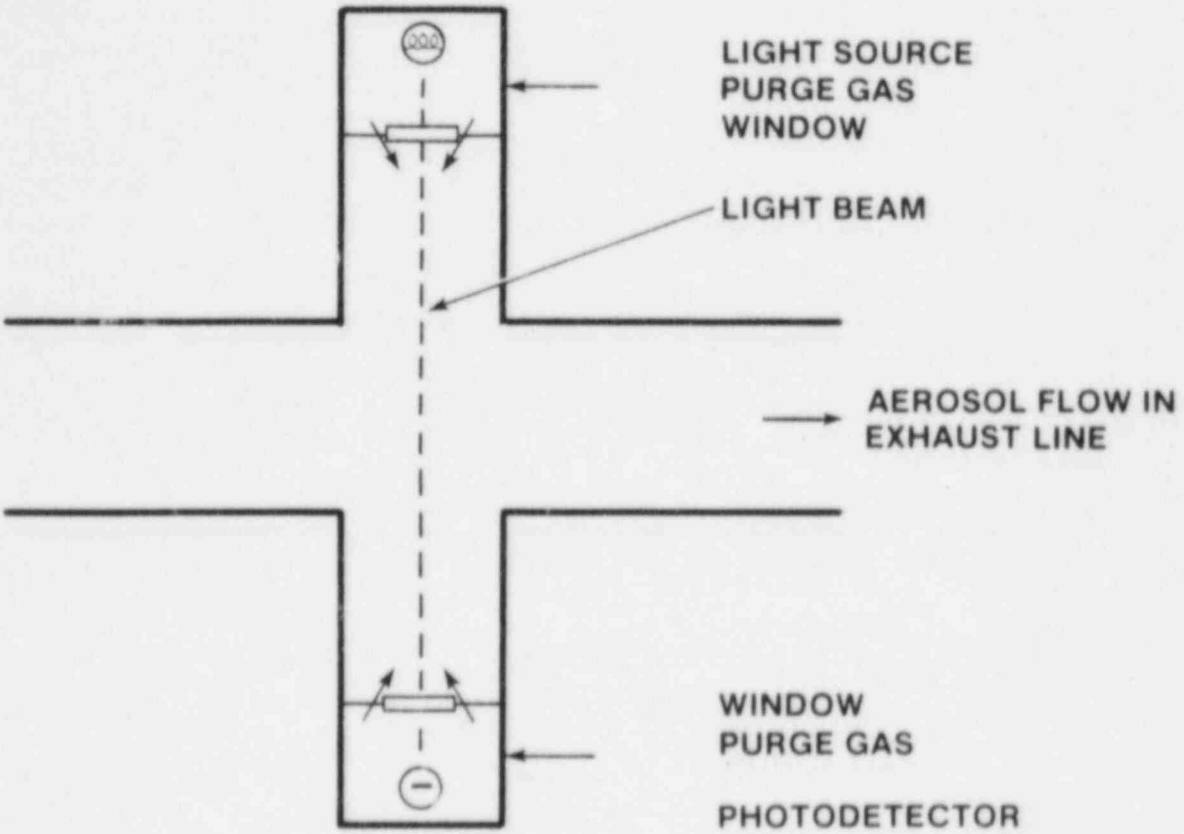

Figure 2.23 Opacity Meter

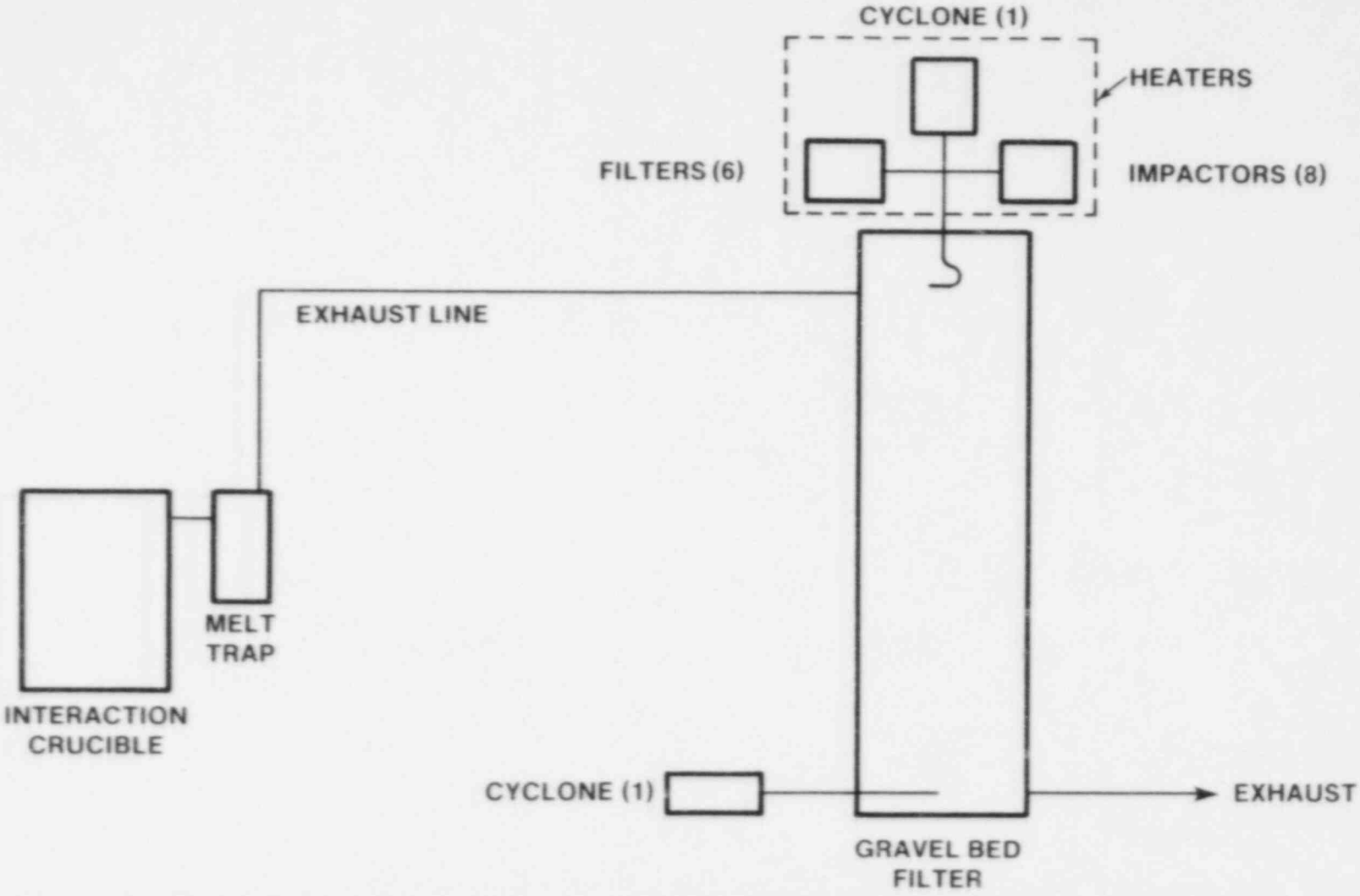

Figure 2.24 TURC1T Location of Sampling Trains

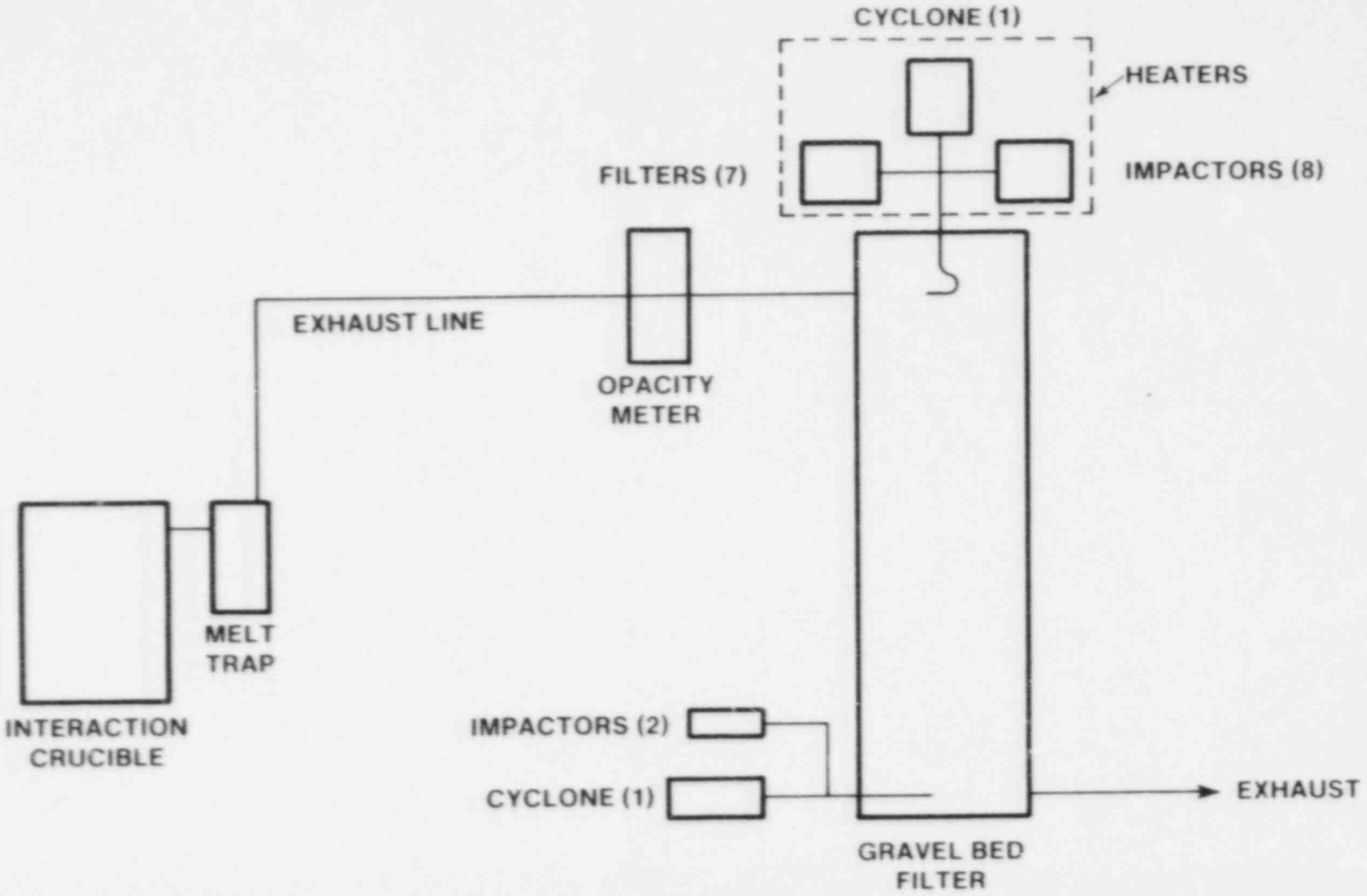

Figure 2.25 TURCISS Location of Sampling Trains

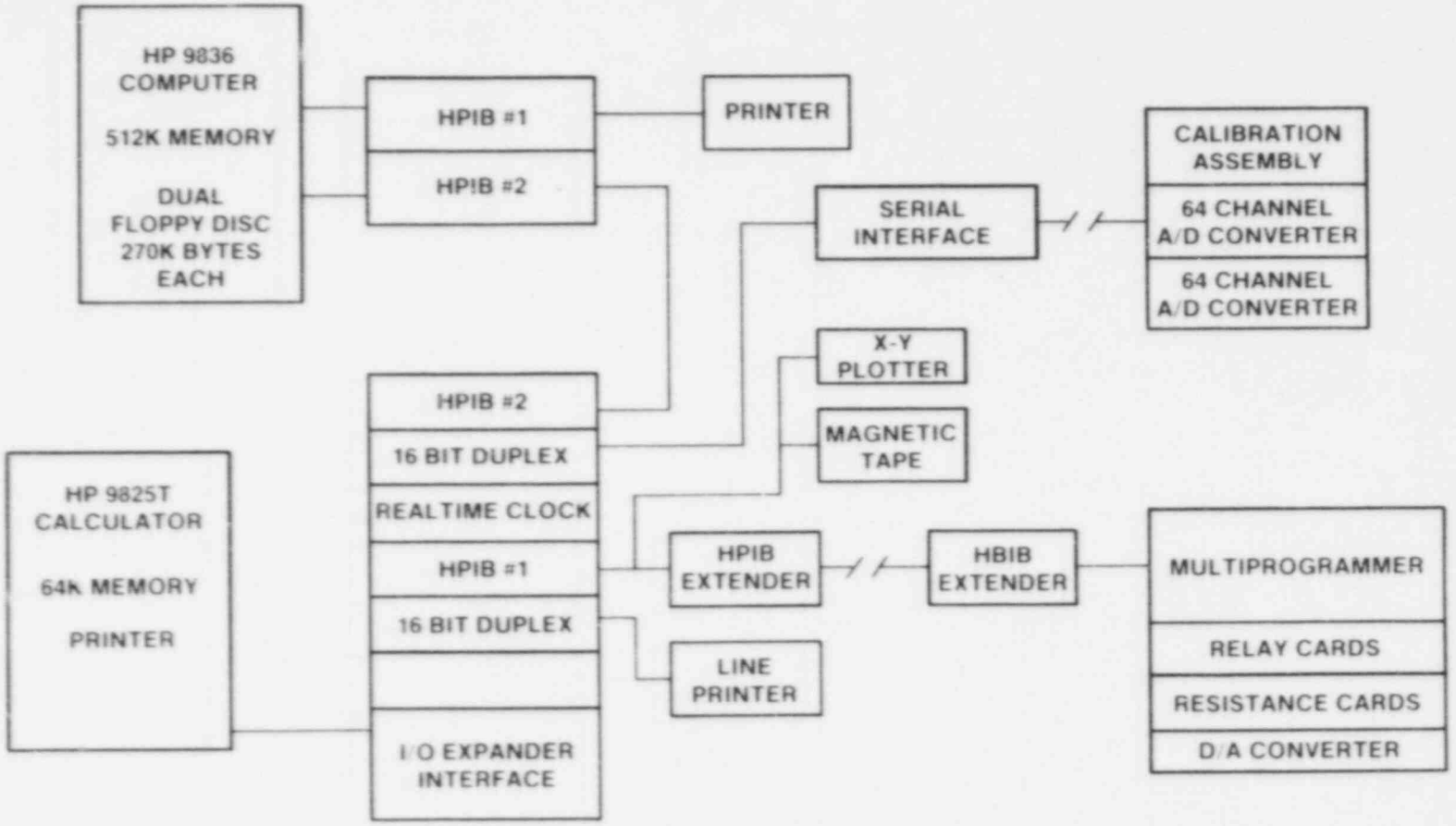

Figure 2.26 Data Acquisition System

3 EXPERIMENTAL RESULTS

3.1 EXPERIMENT CONDUCT

3.1.1 TURC1T

The first experiment conducted was TURC1T. The experiment was initiated by igniting the pyro-fuse wire embedded within the top centimeter of the thermite charge. At first, the thermite reaction appeared to be proceeding in a quasi-controlled manner, with the melt generator containing the thermite reaction products. Approximately 10 s after the ignition, vigorous ejection of molten material from the top cover plate-vent stack was observed. The ejection of material continued until the teeming of the melt.

The ejected material essentially "rained" upon the equipment located outside of the interaction chamber, resulting in the failure of the control cables for aerosol instrumentation, gas sampler, and the portcullis closure systems. As a consequence, the portcullis did not close; and no gas or aerosol samples were taken.

Once the pour of the molten debris was complete, a vigorous melt-concrete interaction was observed. Initially, all observation of the interaction was impeded by a brilliant fireball and dense aerosol cloud. This phase of the interaction lasted approximately 10 seconds.

For the next 8-10 min, molten material was observed being ejected from the crucible, as well as a large bright yellow flame and aerosol cloud. The aerosol release rate was observed to decrease rapidly over this time period. The flame and ejection of material continued at a fairly constant intensity. (Along with a video record, audio recordings were made of the experiment.) From the audio record, the melt pool initially may have been churning, releasing gas at a constant rate; this was followed by a chugging audio signature suggesting rapid periodic releases of gases.

For 10-15 min after the teeming of the melt, the interaction rate was obviously slowing down rapidly, the aerosol cloud was of low density, the flame was nonuniform and dying down, no ejection of material was observed and the audio record was relatively quiet.

The experiment data acquisition was terminated 30 min after teeming of the melt, when it was apparent that the debris-concrete interactions had long since abated.

In Sections 3.2.1.1 and 3.2.1.2, the posttest observation and thermal analysis of the experiment will be discussed.

3.1.2 TURC1SS

The TURC1SS experiment was conducted with much less excitement. The induction furnace performed smoothly, providing a melt of uniform temperature. The firing of the explosive charge initiated teeming of the melt and was followed 10 s later by the closing of the portcullis.

Aerosol and gas samples were taken repetitively throughout the experiment. The argon gas purge within the crucible, discussed in Section 2, was terminated shortly after the closing of the portcullis due to the late draining of ~2 kg of molten stainless steel from the furnace above, resulting in the destruction of the gas inlet port.

During the melt teem, a dense aerosol cloud was ejected from the crucible opening. A fireball was briefly observed, but only during the teeming of the melt, since the portcullis closure eliminated the reaction products' direct path of escape.

Once the portcullis was closed, aerosol release was observed exiting the filter port. The duration of aerosol release was less than 1 min. The audio record was nonexistent after the firing of the explosive charge. The intensity of the explosion had permanently damaged the microphone.

The experiment duration was considerably less than that for the TURC1T experiment. The acquisition of data was terminated 20 min after the melt teem. Within Section 3.2.2, the TURC1SS experimental results will be presented.

3.2 EXPERIMENTAL RESULTS

3.2.1 TURC1T

3.2.1.1 Posttest Observations

Following a cool-down period of two days, the TURC1T experiment crucible was removed from the interaction chamber. The crucible was covered and stored for several months until the completion of the TURC series of experiments.

The TURC1T crucible appeared to have withstood the intense experiment environment quite well. The MgO annulus contained

several radial and axial cracks, which apparently extended through the annulus wall.

Considerable amounts of debris were found on the portcullis and floor of the interaction chamber. The appearance of this material suggests that it was oxidic in nature, with entrained metal spheres 1-5 mm in diameter.

The interior sidewall of the crucible had a thick crust (2-15 mm thick), which completely covered the sidewall surface above the melt pool. A closer examination of the sidewall crust showed that it was deposited in several layers. This is consistent with the observation of the ejection of material during the experiment.

The top surface of the melt pool, shown in Figure 3.1, was convoluted and glassy in appearance. The material was similar to that found on the sidewall. No chemical analysis of the material was performed.

Shown in Figure 3.2 is an x-ray of the lower section of the crucible. The x-ray shows three distinct layers within the melt pool:

(1) Top crust, 4.8 cm thick
(2) Gas gap or layer, 4.9 cm thick
(3) Debris pool, 15.5 cm thick

The crucible was sectioned by removing a 120° arc of the MgO annulus, leaving the melt pool and concrete slug intact. As shown in Figure 3.3, the removed section revealed the extent of the radial cracking of the MgO annulus. As shown in this photograph, the three layers of the melt pool are not apparent due to the adherence of a thin layer of degraded MgO to the frozen melt pool.

With the MgO layer removed (Figure 3.4) the three layers are clearly seen. The top layer consisted mostly of oxide material, with entrained metal spheres. The mass of this layer was 30.2 kg. The layer was porous, with gas pockets and bubbles ranging in size from 1 to 10 mm in diameter. The top surface, although convoluted, was uniform and relatively flat. The bottom surface of the crust was severely convoluted with the thickness of the crust layer varying by a factor of 2 across the diameter. The bottom surface of the crust was smooth and glassy.

The gas gap or layer contained several regions in which metal stringers or stalactites were formed by draining or dripping off the top oxide crust.

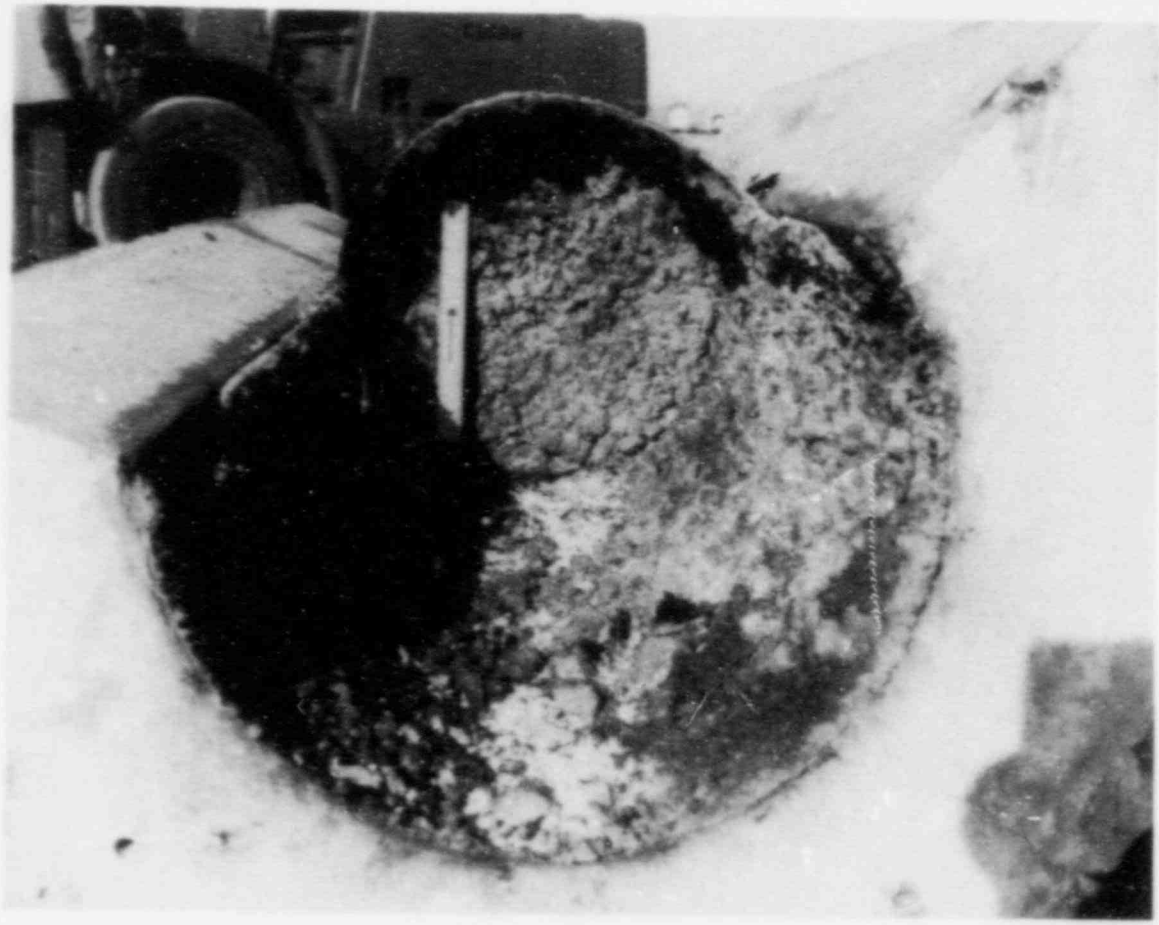

Figure 3.1 Posttest Photograph of Top Surface of TURC1T Melt Pool

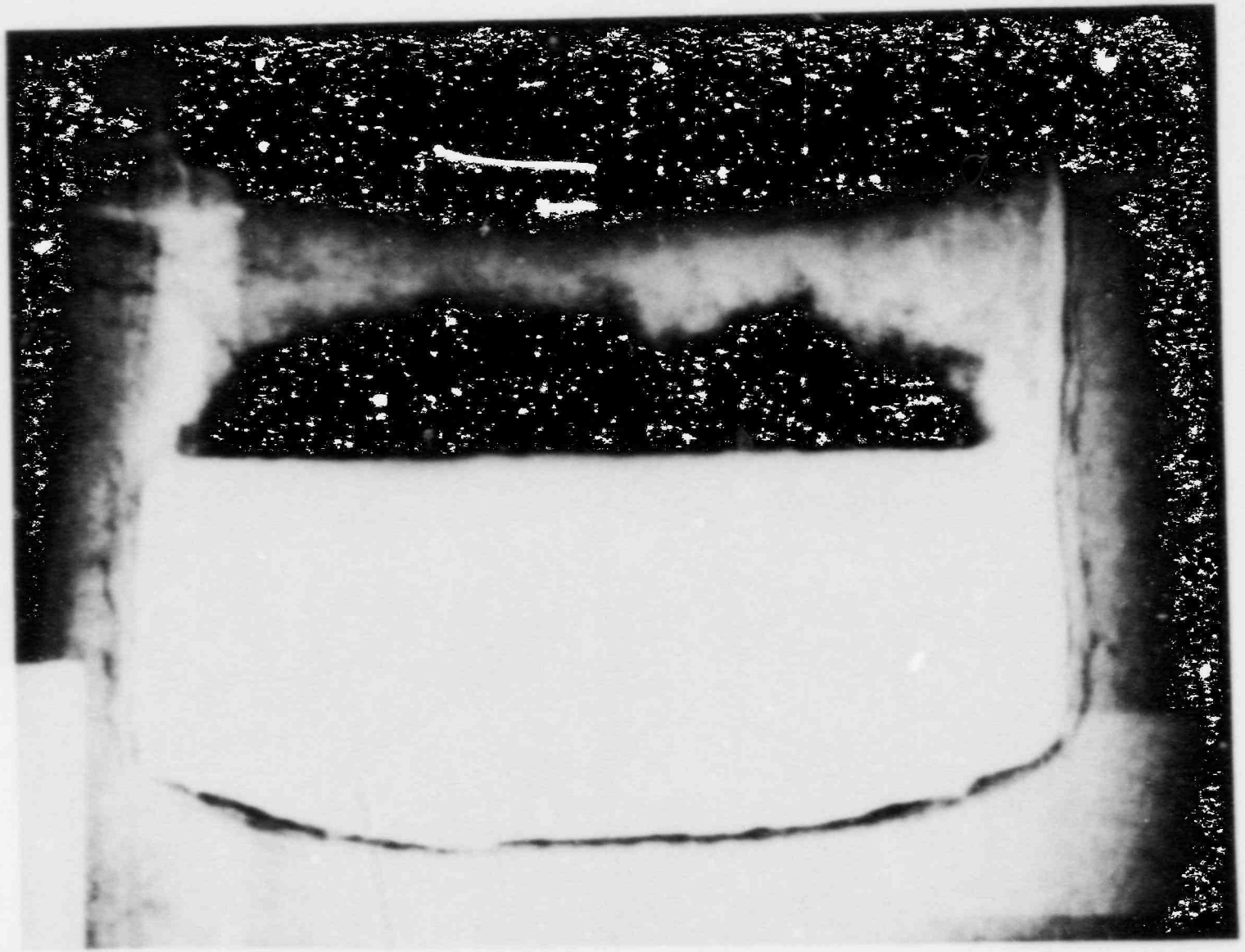

Figure 3.2 Posttest X-ray of Lower Section of TURC1T Crucible

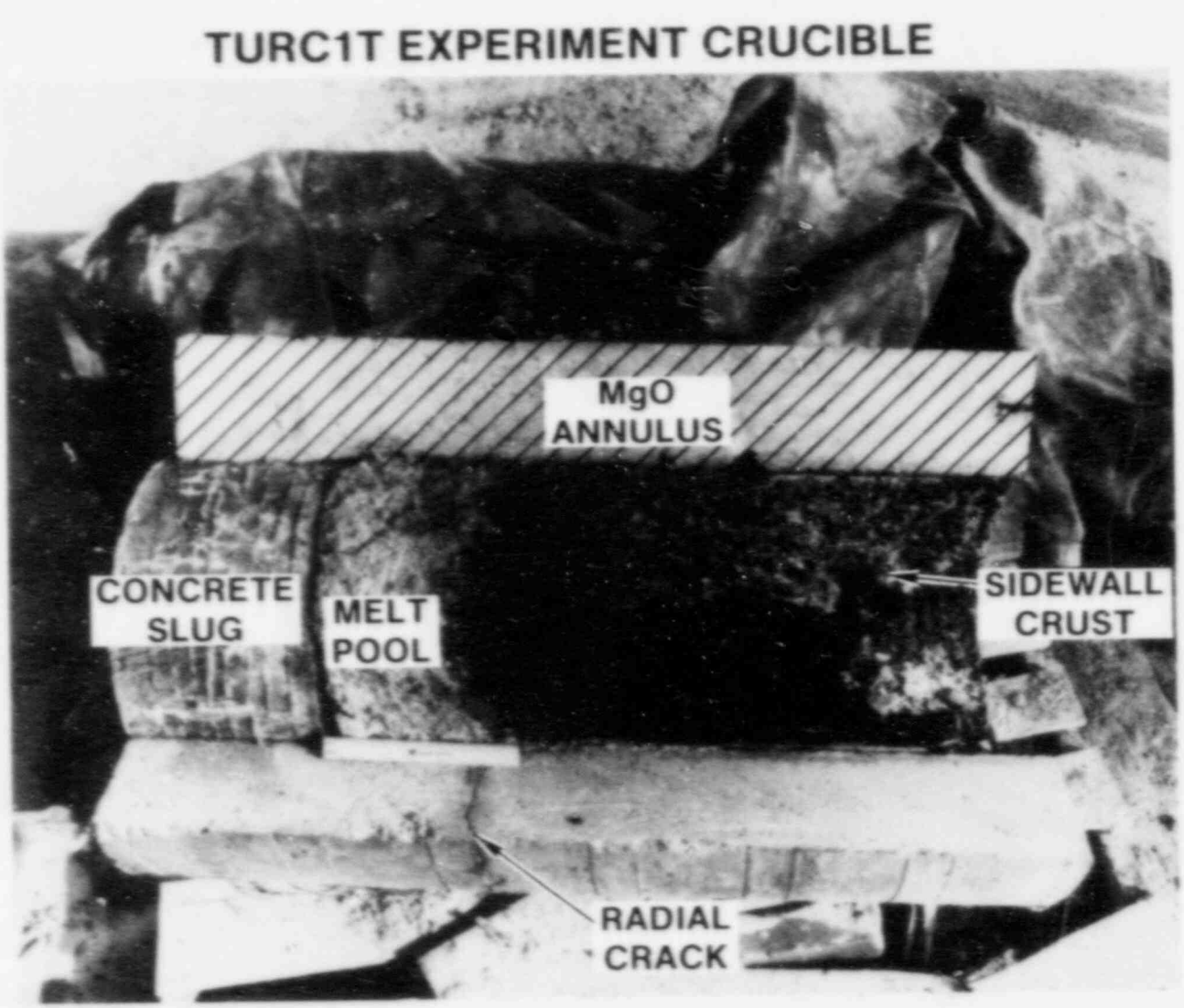

Figure 3.3 Sectioned Crucible of TURC1T Experiment

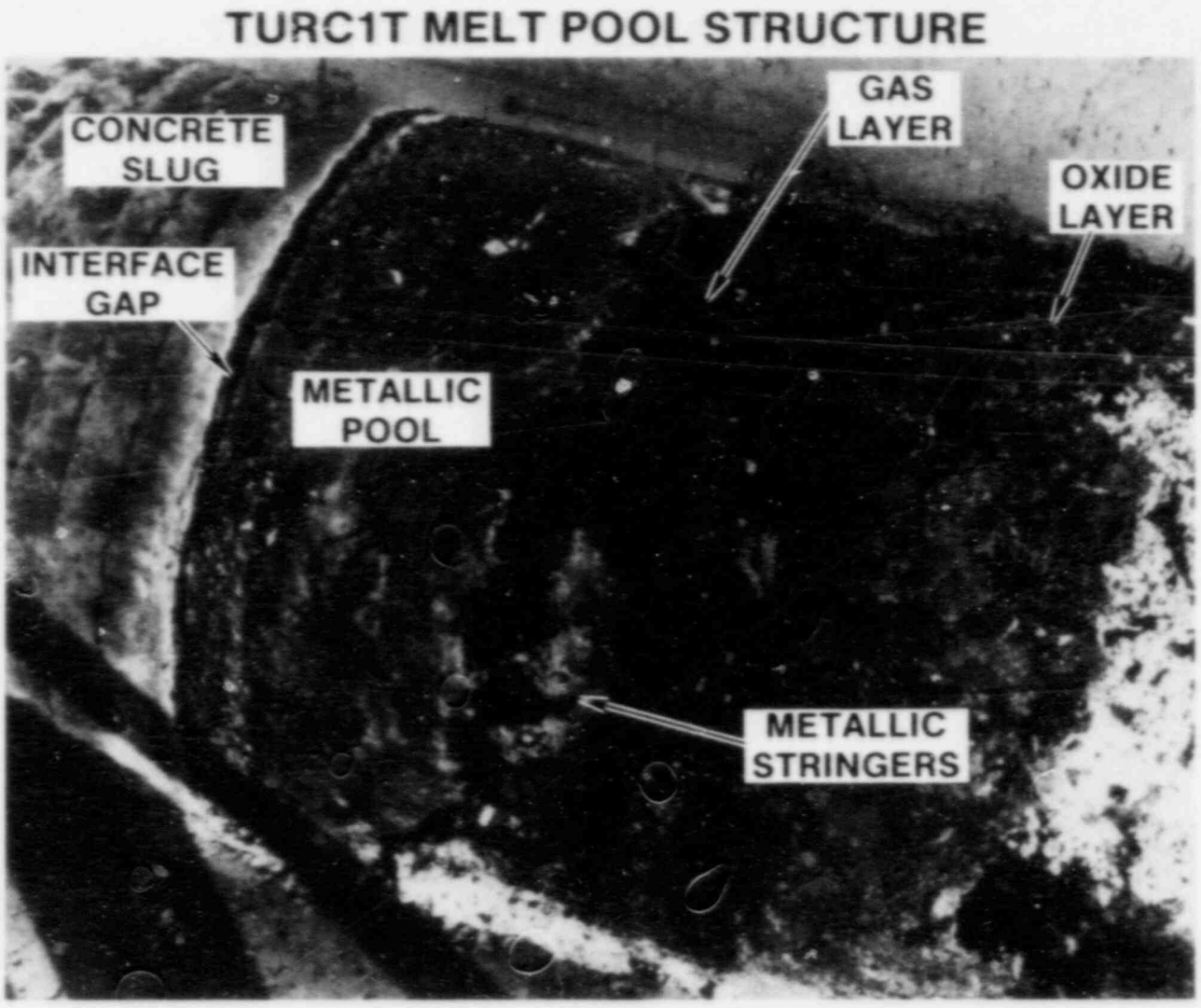

Figure 3.4 TURC1T Melt Pool Structure

The lower layer or metallic debris pool was removed from the crucible and sectioned. As shown in Figure 3.5, the sectioned layer consists of two regions or material types. Most of the pool is metallic, but near the top surface a torus or ring of oxidic material was found. Due to the location and shape of the oxide ring, the circulation or mixing flow path within the metal pool is suggested to be a toroidal cell flowing down the centerline of the pool, and up along the sidewalls.

The metal phase of the debris pool was observed to contain voids or bubbles 0.2 to 1.3 cm in diameter. The inside surface of the voids typically contained a small amount of oxide material. The mass of molten debris pool was 117 kg.

The bottom surface of the metal layer or pool contained numerous depressions or dimples. (It resembles a cratered surface.) The bottom surface also appeared to be coated with a thin layer of oxide material (< 0.05 mm). There did not appear to be coarse concrete aggregate entrained within the pool or on the bottom surface. From the x-rays and the physical disassembly, a gap 0.25-1.2 cm exists between the concrete slug and the melt pool.

The concrete surface was hemispherical in shape. A typical cross-section profile of the concrete surface is shown in Figure 3.6. The top surface of the concrete was black in color, and rough to the touch. The material appeared to be decomposed concrete. This layer of material was 2-5 mm thick and was found pooled in the center of the concrete slug.

3.2.1.2 Concrete Erosion and Crucible Thermal Response

As noted earlier, the melting range of limestone/common sand concrete is 1425 K to 1673 K. Figures 3.7 through 3.9 show the temperature history measured by thermocouples embedded at various depths within the concrete slug. The erosion front of the concrete was tracked by the failure of the thermocouple junction or the temperature exceeded 1600 K. For the shallow embedded thermocouples, as shown in Figure 3.7, the ablation rate was very high and the slope of the temperature rise was steep. As one reviews temperature traces of thermocouples embedded deeper in the concrete, for example at a depth of 7 or 8 cm, one can see the thermal arrest at 400 K-450 K where the evaporable water vaporizes and escapes from the concrete. Thus, the depth of the release of water on the dehydration front can be tracked. A comparison of the thermocouple traces at various radial locations is consistent with the erosion profile observed, suggesting at the r = 18 cm location, the heat flux into the concrete was less than at locations more towards the center of the concrete slug.

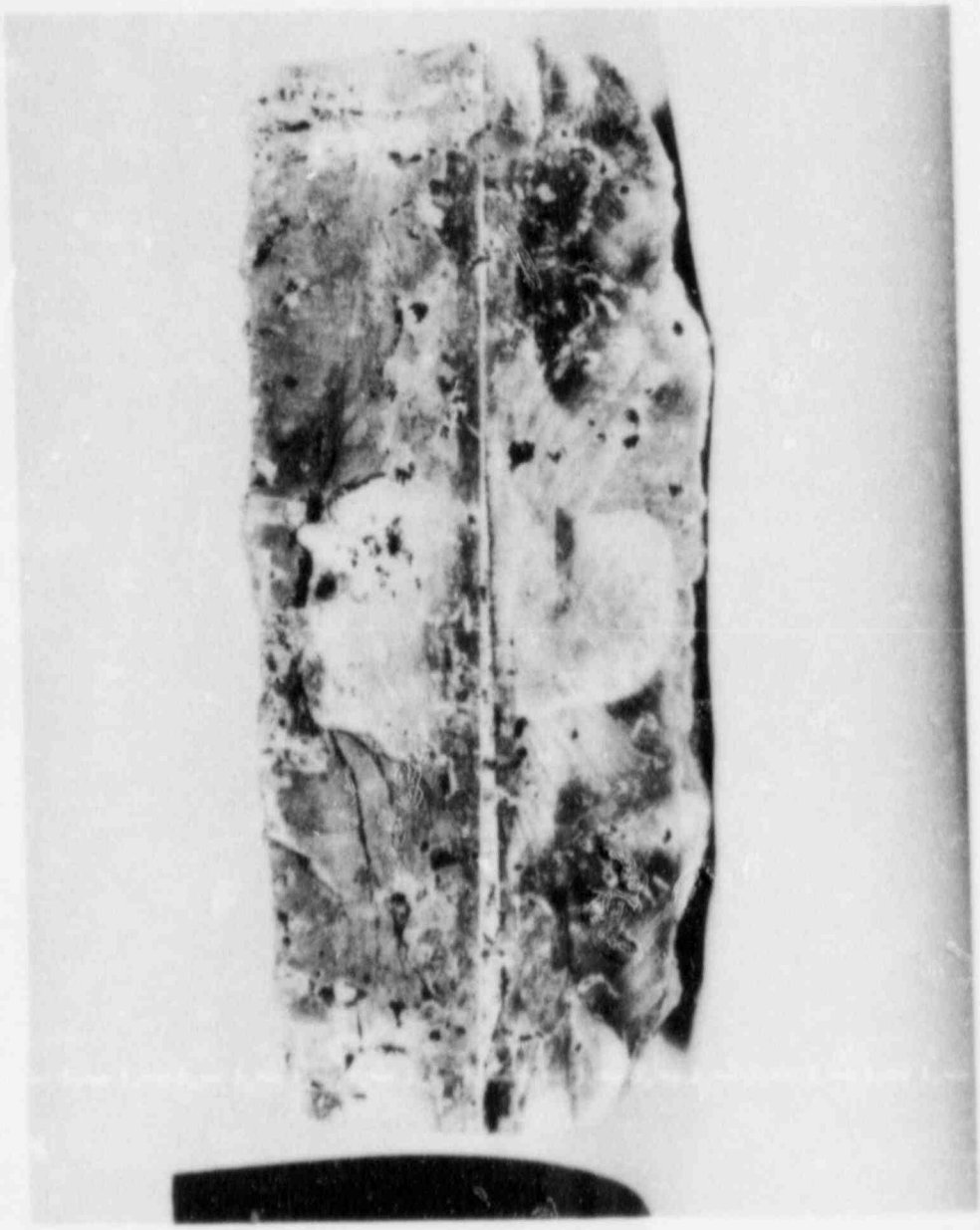

Figure 3.5 Sectioned TURC1T Metal Pool

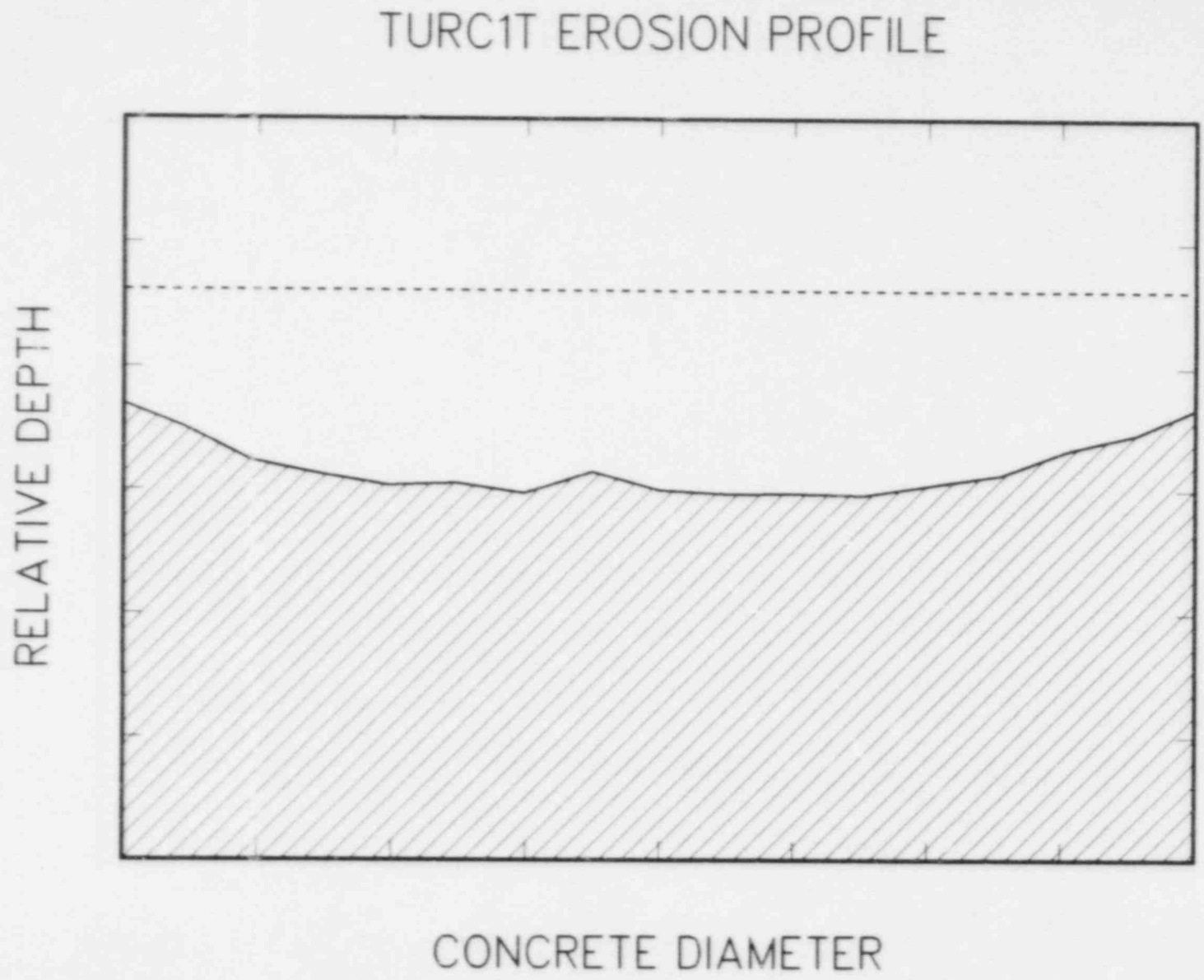

Figure 3.6 Typical Posttest Cross Section of TURC1T Concrete Surface

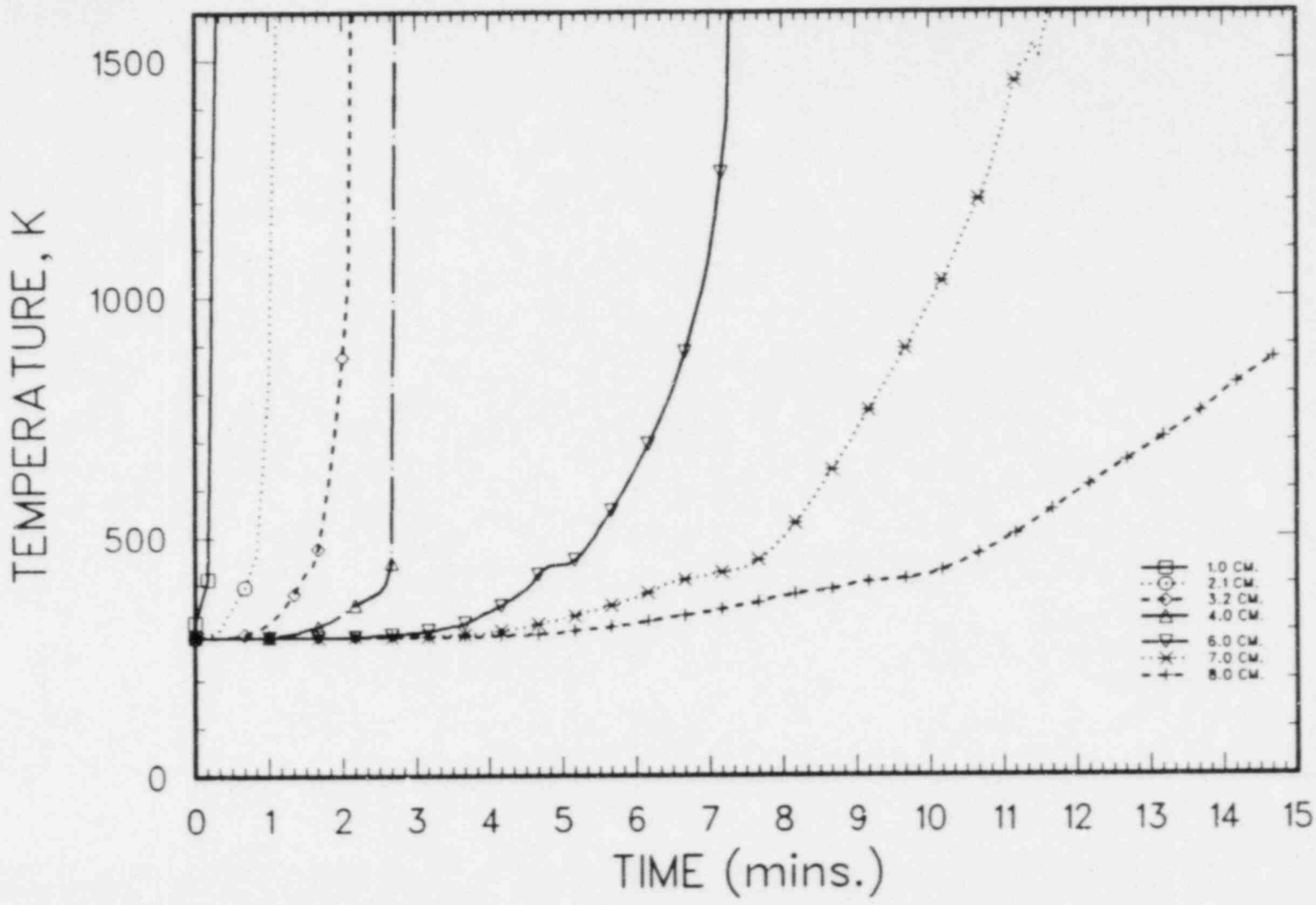

Figure 3.7 TURC1T Concrete Thermocouple Data, Location: Concrete Slug Centerline

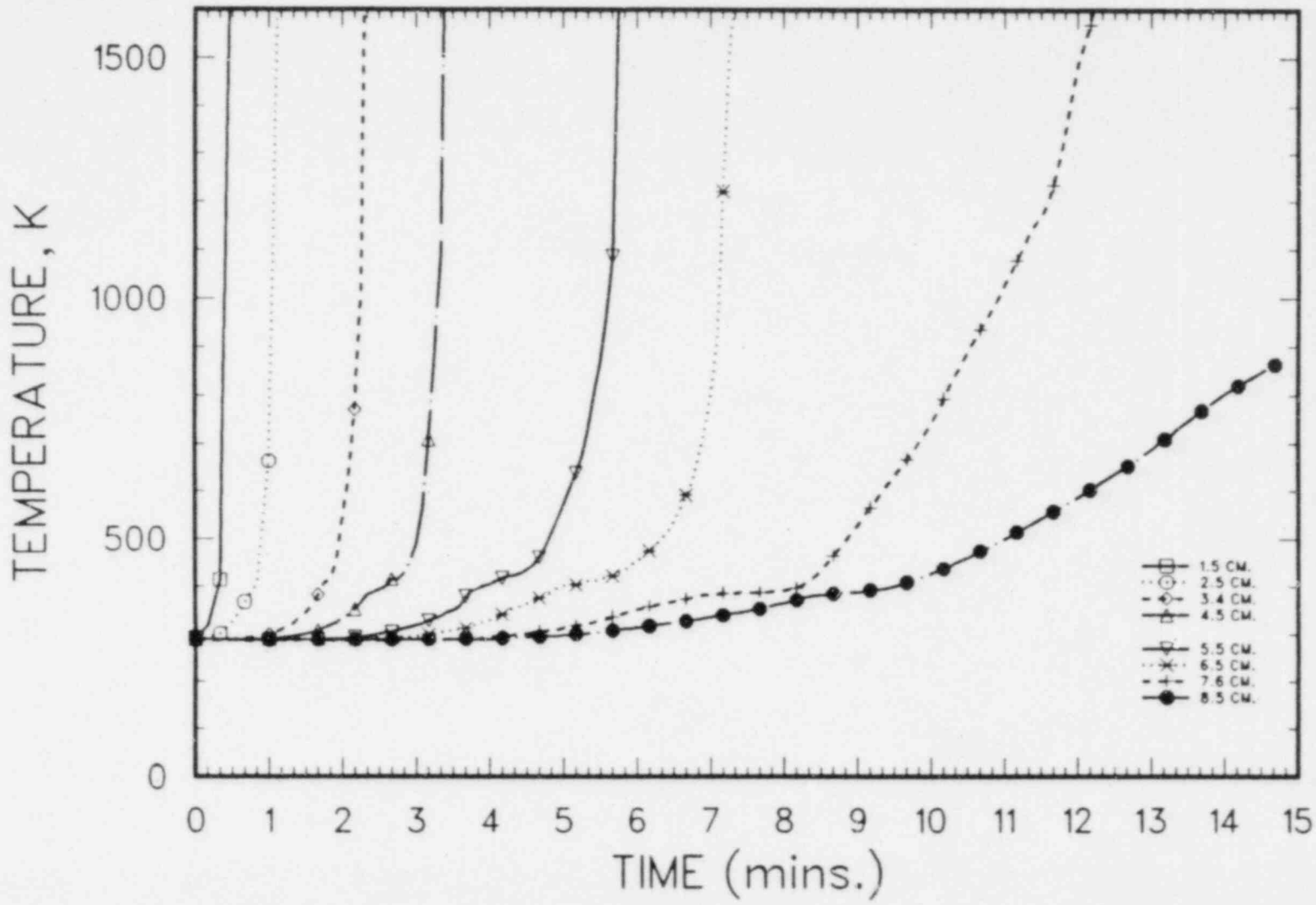

Figure 3.8 TURC1T Concrete Thermocouple Data, Location: r = 3 cm

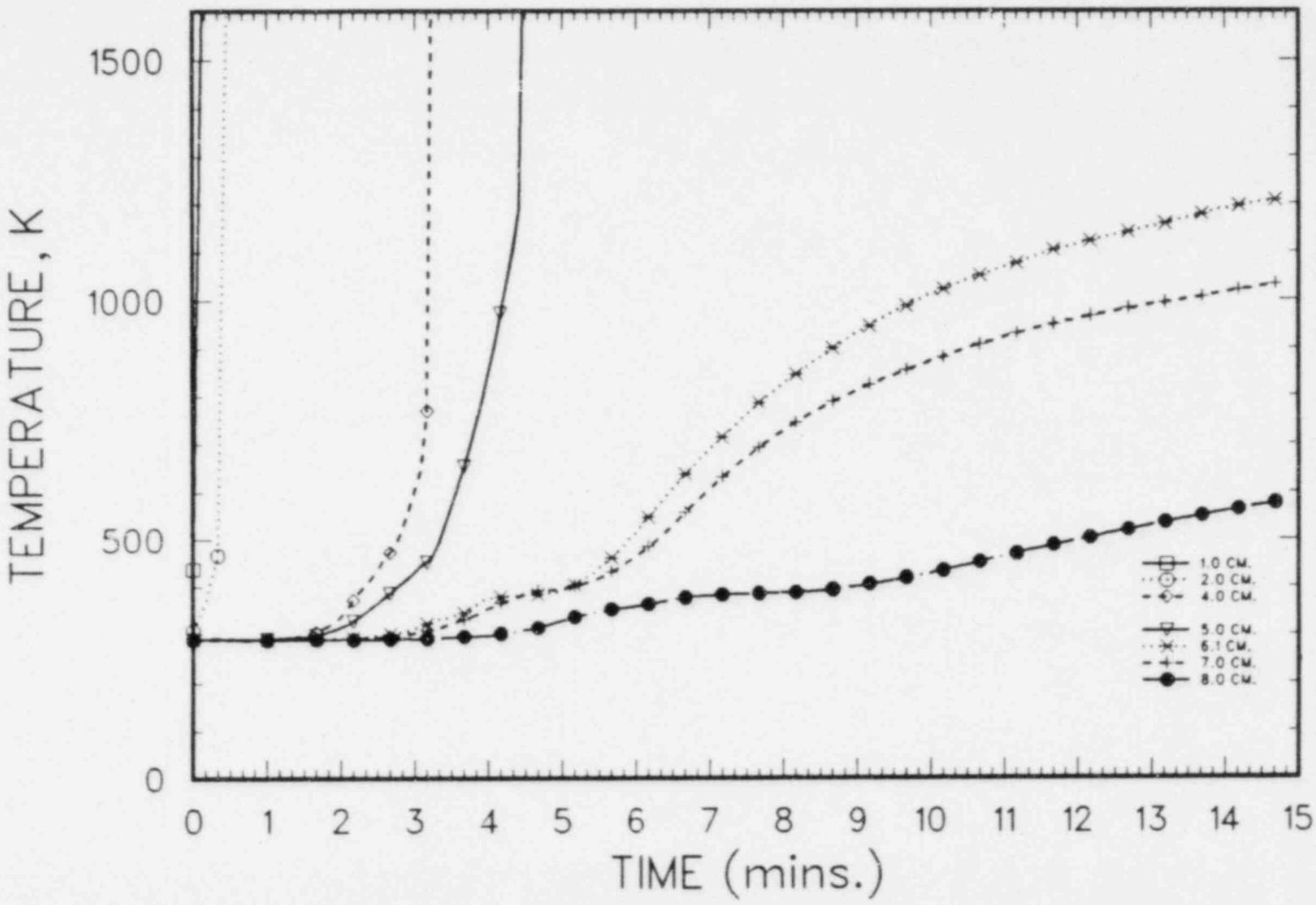

Figure 3.9 TURC1T Concrete Thermocouple Data, Location: r = 18 cm

Shown in Figure 3.10 are the locations of the eroded concrete and the wet-dry interfaces determined from the thermocouple response at radial locations 0.0 cm, 3.0 cm and 18.0 cm. The wet-dry interface is defined as the location in which the concrete is dehydrated of free water. As shown, a maximum depth of 7.5 cm of concrete was eroded.

At early times 0-1 min, the wet-dry interface is essentially at the erosion front, but as the concrete has time to respond to the high heat flux at the ablation front, the wet-dry interface is ahead of the erosion front. Therefore, the release of H_2O would be higher than if only the ablated concrete volume were considered.

The erosion rate of the concrete is shown in Figure 3.11. As the front location data suggest, the erosion of the concrete occurs over three distinct regions. The initial interaction rate of >100 cm/hr occurs from 0 to 1 min, followed by a sharp decrease to an erosion rate between 50 and 80 cm/hr from 1 to 4 min. This erosion rate then falls off gradually until the erosion is terminated. Presented in Section 5.3 is a detailed analysis of the heat transfer to the concrete and discussion of the above observations. Another observation is the apparent radial dependency on the erosion rate from 1 to 4 min. At the radial centerline of the concrete slug the erosion rate is greater than that observed at 3 cm and 18 cm from centerline. This is consistent with posttest hemispherical shape of the concrete surface.

As will be discussed in later sections, the heat transfer into the MgO sidewall during the interaction has a global effect on the melt pool temperature and, therefore, the heat transfer to the concrete. As discussed in Section 2, thermocouple arrays were installed at various locations within the MgO annulus to determine the thermal response of the sidewalls to the heat flux imparted by the melt pool.

The calculation of heat flux to the MgO walls is a classic example of an "inverse" heat conduction problem (IHCP) where the boundary condition (e.g., heat flux) is determined from known interior temperatures. Of the available methods for solving the IHCP, the one that appears to be the most successful for the widest variety of applications is the nonlinear estimation technique proposed by Beck.[22] In this method, the value of the calculated heat flux minimizes the square of the differences between the calculated and experimental temperatures. A computer code, IHCP, has been written based on Beck's methods by Bradley.[23] The code was tested using a variety of exact solution problems and was found to perform excellently. The accuracy of this method is strongly dependent upon the thermocouple temperature data. In

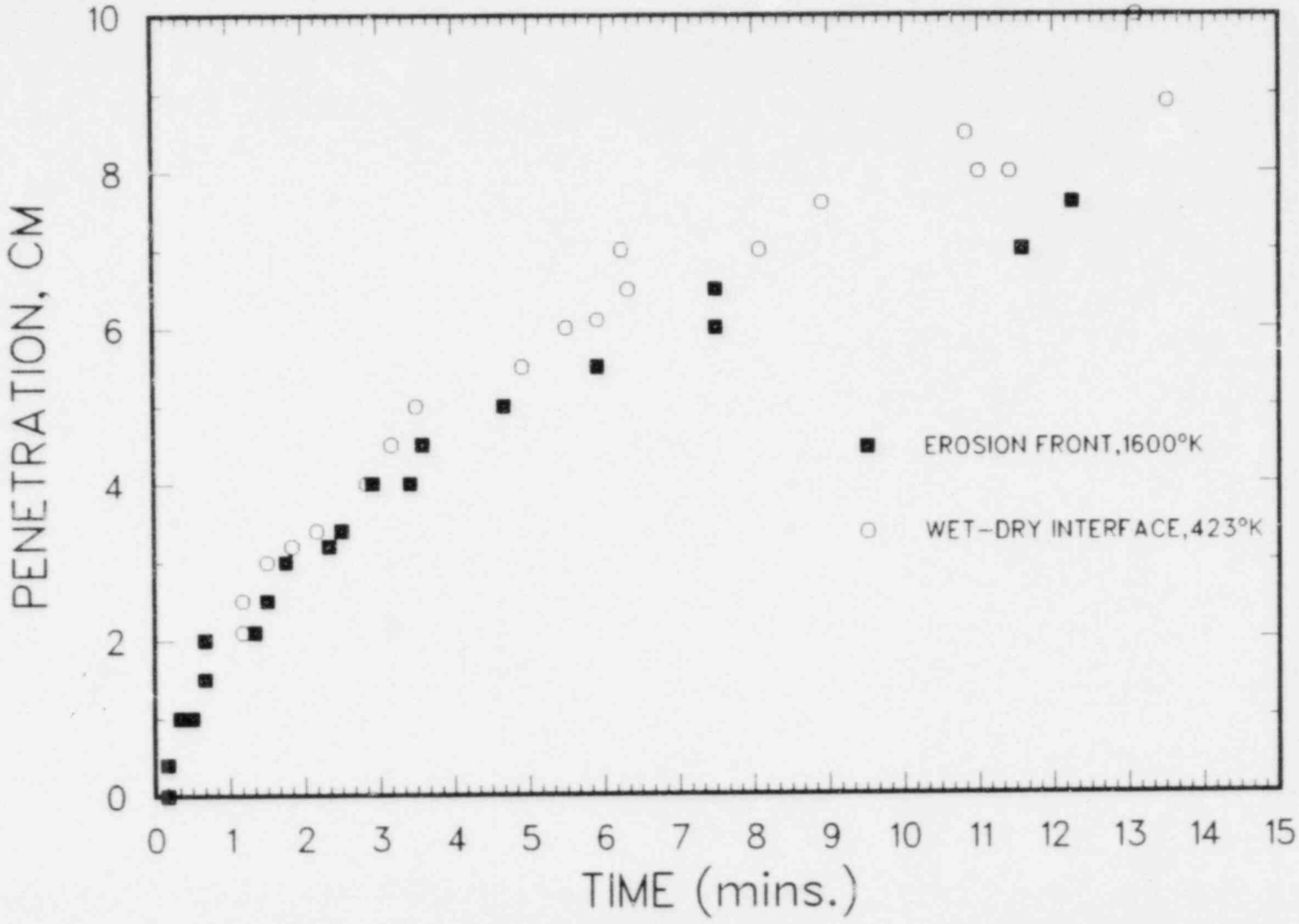

Figure 3.10 TURC1T Concrete Erosion Front and Wet/Dry Interface

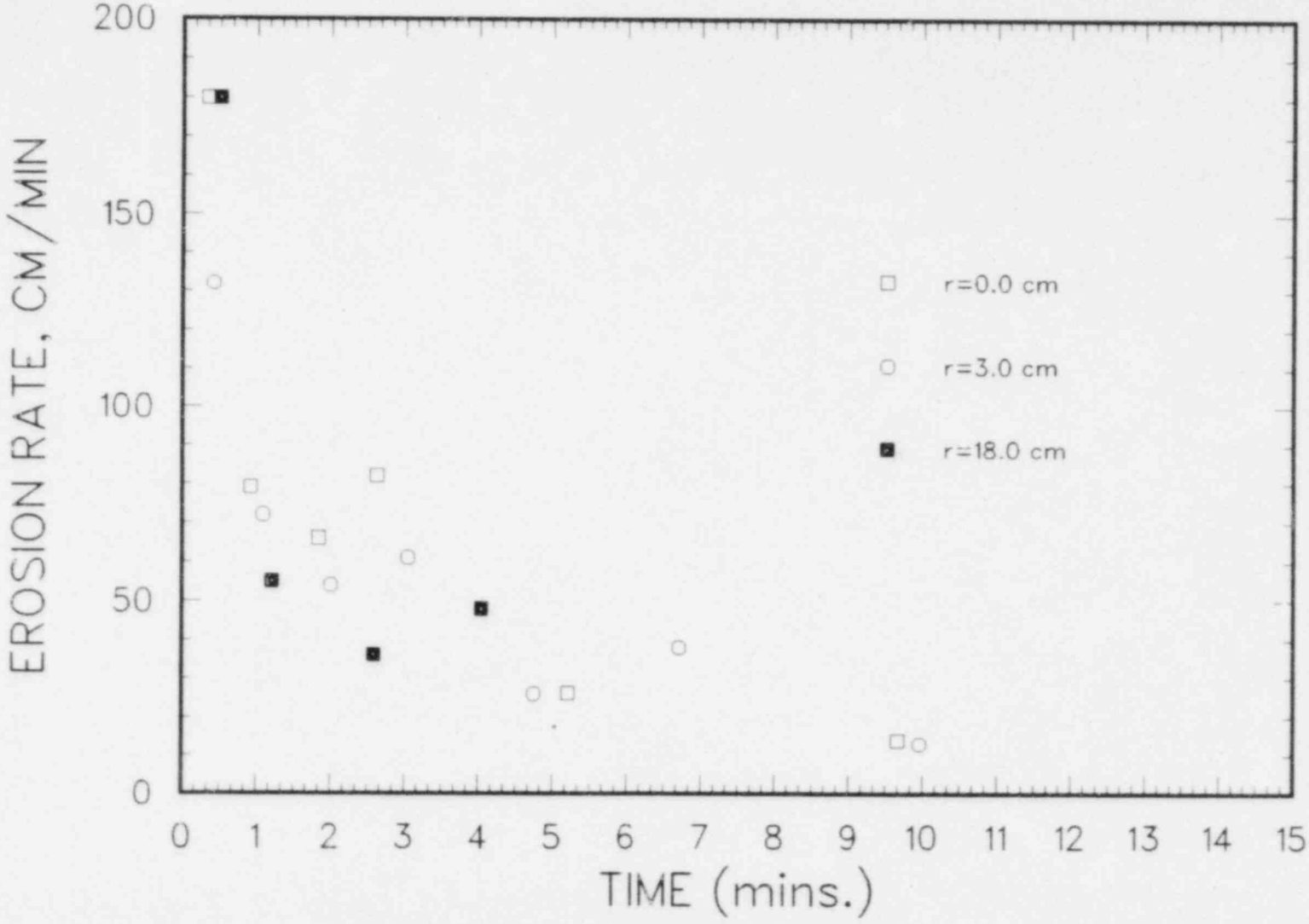

Figure 3.11 TURC1T Erosion Rate

general, it was found that the greater the number of thermocouples utilized in the analysis, the greater the accuracy of the solution. However, Bradley found that beyond three thermocouples, the improvement in accuracy was not sufficient to justify additional thermocouples. The experimental data recorded, and utilized in IHCP, consisted of at least three thermocouples at depths ranging from the surface to 3 cm into the MgO sidewall.

The IHCP solution was calculated for an array of thermocouples that were embedded in the MgO sidewall at an axial location 0 cm (corresponding to the original location of the concrete) and therefore is assured of being in contact with the debris pool throughout the experiment. The result, shown in Figure 3.12, is the heat flux into the MgO sidewall for the TURC1T test.

A close look at the results shows a constant heat flux for ~1 min at 6.5×10^5 W/m^2. The heat flux falls at a constant slope for ~2 min into the experiment, when the slope or rate of decrease in heat flux suddenly change. The heat flux continues to decrease for ~5 min when the slope changes once again. Within Section 5.3, discussion of the global melt pool heat transfer will be presented. Discussion of the significance of the above observations will be presented.

3.2.2 TURC1SS

3.2.2.1 Posttest Observations

As with the TURC1T crucible, the TURC1SS crucible was removed, covered, and stored until the completion of the TURC series of experiments. The posttest observations are summarized in the following paragraphs.

The crucible instrumentation and portcullis were removed, and x-rays of the lower section of the crucible were taken. The x-rays, shown in Figure 3.13, were considerably different from the TURC1T results. First of all, layering of an oxidic and metallic phase was not apparent. This in itself is not surprising due to the initial composition of the melt. Secondly, the melt-concrete interface was severely convoluted, with the concrete erosion uneven. Figure 3.14 shows a typical cross-section profile of the concrete surface; note the erosion pattern forms two cusps at a radius of half the distance to the wall. As with the TURC1T experiment, stirring of the melt pool by released gases seems to form a rotating torus.

The x-rays indicate a pool depth from 14 to 20 cm. The volume of concrete eroded was 7067 cm^3, resulting in an average erosion depth of 4.3 (-0.5/+0.0) cm. The melt pool posttest mass was 106 kg with the remainder of the initial charge on the sidewalls in the melt generator and experiment crucible.

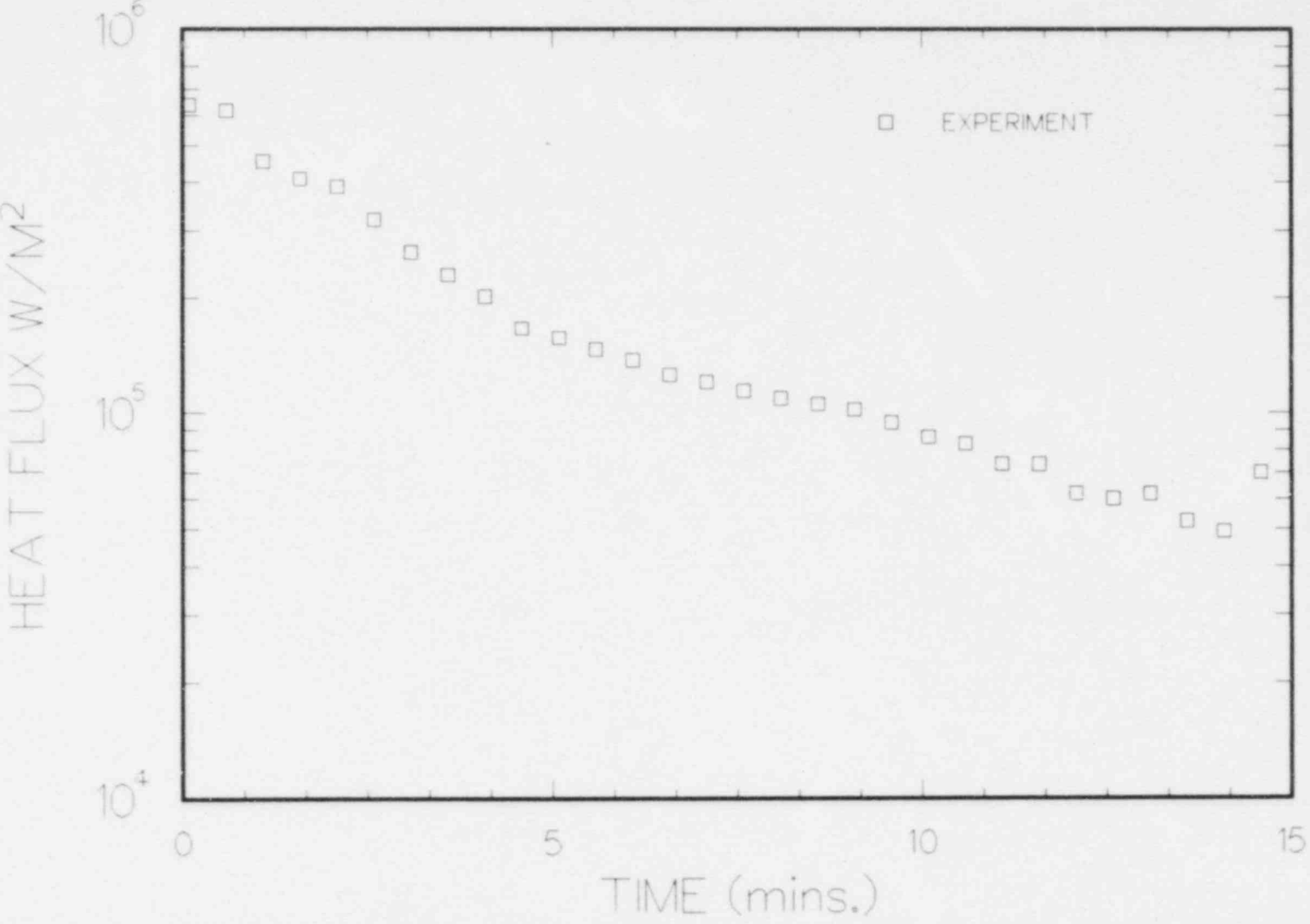

Figure 3.12 TURC1T MgO Sidewall Heat Flux

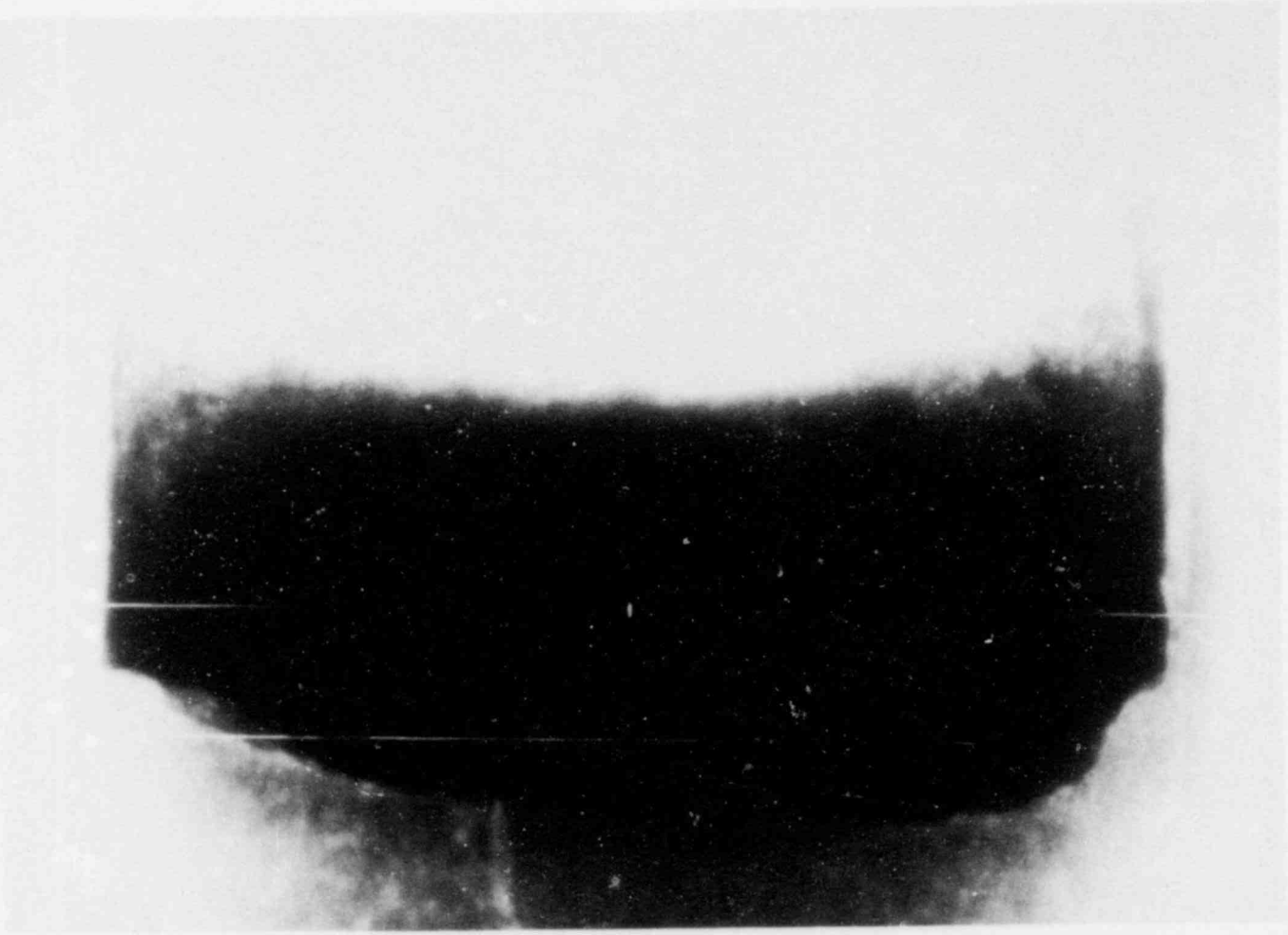

Figure 3.13 TURC1SS Posttest X-Ray

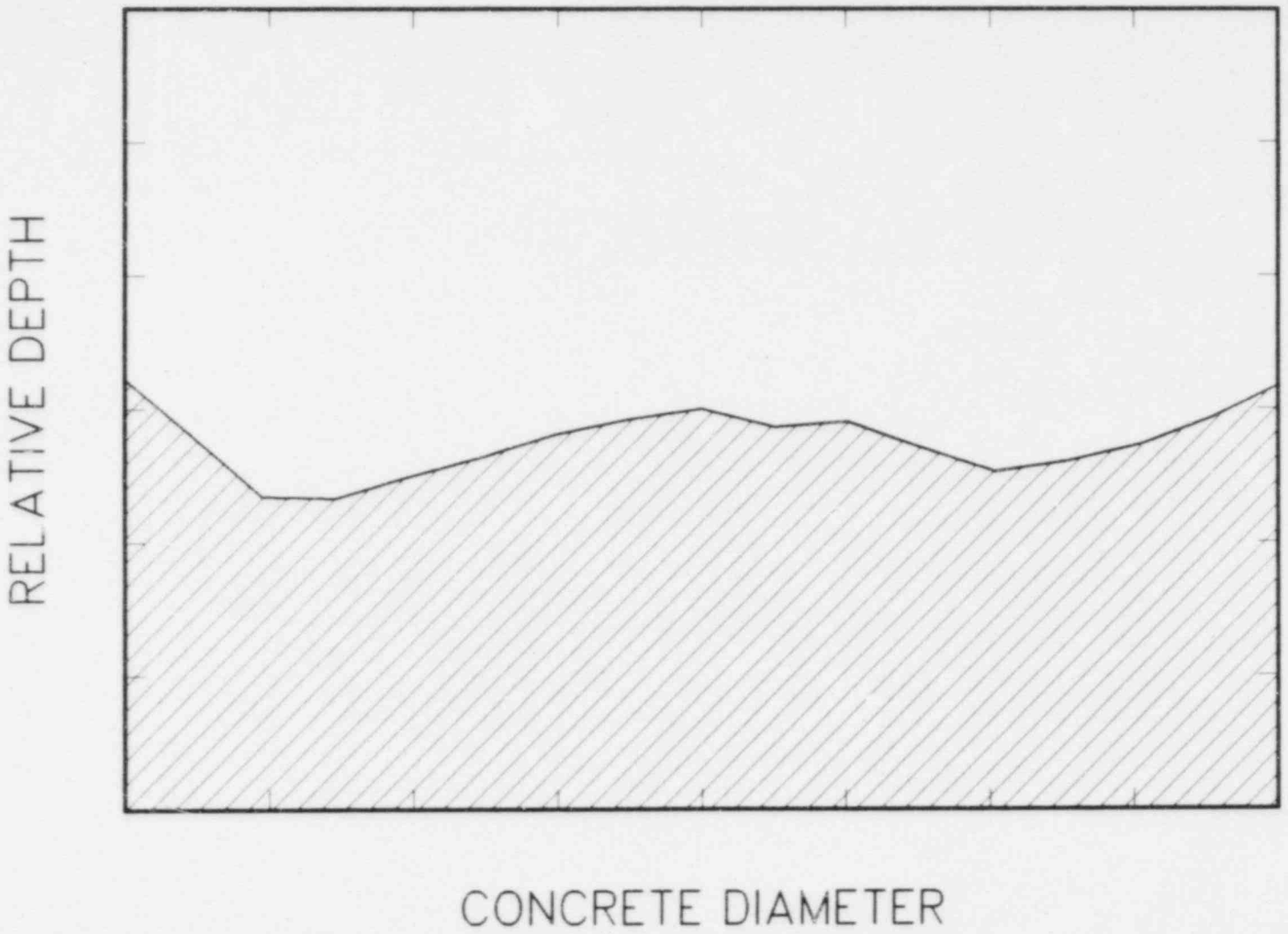

Figure 3.14 TURC1SS Typical Concrete Erosion Profile

As shown in Figure 3.15, the crucible was sectioned in the same manner as the TURC1T test. As with the previous experiment, the crucible showed both axial and radial cracking of the MgO annulus.

An inspection of the interior of the crucible showed a melt pool at the base of the crucible, with a crust on the upper sidewall. The crust was nearly all metal and varied in thickness from 2-3 cm closest to the melt pool to 0.5-1.0 cm at the top of the crucible.

In Figure 3.16, the melt pool and concrete slug are clearly shown. Note the wide gap between the melt pool and concrete slug. As with TURC1T, it is not clear whether or not this is a result of shrinking and pulling away of the steel during the cooling of the frozen melt pool or an artifact of the interaction mechanism.

The MgO annulus in contact with the melt pool was not severely degraded as was the TURC1T crucible, probably due to the lower initial temperature and duration of the experiment.

The solidified melt pool was removed from the crucible and sectioned to reveal its internal structure. Figure 3.17 is a photograph of the sectioned melt pool. Note the top surface; it consisted of both oxidic and metallic phases intermixed with one another, with a slight preference for the light oxide material to be closer to the top surface. A look at the internal composition of the melt shows large quantities of oxidic material surrounded by metal. Additionally, intact pieces of coarse concrete aggregate are found both within the melt pool and adhered to the bottom surface. The quantity of trapped gas bubbles is considerably less and the size was smaller, < 0.5 cm than the TURC1T metal pool. Prior to the removal of the melt pool, fine debris ~0.5-1 mm in diameter was found between the MgO annulus and melt pool.

As shown in Figure 3.18, the concrete surface was heavily convoluted, discontinuous, and rough. Exposed coarse aggregate protruding from the interface was observed. The concrete material between the two cusps (the center of the concrete slug) was severely degraded. The color of the material was a light gray instead of the black appearance of the TURC1T interface. No exposed sheaths of thermocouple were observed.

3.2.2.2 Concrete Erosion and Crucible Thermal Response

As was the case with TURC1T, the erosion front through the concrete slug was determined from the signatures of the thermocouples embedded within the concrete. Shown in Figures 3.19-3.21 are the thermocouple temperature traces at locations varying from 0.0 to 8 cm below the original concrete surface.

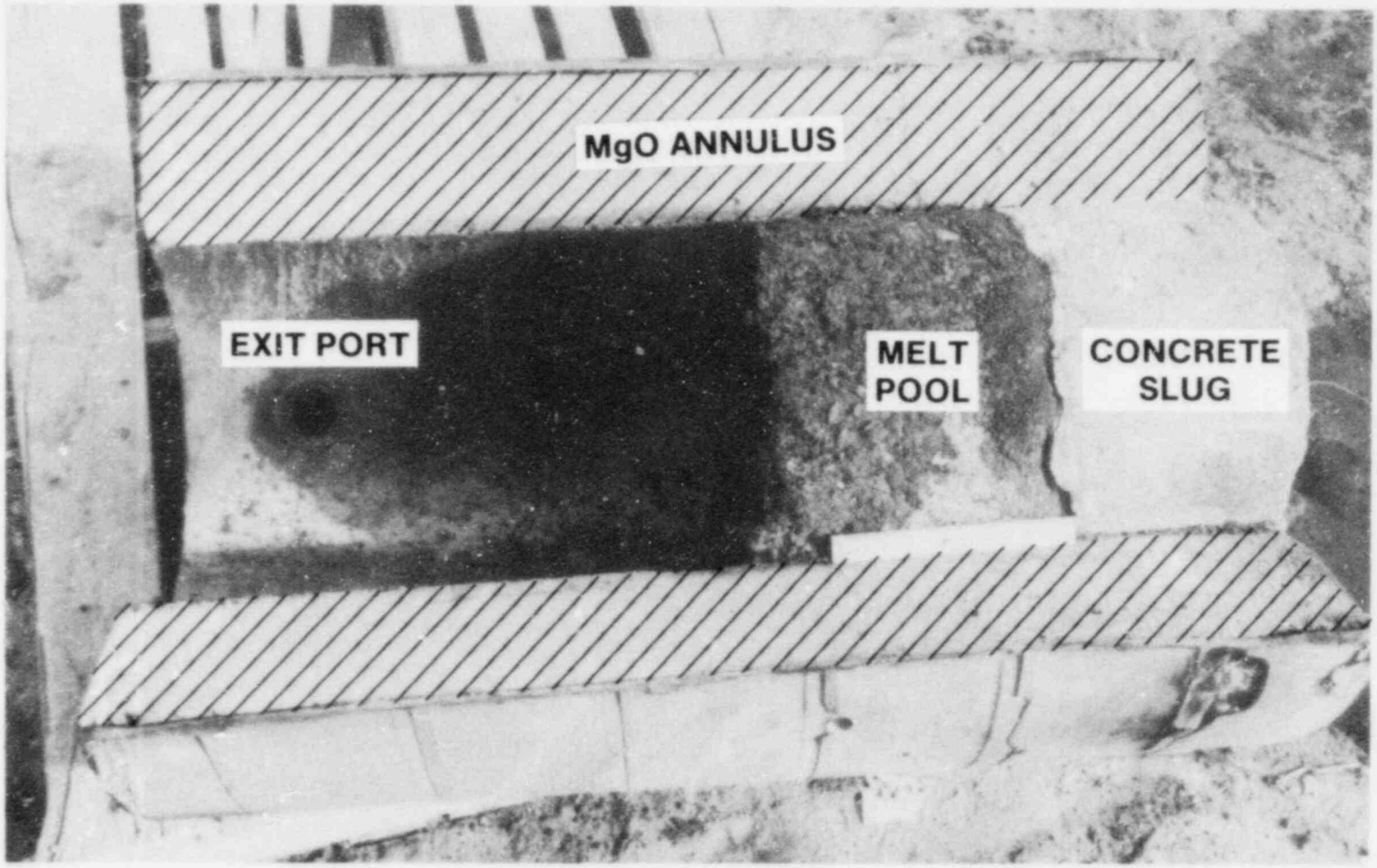

Figure 3.15 Sectioned TURCISS Crucible

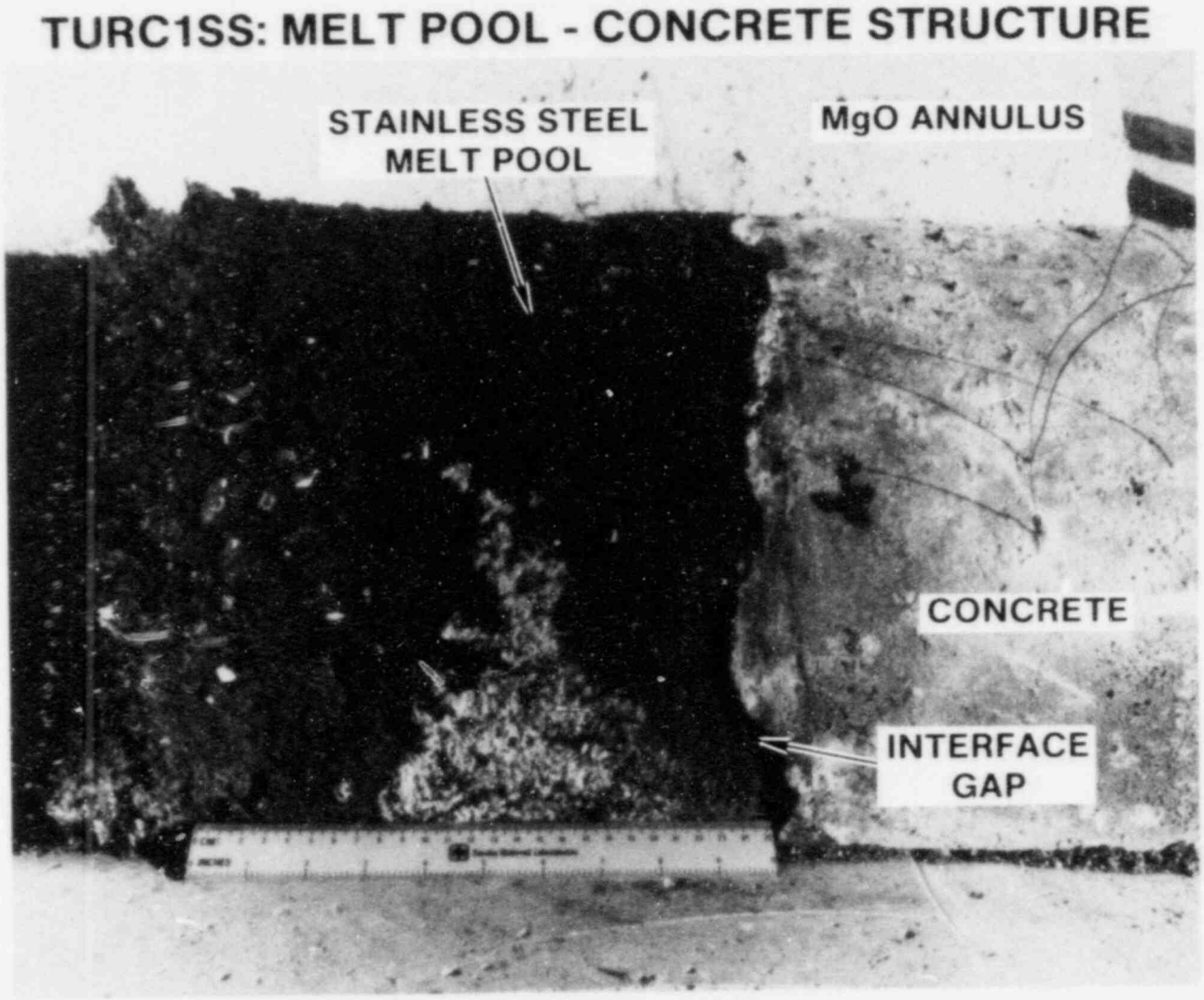

Figure 3.16 TURC1SS Concrete Slug and Melt Pool

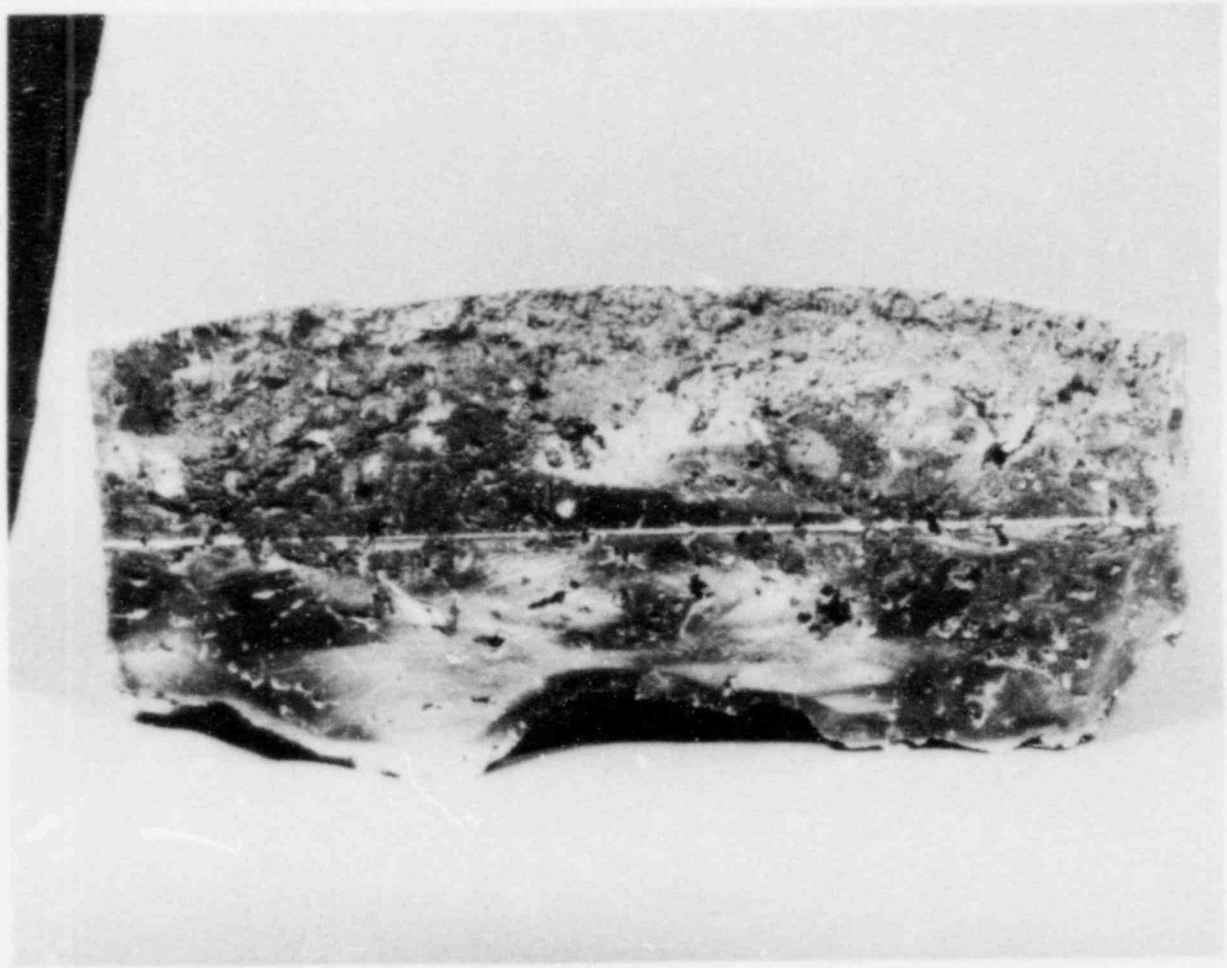

Figure 3.17 Sectioned TURC1SS Melt Pool

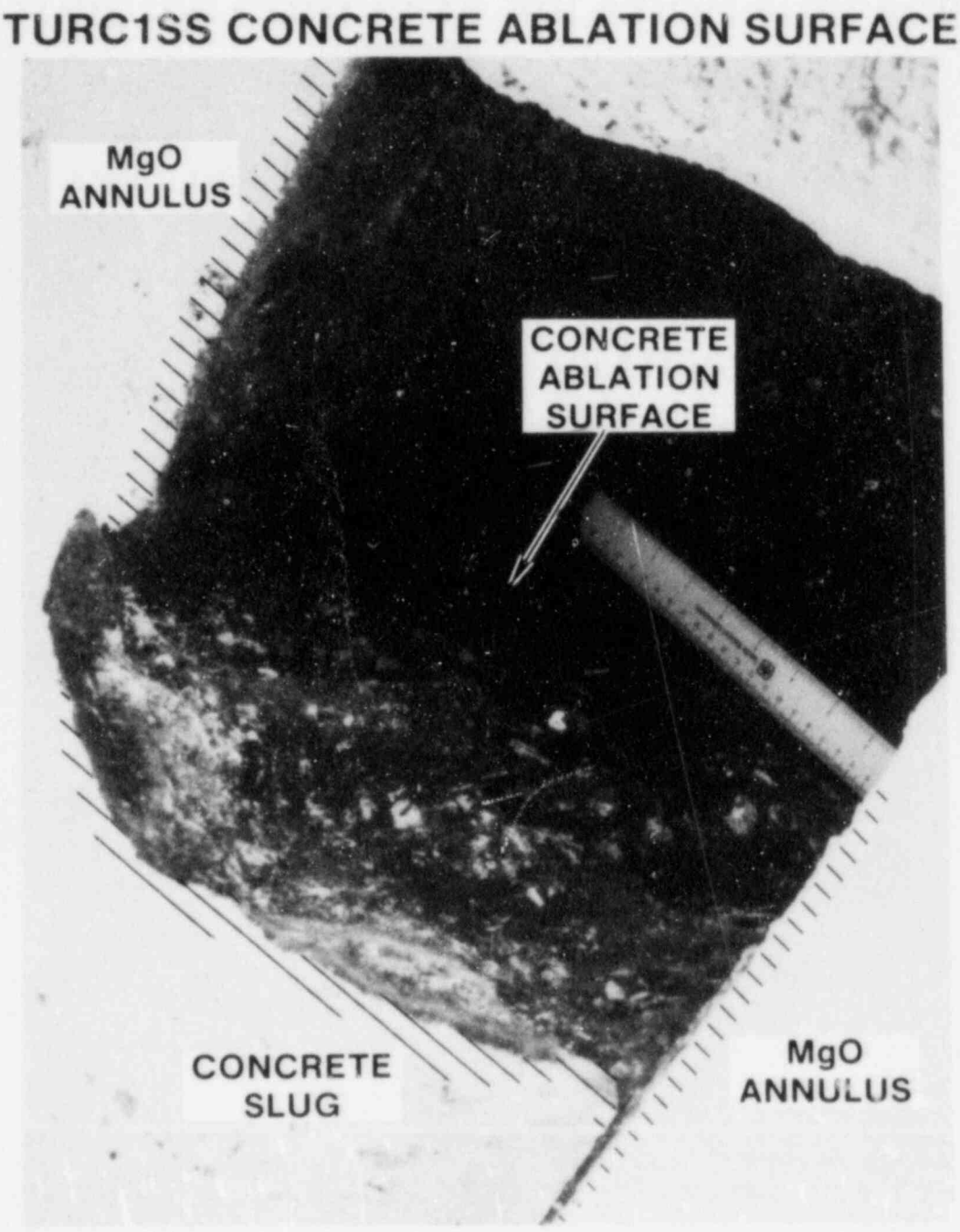

Figure 3.18 TURC1SS Concrete Surface

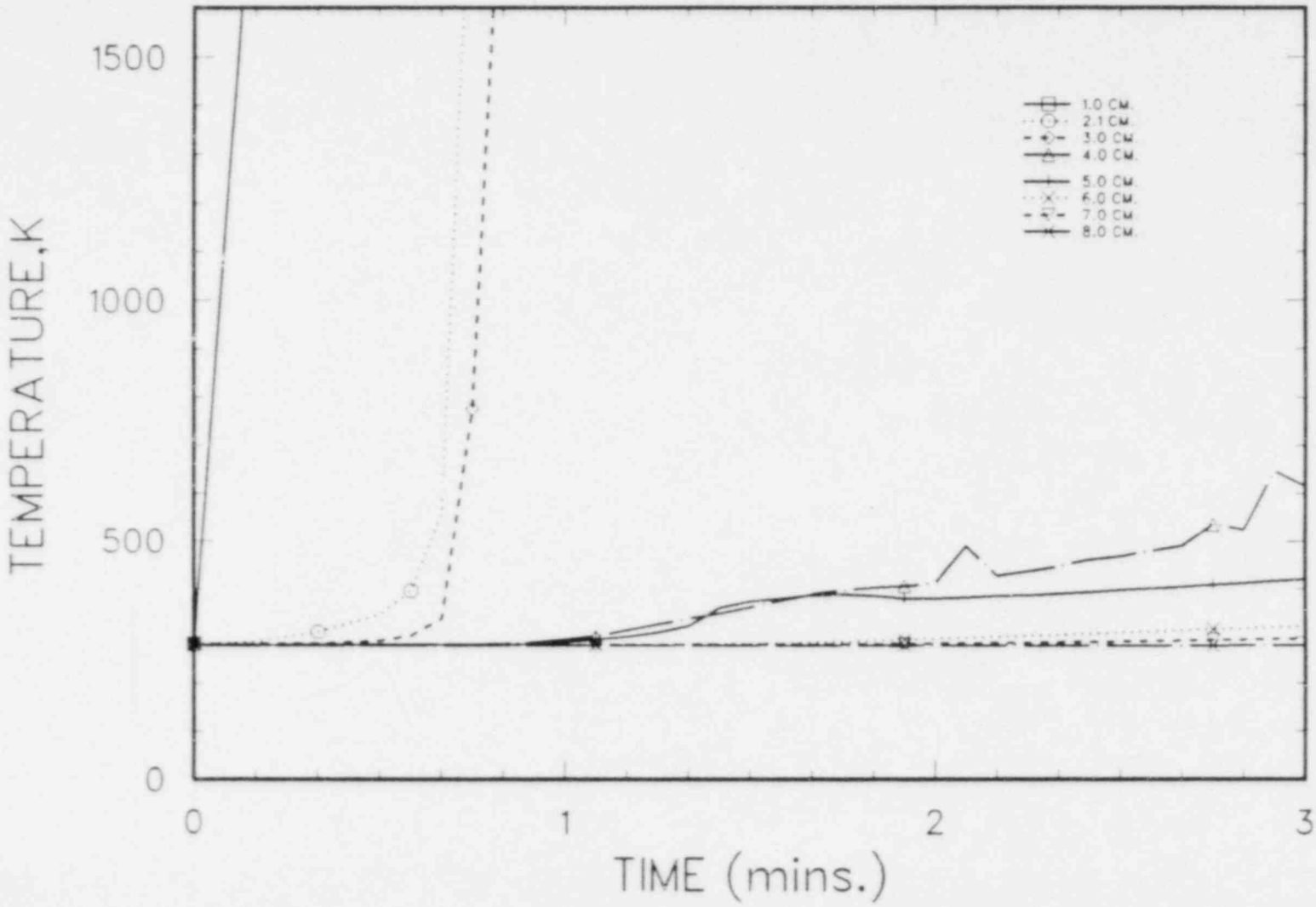

Figure 3.19 TURC1SS Concrete Thermocouple Data, Location: Concrete Slug Centerline

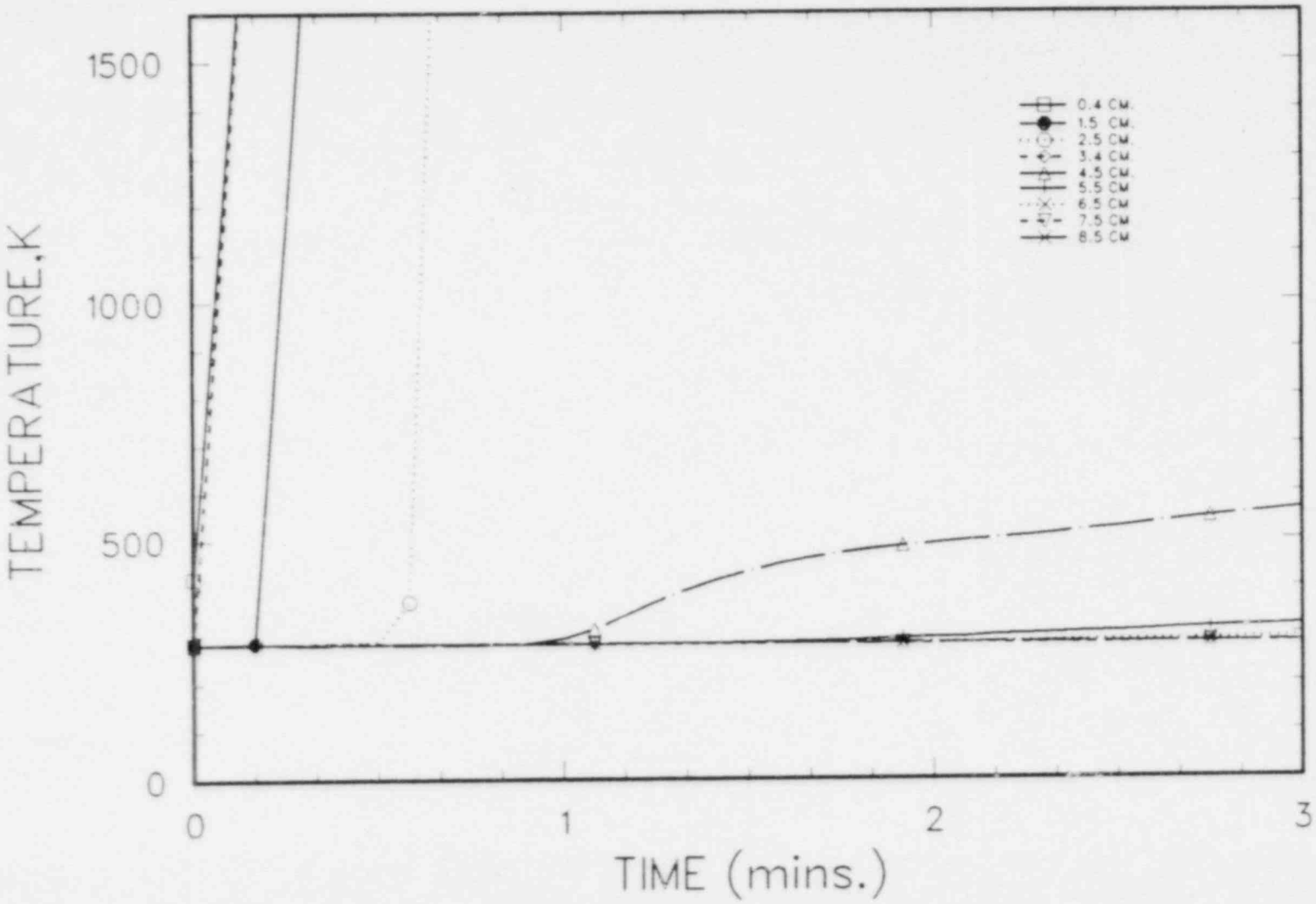

Figure 3.20 TURC1SS Concrete Thermocouple Data, Location: r = 3 cm

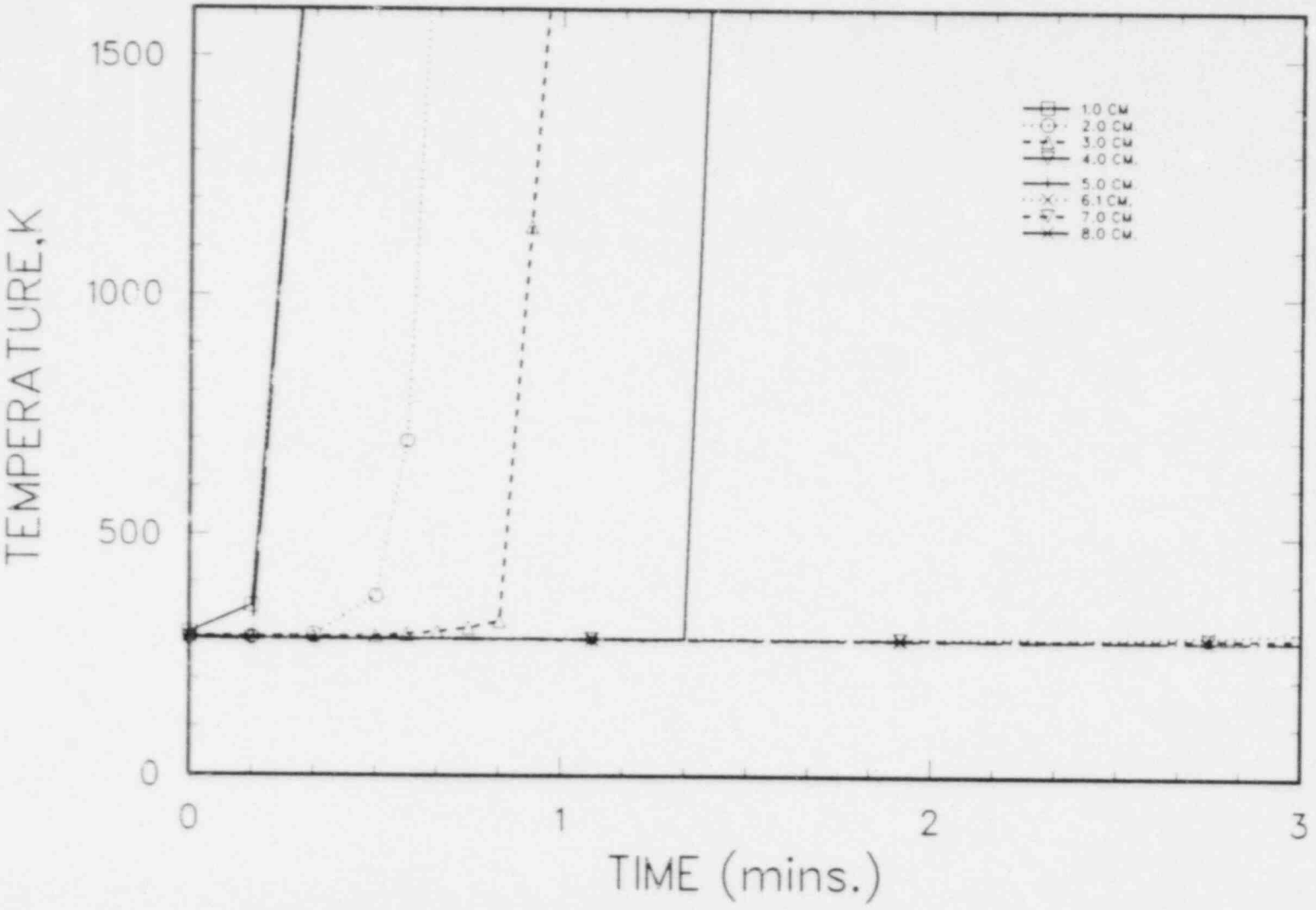

Figure 3.21 TURC1SS Concrete Thermocouple Data, Location: r = 18 cm

A careful examination of the traces shows several thermocouples to have failed at times that are not consistent with their location. For example, a thermocouple 3.4 cm deep fails before a thermocouple at 1.5 cm (within the same thermocouple array). In light of the method of installing the thermocouples (see Section 2.3.0) and the irregular posttest erosion profile, it is speculated that the thermocouple junctions did not fail, but the stem or sheath was attacked at another location, far from the junction, thus failing the thermocouple. This mode of thermocouple failure was discriminated from the data used to reconstruct the erosion front.

The erosion front location is plotted in Figure 3.22. The maximum depth indicated varied from 5.0 cm at r=18 cm, to 3.0 cm at r=0 cm. The erosion rate was 180-210 cm/hr.

As with the TURC1T experimental data, the heat flux into the MgO sidewall was determined from an array of thermocouples embedded within the wall at the original concrete surface. The IHCP solution, shown in Figure 3.23, consists of an initial heat flux of ~ 3.4 x 10^5 W/m^2 for a brief time (0-15 sec) followed by a gradual relaxation over the next 3 min. As an indication of the IHCP codes success at the surface heat flux calculation, a comparison between the measured and calculated temperatures at several depths within the MgO sidewall is shown in Figures 3.24 through 3.27.

Further analysis and discussion of the experiment data are presented in Section 3.2.3.

3.2.2.3 Gas Composition

As described in Section 2.4.2, discrete grab gas samples of evolving gases were taken throughout the test. The compositions of the gases sampled are listed in Table 3.1.

Sample #1 was taken prior to the seeming of the melt. This sample was of air from the interaction chamber. A comparison between published composition of air[24] and sample #1 indicates a 0.2% difference for N_2 and O_2 and approximately 13.5% for argon. The error for the argon constituent is due in part to the relatively small quantity found in the sample and in part to the close proximity of the O_2 and Ar peaks in the chromatograph, making resolution difficult.

Past experiments[2,3,4,5] utilizing grab samples similar to those used in this experiment have shown the determined compositions to be consistent with gas mixtures that have been quenched at temperatures ranging from 1000 K - 1100 K. At the gas sampling location, the temperature was well above 1000 K; thus the gases maintained chemical equilibrium until they cooled below 1000 K.

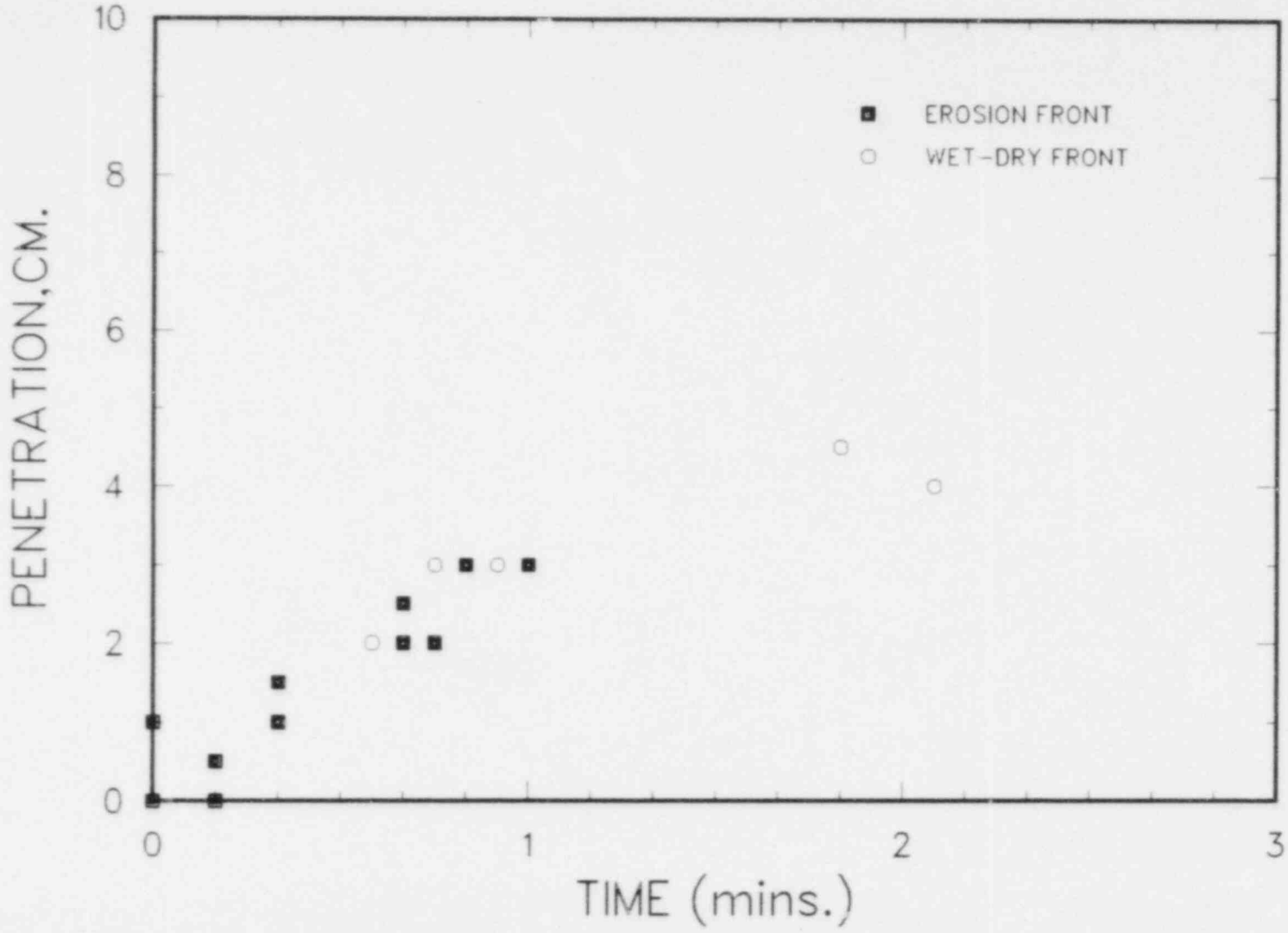

Figure 3.22 TURC1SS Erosion Front and Wet-Dry Interface

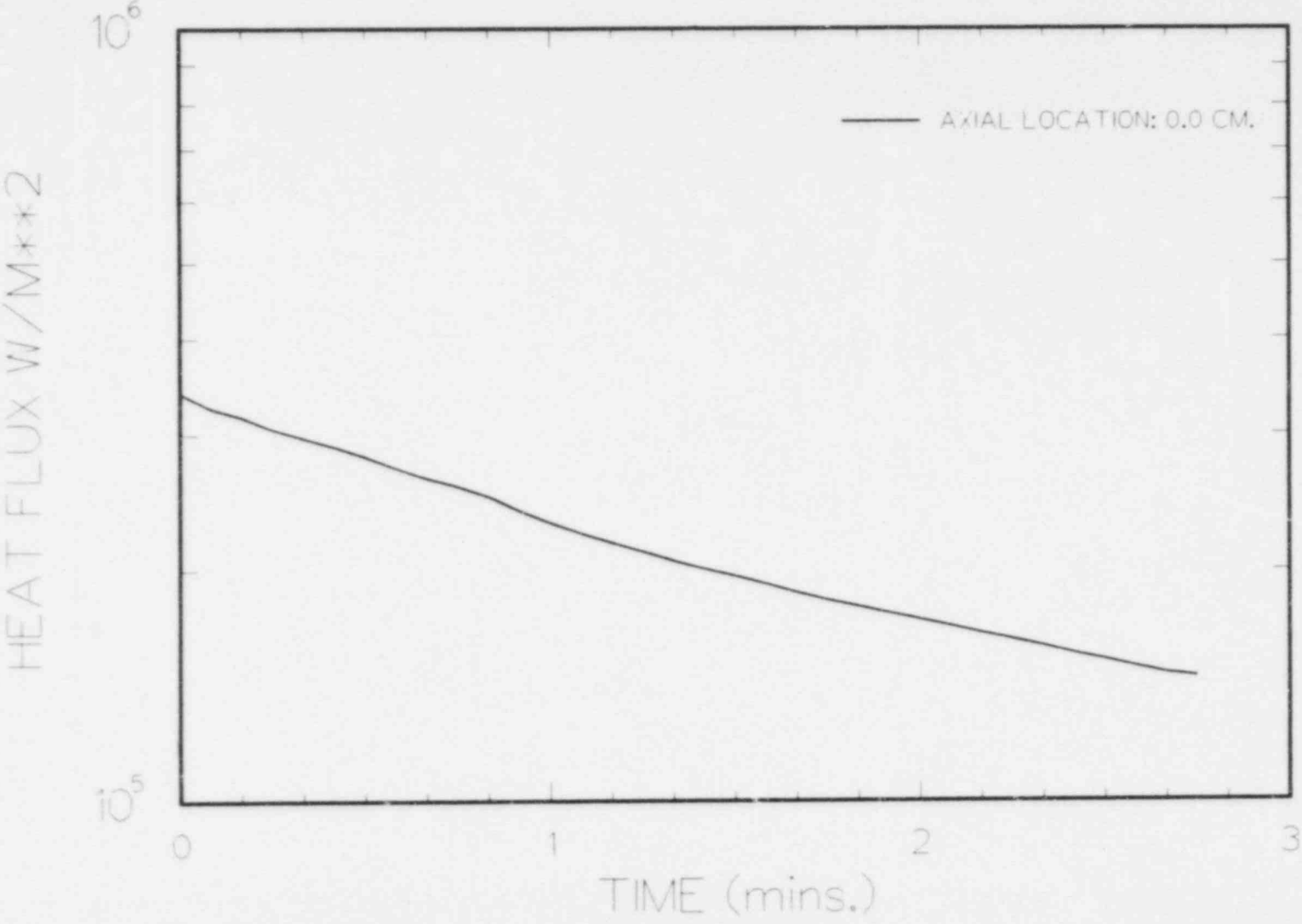

Figure 3.23 TURC1SS Sidewall Heat Flux

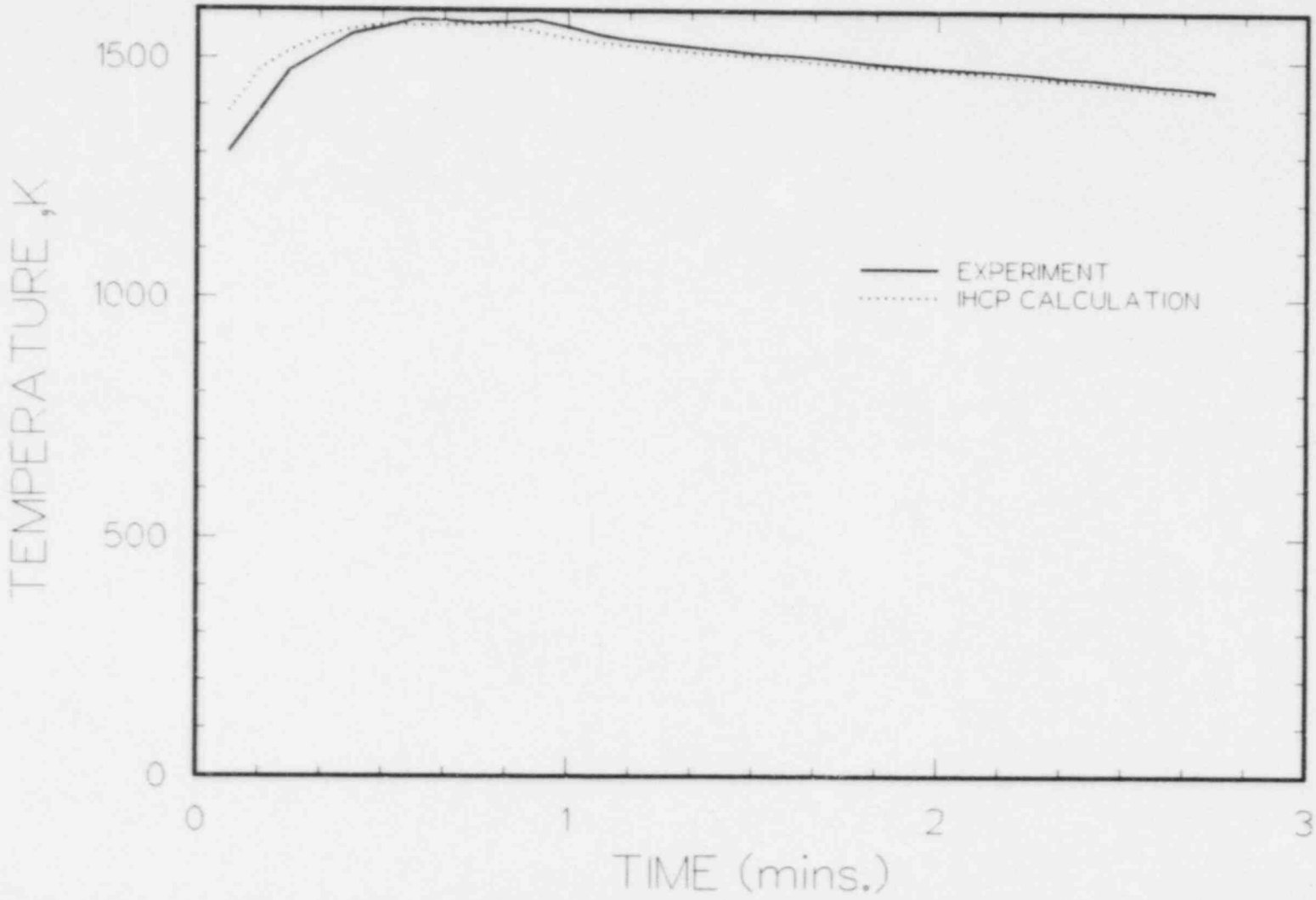

Figure 3.24 Comparison of IHCP Prediction and Experimental Data, Depth: Surface

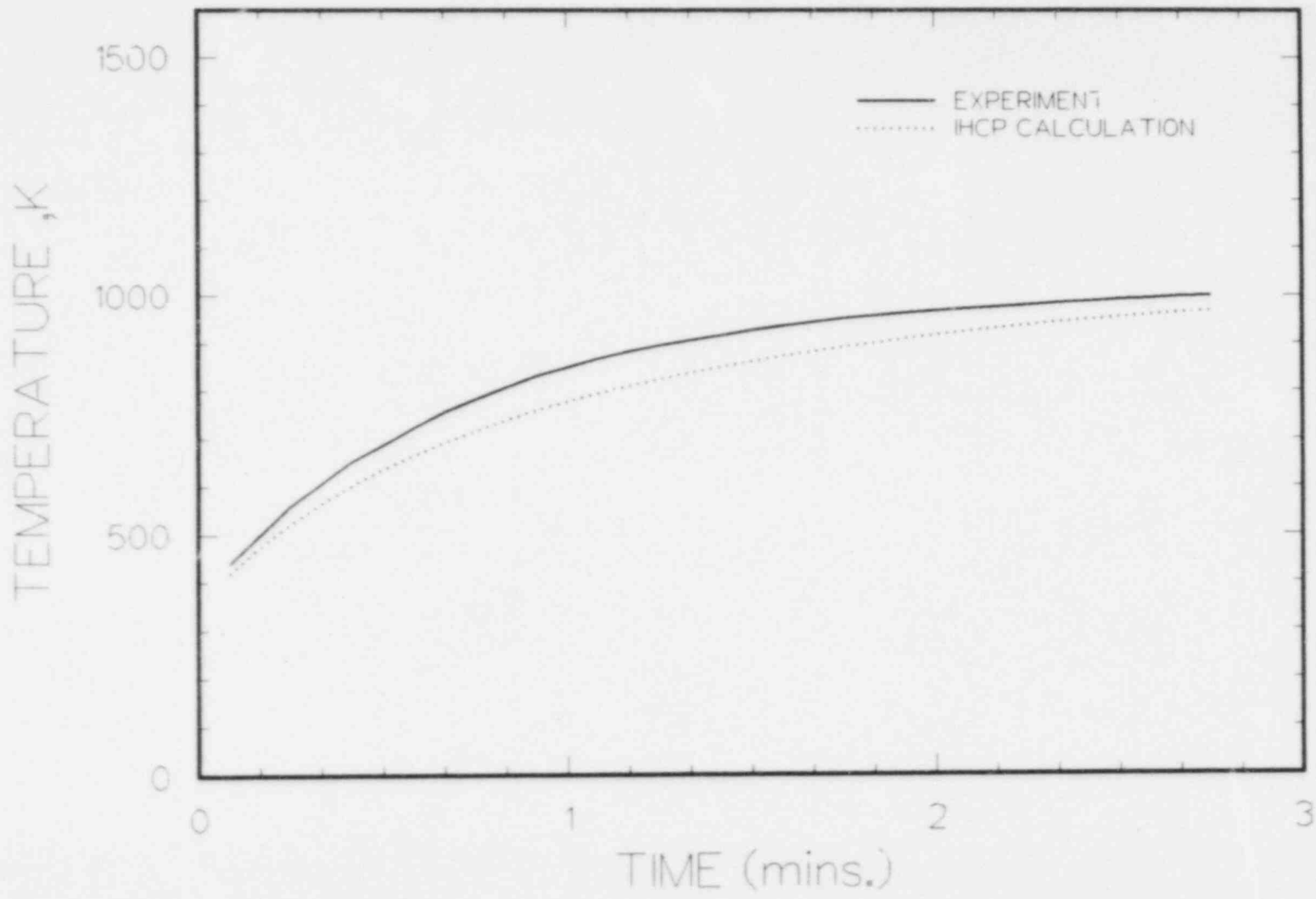

Figure 3.25 Comparison of IHCP Predictions and Experimental Data, Depth: 1 cm

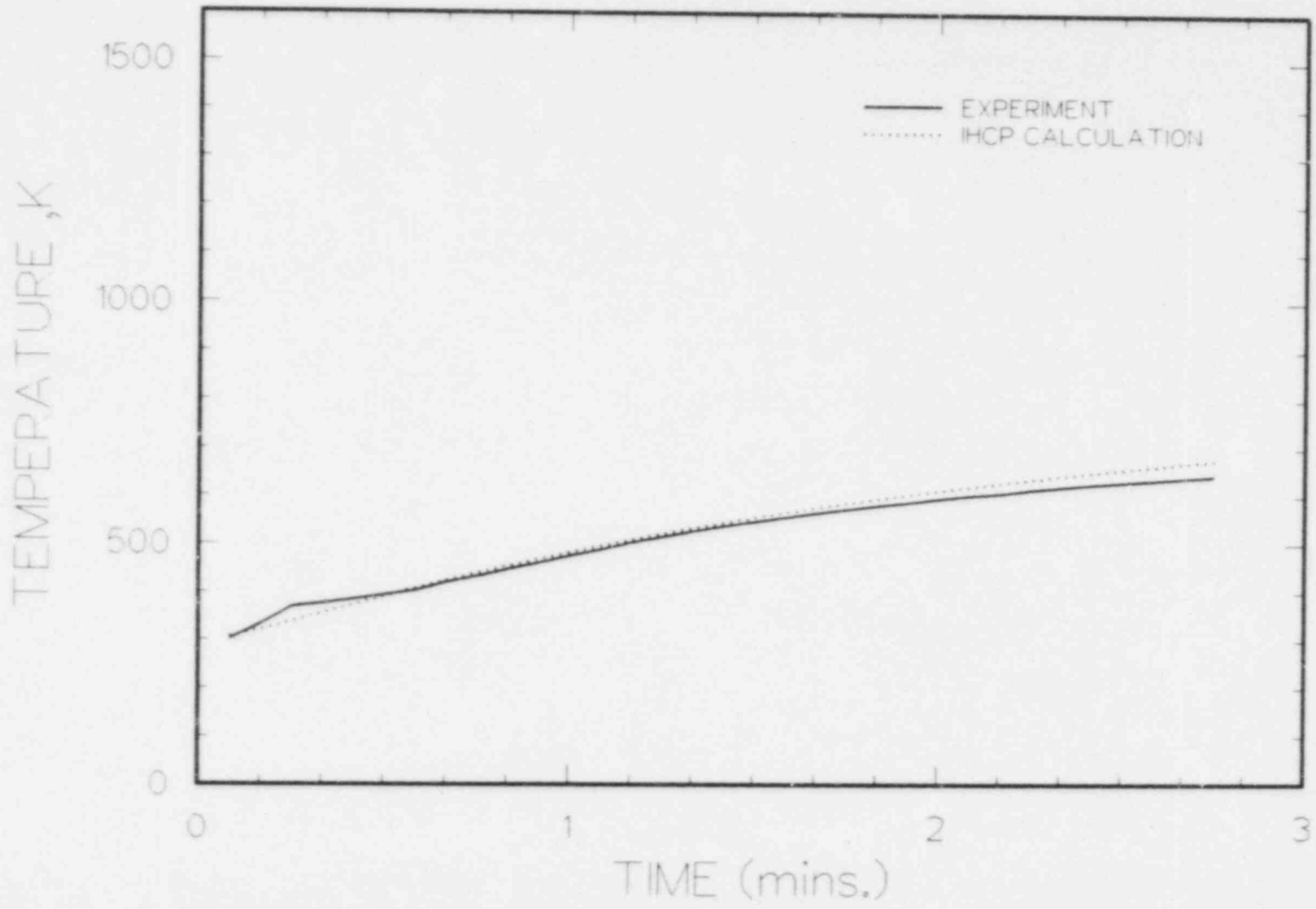

Figure 3.26 Comparison of IHCP Prediction and Experimental Data, Depth: 2 cm

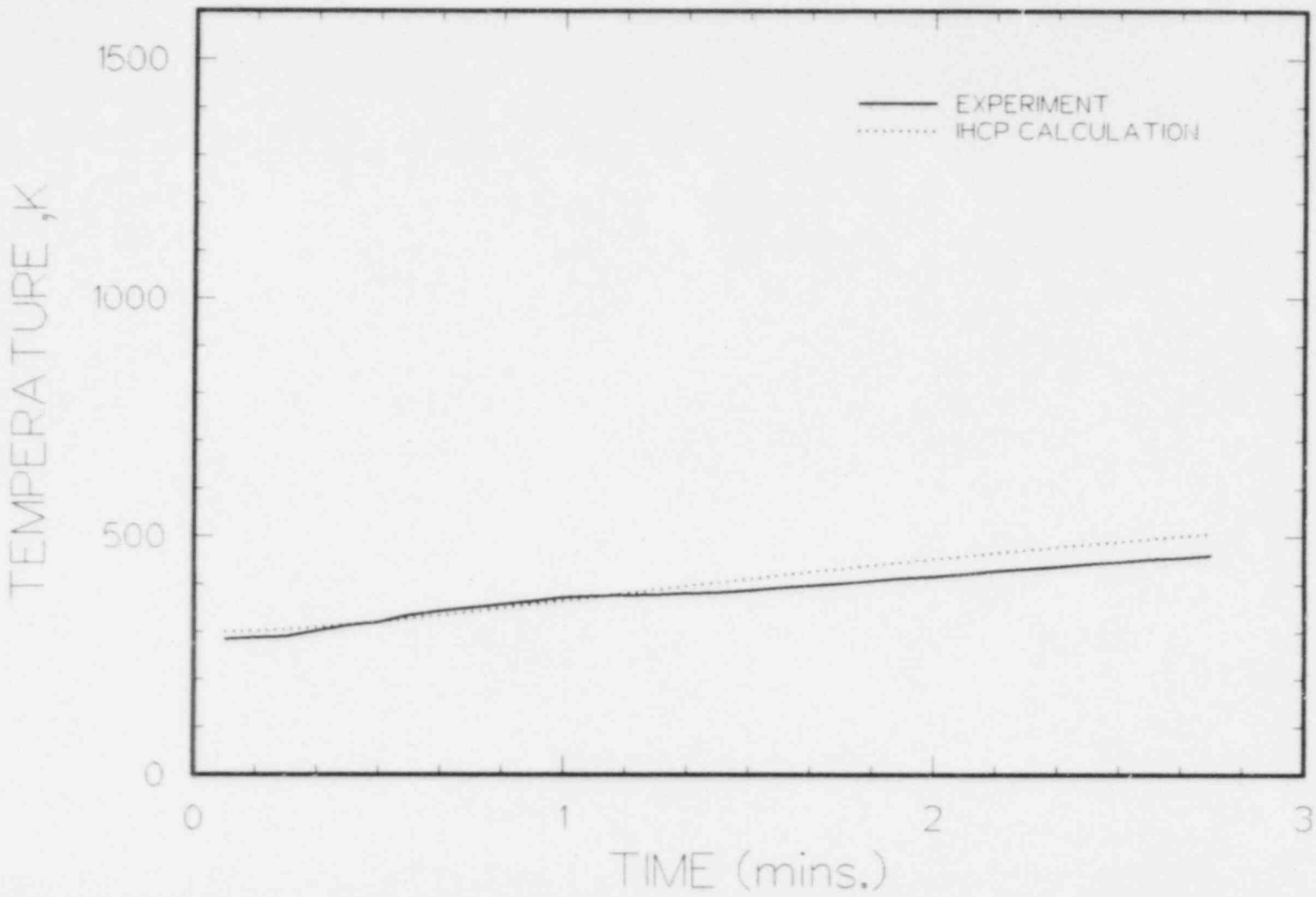

Figure 3.27 Comparison of IHCP Prediction and Experimental Data, Depth: 3 cm

Table 3.1 TURC1SS Gas Composition

Result of Analysis

Sample No.	Time Secs	Sample Extraction: Exit Port	Sample Extraction: Filter Exit	Volume Percent: H_2	N_2	O_2	Ar	CO	CH_4	CO_2	C_2H_4	H_2O*
1	-60.0	X			78.236	20.956	0.808					
2	+6.0	X			74.231	19.927	5.842					
3	15.0	X			78.214	20.834	0.951	tr		tr		
4	25.0	X		46.305	3.263	0.694	0.240	47.329	0.169	1.999	tr	
5	35.0	X		35.009	4.199	0.978	0.369	56.807	0.166	2.472	tr	
6	50.0	X		59.783	1.686		tr	36.030	tr	1.325		1.175
7	70.0	X		60.056	1.120	tr		36.712	tr	2.113		
8	90.0	X		65.462	0.942	tr		31.042		2.554		
9	120.0	X		44.252	1.960	0.272		49.671	tr	3.845		
10	150.0	X		40.431	1.835	0.217		53.153	tr	4.364		
11	180.0	X		46.926	1.870	0.201		46.156	tr	4.847		
12	210.0	X		52.991	1.246			40.986	tr	4.777		
13	240.0	X		59.943	0.836			36.874	tr	0.275		2.072
14	270.0	X		53.878	1.882			34.145	tr	8.634		1.461
15	300.0	X		57.502	2.860	0.531		29.608	tr	9.499		
16	330.0	X		58.453	0.740			28.894	tr	11.913		
17	450.0	X		49.731	31.543	8.224	tr	7.272		3.230		

Note: tr = trace

* H_2O measurements may not be representative of actual quantities within gas sample.

Thermodynamic calculations would be required to assess the composition at the sample temperatures. Unfortunately, measurements of the water vapor content within the sampled gas were unsuccessful; therefore, quantitative equilibrium calculations are not possible.

Shown in Figure 3.28 is the ratio of CO/CO_2 in the sampled gases. For time 0:00-1:00 the ratio appears constant. In all likelihood the evolved gases from the ablating concrete are passing up through the melt pool.

From 1:00-1:40 the ratio of CO/CO_2 is decreasing, even though the bulk melt pool temperature (discussed in Section 5.3) was constant. One possible explanation is that due to the increased viscosity of melt pool (due to its solidification), the evolved gases are bypassing the melt pool and flowing along the MgO; and sidewalls are exposed to a rapidly decreasing metal pool crust temperature.

At 1:40-3:00 the ratio of CO/CO_2 is once again constant. As discussed in Section 3.2, the melt-concrete interaction terminated at 1:40 suggesting that evolving gases from the concrete must be circumventing the metal mass at this point.

The H_2/C molar ratio shown in Figure 3.29 from 0 to 1 min is consistent with the thermal attack of the concrete by the melt pool. (Note: The data presented is the molar H_2 gas content without water vapor.) The initial high value ~3.8 indicates dehydration of the concrete surface with little erosion of concrete. Ten seconds later, as the concrete ablation is well established, the H_2/C ratio falls to the H_2/C ratio found in concrete, indicating that the concrete erosion front and the dehydration front are stationary with respect to each other. At approximately 1 min into the experiment, the H_2/C ratio increases, indicating the dehydration front continues to penetrate the concrete, while the rate of penetration of the decomposition front into the concrete, i.e., temperatures >900 K, has considerably slowed down or stopped. As the heat flux into the concrete continues to decrease, the decomposition front penetration rate decreases, while the lower temperature dehydration front continues to penetrate the concrete, thus accounting for the increased H_2/C ratio and the maintained level of H_2 observed in the late gas samples.

The density of the grab samples at standard conditions is shown in Figure 3.30. An average value of 0.7 kg/m^3 for most applications would be appropriate.

3.2.2.4 Aerosol Data and Analysis

Upon retrieval of the instruments and disassembly, the following observations were made:

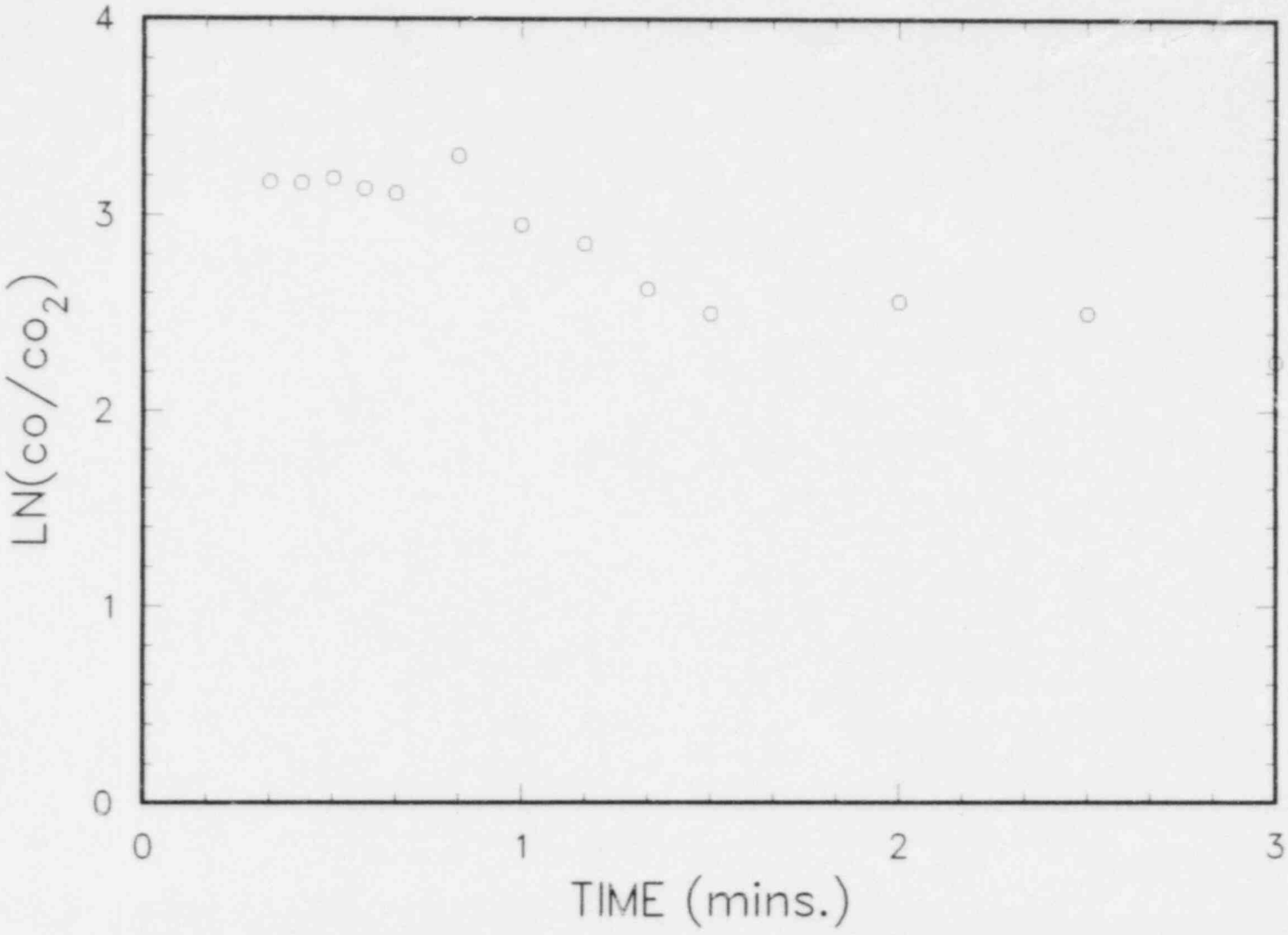

Figure 3.28 TURCISS Gas Sample Ratio of CO/CO_2

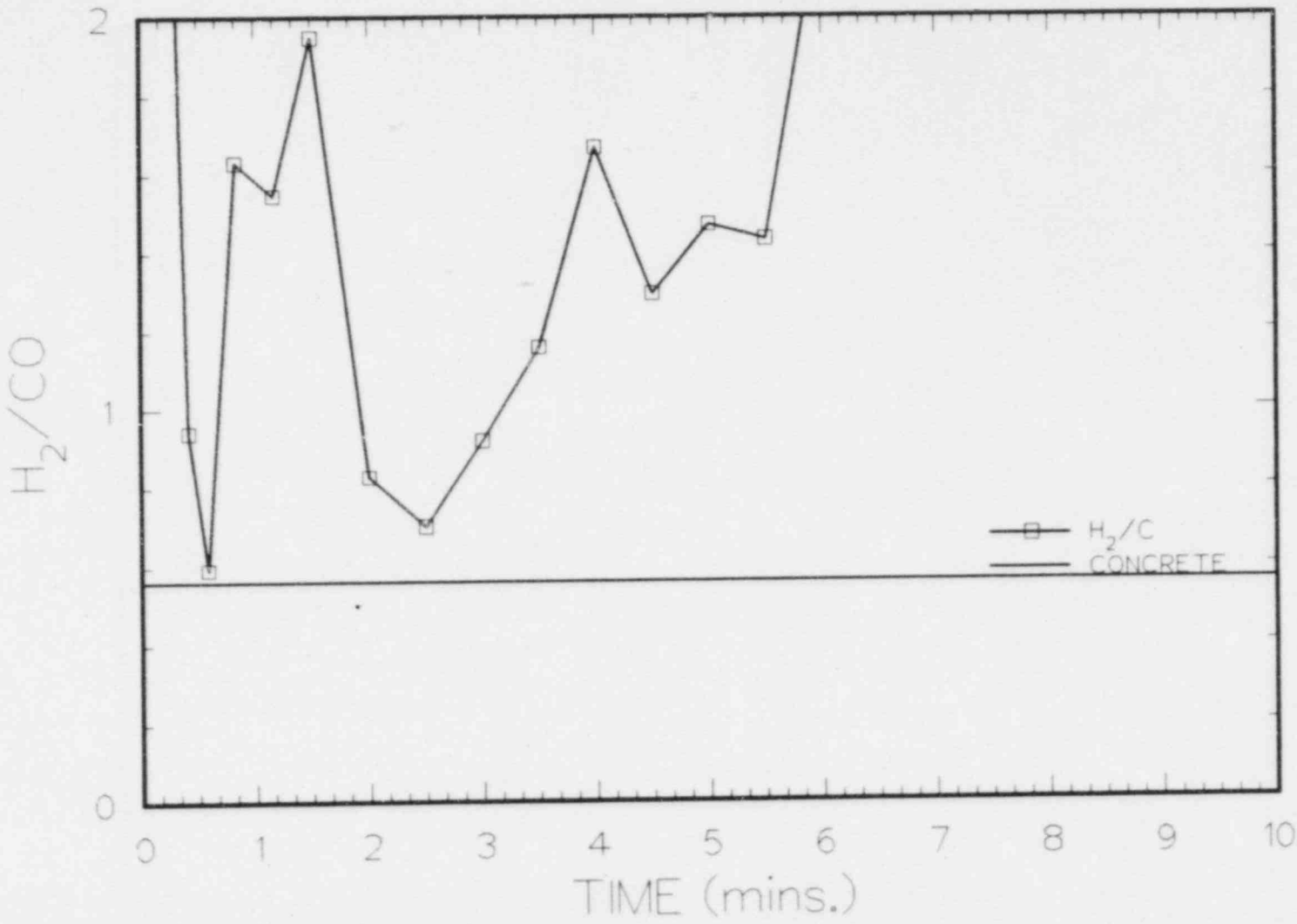

Figure 3.29 TURC1SS Gas Sample H_2/C Molar Ratio

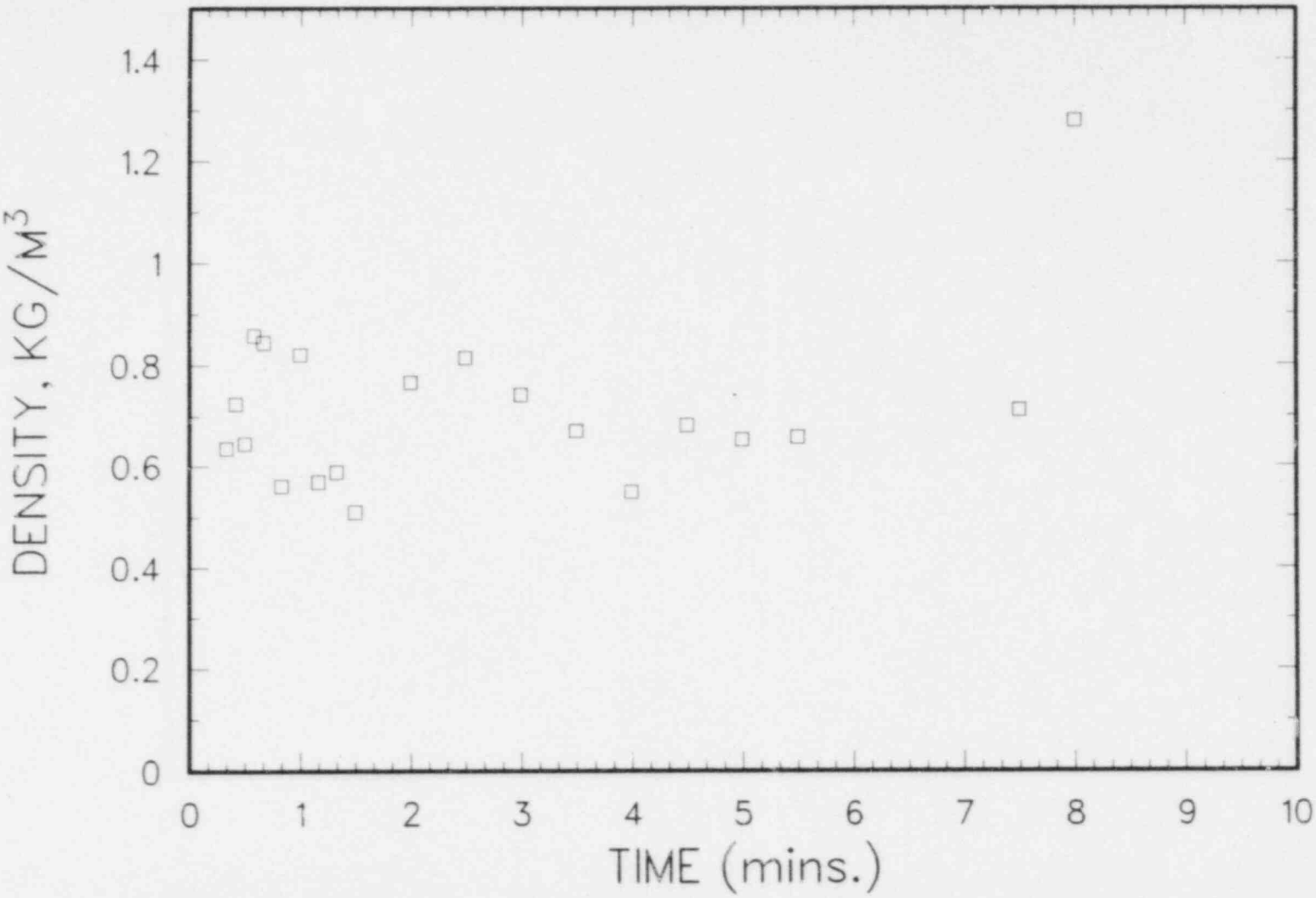

Figure 3.30 TURC1SS Gas Sample Density

1. The view windows of the opacity monitor were observed to be wet with condensed water. Aerosol deposits were observed coating the central portion of the windows. (A sheath air injection system to be included on subsequent tests should remedy the view window fouling.)

2. The impactor samples exhibited overloading beginning at stages 5, 6, and 7. The deposition on earlier stages was normal in appearance and within the mass collection limit of the stages.

3. The aerosol collected in the impactors and on the filter samples was dark, almost black in appearance.

The data taken for the test TURC1SS yielded an estimate for the aerosol mass source rate as a function of time. Even though the impactors were overloaded, the point at which overloading began gives an indication of the aerosol distribution. The cyclone samples were collected over the duration of the test in order to collect aerosol material, segregated by size, for analysis. This analysis has not yet been performed.

Opacity Monitor: The reading went to 100% opacity and remained there during and after the test. The windows were fouled by aerosol and condensed water and no useful data was obtained.

Filter Data: The filter samples gave concentrations where the exhaust line entered the top of the gravel bed filter during the test. The mass concentration times the volumetric flow gives the mass source rate, which can be normalized with respect to the melt surface.

Table 3.2 gives the aerosol concentration, the gas evolution rate calculated by the Experiment Analysis Model (discussed in Section 5), and the calculated aerosol mass source rate. The concentrations and flow rates are given at STP conditions. The melt surface area is taken as 0.1338 m^2. Figure 3.31 is a plot of the aerosol mass source rate as a function of time. Included in this figure are the calculated gas evolution rate and melt temperature. It should be noted that aerosol losses during transport have not been calculated so that the reported source term represents a lower-bound estimate on the aerosol mass source term.

The time axis corresponds to events at the melt surface with zero time indicating portcullis closure. Delay times for gas to travel from the melt surface to the sampling point are calculated to be on the order of 1 second or less and, therefore, introduce no adjustments into the data analysis.

Table 3.2 Aerosol Mass Source Term for TURC1SS

Time After Portcullis Closure (sec)	Measured Aerosol Concentration (g/m^3 @ STP)	Estimated Gas Flow (g-moles/sec)	Estimated Mass Source Rate (g/sec)
0- 15	80	3.2	5.7
15- 30	68	1.4	2.1
30- 60	53	1.1	1.3
60-120	16.4	0.67	0.25
120-180	14.6	0.25	0.08
180-240	1.6		
240-420	2.1		

Cumulative mass generated from 0 to 180 sec ~ 500 g. Gas evolution not calculated beyond 180 sec.

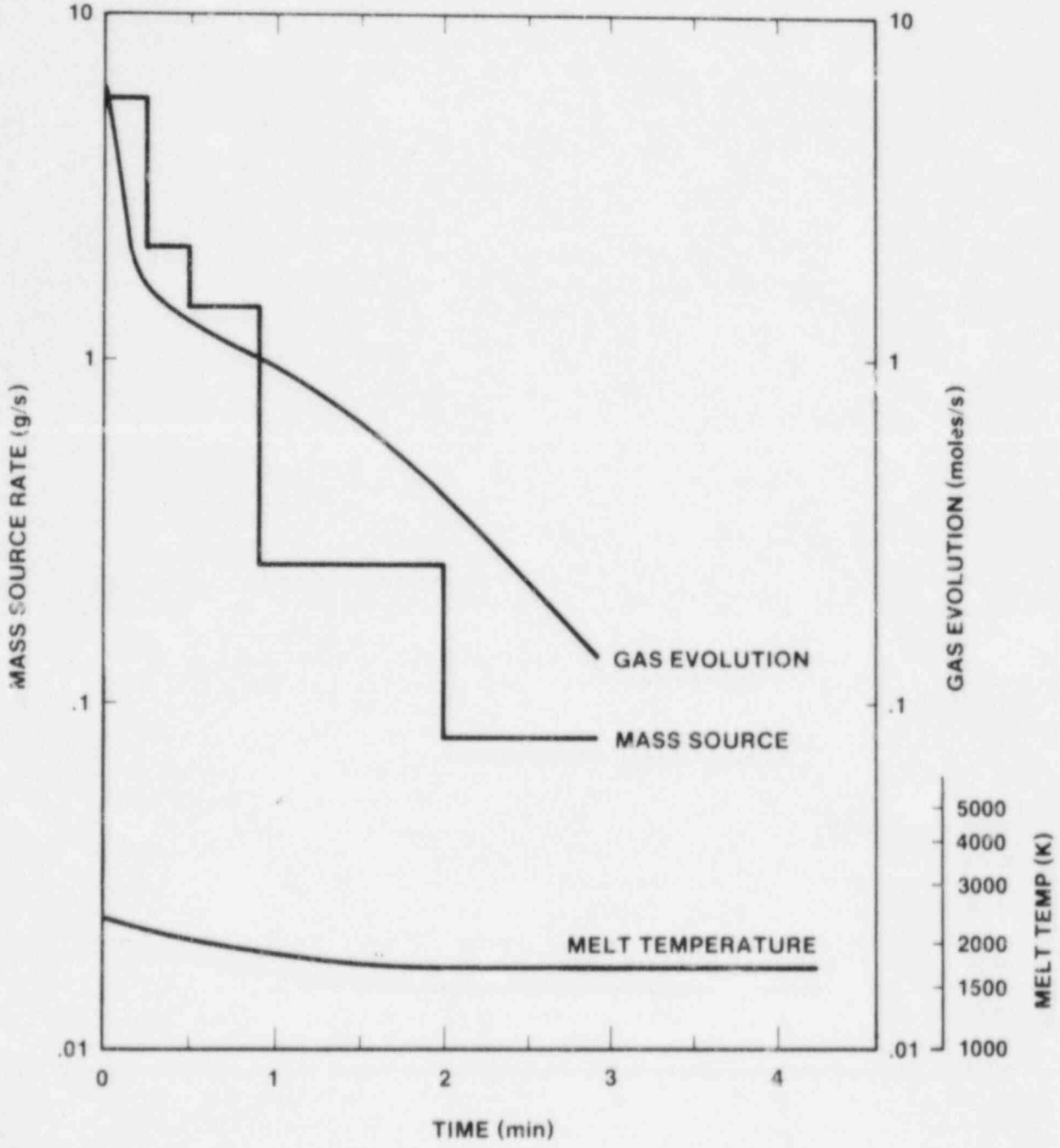

Figure 3.31 TURC1SS Aerosol Mass Source Rate

The samples taken after 3 or 4 min may have been taken from recirculating flow within the interaction crucible and may not accurately reflect the mass source rate at these times. The gas flow rates were taken from the calculated gas flux through the melt surface.

The calculated mass source rates are estimates based on calculated gas flow rates from the melt-concrete interaction. They behave with time as one would expect (they decrease with decreasing melt temperature and gas flux). Their magnitudes are consistent with those values measured in the transient test series.[25]

Impactor Samples: Impactor samples were taken from the top of the gravel bed filter where the exhaust line entered. Although they were all overloaded (i.e., the collected mass exceeds the capacity of an impactor stage) and no distributions can be reported, there is still qualitative information on the aerosol size distribution available. Overloading did not begin to occur until the size of particles being collected dropped below approximately 1 μm in aerodynamic diameter. This indicates that the average mass weighted aerodynamic diameter of the aerosol collected is about 1 μm or less.

Cyclone Samples: No analysis has been performed on these samples. They are not expected to yield detailed aerosol distribution information because they sampled over the duration of the test. This effectively integrates the distribution over time with an unknown weighting function. The purpose of the cyclone sample was to collect bulk aerosol material in a size-segregated fashion for chemical analysis. This analysis has not been performed to date.

Samplers at the Gravel Bed Filter Exhaust: These samplers provide no information on aerosol and fission-product source terms. They were placed on the test to assess the performance of the gravel bed filter. This assessment has not been made and the use of samplers in this location in future tests will be discontinued.

Chemical Analysis: As discussed in Section 2.0 nonradioactive dopants representing fission products were placed in the melt generator and the interaction crucible. Table 2.1 lists the dopants and their location.

X-ray fluorescence (XRF) elemental analysis has been performed for two selected filter samples (sample A; 0 to 15 sec and sample D; 60 to 120 sec). A number of elements have been analyzed qualitatively while, quantitative analysis has been performed for lanthanum and tellurium. The results of the analysis is presented in Table 3.3. Detectability limits influence and

Table 3.3 XRF Analysis of TURC1SS Aerosol Samples

	Qualitative Analysis Sample		Quantitative Analysis Sample	
Element	A (0 to 15 s)	D (60 to 120 s)	A (0 to 15 s)	D (60 to 120 s)
Si	S	T		
Fe	T	T		
Mo	-	-		
Cs	S	S		
Ce	T	T		
Ca	-	-		
Ni	T	T		
Te	M	M	17.7 w/o	29.4 w/o
Ba	-	-		
Mn	S	T		
Zr	-	-		
I	M	M		
La	T	T	0.16 w/o	0.088 w/o

Levels: M = Major Constituent
S = Minor Constituent
T = Trace
- = Uncertain

may hinder detection so that failure to detect a given element does not mean that it is not present.

Of the elements examined, Te, I, and Cs are the principal constituents of the aerosol. This is to be expected when hot molten material is poured onto volatile Te and CsI.

Release rates and release fractions could not be calculated except for the two elements analyzed quantitatively, Te and La. These results are presented in Table 3.4 and calculated from the weight percent of the element in the aerosol (Table 3.3) and the mass source rate of the aerosol (Table 3.2). The weight percentages of Te and La found in the analysis are included in Figure 3.31.

Additional elemental analysis is under way, but results have not yet been obtained. Proton induced x-ray emission (PIXE) analysis is to be performed on filter samples taken in this test. The results will allow a mass source rate for each of the dopants as well as for other concrete and melt constituents to be calculated. These results will be reported as soon as they are available.

Table 3.4 Release Rates for Selected Elements and Filters from TURC1SS

Element	Release Rate (mg/sec)	
	Filter A 0-15 sec	Filter D 60-120 sec
Te	1010.	74.
La	9.1	0.22

4 COMPARISONS OF CORCON CALCULATIONS TO EXPERIMENT RESULTS

CORCON[9,13] is a computational tool for describing core melt-concrete interactions which might occur in a severe reactor accident. The aerosol and fission product source terms resulting from these interactions can be an important contributor to the risk associated with nuclear power plants. It is important to establish confidence in CORCON's ability to calculate the thermal-hydraulic conditions of a melt-concrete interaction, so that the source terms can be properly evaluated. Comparison of code predictions to experiment results is a vital step in this process. These comparisons are also very useful in identifying phenomena that are either poorly modeled by the code or that were omitted.

This section presents a brief description of the three versions of CORCON that were used in this study. Code calculations are then compared to the results of the experiments. Finally, the implications of these comparisons to future CORCON model development are discussed.

4.1 CORCON PHENOMENOLOGY

Although three different versions of the code were used in this study, the primary phenomena described in each version are the same. Also, much of the code structure and many of the phenomenological models used in the codes are the same. In this section, a brief description of the principal interaction phenomena is presented. Note that because CORCON is a reactor accident analysis code, the following discussion refers to phenomena which may not be present in the TURC experiments. Where extrapolation to experiment analysis is not immediately obvious, additional discussion is provided.

When molten core material comes into contact with the concrete basemat below the reactor pressure vessel, a very energetic interaction ensues. Heat transfer from the melt to the concrete causes rapid heating of the concrete surface. Eventually the concrete at the surface begins to melt and subsequently to ablate. Because concrete contains both evaporable and chemically bound water and in many cases, a significant amount of chemically bound carbon dioxide, gas release accompanies the ablation process. For most concretes this gas release is sufficient to vigorously agitate the melt. As a result, melt-concrete heat transfer models are usually based on convective energy exchange

mechanisms which accompany gas bubbling. Because this process is physically similar to boiling on a surface, melt-concrete heat transfer models often closely resemble pool boiling models.

The melt-concrete heat transfer models employed in CORCON are based on an analogy to stable film boiling. Here the assumption is made that gas release from the concrete is sufficient to generate and then maintain a stable film throughout the interaction. Historically, this choice was made based on qualitative observations of earlier experiments.[2,3,4,5,6,7,8]

Heat is transferred across the film by combined radiation and convection as shown in Figure 4.1. The melt radiates from the melt-gas interface temperature, T_{mi}, to the concrete surface which is assumed to be at its ablation temperature, T_a. The code user specifies the emissivity of both melt phases and the concrete as a function of time. Gas flow, either parallel or perpendicular to the concrete surface, induces concurrent convective heat transfer across the film. Depending on the orientation and magnitude of the gas flow, the code chooses among several available heat transfer models. A detailed discussion of these models is provided in Refs. 9 and 13 and will not be repeated here.

Heat transferred across the film causes ablation of the concrete. CORCON uses a quasi-steady ablation model which assumes that energy is deposited at the concrete surface, and transient heat conduction into subsurface concrete is neglected. The simple equation used in CORCON is presented below:

$$\frac{dX_a}{dt} = \frac{q}{\rho_c \Delta H_c} \tag{4.1}$$

Here, q is the incident heat flux, ρ_c and ΔH_c are the density and total enthalpy of ablation for the concrete, and dX_a/dt is the ablation rate. This equation is accurate at high heat fluxes where ablation of the surface occurs before a significant amount of energy has been conducted, and also at a lower but approximately constant heat flux, where a steady-state temperature profile has been attained.

CORCON calculates two-dimensional axisymmetric ablation of the cavity by tracking the recession of a user-specified number of body points. The heat fluxes and resulting ablation rates are calculated at each body point. Recession of the concrete surface is then calculated assuming a constant ablation rate over the time step. By doing this, CORCON takes a snapshot of the cavity geometry at discrete time intervals.

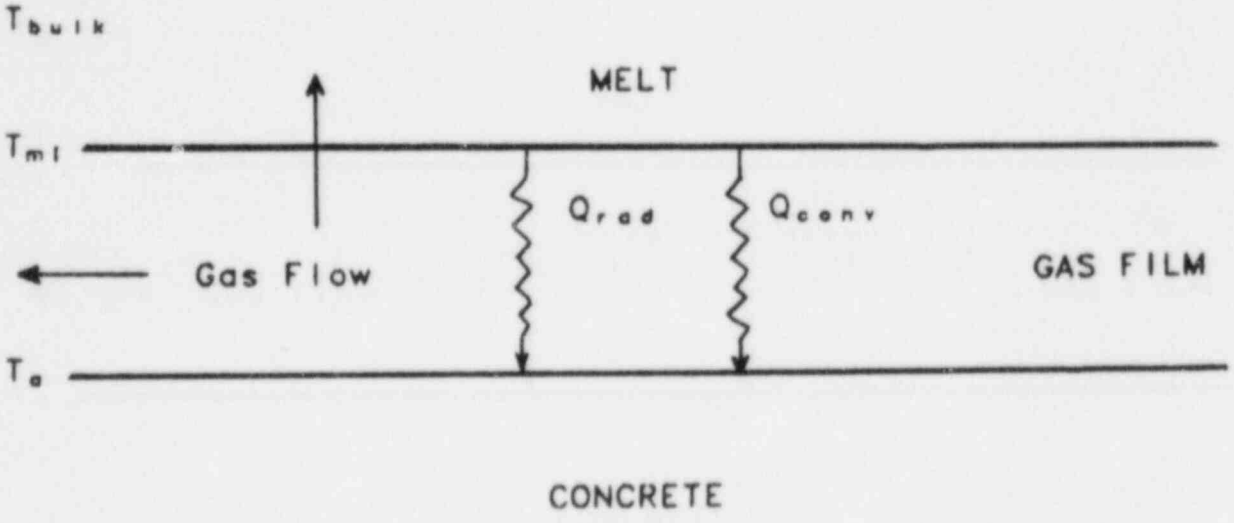

Figure 4.1 Melt Pool-Concrete Interface

As the cavity ablates, it releases water vapor and carbon dioxide. Gases released at the bottom of the melt percolate through the molten debris, while those released from ablating sidewalls enter the gas film and are channeled upward. The released H_2O and CO_2 then react with the metallic constituents of the melt and are reduced to the flammable species, H_2 and CO. In CORCON, all chemical reactions are assumed to go to equilibrium with the composition of the product stream determined by minimizing the Gibbs free energy.

CORCON assumes that the melt pool immediately stratifies into separate metallic and oxidic layers according to relative density. Ablated concrete is composed of low density oxides which either combine with a high-density oxide layer at the bottom of the pool (if one exists) or float to the top of the pool thus forming a separate low density oxide layer. Eventually, the concrete oxides dilute the heavy oxide layer and its density falls below that of the metallic layer. When this occurs, CORCON assumes an instantaneous layer flip takes place, and the metallic layer moves to the bottom of the pool. The code neglects any mixing of metallic and oxidic constituents that might occur at melt layer interfaces, but it does consider energy transfer between melt layers.

In the absence of an overlying coolant, heat transfer from the top of the melt takes place primarily by thermal radiation to surrounding structures. (A natural convection heat transfer coefficient is included for completeness, but this contribution is almost always negligible compared to radiation.) A very simple radiation heat transfer model is currently in CORCON. All surrounding structures are assumed to be characterized by a single effective emissivity and surface temperature which are input as a function of time. An equation for radiation between two infinite parallel plates is then used to calculate the upward heat loss from the melt.

Within molten core-debris, energy is generated by the decay of fission products and by chemical reaction. (The latter can, for some reactions, also be a heat sink.) In most cases, decay heating is much greater than chemical reaction heating, with the exception being a situation with high gas flow and an abundance of metallic zirconium in the melt. The CORCON user also has the option of specifying a time dependent heat source or sink rather than using the default decay heat calculation. Since there is no decay heat generated in the TURC experiments, this option was not exercised in the CORCON comparison calculations.

Because internal heating of the melt decreases as radioactive fission products decay to stable long lived isotopes, the melt temperature decreases and eventually solidification of one or more of the melt layers begins. (Solidification of the melt

is even more significant in the TURC experiments since no internal heat source was provided.) There are two distinct mechanisms for melt solidification: slurry formation and boundary crusting. If a slurry forms, the properties of the melt change dramatically but melt-concrete heat transfer is still convection-dominated. If, on the other hand, a crust forms, melt-concrete heat transfer becomes conduction-limited. The versions of CORCON used in this study consider one or the other solidification mechanisms, but not both.

4.2 VERSIONS OF CORCON USED IN THIS STUDY

Three versions of CORCON were used in this study: MOD1, MOD1v, and MOD2. These three versions were tested because each has been used to some extent in accident analyses. It is therefore important to determine whether one code is significantly better or worse than the others. Only MOD1 and MOD2 have been formally documented (see Refs. 9 and 30). MOD1V represents only a slight modification of MOD1, and thus it has not been reported in a separate document. It was, however, mentioned in the QUEST report,[31] and the reader is referred to that document for further discussion. The following two sections outline the major differences between the three code versions.

4.2.1 Differences Between MOD1 and MOD1v

In some of the accident calculations performed using CORCON-MOD1, the heavy oxide phase of the melt was found to become thermally isolated from the concrete. Heat transfer to the concrete was unrealistically low (i.e., below the pure conduction lower limit) while the oxide phase temperature increased to an unrealistically high value. This artificial behavior was traced to the evaluation of the oxide layer viscosity used in the convective heat transfer calculations.

The code evaluates the layer viscosity at the melt-gas interface temperature rather than at the more commonly used bulk or mean film temperatures. (Mean film temperature is defined here as the average of the bulk and interface temperatures.) Using this temperature causes problems when the interface falls significantly below its liquidus temperature. When this occurs, the code accounts for the effects of slurry formation through the use of a Kunitz Multiplier. Near the solidus temperature, the melt viscosity can be several orders of magnitude greater than for a pure liquid, and as a result, convective heat transfer is dramatically reduced.

While it is reasonable to account for slurry formation in the viscosity and heat transfer calculations, it does not seem reasonable to characterize the entire thermal boundary layer by properties evaluated at the interface temperature, especially

when there is a large temperature drop and/or phase change across the boundary layer. For this reason an intermediate temperature, namely the mean film temperature, was used in the MOD1v version of CORCON.

It should be noted that the convective heat transfer models used in CORCON are empirical correlations based on nonprototypic experiments. In most of these experiments, the temperature drop across the boundary layer was not large, and more importantly, the liquid properties were almost uniform. In the discussion of the experiments and the resulting heat transfer correlations, the authors refer simply to "liquid" properties without specifying a characteristic temperature. While some might argue that the bulk liquid temperature should be used for the viscosity evaluation in CORCON, when there are large temperature and property differences across the boundary layer, using the mean film temperature minimizes the effect of these differences on the heat transfer calculation.

One final comment should be made at this time about the applicability of both the MOD1 and MOD1v versions of CORCON. The heat transfer models in both codes are based on experiments in which the core melt simulant remained liquid. While using the Kunitz Multiplier is a justifiable method for extrapolating these models to a partially solidified melt, its applicability is limited to small solid volume fractions. (Reference 14 gives an upper limit of 50% solids by volume.) In any presentation of CORCON-MOD1 or -MOD1v calculations, this limitation should be noted, and results which are out of the range of applicability should be questioned.

4.2.2 Differences Between MOD1 and MOD2

As more prototypic experiments were performed and melt-concrete interactions were better understood, it became obvious that a new calculational tool was needed to replace CORCON-MOD1. The resulting substantial modeling effort culminated in the public release of the MOD2 version of CORCON. Although the basic phenomenology and code structure are essentially the same, there are numerous differences between MOD2 and its predecessor.

First and foremost, CORCON-MOD2 contains a model for crust formation at melt boundaries. The addition of a crust formation model extends the applicability of the code by allowing it to calculate both the heatup and remelting of initially quenched core debris and the long-term interaction of concrete with a partially or totally solidified melt.

Once a crust is formed, melt-concrete heat transfer becomes limited by the rate of heat conduction through the crust. This change is usually accompanied by a significant reduction in the

concrete ablation rate since conduction is a much less effective heat transfer mechanism than convection.

A model for heat transfer between the core melt and an overlying coolant is also included in MOD2, where none was available in MOD1. The melt-coolant interaction is limited to pool boiling, i.e., vigorous interactions such as steam explosions are not modeled. This change allows a more accurate representation of the ex-vessel phase of an accident, since in many scenarios coolant is present in the cavity at the time of vessel failure.

CORCON-MOD2 also includes an approximate treatment for the effect of suspended aerosols on radiative heat transfer from the top surface of the melt. The net effect of the aerosols is a reduction in upward heat loss due to reradiation of energy from the hot aerosols to the melt surface.

Since the release of CORCON-MOD1, simulant experiments performed by Ginsberg and Green[32] have shown that heat transfer between liquid layers is greatly enhanced by gas bubbling. They also demonstrated that the interlayer heat transfer model used in MOD1 significantly underpredicts this energy exchange. For this reason, Greene's model[33] for heat transfer between liquid layers has been incorporated into MOD2. As a result, energy is transferred more readily between the metallic and oxidic layers and their temperatures are nearly equal. (In MOD2 calculations the two layer temperatures usually differ by less than 20 K, while in MOD1 and MOD1v calculational differences as large as 200 K were sometimes seen.)

There are several other differences between MOD1 and MOD2 that are of lesser importance to accident calculations and will not be discussed here. Instead, the reader is referred to the MOD1 and MOD2 user's manuals (References 9 and 30) for additional discussion.

4.3 CORCON COMPARISON

4.3.1 Code Preparation

Because the CORCON code was designed to calculate two-dimensional, axisymmetric melt-concrete interactions rather than the one-dimensional melt-concrete interactions of the TURC experiments, it was necessary to either modify the code or the code input in order to simulate the experiments. In the current study, the latter approach was taken.

In order to make sidewall heat transfer and ablation a negligible contributor to the overall energy and mass balance, the sidewall surface area for melt-concrete contact was made small relative to the surface of the cavity bottom. This was

accomplished by artificially setting the cavity radius equal to 10 m rather than the actual TURC crucible radius of 0.21 m. For a melt pool that is 15-cm deep (typical of the experiments), the ratio of sidewall surface area to bottom surface area (2 H/R) is 0.03. Sidewall heat transfer and ablation is therefore negligible, and the CORCON calculation will be essentially one-dimensional.

As shown in Section 3.2, while melt-concrete heat transfer is restricted to one dimension in the experiments, there is a significant heat loss through the MgO sidewalls. In CORCON, sidewall heat loss can be included in a global sense by inputting a temporal heat sink. This is done by scaling the experiment heat loss (see Section 5.3) to the size of the CORCON cavity. Since the resulting heat sink is uniformly distributed throughout the melt, the appropriate scaling factor is the ratio of the melt volumes in the calculation and the experiment. For the TURC tests the scale factor is $(10^2/0.21^2)$ or 2268. This factor is also used to scale the experiment melt mass to the melt mass used in the CORCON calculations.

4.3.2 Comparison of Experiment Results with CORCON Calculations

Of the experimental data obtained during the TURC experiments, the most valuable with respect to CORCON validation is the concrete ablation distance as a function of time. Not only is this information easily obtained from the experiments, but it also provides an excellent indication of the melt-concrete heat flux. Other useful data are gas composition results (available for TURC1SS only) which can be used to assess the chemical equilibrium model in CORCON.

TURC1T vs. CORCON

Figure 4.2 presents a comparison between TURC1T and CORCON ablation distances. Two things are immediately obvious from this plot. First, all three versions of CORCON do a reasonable job of matching the experiment, and second, there is very little variation between the three calculations.

It should be noted that the CORCON results presented in Figure 4.2 represent a "blind" calculation of the experiment. Even though there is considerable uncertainty in many of the CORCON input variables, no attempt was made to modify the input to obtain a better match of the experiment. The parameter values used in the input were chosen because they either (a) are consistent with the values used in the Section 5.2 analysis, or (b) represent a best guess. Because the calculated results are uniformly low, it would be a simple matter to change the input to effect a better comparison.

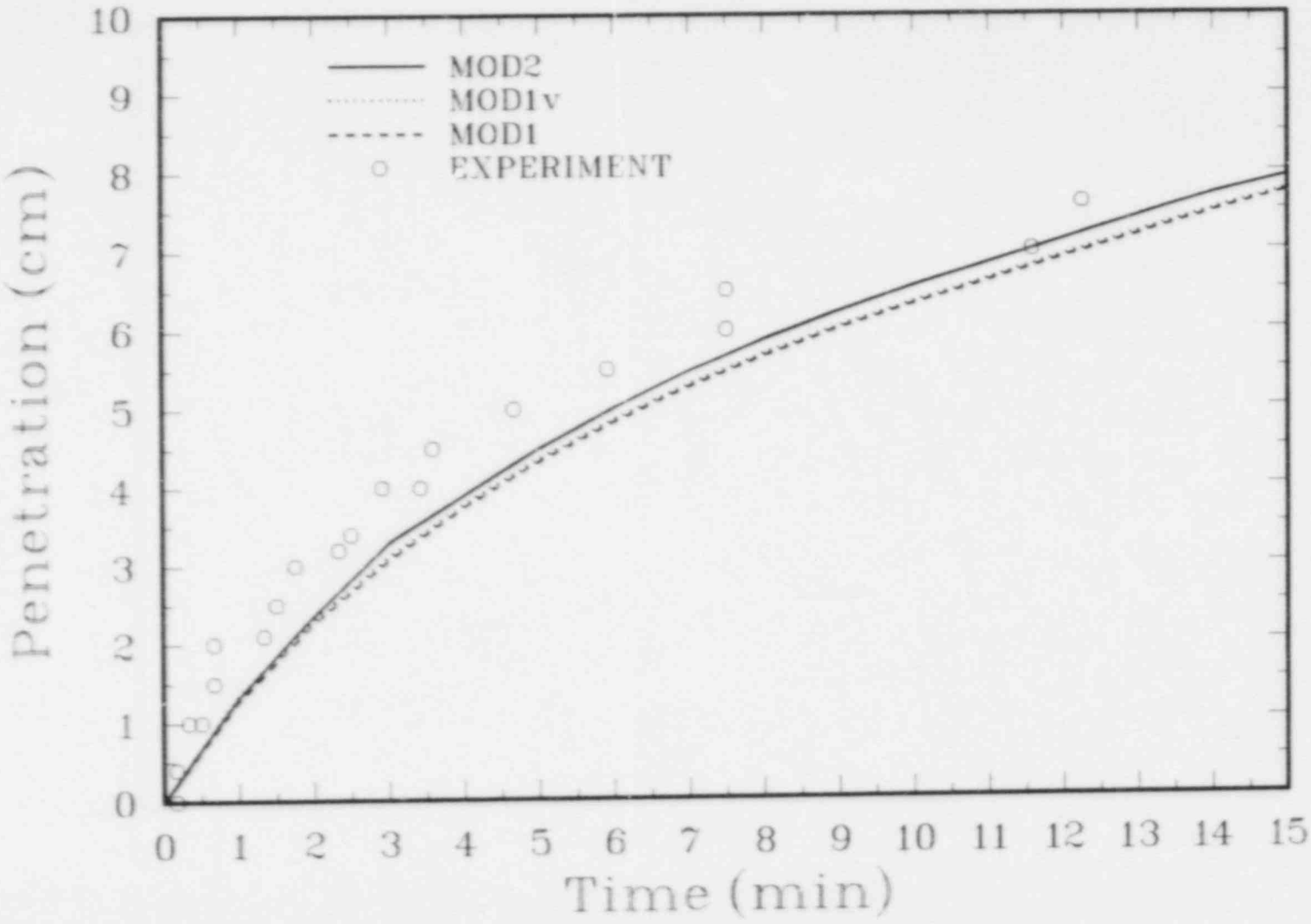

Figure 4.2 Comparison Between TURC1T and CORCON Ablation Distance

Figure 4.3 presents an example of a CORCON-MOD2 result with revised input. In this calculation the concrete ablation temperature was reduced to 1550 K from a previously used value of 1600 K. (The melting range for the limestone-common sand concrete used in the TURC experiments was 1420 K to 1670 K, so that 1550 K is also a reasonable ablation temperature.) This change has the effect of reducing the energy required to ablate the concrete and therefore produces an increase in the calculated ablation rate. Although the code still slightly underpredicts ablation at early times, the overall comparison is better.

One phenomenon not considered by CORCON but that has been observed in experiments is spallation of the concrete surface. In experiments[2] at Sandia in which 200-kg steel melts were teemed into concrete crucibles, spallation fragments with a mean thickness of 0.41 cm were ejected from the crucible immediately after initial contact with the melt. If the original CORCON ablation curves are shifted upward by this amount, they pass almost directly through the experimental points. In light of both the uncertainty in code input and in the effects of spallation, it appears that all three versions of CORCON do an acceptable job of predicting concrete ablation by thermitic melts.

That the three versions of the code give almost identical results is not too surprising since few of the code differences are exercised in these calculations. For example, both the oxidic and metallic phases (top and bottom layers) of the melt remain molten throughout the calculation so that the different solidification models in MOD1 (slurry) and MOD2 (crust) are never employed. Also, since the melt phases are entirely molten, there is little change in viscosity through the thermal boundary layer and thus the MOD1 and MOD1v results are virtually identical.

TURC1SS vs. CORCON

Figure 4.4 presents a comparison between measured and calculated ablation distance for the TURC1SS experiment. As in the TURC1T experiment, two things are immediately obvious from this plot. First, the three versions of CORCON produce virtually identical results; and second the codes significantly underpredict the concrete ablation rate.

As in the TURC1T experiment, the three CORCON results are similar because few of the differences between the codes are exercised in the calculations. Once again, solidification of the melt does not occur either internally or at the melt-concrete interface, and therefore the modifications affecting melt-concrete heat transfer only minimally affect the calculated results.

The second observation noted above is very troublesome in light of the close agreement obtained for the TURC1T experiment.

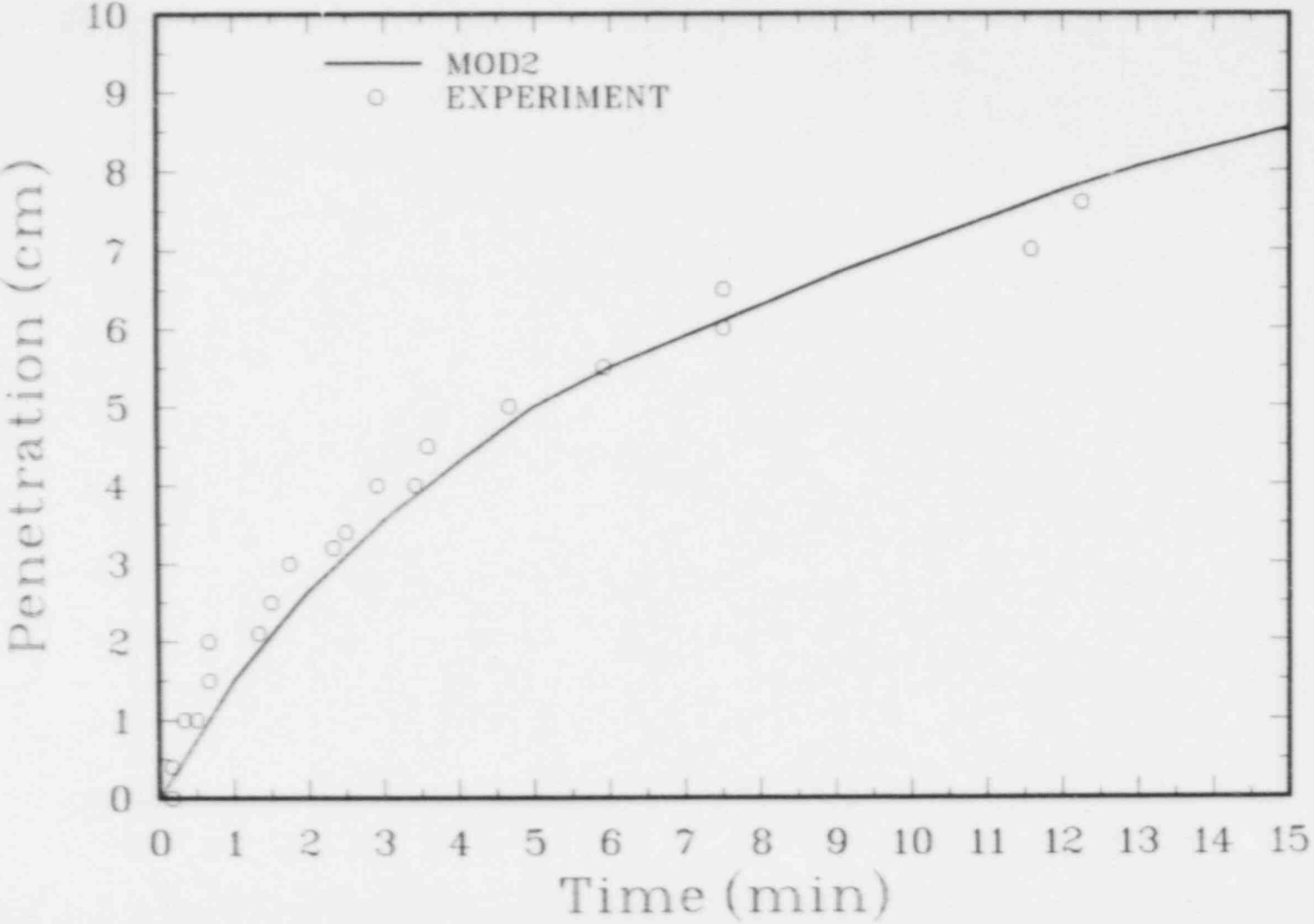

Figure 4.3 CORCON-MOD2, Revised Input - TURC1T Comparison

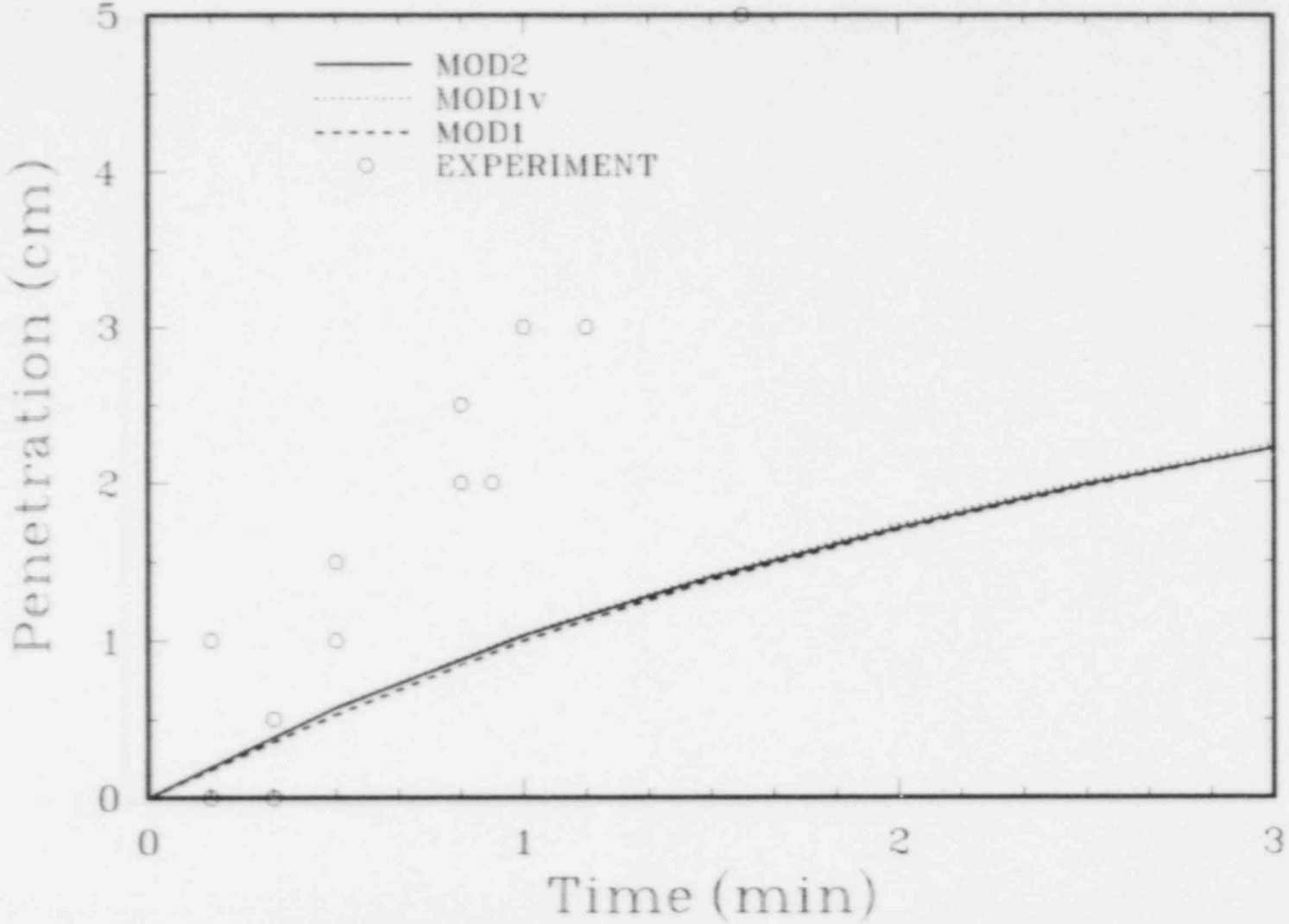

Figure 4.4 Comparison Between TURC1SS and CORCON Ablation Distances

It indicates that the melt-concrete heat transfer models employed by the three CORCON versions are sometimes inaccurate and that these inaccuracies may be nonconservative (i.e., they underpredict basemat penetration and containment loading).

Alternate melt-concrete heat transfer models are currently being assessed at Sandia. The turbulent diffusion model discussed in Section 5.2 is one candidate. Another is the intermittent contact model proposed by Lee, et al.,[34] which assumes that the gas film is unstable and there is periodic contact between the melt and the concrete. Whatever model is chosen, it is doubtful that it will suffice under all conditions. Instead, it is more likely that there are transitions in behavior as the interaction conditions change, and two or more melt-concrete heat transfer models are therefore needed.

In addition to concrete ablation data, experimental gas composition results are also available for the TURC1SS experiment (see Figures 3.28 and 3.29). This information can be compared to CORCON calculations to evaluate (a) the chemical equilibrium model in the code, and (b) the significance of subsurface gas release which is neglected by CORCON.

Because the gas stream concentration of H_2O was not measured in the experiment, only the CO/CO_2 ratio can be used to validate the CORCON chemical equilibrium model. During the calculation, the CO/CO_2 ratio (i.e., mole fraction CO divided by mole fraction CO_2) varies from an initial value of 119 to a value at three minutes of 143. During the ablation period of the experiment, this ratio was approximately constant with a value of 25. While this difference appears to be significant, it is important to assess it in the context of the overall problem. For example, the CORCON calculation yields a 99+% reduction of CO_2 to CO while the experiment showed a 96% reduction. It is unlikely that this slight difference in gas composition would have a significant effect on an accident calculation. Furthermore, there may have been some change in gas composition between the pool exit and the sampling device. For example, it is likely that the sampling temperature was somewhat below the pool temperature, and a reduction in temperature favors the $CO_2 + H_2$ gas combination relative to the $CO + H_2O$ combination. The slight difference between the calculated and measured gas composition is therefore not unexpected.

The high degree of reduction of both H_2O and CO_2 allows the molar ratio, H_2/CO, to be used to characterize the gas released from the concrete (see Section 3.1). Because CORCON assumes that all energy transferred to the concrete produces ablation and only gas in the ablated concrete is released, the H_2O and CO_2 are released in stoichiometric proportions. For this reason the H_2/CO ratio remains approximately constant at 0.53. However, in

the TURC1SS experiment this ratio varies over a wide range from 0.6 to 1.9. This difference can be only partially explained by a reduction in temperature between the pool and the gas sampler (shifting the gas composition to the CO_2 + H_2 combination). The major contributor to this shift in composition is most probably the release of subsurface gas, predominantly H_2O. (Note that the water vapor content within the gas samples was not measured.)

Water vapor is released from concrete at lower temperatures, and it is therefore released earlier and continues to be released over a longer time once the melt solidifies and cools. This is clearly demonstrated by Figure 3.29 where after 2.5 minutes the gas composition in the experiment shifts strongly in favor of H_2 (and by implication, H_2O).

4.4 SUMMARY

This comparison of CORCON calculations to experiments results demonstrates that while some parts of the code perform well, other parts require further model development. Specifically, CORCON's chemical equilibrium model adequately calculates reduction of CO_2 and H_2O to CO and H_2 as the gas stream percolates through the melt. Also, the melt-concrete heat transfer models in the code predict experiment ablation rates under some conditions (TURC1T). However, under different conditions (TURC1SS), CORCON significantly underpredicts ablation. It was also demonstrated in the experiments that conduction into subsurface concrete can be significant when the melt cools; and as a result, gases are released from the concrete in nonstoichiometric proportions. Since H_2O is released at lower temperatures, conduction favors H_2O release over CO_2 release.

Alternate melt-concrete heat transfer models are currently being investigated. Special emphasis is being placed on models analogous to nucleate boiling. Numerous methods for including conduction into the concrete are also being considered. Here calculational accuracy will be weighed against computational efficiency and expense.

5 EXPERIMENT ANALYSIS

5.1 INTRODUCTION

5.1.1 Purpose and Background

This section presents the analysis of the TURC1 series experiments. An analysis of the results is performed using two different codes. The first code is a heat balance model that has been written primarily for analysis of these and other similar experiments of 1-D concrete ablation with refractory sidewalls. The second code is the CORCON code, which has been written for reactor safety analysis. Discussion of the CORCON code is in Section 4 of this report.

There are two purposes in performing an experiment analysis. One is to understand what happened during the experiment and the other is to provide data for CORCON validation. Ideally, CORCON should be used for the experiment analysis. However, CORCON was written for reactor safety analysis; and, as a result, it is not flexible enough for direct experiment analysis. This inflexibility arises from several areas: the penetration rate, wall heat losses, transient conduction into the concrete, and possibly neglecting pool mixing effects. The penetration rate in CORCON is calculated from a set of models based upon assumed physical phenomena. The user has no ability to modify the rate without rewriting sections of the code. It is the penetration rate that determines not only pool temperature history, but also, albeit indirectly, heat loss by other mechanisms such as conduction into the wall. Wall heat loss, that occurs in the experiments, is not calculated at all by the CORCON code. Instead, the CORCON code assumes the wall is made of concrete and hence ablates in a manner similar to the floor. Neglecting wall heat loss, or allowing it to ablate, leads to very large errors in a heat balance calculation, because in many experiments, including the ones reported here, the wall heat loss can be quite significant when compared to the other heat loss mechanisms. Transient conduction into concrete is important when the ablation rate changes with time or has ceased altogether. Transient conduction models allow gas release from the concrete to be calculated at all times. Pool mixing is ignored in CORCON which assumes a completely layered structure. A mechanistic approach to pool mixing would include agitation of the pool by the escaping gases being counteracted by the buoyant separation effect of immiscible oxides and metals. Pool mixing could be an important effect because it will affect the thermophysical properties of the melt pool, which in turn may have a strong effect upon the heat transfer rates.

Thus, in order to make a reasonably accurate heat balance calculation, a code which is expressly designed for these experiments should be used. Of the various codes that are available, the SLAM[26] code was chosen because it required a minimum of modifications and time in order for it to be converted into a heat balance model with all the features mentioned above. A description of the modified version of SLAM, hereafter referred to as the model, will be presented.

5.1.2 Method of Analysis

The model consists of a collection of modules that predict the various heat losses. The major heat loss mechanisms are: losses to the ablating concrete, wall losses, radiative losses from the top of the pool, and losses to the gases escaping from the concrete. All of the heat losses and the gas and aerosol evolution depend either directly or indirectly upon the ablation rate. Thus, the ablation rate (plus pool temperature for fission-product release) is the single most important phenomena in these experiments. In the heat balance code, there are two options concerning the ablation rate: input the ablation rate from the experimental data, or calculate the ablation rate from the temperature and composition distributions in the systems. Only the latter option was used because the comparison between experiment and the model was not improved by inputting the measured ablation rate.

When a heat balance calculation is made and the results yield thermocouple predictions that are consistent with experimentally measured responses, then one has some confidence that the predicted state of the pool is near the true state in the experiment. This is especially true when the model predicts correct thermocouple responses for a number of experiments without varying any of the parameters in the model.

5.2 DESCRIPTION OF HEAT BALANCE MODEL

The model that is used in making the heat balance calculations for the TURC1 experiments is a three region model. The three different regions are: the pool/melt region, a wall region, and a concrete region.

The pool region includes conservation equations that solve for both chemical species distributions and the temperature distribution. The equations are one-dimensional, yielding vertical distributions as a function of time and boundary conditions.

The wall region represents the refractory MgO wall that surrounds the pool melt. A two-dimensional (r/z) conservation equation for the temperature distribution is solved in this region.

The concrete region includes both a wet and dry zone. The wet zone is that area where liquid water exists, and the dry zone is that region where no liquid water exists. Both zones include conservation equations for temperature and mass distributions. All of the equations in this region are one-dimensional.

The melt/concrete interactions typically involve ablation of the concrete. Thus the boundaries of the various regions move with time. There are two approaches to analyzing moving boundary problems. The first approach is with a fixed coordinate system that has moving boundaries. The second approach is to have a coordinate system that is attached to the boundaries of the region and the motion is accounted for by advection of material and/or energy through the region. The second approach has been selected for the model reported here because it is a proven technique (the SLAM[26] code) that can accommodate other variables such as swelling and shrinking of the region without additional complexity.

A schematic diagram of the different regions and their respective coordinate systems is shown in Figures 5.1 through 5.3.

5.2.1 Pool Region

Continuity Equation:

The continuity equations in the pool region provide concentation distributions of the various chemical species in the system. The concentration distributions are important in determining the thermophysical properties of the materials in the pool, and in keeping track of the ablated material. Both the thermophysical properties and the ablated material will affect the energy balance by determining the transfer rates and the thermal inertia of the pool region.

There are 19 chemical species that are kept track of by the model, although in the TURC1 experiments not all of the chemicals were present. Nevertheless, in later experiments the chemicals may be present. The 19 chemical species are: CO_2, H_2O, CO, H_2, $Al_2O_{3(s)}$, $Al_2O_{3(\ )}$, $Fe_{(s)}$, $Fe_{(\ )}$, $UO_{2(s)}$, $UO_{2(\ )}$, $CaO_{(s)}$, $CaCO_{3(s)}$, $SiO_{2(\ )}$, C, $MgCO_{3(s)}$, $MgO_{(s)}$, $Zr_{(\ )}$, $ZrO_{2(\ )}$ and inert. Note that either the solid (s) or liquid ( ) form of some chemicals are treated as separate species. The reason for this is that during freezing or melting, the phase change process can provide a significant source/sink of energy.

The continuity equation for each chemical species is[26]

$$\frac{\partial \rho_i}{\partial t} + V_i \frac{\partial \rho_i}{\partial Z} = \frac{\partial}{\partial Z} \Gamma \frac{\partial \rho_i}{\partial Z} + S_i \qquad (5.1)$$

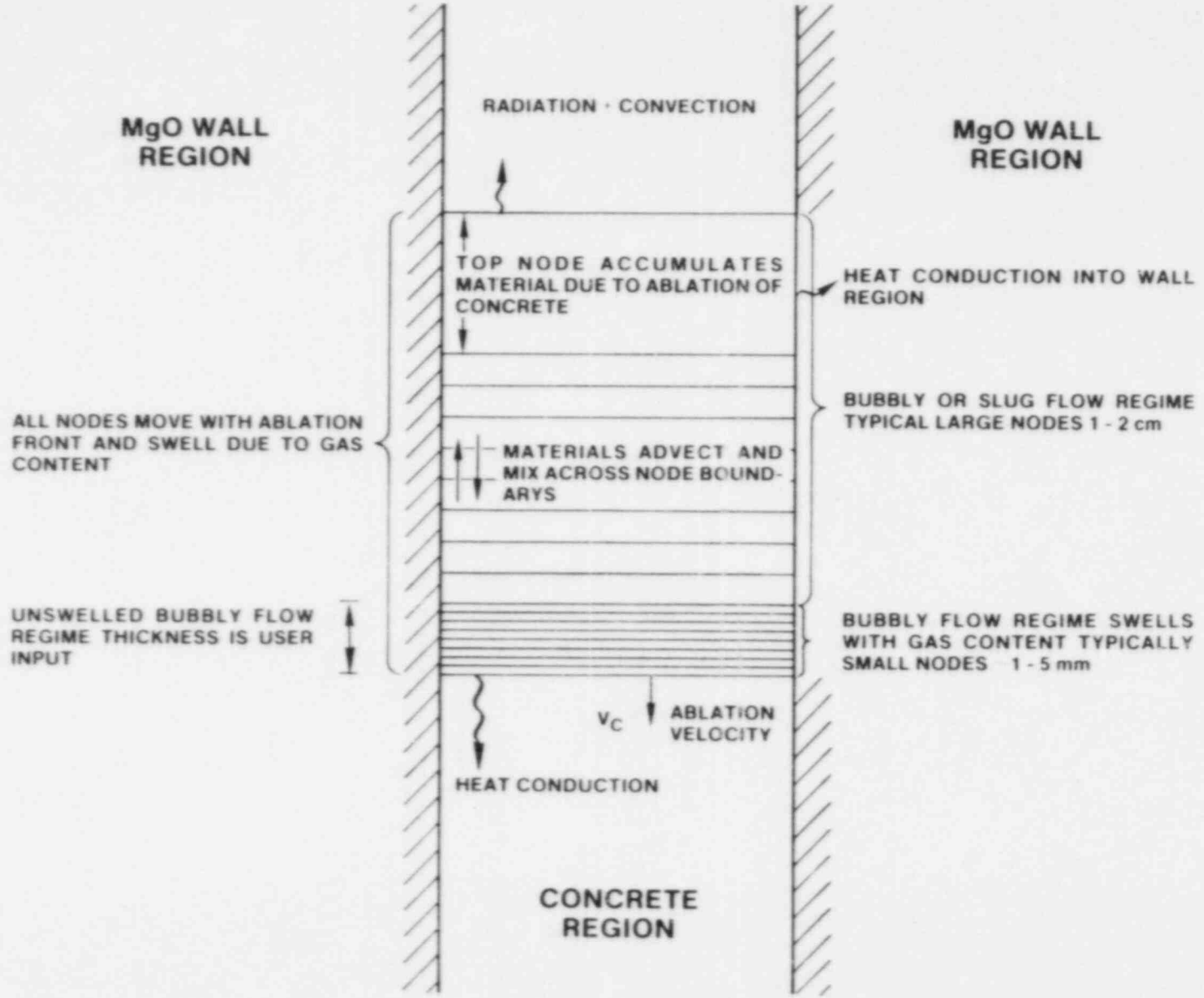

Figure 5.1 Melt Pool Region Coordinate System

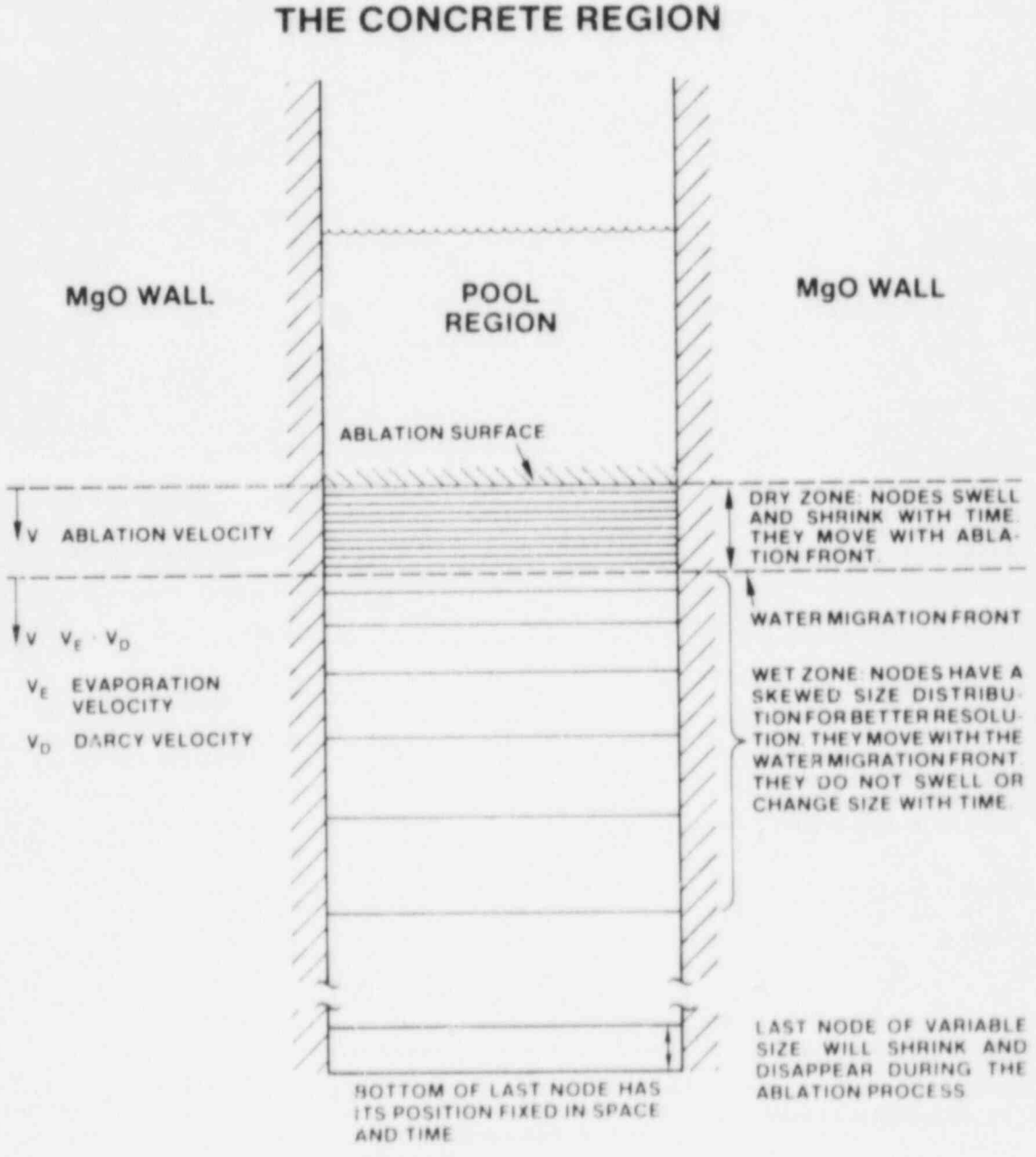

Figure 5.2 Concrete Region Coordinate System

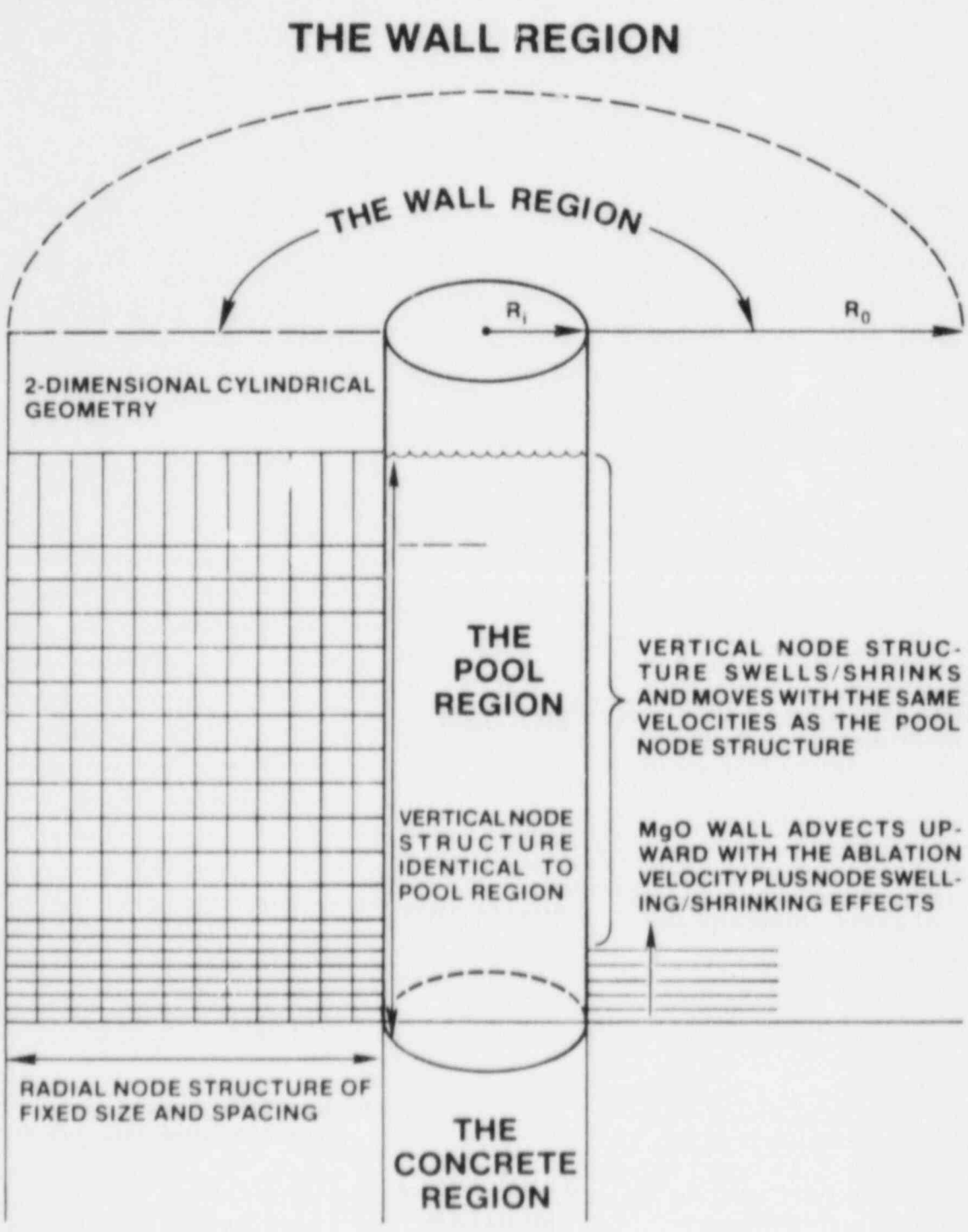

Figure 5.3 MgO Sidewall Region, Coordinate System

where ρ_i = the macroscopic density of material i (where macroscopic density refers to the mass per unit volume of a material in a multicomponent system)

V_i = the advective velocity associated with material i

S_i = the source of material i due to phase change or chemical reaction

Γ = a position dependent turbulent mass exchange coefficient

t = time

Z = vertical position

The boundary conditions for these equations are

$$\text{upper boundary } \frac{\partial \rho_i}{\partial Z} = 0 \ , \ V_i = \frac{\partial Z}{\partial t} \tag{5.2}$$

$$\text{lower boundary } \frac{\partial \rho_i}{\partial Z} = 0 \ , \ V_i = 0 \tag{5.3}$$

The zero slope on density boundary condition prevents mass diffusion into or out of the pool region. Zero velocity at the lower boundary prevents material from leaving or entering due to relative advection. The upper boundary condition for velocity is set equal to the rate of change of the region size. This boundary condition allows the pool region to grow in size due to the accumulation of ablated material from the concrete region. Ablated material enters the pool region through the source term S_i at the lower boundary, rather than an advective term.

The advective velocity V_i depends upon the material i. The material dependence allows slip to occur between the different materials. Slip allows bouyant motion of light materials and settling of heavy materials, thus separation of phases is allowed to occur during the calculation. Separation of phases often occurs in systems that contain both oxides and metals due to their immiscibility and differing densities. The velocity, V_i, is unknown a priori because conservation of mass must be insured. Whenever there is relative motion of one material upward, some other material must move downward to occupy the void created by the upward moving material. Thus, the absolute velocity of all the materials is unknown and must be found by a numerical technique to be described later.

The turbulent mass exchange coefficient Γ simulates the mixing of materials due to the agitation and swirling of the pool materials by the evolving gases from the concrete.

Method of Solution:

The continuity equations are solved by a finite difference multistep technique. The equations cannot be solved by simple matrix inversion because they are coupled to one another non-linearly through the advective velocity V_i. The velocity V_i depends not only upon ρ_i but upon all of the other material densities as well.

The solution technique for this set of equations is to separate the solution into three steps. The end of time step density (ρ^{n+k} where k is the step) appears as the beginning of time step density in the next step. By summing the steps, the intermediate densities (ρ^{n+k}) cancel out and the original equation is obtained. The error introduced by this technique is due to the use of intermediate densities in calculating the rates of change of the various processes. The error can be kept small if small time steps are used.

The three steps that are used are:

STEP 1 - calculate the rate of change due to sources and sinks from chemical reaction or phase change.

$$\frac{\partial \rho_i}{\partial t} = \frac{\rho_i^{n+1} - \rho_i^{n}}{\Delta t} = S_i \qquad (5.4)$$

STEP 2 - calculate the rate of change due to turbulent diffusion

$$\frac{\partial \rho_i}{\partial t} = \frac{\rho_i^{n+2} - \rho_i^{n+1}}{\Delta t} = \frac{\partial}{\partial Z} \Gamma \frac{\partial \rho_i^{n+2}}{\partial Z} \qquad (5.5)$$

STEP 3 - has two parts: the firt part is to calculate the rate of change due to advection, and the second part is to calculate the material velocity that conserves total mass.

STEP 3a. Advect material i

$$\frac{\partial \rho_i}{\partial t} + V_i \frac{\partial \rho_i}{\partial Z} = 0 \tag{5.6}$$

which in finite difference form becomes

$$\rho_i^{n+3} = \frac{\frac{\rho_i^{n+2}}{\Delta t} + \frac{\rho_{j-1}^{n+3} V_{i,j}^{+} - \rho_{j+1}^{n+3} V_{i,j+1}^{-}}{\Delta x}}{\frac{1}{\Delta t} + \frac{V_{i,j+1}^{+} - V_{i,j}^{-}}{\Delta x}} \tag{5.7}$$

Note that the implicit form for the adjacent node density, $\rho_{j\pm1}^{n+3}$, is used. The subscripts i and j refer to material i and node j. The implicit density is found by iteration rather than tri-diagonal inversion because the velocities $V_{i,j}$ are non-linear functions of the densities. They are found stepwise from one node to the next as follows:

STEP 3b. find the advective velocity that conserves total mass.

The advective velocity $V_{i,j}$ is composed of two parts, a mass average velocity $\bar{V}_j$ and a material-dependent relative velocity $V'_{i,j}$ such that:

$$V_{i,j} = \bar{V}_j + V'_{i,j} \tag{5.8}$$

The material dependent relative velocity $V'_{i,j}$ is the buoyant (or slip) velocity associated with material i, relative to the local conditions. The mass average velocity $\bar{V}_j$ is the unknown velocity that allows conservation of mass.

The mass average velocity is found by starting at some location where the velocity is known, i.e., at the bottom where $\bar{V}_{j+1} = V'_{i,j+1} = 0$.

At the j^{th} interface, a velocity is calculated by using a Newton-Raphson technique. Within each node, mass is conserved if

the sum of the volume fractions of all the materials within the node is equal to one. The gases are treated separately so that

$$\Sigma \frac{\rho_{i,j}^{n+3}}{D_i} = 1 - \alpha_g \tag{5.9}$$

where α_g is the gas volume fraction and D_i is the density of material i. Numerically, a function is defined

$$F = 1 - \alpha_g - \Sigma \frac{\rho_{i,j}^{n+3}}{D_i} \tag{5.10}$$

which is reduced to zero by a Newton-Raphson method

$$\bar{V}_j^{k+1} = \bar{V}_j^k - F/\frac{dF}{d\bar{V}_j} \tag{5.11}$$

where k is iteration, and the derivative $\frac{dF}{d\bar{V}_j}$

is found by differentiating and summing the advection equations (eqn's 5.6).

This method has been found to converge with sufficient accuracy with 3 to 5 overall iterations in steps 3a and b.

Constitutive Relationships:

The constitutive relationships are those formulas that provide closure for the system of continuity equations.

The relative velocities V_i' are the buoyant or slip velocities of the different materials relative to the local conditions. These velocities could be calculated based upon the density difference between the material i, the local mean density and the effective droplet size. However, in this current version the bouyant oxidic materials are all assigned a slip velocity of 0.5 cm/sec, relative to the mass average velocity.

The turbulent mass exchange coefficient, Γ, is used in the continuity equations to model the mixing of materials due to the

escaping gases from the heated concrete. The form that has been chosen for the mass exchange coefficient is[26]

$$\Gamma\ (z) = \gamma_o\ V_g\ (1 + \gamma_1\ \gamma_2\ Z^{1.15}\ (1 - e^{-\gamma_2\ Z^{1.15}}))\eta \qquad (5.12)$$

where γ_o, γ_1, and γ_2 are user-selected parameters, and η is a viscosity correction factor. The parameters γ_o, γ_1, and γ_2 are to be set from an array of experimental data. The data would include both the TURC experiments as well as other simulant experiments where a liquid is agitated from gases from below. Once selected, the parameters γ_o, γ_1, and γ_2 will remain fixed for the calculation of all future experiments. It is expected that the best set of values and possibly even the functional form of the Γ equation could change as more experimental data becomes available. The current set of values is tabulated in the sensitivity analysis section of this report. The viscosity correction factor, η, reduces the magnitude of the mass exchange coefficient when an increase in viscosity due to solidification of the melt occurs.

The void fraction α_g in the pool region is the volume fraction that is occupied by the gases. Currently a quasi-steady approach is used. By quasi-steady, it is assumed that the mass flux of gases into and out of the pool region is equal. Thus transient storage of gas is ignored. The volume fraction then is simply

$$\alpha_g = \frac{V_g}{V_g + V_B} \qquad (5.13)$$

where V_g is the local superficial gas velocity and V_B is the absolute bubble velocity. The absolute bubble velocity is a function of the materials present and fluid circulations.

Phase change and chemical reaction are accounted for in a similar manner. Chemical reaction is described in detail in the SLAM[26] document and will not be discussed here. Phase change (freezing/melting) is calculated by a technique that utilizes the solution from the energy equation. The energy equation predicts a local temperature which, if different from the melting temperature, will cause a phase change provided the appropriate materials are present. The amount of phase change that occurs is found by equating the sensible heat to the latent heat

$$\Delta\rho_i = \frac{\Sigma\rho\ C_p\ (T - T_{m,i})}{h_{sf,i}} \qquad (5.14)$$

where $\Sigma\rho\ C_p$ = the sum over all species,

T = the temperature from the energy equation,

$T_{m,i}$ = the melt temperature of material i,

$h_{sf,i}$ = the latent heat of fusion of species i, and

$\Delta\rho_i$ = the amount of material melted or frozen.

Note that in this version $T_{m,i}$ and $h_{sf,i}$ are fixed for the duration of the calculation. This ignores the effect of eutectic formation and other material interaction that may change the melt temperature.

The viscosity of the mixture of materials is dependent upon both the type and phase of the materials that are present. For the liquid materials, volume fraction weighting is used. The viscosity of a mixture of solid and liquid materials is calculated from the formula[30]

$$\mu_{mix} = \mu_{liq}\ \left(1 - \frac{\alpha_s/\alpha_L}{\alpha_{sm}}\right)^{-2.5} . \qquad (5.15)$$

where α_s = the solid volume fraction,

α_L = the liquid volume fraction, and

α_{sm} = the maximum volume fraction of solids beyond which fluidization cannot occur. Typically $\alpha_{sm} = 0.6$[31].

The viscosity correction factor η is simply set to

$$\eta = \frac{\mu_{liq}}{\mu_{mix}} = \left(1 - \frac{\alpha_s/\alpha_L}{\alpha_{sm}}\right)^{2.5} \qquad (5.16)$$

The Energy Equation:

The energy equation provides the temporal temperature distribution of the pool region. The energy equation is

$$\Sigma\rho C \frac{\partial T}{\partial t} + \Sigma(\dot{m}C)_c \frac{\partial T}{\partial Z} = \frac{\partial}{\partial Z} K \frac{\partial T}{\partial Z} + Q_v - Q_s \qquad (5.17)$$

where $\Sigma\rho C$ = the sum over the macroscopic density of all the materials times their specific heats,

$\Sigma(\dot{m}C)_c$ = the mass flux of the materials emerging from the concrete times their specific heat,

K = the local mixture thermal conductivity,

Q_v = a heat source/sink due to phase change and chemical reaction, and

Q_s = the local volumetric heat loss due to the side walls.

The boundary conditions on the energy equation are:

At the upper surface:

$$H_\infty (T_s - T_\infty) = -K \frac{\partial T}{\partial Z} \qquad (5.18)$$

where H_∞ is the convective and radiative heat transfer coefficient from the top surface,

T_s is the surface temperature, and

T_∞ is the ambient temperature above the upper surface.

At the lower surface:

$$-K \frac{\partial T}{\partial Z} = q_{c,o} \quad \text{if } T_R < T_m \qquad (5.19)$$

or

$$T_R = T_m \quad \text{if ablation occurs}$$

where T_R = the lower surface temperature,

$q_{c,o}$ = the heat flux into the concrete region, and

T_m = the melting temperature of the concrete.

The method of solution of the energy equation is implicit finite difference with tridiagonal matrix inversion.

The constitutive relationships that provide closure for the solution of the energy equation consist of those that define the turbulent mixture thermal conductivity, heat sources due to phase change and chemical reaction, and lastly the ablation rate.

The turbulent mixture thermal conductivity is calculated from the following formula

$$K = \Sigma \ (\alpha_i \ K_i + \Gamma \ \rho_i C_i) \tag{5.20}$$

where α_i = the volume fraction of material i,

K_i = the thermal conductivity of material i,

C_i = the specific heat of material i, and

Γ, ρ_i previously defined.

The summation is carried out over all the materials.

The heat source or sink due to phase change is simply

$$Q_v = h_{sf} \ \Delta\rho_i \tag{5.21}$$

where the terms have been previously defined. The heat source or sink due to chemical reaction is described in the SLAM[26] document.

The ablation rate is calculated from the rate at which melting occurs at the concrete interface. The heat flux into the concrete region, $q_{c,o}$, is known from the solution to the energy equation in the concrete region. This heat flux coupled with the temperature distribution in the pool region predicts a surface temperature at the interface between the two regions. If the predicted temperature exceeds the melt temperature of the concrete, then the ablation rate, V, is calculated from the formula

$$V = \frac{2K}{\rho_c h_{sf,c}} \left(\frac{T_p - T_M}{\Delta Z}\right) - \frac{q_{c,o}}{\rho_c h_{sf,c}} \tag{5.22}$$

where T_p = the temperature of the lower pool node,

ρ_c = the concrete density,

$h_{sf,c}$ = the latent heat of melting of the concrete,

ΔZ = the finite difference node size,

T_M = the melt temperature of the concrete, and

K = the effective turbulent mixture conductivity between the center of the bottom node and the interface between the two regions.

The second option for ablation rate is to input the rate from the experimental data. When using this option, only one pool thermal node is used so that only a bulk pool temperature is predicted. When the second option is used, the heat loss from the pool region into the concrete region is

$$q_p = \rho_c V_a h_{sf,c} + q_{c,o} \tag{5.23}$$

where q_p = the heat loss from the pool region,

V_a = the ablation rate, and

ρ_c, $h_{sf,c}$, $q_{c,o}$ have been previously defined.

5.2.2 Concrete Region: Dry Zone and Wet Zone

The concrete region consists of two separate zones: a dry zone and a wet zone. The dry zone is that volume of the concrete where all liquid water has been boiled off. Chemically bound water and CO_2 still exist in this zone, and they are released at a rate which is temperature dependent. The dry zone is initially very thin. When hot material contacts the concrete, the liquid water boils off and the evaporation front recedes away from the hot surface. Thus the dry region can swell, shrink, and move with the ablation front.

The wet zone is that region of the concrete that contains evaporable (liquid) water. The water is able to migrate through the pores in this region under the influence of a pressure gradient. The pressure gradient is created by the gas evolution in the dry zone. Since the evaporation front moves into the wet zone, this region shrinks with time.

The numerical methods employed in this region are identical to those in the SLAM document[26] with one exception--the energy equation in the dry region. Since most of the numerical methods

have been reported in detail elsewhere, they will only be summarized here, except the energy equation in the dry zone which has not been otherwise reported.

The Dry Zone

There are three governing equations that are solved in the dry zone. Continuity equations to keep track of the chemically bound gases, H_2O and CO_2, and other materials in concrete, an energy equation for the temperature distribution, and a momentum equation for the pressure distribution. The pressure distribution is required to provide a thermal boundary condition between the dry and wet zones via a temperature-pressure thermodynamic relationship.

The coordinate system in this zone is attached to the ablation surface and moves with it. The opposite end of this zone, the evaporation plane, moves according to the rate of evaporation which is calculated from the solution to the energy equation. Thus an internal, implicit boundary condition exists between the dry and wet zones. Since the motion of both ends of the dry region is unrelated, except through a solution to the equations, this region will swell and shrink according to the physics of the problem.

The Dry Zone Continuity Equations

The continuity equations in the dry region are solved using a semi-implicit, finite difference technique. The motion of the region, as well as the swelling and shrinkage, are included through advective terms that employ doner cell differencing.

There are currently three continuity equations in the dry zone. The continuity equations in the dry zone calculate the distribution of: bound water, $CaCO_3$, and $MgCO_3$. The other materials include all other chemicals that are present, such as CaO, MgO, SiO_2, and inert materials. The concentrations of materials other than those of water and the carbonates are not included in the form of continuity equation solutions, because their concentration does not change as it passes through the dry zone, or the concentration is directly related to the carbonate density through a molecular weight ratio. For example, at any location in the dry zone the concentration of CaO is directly related to the concentration of $CaCO_3$ through the formula

$$\rho_{CaO} = (\rho_c f_{CaCO_3} - \rho_{CaCO_3}) \frac{W_{CaO}}{W_{CaCO_3}} \qquad (5.24)$$

where ρ_{CaO} = the macroscopic density of CaO,

f_{CaCO3} = the mass fraction of concrete that is $CaCO_3$,

ρ_c = the macroscopic density of concrete,

W = the molecular weight, and

ρ_{CaCO3} = the macroscopic density of $CaCO_3$ as calculated by the continuity equation.

The three continuity equations in the dry region are of the form

$$\frac{\partial \rho_i}{\partial t} + V \frac{\partial \rho_i}{\partial x} = S_i \tag{5.25}$$

where ρ_i is the macroscopic density of material i,

S_i is a source term to account for the gas release, and

V is the advective velocity associated with coordinate system motion and swelling/shrinkage.

The equations are solved using a two-step finite difference procedure similar to that which is used in the pool region.

The first step is to calculate the mass sink term due to bound gas release.[26,31]

$$\rho_i^{n+1} = \rho_i^n \exp (s' \Delta t)$$

$$s_{CaCO_3} = -3.6 \times 10^5 \exp \left(\frac{-19362}{T_j}\right)$$

$$s_{MgCO_3} = -4.2 \times 10^8 \exp \left(\frac{-19362}{T_j}\right) \tag{5.26}$$

$$s_{H_2O} = -3.3 \times 10^{10} \exp \left(\frac{-20560}{T_j}\right)$$

where T_j = the temperature of the jth node,

Δt = the time step size, and

ρ_i^{n+1} = the intermediate time step density.

The second step is to calculate the change in density due to advective effects. In fully implicit finite difference form the equation reduces to

$$a\rho_{j-1}^{n+2} + b\rho_{j}^{n+2} + c\rho_{j+1}^{n+2} = \frac{\rho_{j}^{n+1}}{\Delta t} \tag{5.27}$$

where

$$a = \frac{-V_j^+}{\Delta x} ,$$

$$b = \frac{1}{\Delta t} + \left(\frac{V_{j+1}^+ - V_j^-}{\Delta x}\right) + \frac{\dot{\delta}}{\delta} , \tag{5.28}$$

$$c = V_{j+1}^-/\Delta x ,$$

where j is the finite difference node of thickness Δx, and the velocities are defined according to a doner cell formulation

$$\begin{aligned} V_j^+ &= \max\ (0,\ V - \dot{\delta} \times (j)) \\ V_j^- &= \min\ (0,\ V - \dot{\delta} \times (j)) \\ V_{j+1}^+ &= \max\ (0,\ V - \dot{\delta} \times (j+1)) \\ V_{j+1}^- &= \min\ (0,\ V - \dot{\delta} \times (j+1)) \end{aligned} \tag{5.29}$$

δ is the dry region thickness, and the dot implies time derivative.

Note that in this region the velocity, V, is the ablation velocity, and it is fixed for the entire region. It is the swelling term $\dot{\delta}x$ which creates a position dependence upon the advective term.

In the original SLAM[26] document two options were available for the wet zone. The first option included a simultaneous solution to the energy, momentum, and two continuity equations (water and air). The second option used a simplified approximation to

the Darcy velocity for the liquid water and thus did not require a separate continuity and momentum equation solution. The study[26] found that the simplified approach was of sufficient accuracy for experiment analysis so that only this second approach is used in this report.

The Dry Zone Energy Equations

The energy equations in the dry region are

$$\rho c \frac{\partial T}{\partial t} + \rho c V \frac{\partial T}{\partial x} = \frac{\partial}{\partial x} K \frac{\partial T}{\partial x} + Q_V \qquad (5.30)$$

where ρ = the concrete density,

c = the concrete specific heat,

K = the concrete thermal conductivity, and

Q_V = the heat sink due to gas release.

The transpiration cooling effect of the gases is included through the advective term $\rho c V \partial T/\partial x$.

These equations are solved using a fully implicit tridiagonal finite difference technique. The equation is the same as that in the pool region with the exception that the doner cell velocity is defined according to the appropriate region. In the dry zone the doner cell velocity is defined the same as in the continuity equation. In the wet zone the velocity is

$$V_j^- = V_{j+1}^- = \frac{-\dot{m}_w}{\rho_w} + V_o \qquad (5.31)$$

where $\dot{m}_w$ is the water evaporation rate, and ρ_w is the macroscopic density of liquid water in the wet zone and V_o is the simplified Darcy velocity of the liquid water. The wet zone velocity does not depend upon position because the coordinate system mesh size does not vary in time as it does in the other zones and regions.

Concrete Region Momentum Equations

In the concrete region there is only one momentum equation to be solved--the dry zone. The wet zone momentum equation is

ignored altogether because, as stated earlier, it is assumed not to have a very large impact upon the results of experiment simulations.

The momentum equation in the dry zone can be solved independently of any gas continuity equations because any gas that is formed by evaporation or chemical release will flow to the reaction zone in less time than all other significant changes in the system.

The mass flux of gas at any location is equal to the evaporated flux from the wet/dry interface plus any sources accumulated along the way. Thus,

$$\dot{m}(x) = \dot{m}_w + \int_x^{\delta} S dx' = \frac{-k}{\mu} \frac{P}{RT} \frac{dP}{dx} \qquad (5.32)$$

where

$\dot{m}_w$ = the evaporable water mass flux from the wet/dry interface

k	= the permeability	(m^2)
μ	= viscosity	(kg/m-sec)
P	= pressure	(pascal)
R	= gas constant	(m^2/sec^2-K)
T	= temperature	(K)
S	= the source rate of gases (H_2O and CO_2) due to chemically bound release	(kg/m^3)

Rearranging and integrating yields the pressure P_s at the wet/dry interface

$$P_s = \left[P_\infty^2 + 2 \dot{m}_w \int_0^{\delta} \frac{\mu RT}{k} dx + 2 \int_0^{\delta} \frac{\mu RT}{k} \int_x^{\delta} S dx' \, dx\right]^{1/2} \qquad (5.33)$$

where P_∞ is the atmospheric plus melt head pressure.

The integrals above are carried out numerically. The pressure at any location within the dry zone can be evaluated from the same equation simply by changing the limit of the outer integrals from δ to the desired location.

Concrete Region Constitutive Relationships

There are two constitutive relationships that remain to be defined in the concrete region: The equations for the thermophysical properties and the temperature and pressure at the evaporation plane.

The thermophysical properties of density composition and specific heat are input by the user. Typical values are

ρ = 2400 kg/m^3 and

C = 1275 J/kg K, $\rho_{w,e}$ = 64 kg/m^3, $\rho_{w,B}$ = 49 kg/m^3.

The thermal conductivity is assumed to be

$$K = -0.0012\ T + 2.4\ \frac{W}{mK} \tag{5.34}$$

The Temperature at the Wet/Dry Interface

The interface between the wet zone and the dry zone is the location where the liquid water evaporates. The pressure at this location is governed by the resistance to flow of the evaporated water as it leaves the dry zone. Thus by combining the set of equations that describe the heat fluxes into this interface, the temperature-pressure relationship for saturated water and the pressure-mass flux relation for flow through the porous dry zone, an interface temperature, T_s, can be solved for.

The mass flux of evaporated water can be found by an energy balance at the wet/dry interface. Thus

$$\dot{m}_w = \frac{1}{h_{fg}} \left[- 2K_D \frac{(T_d(N) - T_s)}{\Delta X_d} + 2\ K_w \frac{T_w(1) - T_s)}{\Delta x_w} \right] \tag{5.35}$$

where subscript w implies wet zone, d implies dry zone, and h_{fg} is the latent heat. (N) refers to the last node in the dry zone, and (1) refers to the first node in the wet zone.

The pressure at the wet/dry interface is the saturation pressure of water at temperature T_s.

$$P_s = P^* \exp(-T^*/T_s)$$

$$P^* = 1.758 \times 10^{10} \text{ pascals}$$

$$T^* = 4500 \text{ K}$$

The T^* and P^* values were determined by curve fitting the above formula to steam table data.

The pressure at the wet dry interface is also defined by the Darcy equation in Section 5.1. Thus a Newton-Raphson functional f can be defined which is the difference in the two formulations for pressure, hence the functional

$$f = P_s^2 - P_\infty^2 - 2\dot{m}_w \int_o^\delta \frac{\mu RT}{k}\, dx - 2 \int_o^\delta \frac{\mu RT}{k} \int_{x'}^\delta S\, dx'dx \qquad (5.36)$$

is equal to zero at the correct value of T_s.

5.2.3 The Wall Region

The experimental apparatus that are used in the melt-concrete interaction experiments typically have a concrete floor surrounded by castable MgO sidewalls. The MgO has a relatively high-thermal conductivity (~4-6 W/mK) compared to the concrete. Thus the heat loss to the sidewalls can be a significant and sometimes a major portion of the total heat loss.

Heat loss in the sidewalls is by conduction only. However, since the pool region moves downward as ablation occurs, new sidewall is exposed to the melt. Two options present themselves for this type of situation: (1) a fixed-coordinate system which models the entire crucible, or (2) a moving-coordinate system that follows the pool region. The latter option was chosen because of the simplicity of implementation when considering aspects such as pool swelling and computer execution time.

The heat loss in the sidewalls is a two-dimensional phenomena having both radial and vertical components. The energy equation is

$$\rho c \frac{\partial T}{\partial t} + V_z \frac{\partial T}{\partial Z} = \frac{\partial}{\partial r}\left(K \frac{\partial T}{\partial r}\right) + \frac{\partial}{\partial Z}\left(K \frac{\partial T}{\partial Z}\right) \qquad (5.37)$$

with the boundary conditions

$$@\ r = r_i,\ T(Z) = T_{pool}\ (Z) \qquad @\ r = r_o,\ \partial T/\partial r = 0.0$$
$$@\ Z = 0,\ T(r) = T_o \qquad @\ Z = \delta,\ T(r) = T_o \tag{5.38}$$

In the wall region the method of solution is an alternating direction implicit method. First, the vertical direction reduces to a matrix equation of the form:

$$a\ T_{j-1}^{n+1} + b\ T_j^{n+1} + c\ T_{j+1}^{n+1} = d \tag{5.39}$$

where

$$a = \frac{-V_j^+}{\Delta Z} - \frac{K}{\rho c \Delta Z^2}$$

$$b = \frac{1}{\Delta t} + \frac{(V_{j+1}^+ - V_J^-)}{\Delta Z} + \frac{2\ K}{\rho c \Delta Z^2} + \frac{\Delta \dot{Z}}{\Delta Z} \tag{5.40}$$

$$c = \frac{V_{j+1}^-}{\Delta Z} - \frac{K}{\rho c \Delta Z^2}$$

$$d = \frac{T_j^n}{\Delta t}$$

The doner cell velocities are defined as usual

$$\begin{aligned} V_j^- &= \min\ (0,\ V_w(j)) \\ V_j^+ &= \max\ (0,\ V_w(j)) \\ V_{j+1}^- &= \min\ (0,\ V_w(j+1)) \\ V_{j+1}^+ &= \max\ (0,\ V_w(j+1)) \end{aligned} \tag{5.41}$$

The wall velocities V_w depend upon both pool swelling and the ablation rate.

Since the location of the ablation surface is known, the location, and node size of the swelled nodes above the surface are

obtained by summation from this surface. The nodes in the pool region and the vertical direction in the wall are identical, hence the actual sizes and their rates of change are determined by the predicted gas flow rates. The wall velocities are obtained by differentiation.

$$V_w(j) = V_a + \frac{Z|_j^{n+1} - Z|_j^n}{\Delta t} \qquad (5.42)$$

where V_a = the ablation rate
Z = the location of the jth interface
Δt = the time step size

After calculating an intermediate time step temperature from the vertical tri-diagonal inversion, a final end of time step temperature is calculated in the horizontal direction. The equation is

$$a\ T_{j-1}^{n+2} + b\ T_j^{n+2} + C\ T_{j+1}^{n+2} = d \qquad (5.43)$$

where

$$a = \frac{-K}{\rho c \Delta r}\ ,\ b = \frac{1}{\Delta t} + \frac{2K}{\rho c \Delta r^2}\ ,\ c = \frac{K}{\rho c \Delta r}\ ,\ d = \frac{T_j^{n+1}}{\Delta t}$$

5.3 COMPARISON WITH EXPERIMENT

The results of the experiment analysis will be separated into three categories. The first category is comparisons with the measured thermocouple responses. The second category is the predictions that are made. The last category is the implications resulting from the predictions.

5.3.1 Comparisons with Measured Thermocouple Data

Figures 5.4 and 5.5 show predicted and measured thermocouple responses at different depths in the concrete. As can be seen, the comparison is good at early times but deviates at later times. This is expected for two reasons: first the total eroded depth is not predicted exactly by the model; and second, the penetration is uneven as revealed by the final floor contour in posttest observation. The model, in contrast, predicts a planar, or average, penetration. The results for the TURC1SS test average is not shown because the erosion in that test was very uneven.

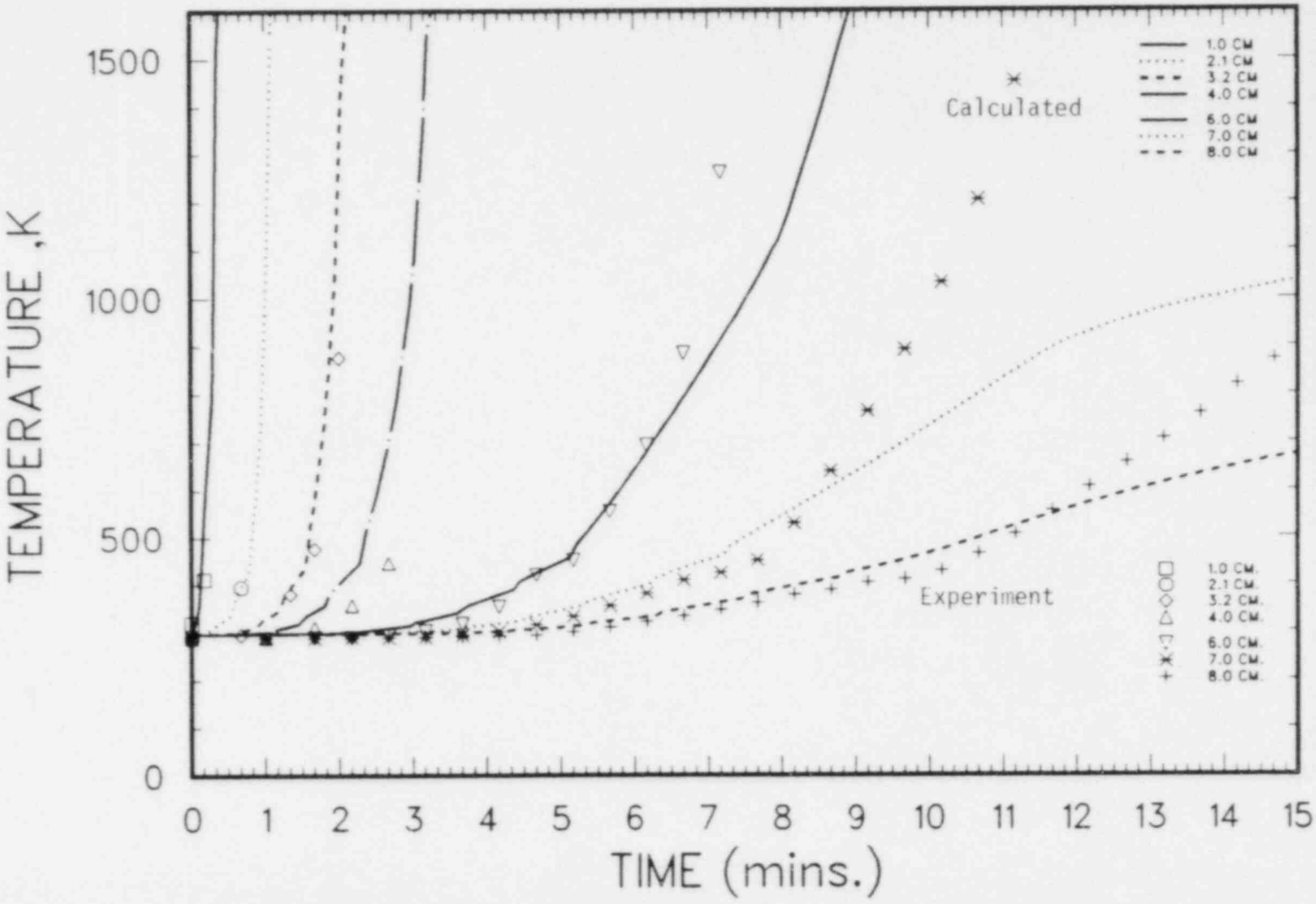

Figure 5.4 TURC1T Comparison of Predicted and Experimental Data in the Concrete Centerline at Various Depths

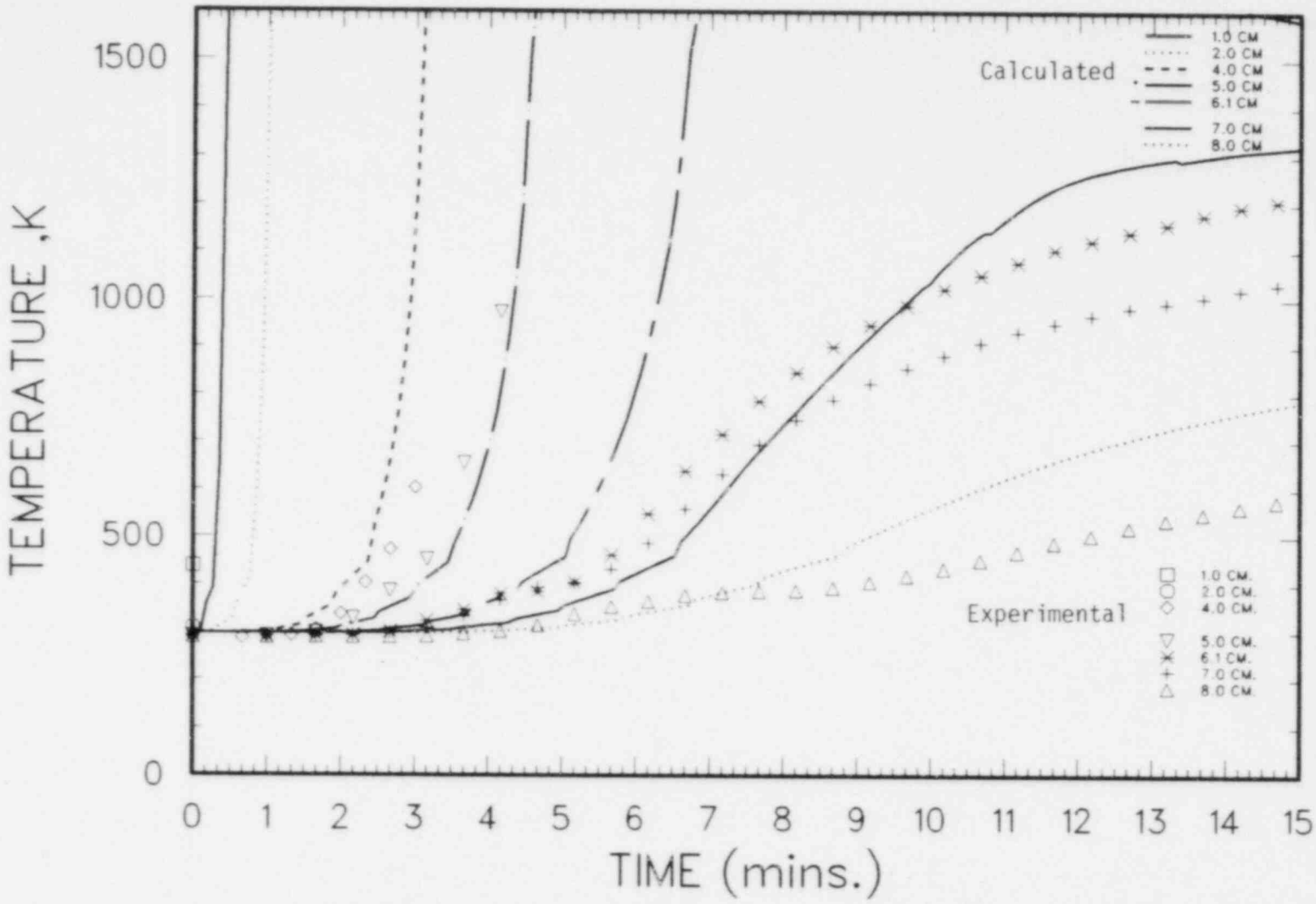

Figure 5.5 TURC1T Comparisons of Predicted and Experimental Data at a Radius of 18 cm and at Various Depths

An alternative method of comparing predictions vs measurements is to compare the thermocouple failure times to the erosion front. A plot of this type allows the reader to average the data visually, and hence a more realistic comparison can be achieved. Figures 5.6 and 5.7 are plots of the predicted erosion and wet fronts as a function of time compared with the experimental data. As can be seen, there is good agreement between the predictions of the model and the experimental measurements. The experimental volume average penetration indicate a total erosion of 7.0 cm for the TURC1T and 4.3 cm for the TURC1SS tests. These values can be compared to the predicted total erosion of 7.0 and 3.8 cm respectively. Since the model has good agreement for both experiments, without any variation in model parameters, it can be concluded that the model as described in this report provides a fairly accurate picture of the phenomena that occur in the experiments. (Ideally, the model should be compared with many more experiments, and indeed it has, though the results are not reported here. It will simply be stated that good agreement was obtained in the other comparisons of experiment data and predictions using this model.)

The model predictions for the wall heat fluxes are shown in Figures 5.8 and 5.9. The data points shown are from the inverse heat flux calculations that are based upon the measured thermocouple responses in the MgO wall.

The wall heat flux comparison shown is good for early times and poorer at later times for the TURC1T test. However, at later times the inverse heat flux calculation was unable to converge upon an accurate solution. The reason for the larger error could be due to degradation of the MgO during the course of the experiment which would cause a large variation in properties that are not accounted for in the inverse heat flux calculation.

Figure 5.9 shows a comparison of the wall heat flux for the TURC1SS test. Good agreement is shown for this test. It was found that if perfect contact between the pool and the MgO wall was assumed, then the predicted stainless wall heat flux overpredicted the measure flux. The magnitude of the overpredicted flux was similar to the thermite heat flux. However, excellent agreement is obtained by putting a thermal resistance in series with the wall. The thermal resistance would represent the combined convective and radiative resistance of a gas film adjacent to the wall. For the thermite test a large heat transfer coefficient was required ($h > 1000$) indicating that the gas film was either not present or was enhanced by intermittent liquid-wall contact. For the stainless test, the best wall heat flux agreement was found with a heat transfer coefficient of 335 W/m^2K. Such a low value seems to imply that a stable gas film existed in stainless test for the duration of the experiment.

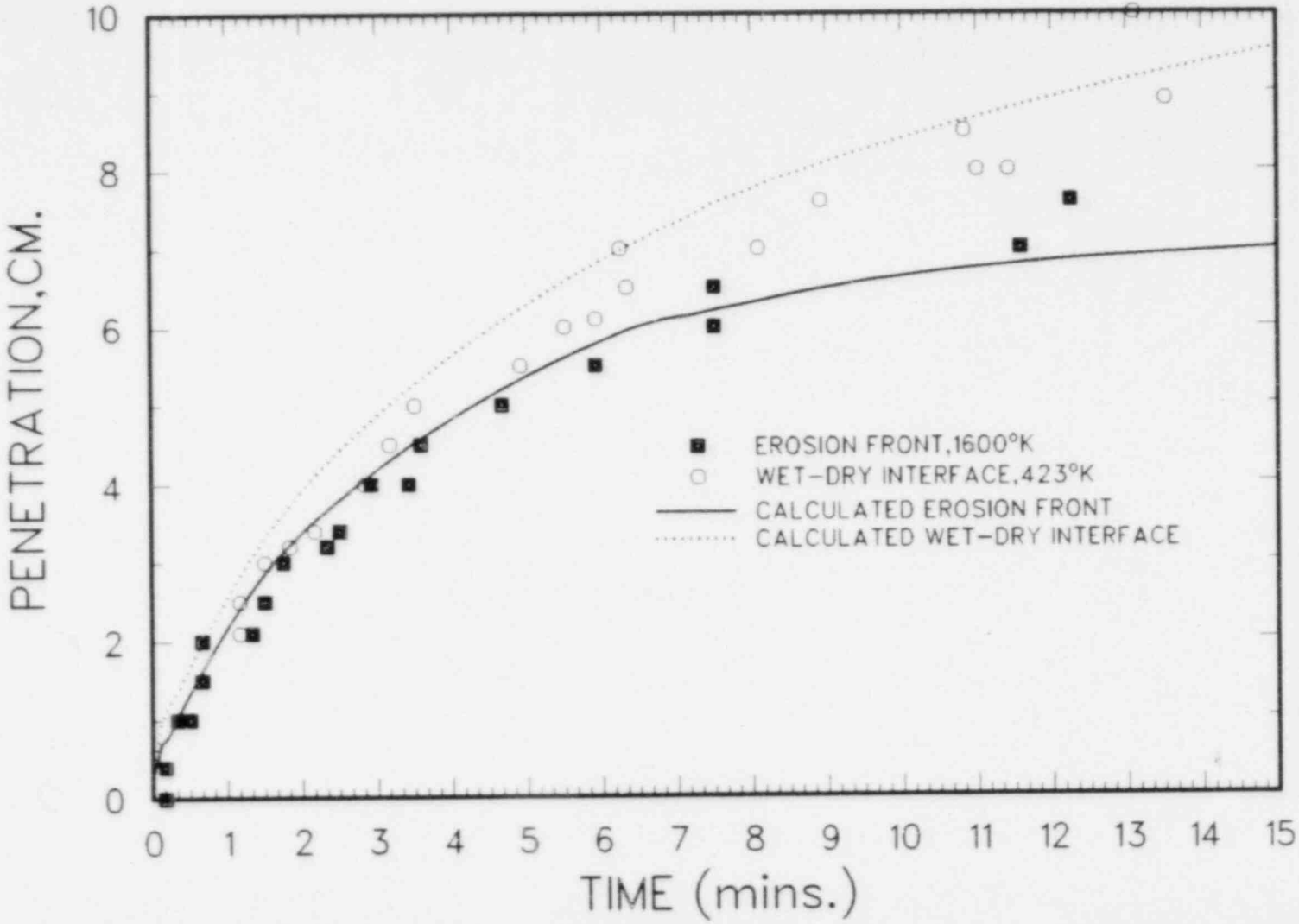

Figure 5.6 Comparison of Predicted and Experimental Data for the TURC1T Erosion and Wet Front

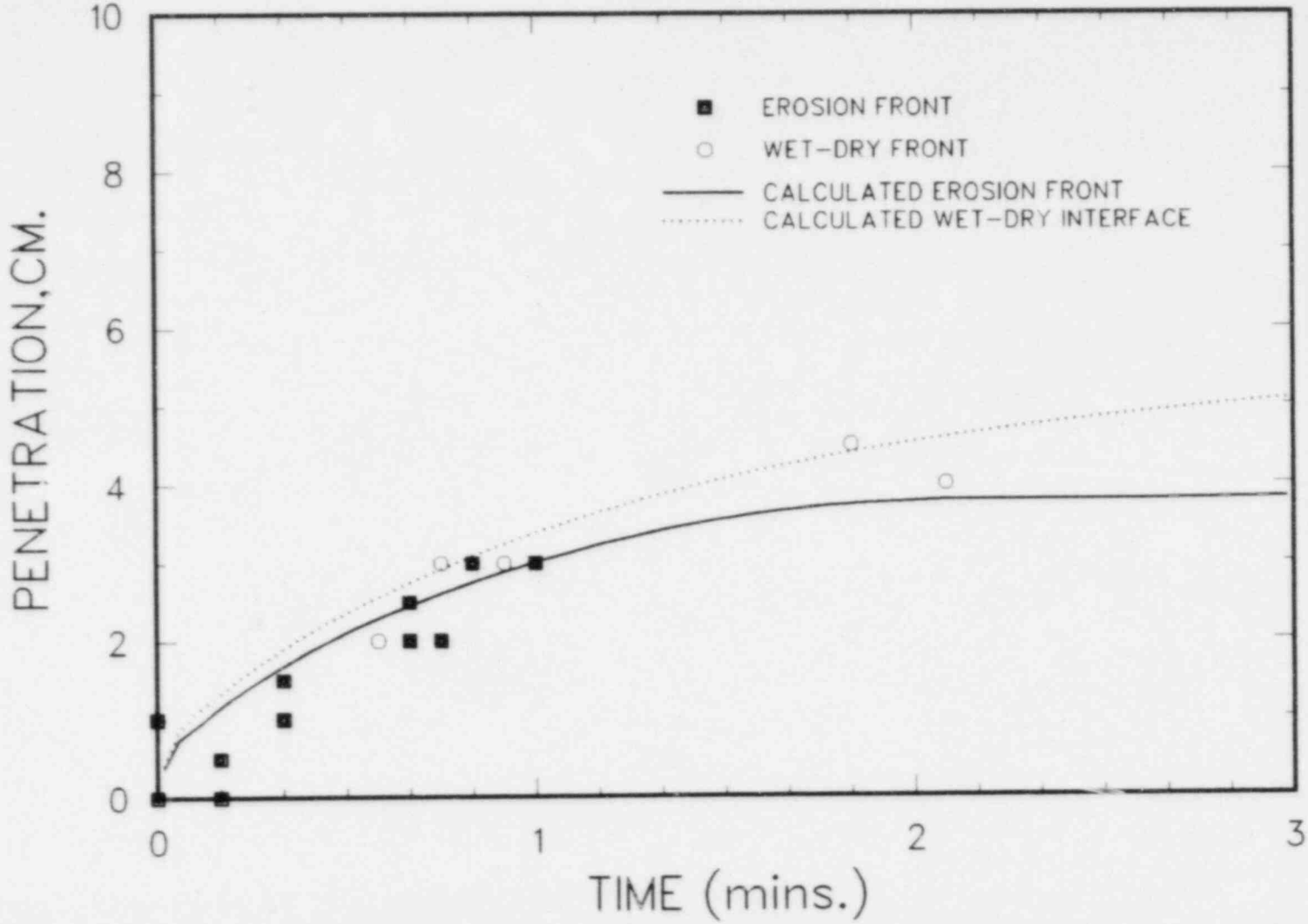

Figure 5.7 Comparison of Predicted Data and Experimental Data for the TURC1SS Erosion and Wet Fronts

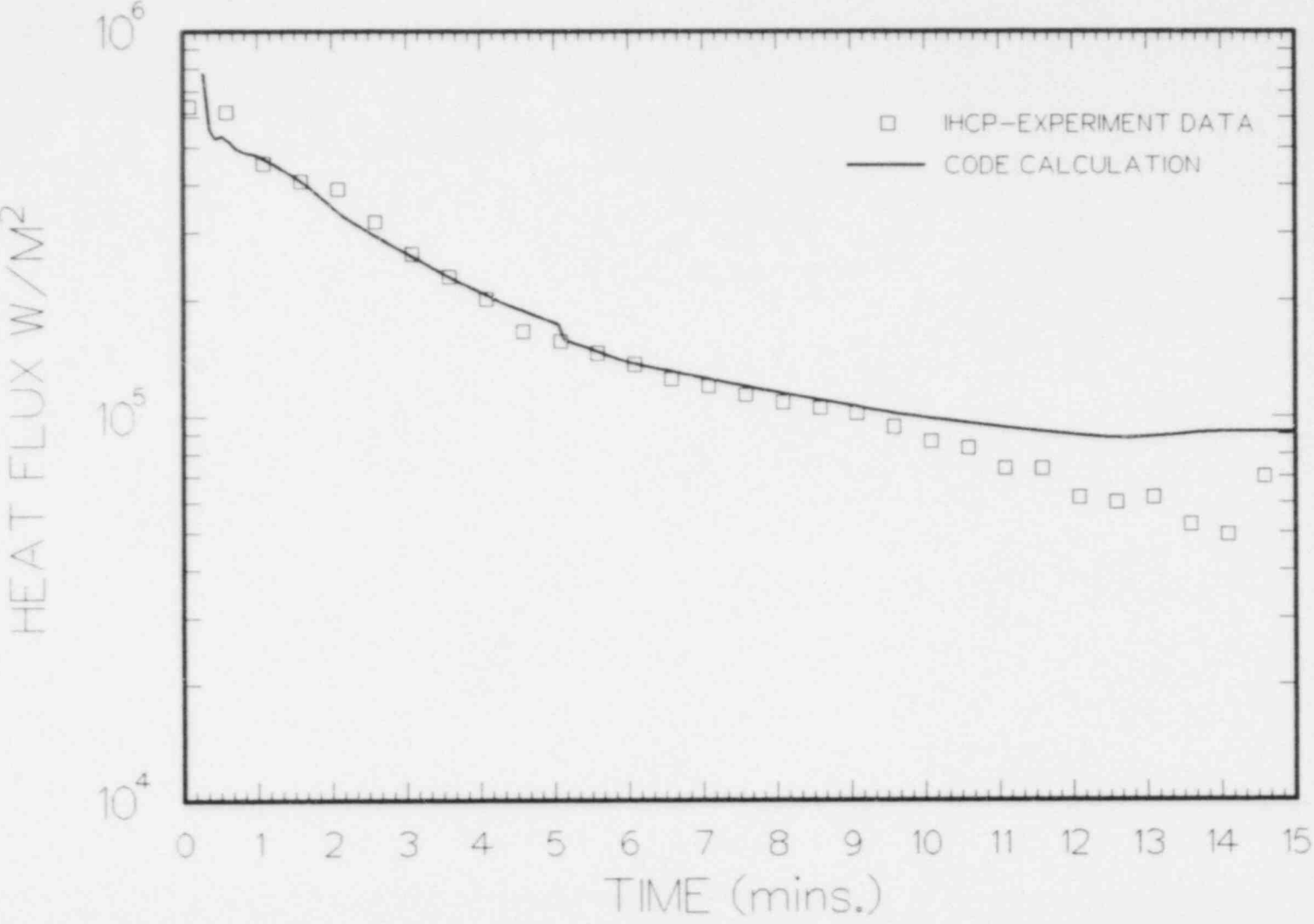

Figure 5.8 Comparison of Predicted and Measured Wall Heat Fluxes for the TURC1T Test

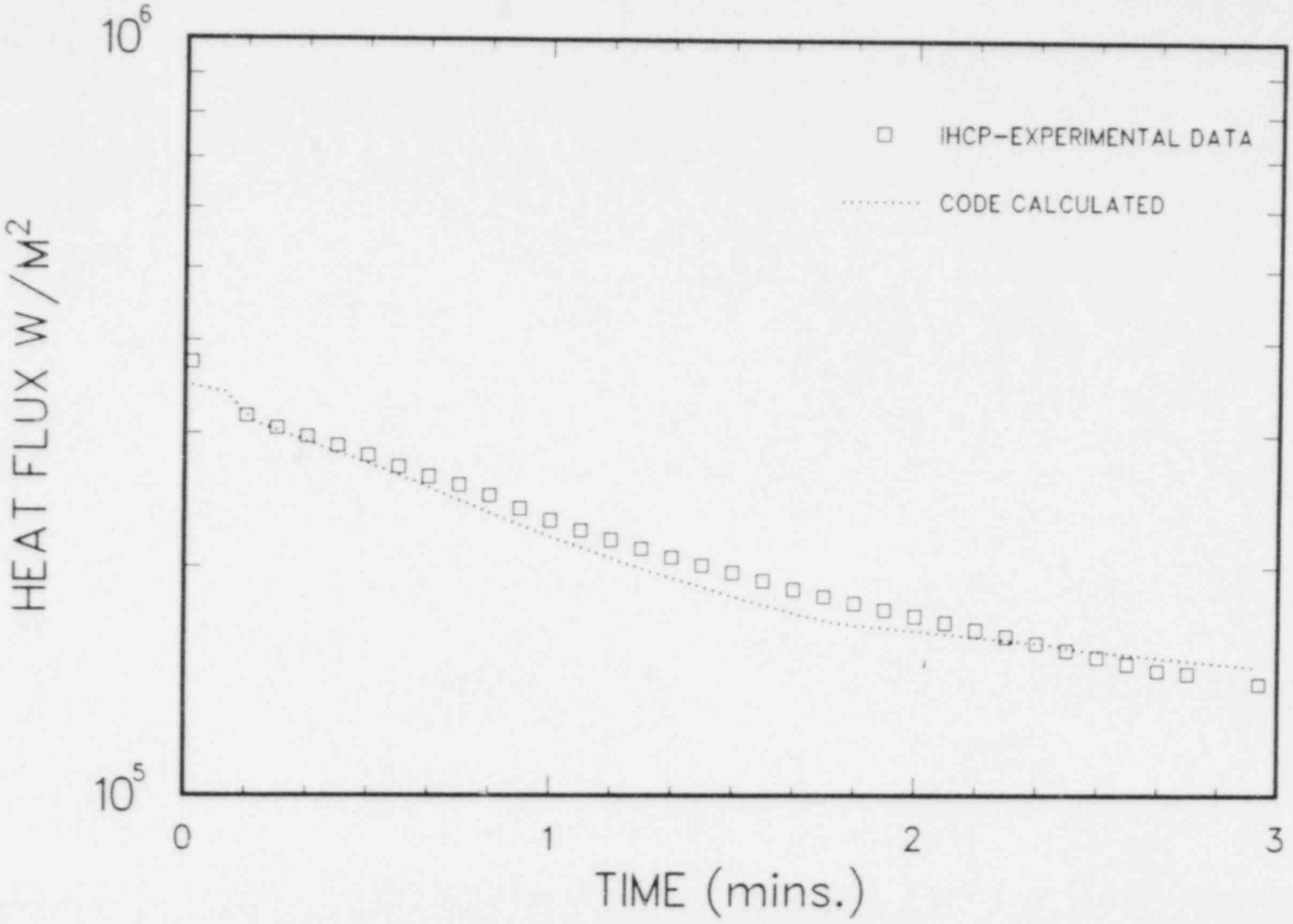

Figure 5.9 Comparison of Predicted and Measured Wall Heat Flux for TURC1SS Test

5.3.2 Model Predictions for the Experiments

Figure 5.10 is a plot of the predicted pool temperature for the TURC1T test. The slight plateau at ~ 2300 K is due to the alumina freezing process. The freezing process takes approximately 2 minutes, after which the pool temperature decreases to the steel freezing point at 1700 K. Steel freezing at the lower surface begins at 10-1/2 minutes into the test. The steel freezing initiation seems to occur at about the same time when the differences between MgO wall heat flux data and model calculation becomes large, possibly indicating some connection. The freezing process also corresponds with the termination of the ablation process, although hot solid penetration could still occur, it is not calculated by the model.

The predicted pool temperature in the TURC1SS (stainless) test is shown in Figure 5.11. In this test the steel begins to freeze at 1 minute 40 seconds causing the pool temperature to level off at 1700 K. By examining the slopes of the experimental MgO wall flux (Figure 5.9), it is found that a small change in the slope occurs at this time, a similar change in slope is seen in the predicted wall flux. Additionally, the gas sample data may have indicated a change in the flow path of evolved gases at 1:40. Thus the time to steel freezing seems to be predicted quite accurately.

Figures 5.12 and 5.13 are the total heat losses and fluxes for the thermite test. The heat losses are the fluxes multiplied by the respective transfer areas of various processes. The total heat lost into the refractory walls is approximately equal to that lost into the ablating concrete. This is clear evidence that the wall heat loss cannot be ignored. Heat loss from the evolving gases is quite large at early times (the first few seconds) when temperatures and gas fluxes are very high. Radiative heat lost from the top surface is minimal, although this is a user-selected quantity because the surface emissivity is user input. The surface emissivity for the thermite test was selected to be 0.01 because it was assumed that the escaping aerosols would provide a radiation barrier effectively insulating the surface.

The total heat losses and fluxes for the stainless steel test are shown in Figures 5.14 and 5.15. The results are similar to the thermite test with the exception that the majority of the heat loss is to the ablating concrete.

Figures 5.16 and 5.17 are plots of the predicted heat transfer coefficients between the pool and the surface of the ablating concrete. The heat transfer coefficient is defined as the heat flux from the pool to the concrete surface divided by the pool to concrete temperature difference. An examination of the figures

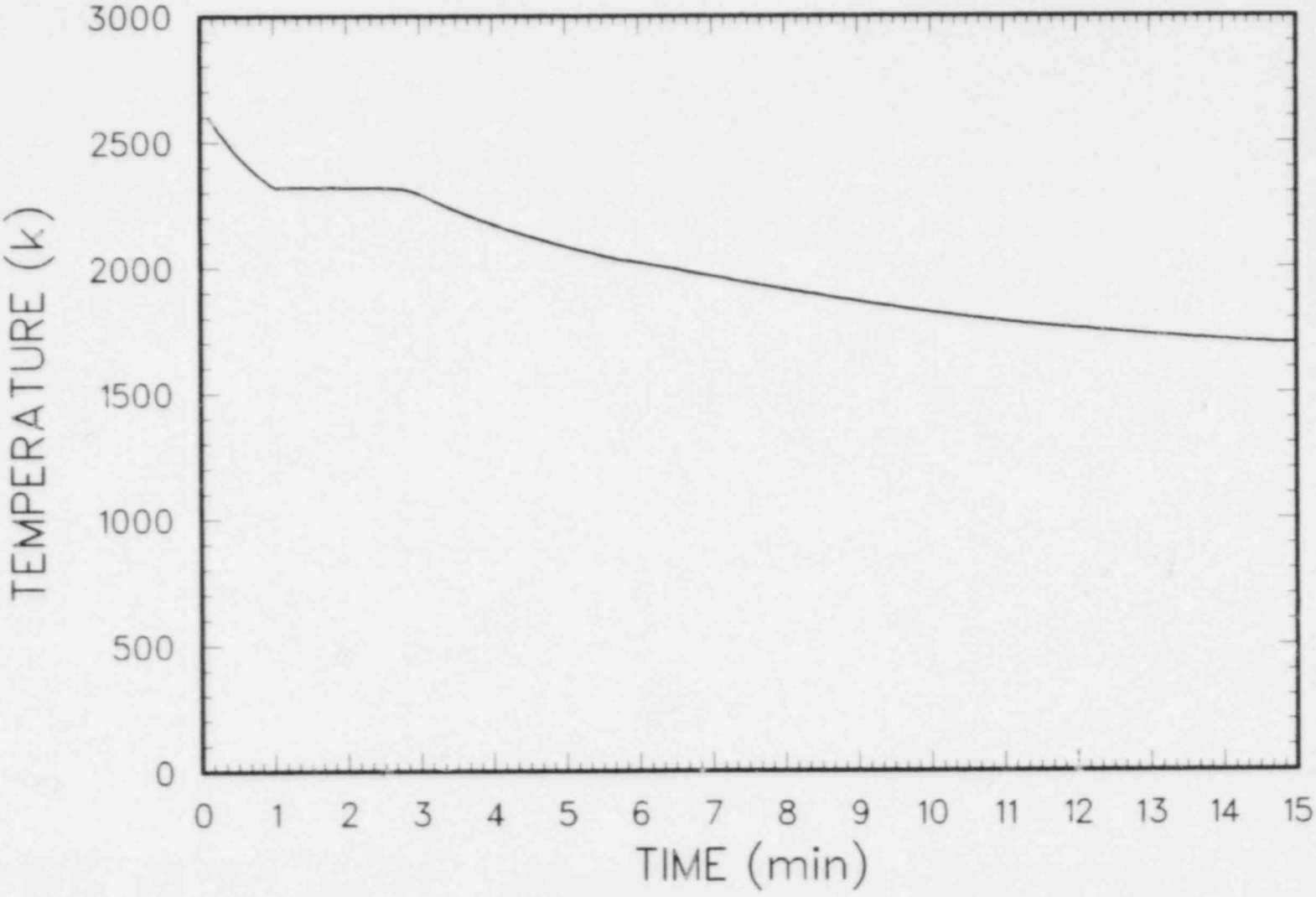

Figure 5.10 Calculated Melt Pool Temperature for TURC1T Experiment

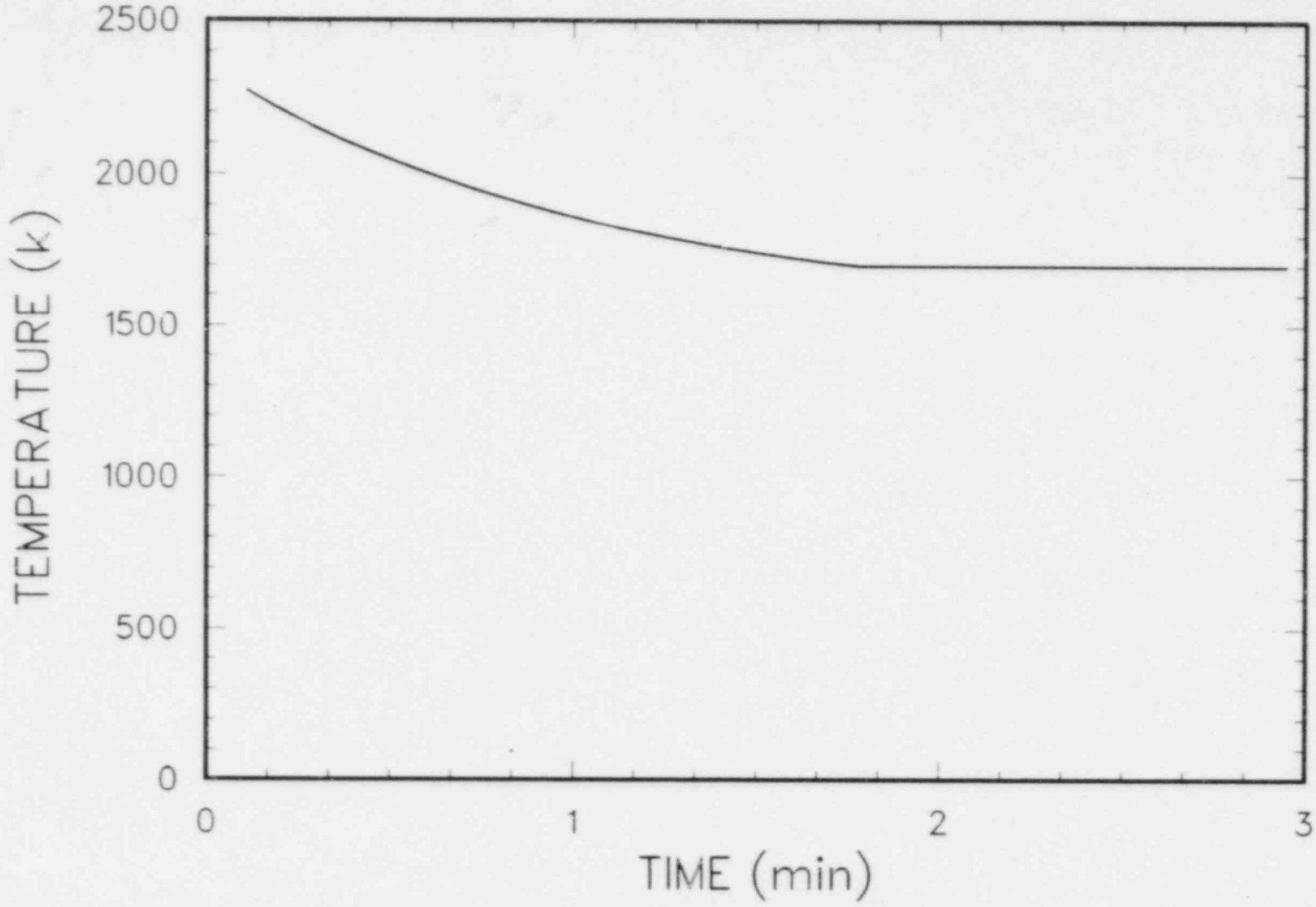

Figure 5.11 Calculated Melt Pool Temperature for TURC1SS Experiment

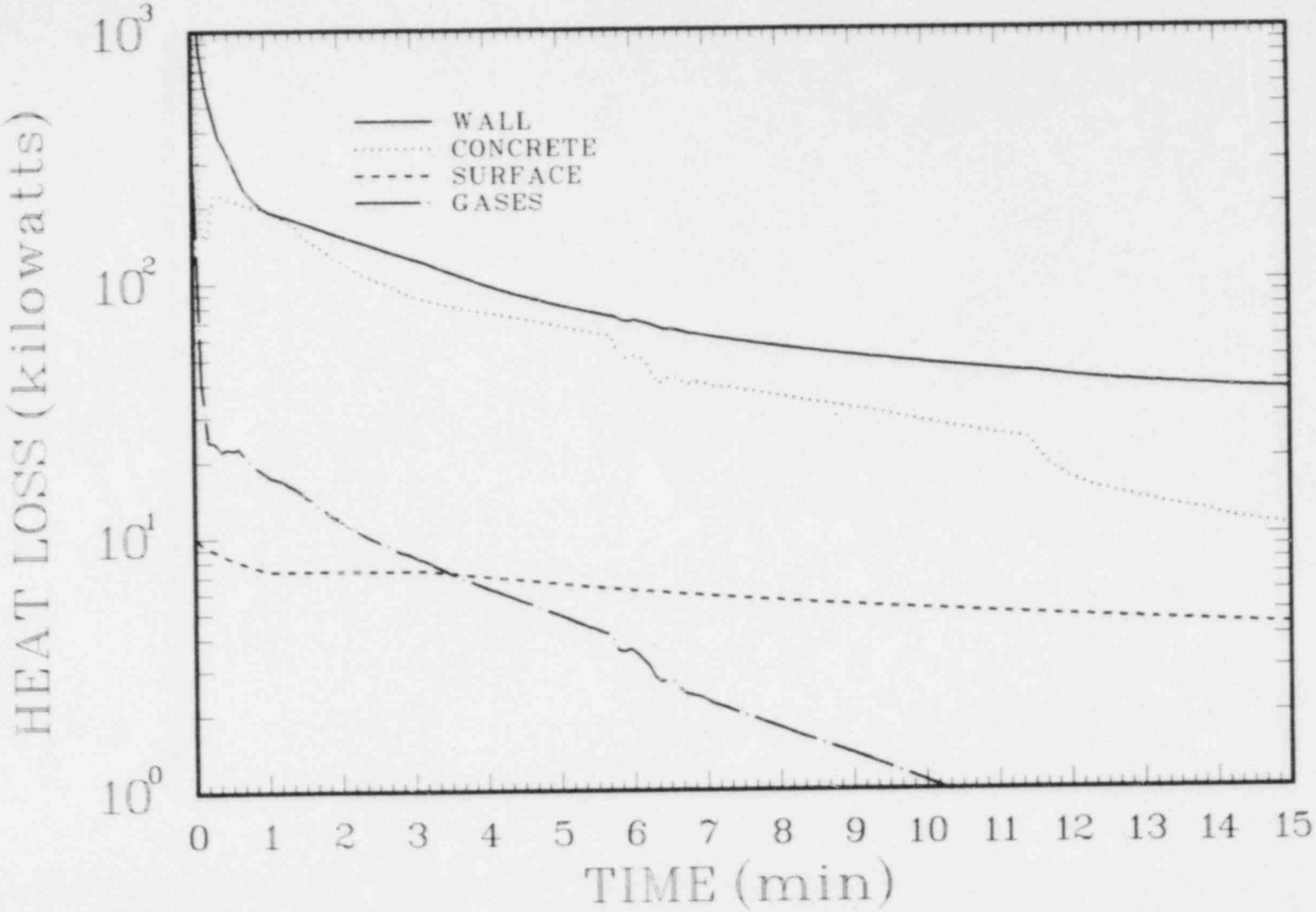

Figure 5.12 Total Heat Losses for TURC1T

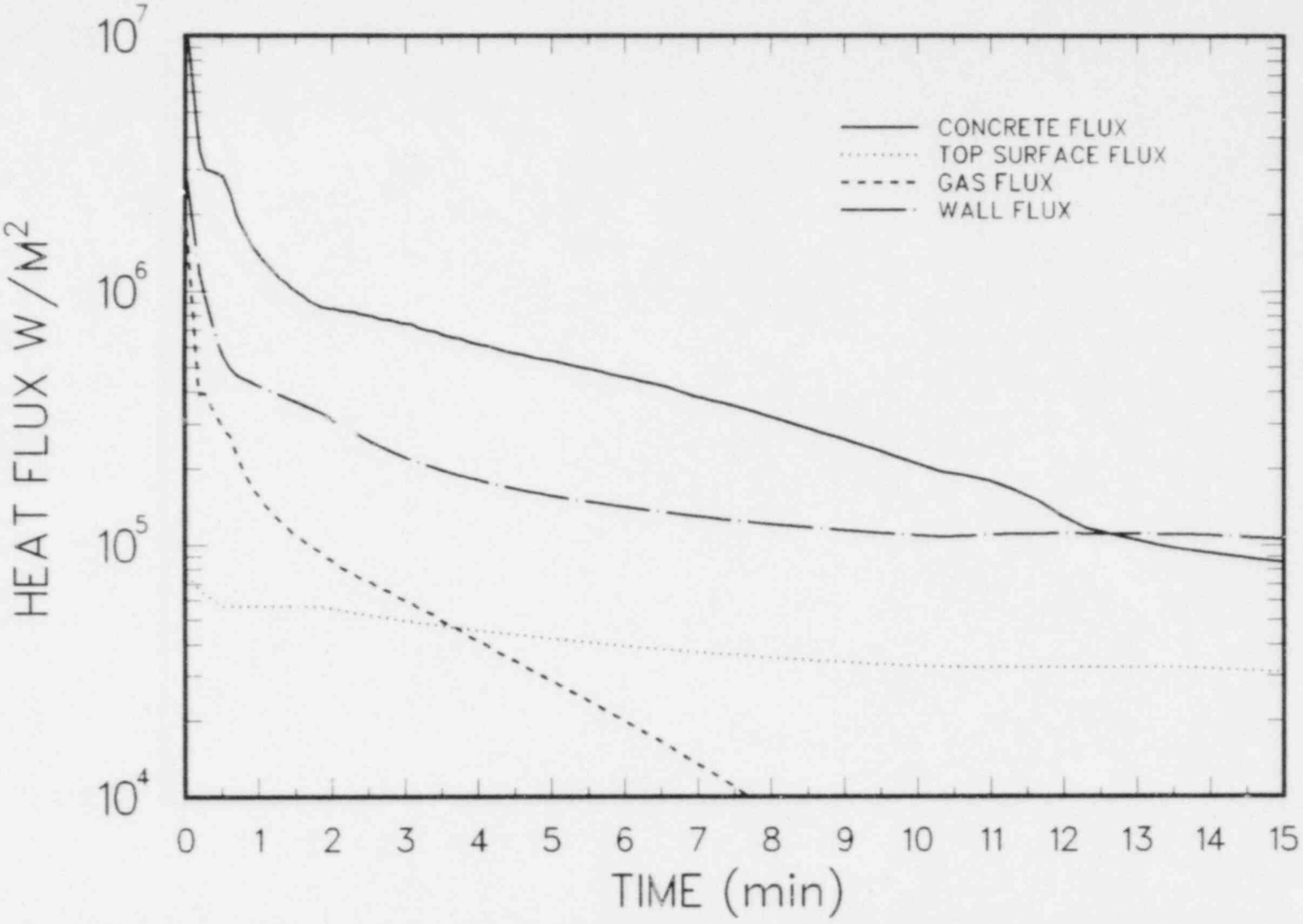

Figure 5.13 Calculated Heat Fluxes for TURC1T

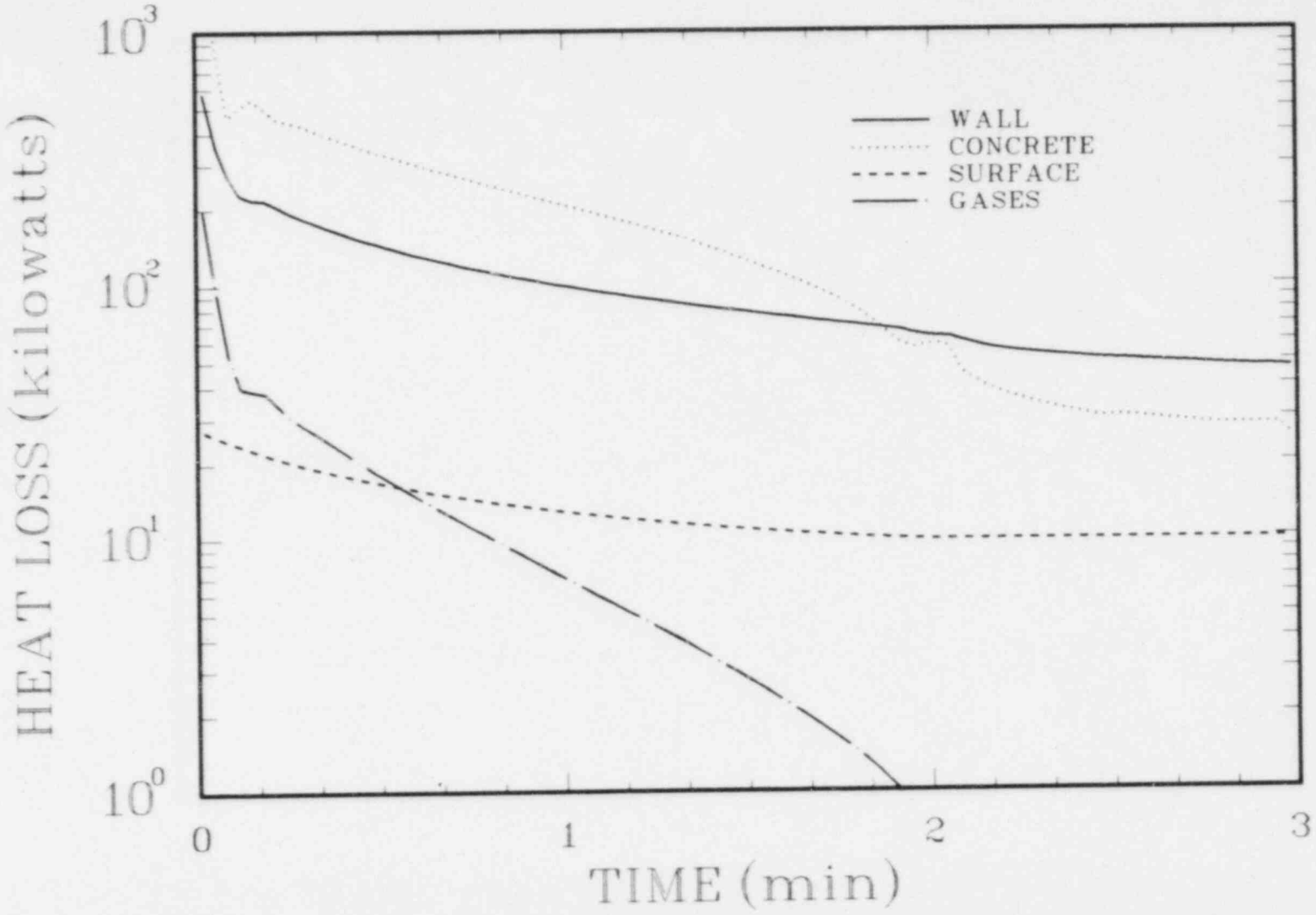

Figure 5.14 Total Heat Losses for TURC1SS

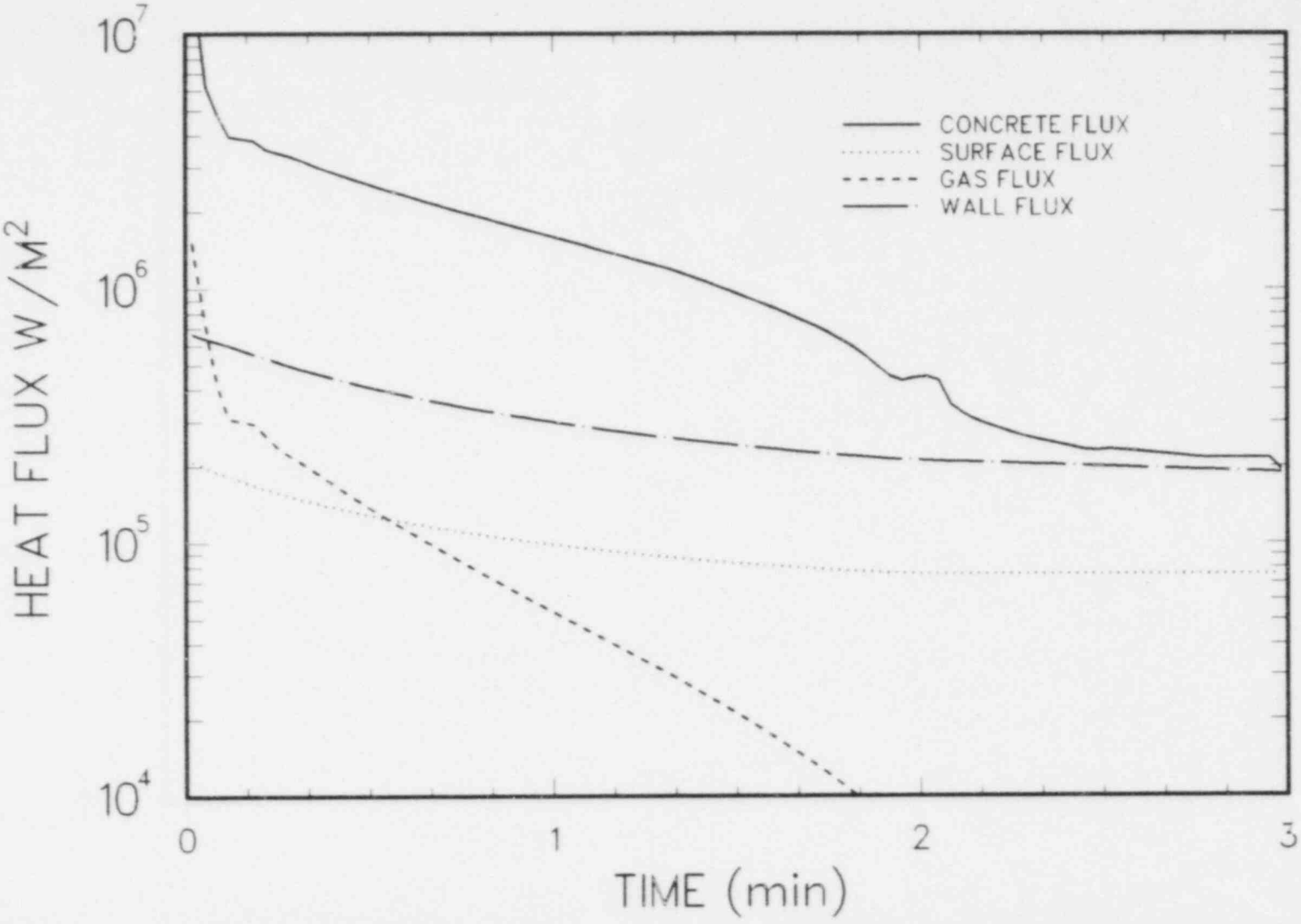

Figure 5.15 Calculated Heat Fluxes at Various Locations for TURC1SS

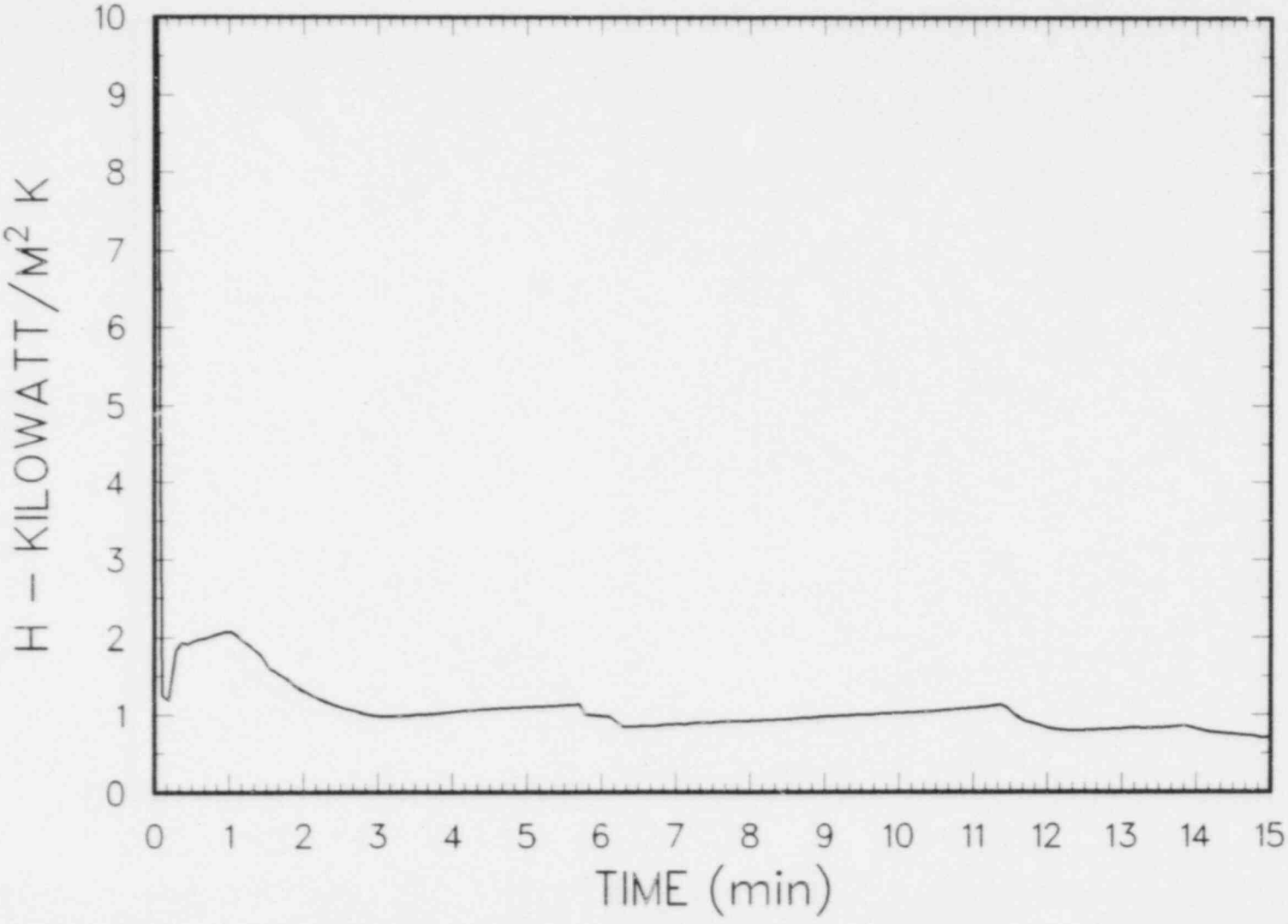

Figure 5.16 Calculated TURC1T Heat Transfer Coefficients Between Melt Pool and Concrete

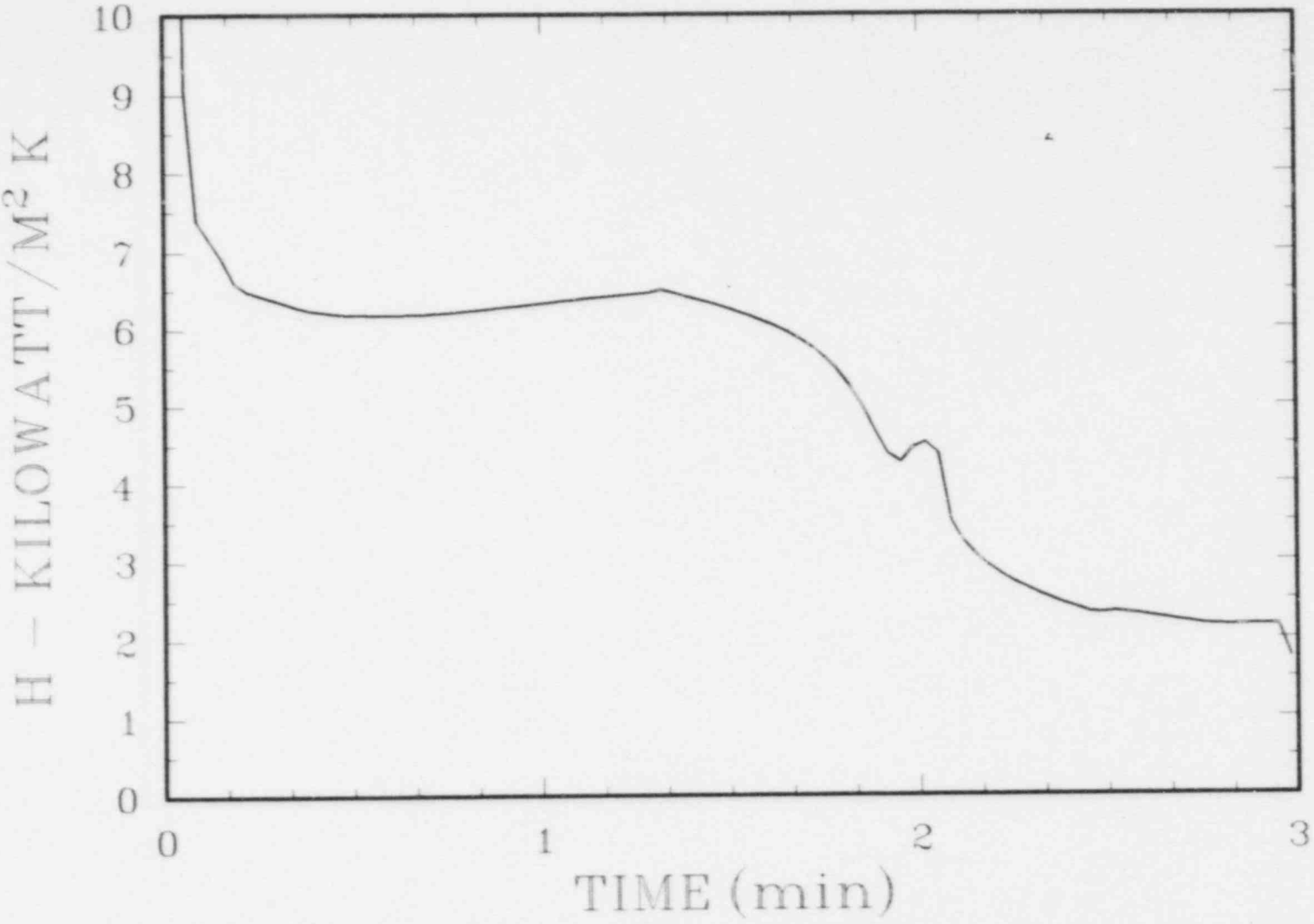

Figure 5.17 Calculated TURC1SS Heat Transfer Coefficients Between Melt Pool and Concrete

reveals that the heat transfer coefficient varies as function of time for both tests. The magnitude of the heat transfer coefficient is quite large--from 1 to 7 kW/m^2K. If a vapor film were assumed to be the only heat transfer resistance, then its thickness would be from 0.13 to 0.02 mm thick for the thermite and stainless tests respectively. The upper bound of 0.13 mm is a reasonable thickness under some conditions. The lower bound of 0.02 mm is not physically consistent with the smoothing effect of metallic surface tension over a rough concrete surface. Thus it appears that a vapor film may not be a suitable concept upon which to model all melt-concrete interactions.

The gas velocities and fluxes are shown in Figures 5.18 and 5.19 for the thermite and stainless tests respectively. At early times (<1 min) the gas velocity is very large--several m/sec. A velocity of that magnitude would imply a slug flow regime in the pool region. The heat transfer phenomena in a melt-concrete interaction consists of a hot liquid material melting a colder solid that contains significant quantities of gas. The gas that evolves stirs the system and enhances the heat transfer mechanism in a manner entirely analogous to boiling and/or pool barbotage.[27] Pool barbotage, as used here, is defined as the process of bubbling a gas through a drilled or porous heat transfer surface to a liquid. Both pool boiling and barbotage are known to enter the same regimes of gas-liquid behavior at the solid-liquid interface. The behaviors have been classified as nucleate and film boiling. An intermediate regime also exists when the film exists in an intermittent state. The intermediate regime is difficult, though not impossible, to achieve experimentally in pool boiling. In pool barbotage it is much easier to create the intermittent state because the experimenter has full control over the gas velocity. In a melt-concrete interaction what state the liquid-solid interface is in depends upon the gas velocity and the properties of the liquid at the surface. The Kutateladze number indicates whether or not a film heat transfer type of phenomena occurs at the concrete-pool interface. The Kutateladze number determines if conditions are sufficient for a departure from nucleate boiling type heat transfer. Once film boiling has been established, different conditions determine its stability--i.e., the Liedenfrost phenomena in pure liquids. However, in concrete ablation, melted concrete is continuously being injected into the film, if it exists, thereby changing the conditions required for stability. In addition, there exists a finite distance between the source of the gases within the concrete and the melting surface. This distance would cause a time delay between any sudden pool-surface contact and vapor production, thus the Liedenfrost phenomena cannot occur in concrete ablation in the same way that it occurs in pure liquids and clean hot surfaces. Hence, it appears that there are at least two mechanisms tending to collapse or fill in any film that is created and the only way to reestablish the film is to have conditions similar to the

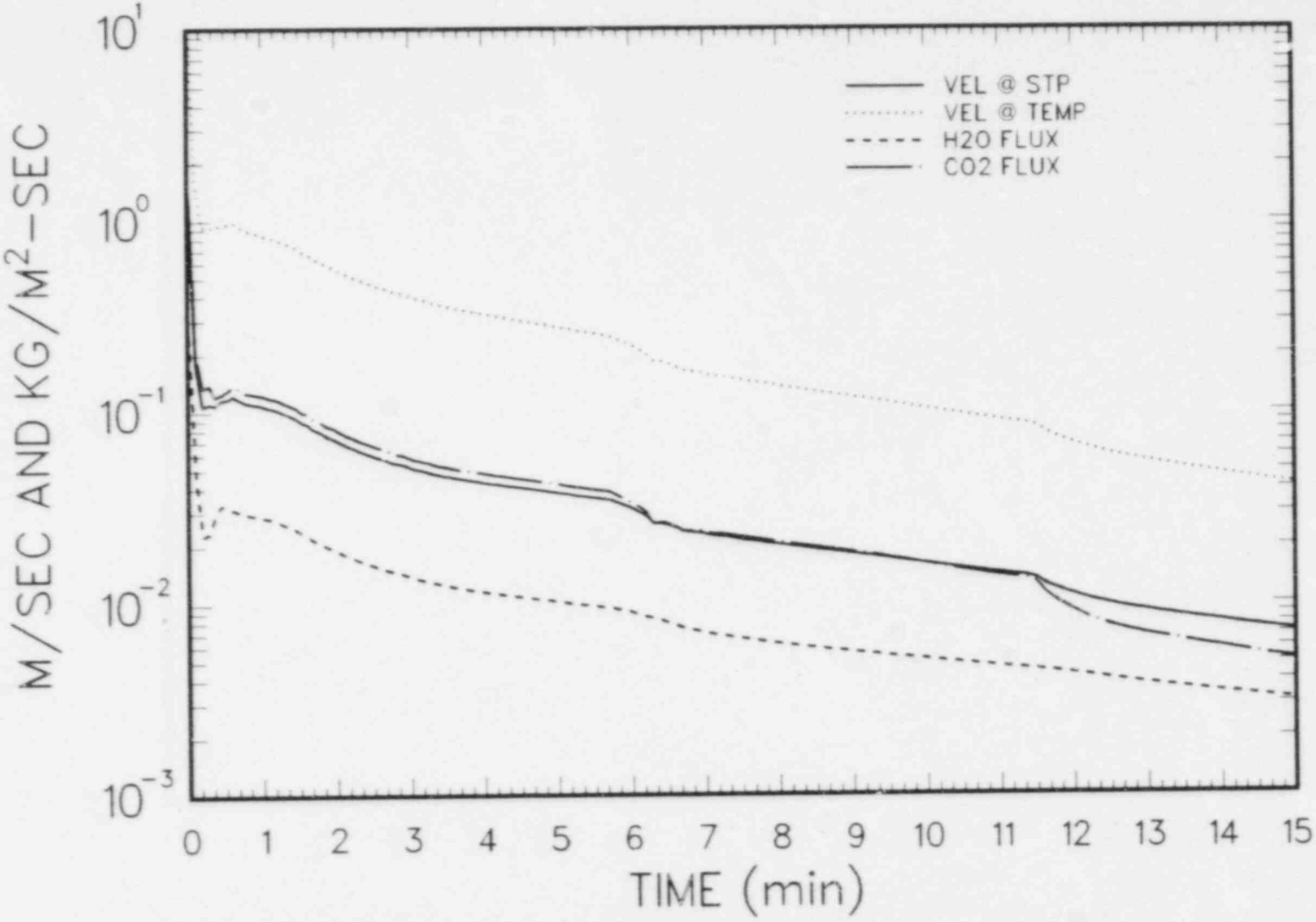

Figure 5.18 Calculated Gas Velocities and Mass Flux for TURC1T

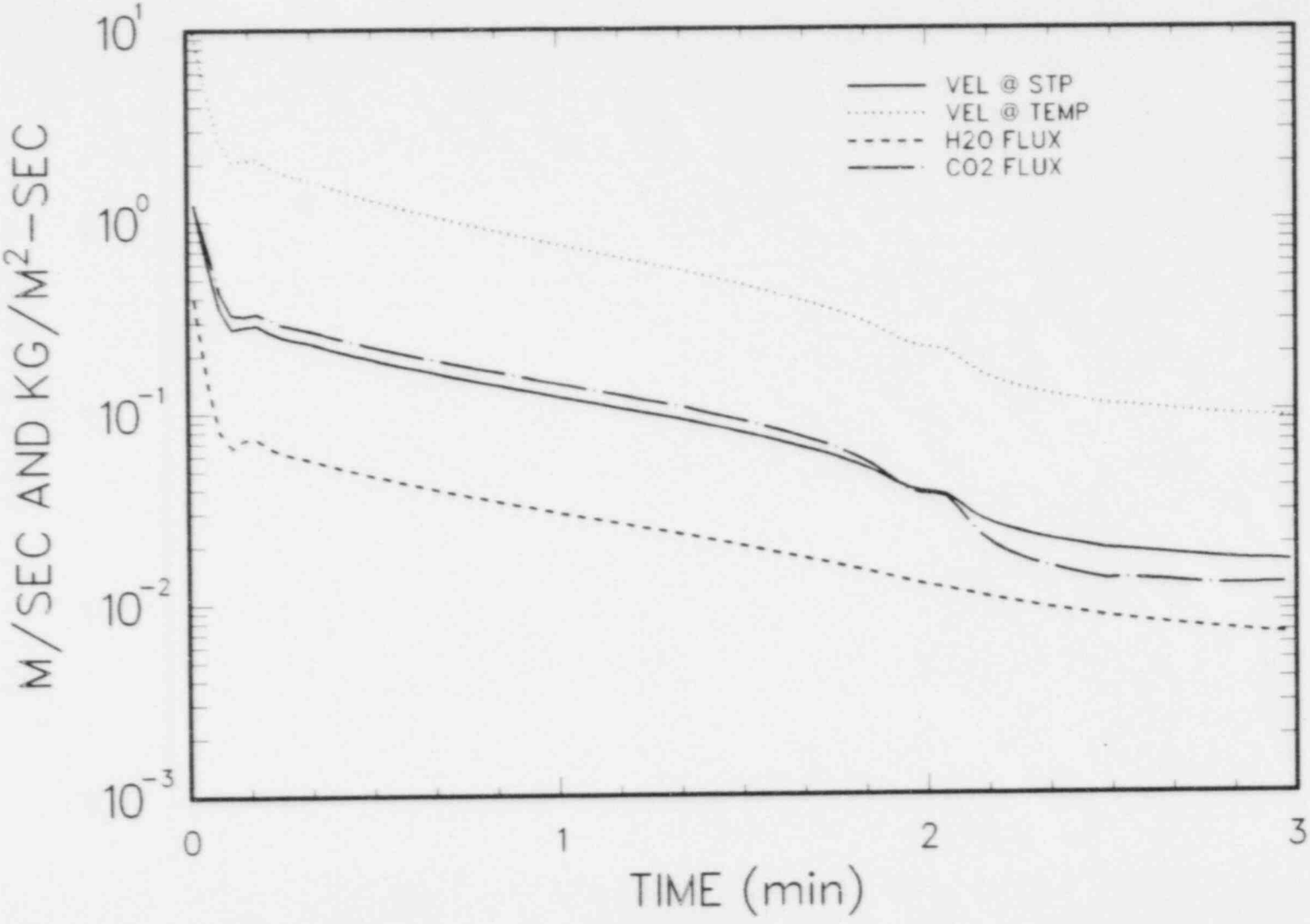

Figure 5.19 Calculated Gas Velocities and Mass Flux for TURC1SS

critical heat flux in nucleate boiling. Departure from nucleate boiling typically occurs at a Kutateladze number of around 0.08 to 0.16 depending upon a variety of experimental parameters.[28] In the melt-concrete experiments reported here, the Kutateladze number is always around 0.01 or less if liquid steel properties are assumed. Thus it appears that a nucleate boiling-like phenomena is more likely in these experiments. This, of course, could easily explain the large values of the heat transfer coefficients predicted for the experiments.

Insofar as the flow regime in the model is concerned, the boundary layer region does not support slug flow, but rather is always in a bubbly flow regime. At very high gas velocities, the void fraction in the boundary layer approaches 1, hence the boundary layer region resembles a foam of melted concrete mixed with the pool materials. The foam collapses above the boundary layer region to form the fast moving large bubbles characteristic of slug flow.

5.4 SENSITIVITY ANALYSIS

A sensitivity analysis of the TURC1 simulations has been performed. The purpose of the sensitivity analysis was to uncover the most important variables in the model. Other benefits from performing such an analysis are error location--a sensitivity analysis permits discovery of coding errors due to nonphysical behavior that would result. Selection of optimum values of a set of variables is possible if the correct or experimental solution is known. It can also direct one in future model development in that the most important phenomena are brought to light. One of the more important results of a sensitivity analysis is to display different regimes of behavior that can be encountered in the experiment.

The sensitivity analysis is performed by selecting a group of variables and their ranges of variation, operating on these variables by the Latin hypercube sampling technique,[29] running the code for a large range of random variations of the input variables and then performing a regression analysis upon key output variables.

5.4.1 Input Parameters

The input parameters chosen for this sensitivity analysis are of three general categories. The categories are experimental input, thermophysical properties, and modeling parameters. The weighting chosen for the experimental and thermophysical property variables was within the range of expected uncertainty. For example, the thermite temperature had an upper limit of 2900 K based upon the iron boiling point (3000 K), less a small amount

of cooling during the melt generator to crucible transfer process. The lower limit was set at 2520 K based upon the boiling points of aluminum less melt generator/teem cooling. The thermophysical properties were typically allowed to vary ± 20% unless a better range was actually known.

The range of variation chosen for the modeling parameters was purposely chosen to be quite large (often a factor of 2 or more). A large range of uncertainty for the modeling parameters was chosen so that if the results were sensitive to the modeling parameters it would definitely show up. In addition the modeling parameters were ranked according to their importance, thereby providing information about the key processes of the ablation mechanism.

Table 5.1 is a list of all the parameters that were varied, the range of variation, and a brief description of the parameter.

5.4.2 Output Variables

The output variables chosen for the sensitivity analysis are the melt temperature, the ablation front location, the effective melt-concrete heat transfer coefficient, and the difference between the measured and the predicted erosion front.

Since the simulations are time-dependent problems, the regression analysis was performed at several discrete times. Tables 5.2 and 5.3 give a ranking of the most important variables at several points in time during the course of the experiment. The ranking can be ascertained from the absolute magnitude of the numbers in parenthesis next to the variable. A negative number indicates that an increase in the parameter causes a decrese in the output variable. The correlation coefficient (R^2) is a measure of the degree of correlation that can be achieved with the variables listed at that specific time. (An R^2 of 1.0 indicates a perfect correlation.) From those tables it becomes evident that the most important variable turns out to be the product of γ_o and V_B. An analysis of the structure of the models reveals that the product represents the effective (turbulent) thermal conductivity of the pool. Both γ_o and V_B also appeared independently in the analysis as being important. γ_o is obviously important because it is directly proportional to the degree of mixing. V_B affects the eddy thermal conductivity as noted above, but it also affects the flow regime behavior. Large values of V_B result in lower void fractions.

Another modeling parameter that turns out to be quite important is the viscosity-freezing parameter α_{sm}. This parameter is the volume fraction of solid material at which the pool region becomes a viscous slurry. For some thermite cases the alumina freezes out first causing the pool to become a viscous slurry,

Table 5.1 Experimental Parameters

			TURC1SS		TURC1T		
	Parameter	Units	Min	Max	Min	Max	Definition
1	T_i	K	2325	2375	2560	2900	Initial melt temperature
2	M	kg	106	133	131	161	Melt mass
3	$\%Al_2O_3$	-	0	5.0	23	45	Percent alumina in melt

Thermophysical Property Parameters

	Parameter	Units	Min	Max	Definition
4	$\rho_{Al,s}$	kg/m^3	2000	2700	Solidified alumina density
5	$\rho_{Al,}$	kg/m^3	2000	2700	Liquid alumina density
6	$\rho_{Fe,s}$	kg/m^3	5000	7000	Solidified iron density
7	ρ_{CaO}	kg/m^3	1200	2400	Calcium oxide density
8	ρ_c	kg/m^3	1000	3000	Liquified concrete density
9	ρ_{MgO}	kg/m^3	2200	3160	Magnesium oxide density
10	$K_{Al,l}$	W/m K	0.4	4.0	Liquid alumina thermal conductivity
11	$K_{Al,s}$	W/m K	0.4	4.0	Solidified alumina thermal conductivity
12	$K_{Fe,s}$	W/m K	10.0	25.0	Solid iron thermal conductivity
13	$K_{Fe,l}$	W/m K	10.0	25.0	Liquid iron thermal conductivity
14	K_{CaO}	W/m K	0.2	4.0	CaO thermal conductivity
15	K_c	W/m K	0.2	4.0	Molten concrete thermal conductivity
16	CKA	W/m K	-1.44×10^{-3}	-1.0×10^{-3}	Concrete conductivity parameter
17	CKB	W/m K	2.0	2.88	$K = CKA \cdot T + CKB$; $K \geq CKC$
18	CKC	W/m K	0.1	0.144	Minimum concrete conductivity

Table 5.1 Experimental Parameters (Continued)

	Parameter	Units	Min	Max	Definition
19	MgOKA	W/m K	-7.5×10^{-3}	-2.5×10^{-3}	MgO conductivity parameter
20	MgOKB	W/m K	4.0	12.0	K = MgOKA . T + MgOKB K> MgOKC
21	MgOKC	W/m K	1.0	3.0	Minimum MgO thermal conductivity
22	$T_{m,Al}$	K	2200	2375	Melting temperature of alumina
23	$T_{m,Fe}$	K	1700	1810	Melting temperature of steel
24	$T_{m,c}$	K	1400	1650	Melting temperature of concrete
25	L_{Al}	J/kg	8×10^5	1.2×10^6	Latent heat of fusion - alumina
26	L_{Fe}	J/kg	2.25×10^5	3.24×10^5	Latent heat of fusion - steel
27	L_c	J/kg	4×10^5	6×10^5	Latent heat of fusion - concrete
28	$C_{p,c}$	J/kgk	1100	1320	Specific heat of concrete
29	$\%CaCO_3$	--	45	60	$\%CaCO_3$ in concrete
30	H_2O_B	kg/m^3	85	100	Concrete bound water density
31	H_2O_E	kg/m^3	100	120	Concrete evaporable water density
			Modeling Parameters		
32	δ_{BL}	m	0.01	0.05	Thickness of boundary/bubbly layer
33	V_B	m/sec	0.3	0.5	Absolute bubble velocity
34	V_{BM}	--	1.5	3.5	Slug flow regime parameter
35	γ_o	m	2.5×10^{-5}	1.0×10^{-4}	Turbulent mixing parameters $\gamma_1 = 10^4$, $\gamma_2 = 2$
36	V_c	m/sec	0	0.04	Bouyant (slip) velocity of concrete
37	V_{Al}	m/sec	0	0.004	Bouyant (slip) velocity of alumina
38	α_{SL}	--	0.4	0.8	Minimum solid volume fraction for fluidization

Table 5.2 Regression Results for TURC1T

Output Variable = Pool Temperature

Time (sec)					
30	60	90	120	150	300
T_i (.56)	T_i (.40)	T_i (.28)	$\%Al_2O_3$ (.47)	$\%Al_2O_3$ (.50)	$\%Al_2O_3$ (.46)
$T_{m,Al}$ (.28)	$\%Al_2O_3$ (.29)	$\%Al_2O_3$ (.40)	γ_o (-.42)	γ_o (-.40)	MgOKA (-.27)
MgOKB (-.33)	$T_{m,Al}$ (.41)	$T_{m,Al}$ (.33)	α_{sl} (-.40)	MgOKA (-.24)	V_{AL} (.35)
$\gamma_o V_B$ (-.52)	α_{SL} (-.26)	α_{SL} (-.36)		V_{Al} (.27)	α_{SL} (-.43)
	$\gamma_o V_B$ (-.41)	$\gamma_o V_B$ (-.44)		α_{SL} (-.41)	$\gamma_o V_B$ (-.30)
R^2 .67	.57	.60	.52	.67	.65

Output Variable = Ablation Front

Time (sec)					
30	60	90	120	150	300
T_i (.16)	T_i (.24)	T_i (.25)	T_i (.26)	T_i (.26)	T_i (.26)
V_B (.26)	MgOKB (-.23)	$\%Al_2O_3$ (-.21)	MgOKB (-.30)	MgOKB (-.31)	MgOKB (-.34)
V_{BM} (.15)	α_{SL} (.31)	MgOKB (-.27)	V_{Al} (-.21)	V_{Al} (-.25)	V_{Al} (-.30)
α_{SL} (.22)	$\gamma_o V_B$ (.68)	α_{SL} (.38)	α_{SL} (.39)	α_{SL} (.39)	α_{SL} (.39)
$\gamma_o V_B$ (.68)		$\gamma_o V_B$ (.61)	$\gamma_o V_B$ (.58)	$\gamma_o V_B$ (.57)	$\gamma_o V_B$ (.53)
R^2 .67	.68	.71	.70	.70	.71

Table 5.2 Regression Results for TURC1T (Continued)

Output Variable = Pool Heat Transfer Coefficient

Time (sec)					
30	60	90	120	150	300
$T_{m,Al}$ (-.34)	$\%Al_2O_3$ (-.34)	V_{Al} (-.39)	V_{Al} (-0.41)	V_{Al} (-.39)	H_2O_E (.31)
α_{SL} (.26)	MgOKB (-.33)	α_{SL} (.37)			V_{Al} (-.56)
$\gamma_o V_B$ (.66)	V_{Al} (-.28)				
	α_{SL} (.44)				
R^2 .56	.48	.30	.16	.15	.39

Output Variable = Predicted Front - Measured Front

Time (sec)					
30	60	90	120	150	300
T_i (-.16)	T_i (-.24)	T_i (-.25)	T_i (-.26)	T_i (-.26)	T_i (-.26)
V_B (-.26)	MgOKB (.23)	$\%Al_2O_3$ (.21)	MgOKB (.30)	MgOKB (.31)	MgOKB (.34)
V_{BM} (-.15)	α_{SL} (-.31)	MgOKB (.27)	V_{Al} (.21)	V_{Al} (.25)	V_{Al} (.30)
α_{SL} (-.22)	$\gamma_o V_B$ (-.68)	α_{SL} (-.38)	α_{SL} (-.39)	α_{SL} (-.39)	α_{SL} (-.39)
$\gamma_o V_B$ (-.68)		$\gamma_o V_B$ (-.61)	$\gamma_o V_B$ (-.58)	$\gamma_o V_B$ (-.57)	$\gamma_o V_B$ (-.53)
R^2 .85	.69	.71	.70	.70	.71

Table 5.3 Regression Results for TURC1SS

Output Variable = Pool Temperature

Time (sec)	5	25	60	105	175
	T_i (.63)	T_i (.16)	M (.23)	$\pi_{Al.1}$ (-.29)	$T_{m,Fe}$ (.97)
	$\%Al_2O_3$ (.20)	M (.24)	$\%Al_2O_3$ (.16)	$T_{m,Fe}$ (.40)	
	$T_{m,Al}$ (.24)	$\%Al_2O_3$ (.19)	γ_o (-.53)	$\gamma_o V_B$ (-.58)	
	$T_{m,c}$ (.20)	$T_{m,c}$ (.23)	$T_{m,c}$ (.27)		
	$\gamma_o V_B$ (.68)	$\gamma_o V_B$ (.87)	V_B (-.70)		
R^2	.90	.92	.92	.56	.93

Output Variable = Ablation Front

Time (sec)	5	25	60	105	175
	$\%CaCO_3$ (-.12)	γ_o (.66)	$\%CaCO_3$ (.13)	$\gamma_o V_B$ (.77)	M (.36)
	$T_{m,c}$ (-.26)	$T_{m,c}$ (.43)	$T_{m,c}$ (.23)		$T_{m,Fe}$ (.30)
	ω_{BL} (.22)		ω_{BL} (.21)		$C_{p,c}$ (.20)
	V_B (.23)		V_B (.33)		ω_{BL} (.20)
	$\gamma_o V_B$ (.71)		$\gamma_o V_B$ (.63)		$\gamma_o V_B$ (.64)
R^2	.93	.61	.92	.59	.71

Table 5.3 Regression Results for TURC1SS (Continued)

Output Variable = Pool Heat Transfer Coefficient

Time (sec)	5	25	60	105	175
	γ_o (.20)	$T_{m,vc}$ (.17)	$T_{m,c}$ (.41)	$\pi_{Al,l}$ (.26)	$\pi_{Fe,s}$ (.33)
	$T_{m,c}$ (.14)	ω_{BL} (-.26)	$\gamma_o V_B$ (.60)	$T_{m,Fe}$ (-.43)	$\gamma_o V_B$ (-.41)
	ω_{BL} (-.46)	V_B (.36)		$T_{m,c}$ (.57)	
	V_B (.82)	α_{sm}		V_B (-.25)	
		$\gamma_o V_B$ (.64)			
R^2	.91	.94	.52	.67	.26

Output Variable = Ablation Predicted--Ablation Measured

Time (sec)	5	25	60	105	175
	γ_o (-.66)	$\%CaCO_3$ (.12)	$\%CaCO_3$ (.13)	$\gamma_o V_B$ (-.77)	M (.36)
	$T_{m,c}$ (.43)	$T_{m,c}$ (.26)	$T_{m,c}$ (.23)		$T_{m,Fe}$ (.30)
		ω_{BL} (.22)	ω_{BL} (.21)		$C_{p,c}$ (.23)
		V_B (-.23)	V_B (-.33)		ω_{BL} (.20)
		$\gamma_o V_B$ (-.71)	$\gamma_o V_B$ (-.63)		$\gamma_o V_B$ (-.64)
R^2	.62	.93	.92	.59	.71

thereby inhibiting heat transfer and slowing down the ablation rate. A closely related parameter that was important in the thermite test was the bouyant velocity of the alumina. The alumina has a bouyant rising velocity, thus it will tend to drift away from the lower surface and rise to the top to form a crust. The pool mixing tends to inhibit the separation effect, hence, for any given superficial gas velocity the alumina tends to settle into some concentration gradient. When freezing of the alumina occurs, the pool viscosity could be greatly increased if the local frozen alumina concentration is great enough. Thus due to the combined effects of pool mixing, alumina bouyancy, and slurry viscosity effects, one could expect significantly different behavior for thermite as compared to steel. This is precisely what Figures 5.20 and 5.21 show. These two figures show the erosion versus time for all of the 60 cases for both the thermite and stainless steel tests. For the case of thermite four different regimes become apparent. There is the rapid ablation mode, an alumina freezing (with high slurry viscosity) mode that terminates the ablation early, a steel freezing mode that terminates the ablation at greater depths, and an intermediate mode that has continuing penetration but at rates significantly reduced from the rapid ablation mode. It is interesting to note that only a few of the cases fell into the intermediate regime. Note that the experiment also falls into the intermediate regime. The sparse scattering of intermediate cases is a consequence of picking an extraordinarily wide range for some of the parameters. The stainless steel simulations only have two regimes: rapid ablation and freezing.

The major thermophysical properties that turned out to be important were the melting temperatures of the materials, the fraction of the concrete that is $CaCO_3$, and in the case of thermite, the MgO wall thermal conductivity.

The melting temperatures of the materials are important because they determine the driving force for heat transfer. The concrete melting temperature range is the cold boundary temperature for the pool heat transfer. The freezing points of the steel determine the extent to which the pool can penetrate before freezing occurs. The melting point of alumina was only important in determining the pool temperature history at early times. This should be obvious because the pool temperature will plateau at the alumina freezing point due to the liberation of its latent heat.

The percentage of the concrete that is $CaCO_3$ is important because it creates most of the gas that provides the mixing in the pool. Pool mixing, and its relationship to the eddy thermal conductivity, was found to be the dominant variable in this analysis.

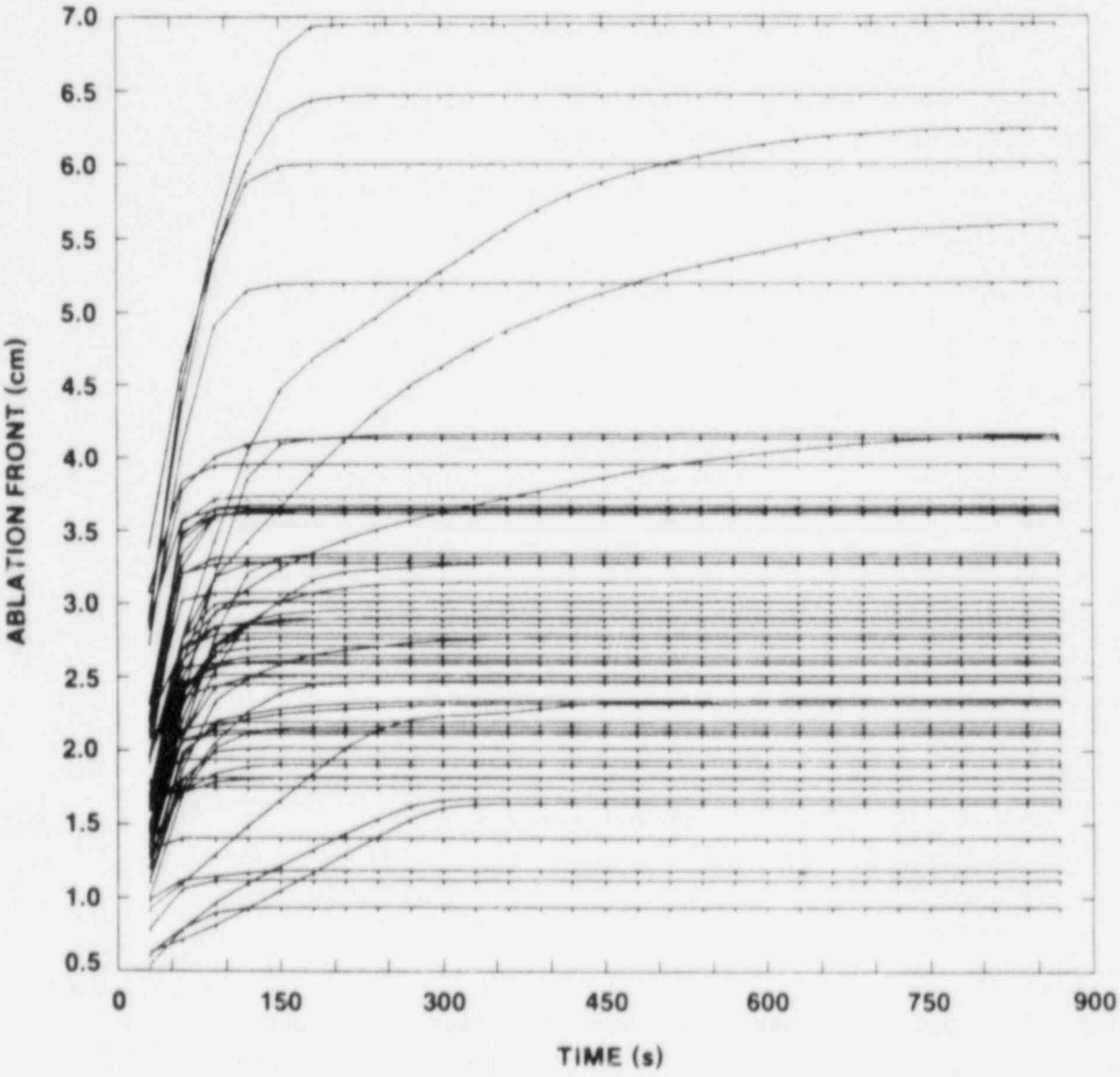

Figure 5.20 Erosion Front Location Prediction for the 60 Cases of the TURC1T Sensitivity Analysis

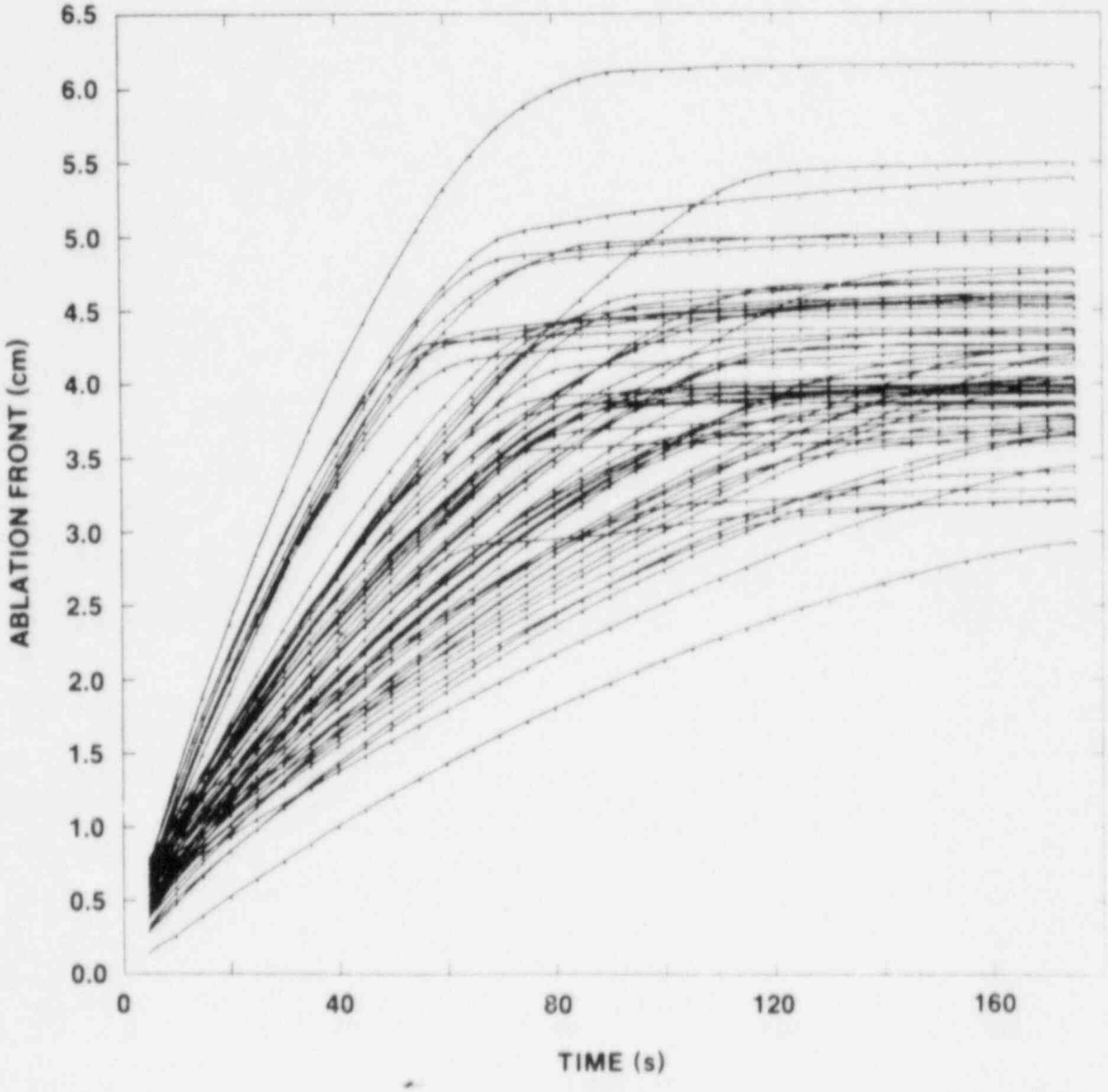

Figure 5.21 Erosion Front Location Prediction for the 60 Cases of the TURC1SS Sensitivity Analysis

In the case of thermite, the wall thermal conductivity was found to be very important. This should be expected because the total wall heat loss (Figure 5.12) was found to be nearly the same as the ablating concrete heat loss. For the case of stainless steel, the wall conductivity played a smaller role because a significant thermal resistance existed between the wall and the pool region.

As far as the experimental parameters were concerned, the initial pool temperature and the melt mass were found to be of importance. These parameters are directly related to the total thermal energy content of the pool, which in turn is related to the total amount of concrete that could be melted.

6 SUMMARY

Two experiments, TURC1T a thermite-concrete interaction experiment and TURC1SS a stainless steel-concrete interaction experiment, are reported here.

The TURC1T experiment consisted of 147.2 kgs of Fe-Al_2O_3 melt interacting with Limestone Common Sand concrete. Due to the loss of control lines to various instrumentation, only the thermal response of the crucible during the interaction was documented. A depth of 7.5 cm of concrete was eroded in ~ 13 mins. The erosion rate steadily decreased from 180-150 cm/hr to 10-20 cm/hr over the duration of the experiment.

The TURC1SS experiment was physically identical to the TURC1T except that the molten debris consisted of 106 kg of 304 stainless steel. Recorded data consisted of the thermal response of the crucible, sampling of evolved gases and the collection of aerosol material. The thermocouple response indicated an erosion depth of 3 cm, but posttest x-ray and physical examination showed a convoluted eroded concrete surface, resulting in an average depth of 4.3 cm. The concrete erosion occurred over 100 seconds resulting in an average erosion rate of 180-240 cm/hr.

Analysis of the TURC1SS gas samples suggests the CO_2 and H_2O released from the concrete are reduced to CO and H_2 as they passed through the melt pool. After the solidification of molten debris, H_2 continued to be released, indicating combustible gas production continues after ablation is terminated.

Aerosol measurements showed aerosol concentrations of 80-15 g/m^3 through the duration of concrete attack. The estimated mass source rate varied from 5.7-1.3 g/sec, with a geometric mass average aerodynamic diameter of 1 μm or less. Release rates were determined for Te and La. Tellurium was observed to be released at 1010 mg/sec for 0-15 seconds into the interaction, decreasing rapidly to 74 mg/sec from 60-120 seconds. Lanthanum follows the same trend decreasing from 9.1 mg/sec to 0.22 mg/sec. Aerosol mass fractions for Te were 17.7 w/o from 0-15 sec and 29.4 w/o from 60-120 sec. La aerosol mass fractions were 0.16 w/o and 0.088 w/o, respectively.

An experimental analysis of the TURC1SS and TURC1T experiments was performed using an analysis model that has been written for these and other similar 1-D concrete erosion experiments. The results of the analysis are threefold. One, the code is able

to reproduce the measured thermocouple data with sufficient accuracy. Two, the predicted thermal history of the melt pool is corroborated by changes in wall heat flux and gas data, implying that predicted temperature is sufficiently accurate for validation of aerosol and gas chemical reaction models in CORCON and VANESA. And, three, the other predictions concerning gas generation, velocities, heat fluxes, and heat transfer coefficients can be compared and evaluated against existing correlations of the same phenomena, such as those in the CORCON code.

A sensitivity analysis has also been performed on both experiments using the model. The results of the sensitivity analysis seem to indicate that pool mixing and flow regime behavior dominate the pool-concrete heat transfer. Thermophysical properties such as total gas content and wall MgO thermal conductivity are important. The importance of component freezing and slurry formation shows up in the TURC1T experiment, and it seems to be the phenomena that accounts for the major difference between the thermite and steel tests.

The results of the analysis seem to suggest that the mechanism of ablation is similar to nucleate boiling rather than film boiling. These conclusions are based upon the magnitude of the Kutateladze number and the predicted heat transfer coefficient associated with the stainless steel test.

The experimental results have been compared to CORCON calculations in order to validate the code. This comparison demonstrates that while some parts of the code perform well, other parts require further model development. Specifically, CORCON's chemical equilibrium model adequately calculates reduction of CO_2 and H_2O to CO and H_2 as the gas stream percolates through the melt. Also, the melt-concrete heat transfer models in the code predict experiment ablation rates under some conditions (TURC1T). However, under different conditions (TURC1SS), CORCON significantly underpredicts ablation. It was also demonstrated in the experiments that conduction into subsurface concrete can be significant when the melt cools; and as a result, gases are released from the concrete in nonstoichiometric proportions. Since H_2O is released at lower temperatures, conduction favors H_2O release over CO_2 release.

Alternate melt-concrete heat transfer models are currently being investigated for inclusion in CORCON. Special emphasis is being placed on models analogous to barbotage or nucleate boiling. Numerous methods for including transient conduction into the concrete are also being considered.

REFERENCES

1. USNRC, Reactor Safety Study: An Assessment of Accident Risks in US Commercial Nuclear Power Plants, WASH 1400, NUREG 75/04, October 1975.

2. D. A. Powers and F. E. Arellano, Large-Scale Transient Tests of the Interaction of Molten Steel with Concrete, NUREG/CR-2282, SAND81-1753, Sandia National Laboratories, Albuquerque, NM, Jan. 1982.

3. D. A. Powers, Sustained Molten Steel/Concrete Interactions Tests, NUREG/CR-1066, SAND77-1423, Sandia National Laboratories, Albuquerque, NM, June 1978.

4. D. A. Powers, D. A. Dahlgren, J. F. Muir and W. F. Murfin, Exploratory Study of Molten Core Material/Concrete Interaction, July 1975-March 1977, SAND77-2042, Sandia National Laboratories, Albuquerque, NM, Feb. 1978.

5. D. A. Powers and F. E. Arellano, Direct Observation of Melt Behavior During High Temperature Melt/Concrete Interactions, NUREG/CR-2283, SAND81-1754, Sandia National Laboratories, Albuquerque, NM, Jan. 1982.

6. V. K. Dhir, I. Catton, and D. Cho, "Heat Transfer from a Liquid Pool to a Decomposing Solid Surface," Proc. Third PAHR Info. Exch., Argonne National Laboratory, 141 (1977a) ANL-78-10.

7. V. Dhir, I. Catton, and J. Castle, "Role of Taylor Instability on Sublimation of a Horizontal Slab of Dry Ice," ASME Winter Annual Mtg., 76-WA/HT-87 (1976).

8. IDCOR. Technical Report 15.3, Core-Concrete Interactions, Sept. 1983, Atomic Industrial Forum Inc., 7101 Wisconsin Ave., Bethesda, MD 20814.

9. J. F. Muir, R. K. Cole, M. L. Corradini, and M. A. Ellis, CORCON-MOD1 - An Improved Model for Molten Core-Concrete Interactions, SAND80-2415, NUREG/CR-2142, Sandia National Laboratories, Albuquerque, NM, July 1981.

10. D. A. Powers, VANESA, Fission Product Release Model, personal communication, Dec. 1984.

11. A. J. Grimly, Memo: Equilibrium Concentration of metals and oxides at 2700 K for the TURC1 Test, Nov. 30, 1984.

12. Smith, R. W. and Missen, R. W., Chemical Reaction Equilibrium Analysis, Wiley, New York, 1982.

13. R. K. Cole et al., CORCON-MOD2: A Computer Model for Analysis of Molten Core Concrete Interactions, Sandia National Laboratories, Albuquerque, NM, NUREG/CR-3920, SAND84-1246 August 1984.

14. Kunitz, Journal General Physiology, Vol 9, p. 715, (1926).

15. H. V. Wartenberg and G. Wehner, 2. Elektrochem. 42, 293 (1936).

16. V. A. Bogulyubov, Stad 17, 531 (1957).

17. R. A. Schan and T. Shimazaki, "Heat Transfer to A Fluid Flowing Turbulently in a Smooth Pipe with Walls at Constant Temperature," ASMC Paper 50-A-128, 1950.

18. ACI-211. 1-74 Recommended Practices for Normal and Heavy Concrete, American Concrete Institute, Detroit, MI.

19. T. Y. Chu, Memo High Heat Flux Evaluation of Castable MgO, Estimation of Thermal Conductivity of Castable MgO, June 11, 1984.

20. J. V. Beck and K. J. Arnold, Parameter Estimation in Engineering and Science, John Wiley & Sons, 1977.

21. M. Pilch, "MgO and 70 w/o UO_2 - 30 w/o Y_2O_3: Thermophysical and Transport Properties," NUREG/CR-2611, SAND81-1230, Sandia National Laboratories, Albuquerque, NM, Feb. 1982.

22. J. V. Beck, "Criteria for Comparison of Methods of Solution of the Inverse Heat Conduction Problem," Nuclear Engineering and Design 53, North-Holland Publishing Company, 1979.

23. W. W. Tarbell, D. R. Bradley, F. E. Arellano, Sustain Concrete Attack by Low Temperature, Fragmented Core Debris, SAND82-2476, NUREG/CR-3024, Sandia National Laboratories, Albuquerque, NM, to be published.

24. R. C. Weast, CRC Handbook of Chemistry and Physics, CRC Press Inc., 1985.

25. Advanced Reactor Safety Research Program Quarterly Report, Nuclear Fuel Cycle Program, Sandia National Laboratories, Albuquerque, NM, July-Sept. 1981, NUREG/CR-2238, SAND81-1529, Oct. 1982.

26. A. Suo-Anttila, SLAM - A Sodium Concrete Limestone Concrete Ablation Model, NUREG/CR-3379, SAND83-7114, Sandia National Laboratories, Albuquerque, NM, Dec. 1983.

27. G. E. Sims and P. L. Duffield, Comparison of Heat Transfer Coefficients in Pool Barbotage and Saturated Pool Boiling, The Engineering Journal, Vol 14, No. B1, May 1971.

28. S. S. Kutateladze and I. G. Malenkov, "Fluid and Gasdynamical Aspects of Heat Transfer in the Injection Bubbling and Boiling of Liquids," High Temperature, 14, 703 (1976).

29. J. C. Helton, R. H. Iman, J. D. Johnson, and C. D. Leigh, "Uncertainty and Sensitivity Analysis of a Model for Multicomponent Aerosol Dynamics," NUREG/CR-4342, SAND84-1307, Sandia National Laboratories, Albuquerque, NM, August 1985.

30. "Reactor Safety Research Quarterly Report July-Sept. 1983 and Oct.-Dec. 1983," Vols 27 and 28, NUREG/CR-3589 (3 and 4), SAND83-2425 (3 and 4), Printed July 1984, pp. 105-107.

31. J. V. Beck and R. L. Knight, Users Manual for USINT, SAND79-1694, NUREG/CR-1375, Sandia National Laboratories, Albuquerque, NM, May 1980.

32. Marshall, W., Personal Communication, Feb. 1985.

DISTRIBUTION:

U.S. Government Printing Office
Receiving Branch (Attn: NRC Stock)
8610 Cherry Lane
Laurel, MD 20707
400 copies for R5, R7

U. S. Nuclear Regulatory Commission (17)
Office of Nuclear Regulatory Research
Washington, DC 20555
Attn: O. E. Bassett
R. T. Curtis
M. Silberberg
C. N. Kelber
G. Marino
L. Chan
C. Ryder
R. W. Wright
T. Walker
R. O. Meyer
J. Mitchell
S.B. Burson (5)
T. Lee

U. S. Nuclear Regulatory Commission (3)
Office of Nuclear Reactor Regulation
Washington, DC 20555
Attn: L. G. Hulman
P. Easky
J. Rosenthal

U. S. Department of Energy (2)
Albuquerque Operations Office
P. O. Box 5400
Albuquerque, NM 87185
Attn: J. R. Roeder, Director
D. K. Nowlin, Director
For: C. B. Quinn
D. Plymale

U. S. Department of Energy
Office of Nuclear Safety Coordination
Washington, DC 20545
Attn: R. W. Barber

Electric Power Research Institute
3412 Hillview Avenue
Palo Alto, CA 94303
Attn: R. Vogel

Brookhaven National Laboratory (3)
Upton, NY 11973
Attn: R. A. Bari
T. Pratt
G. Greene

Professor R. Seale
Department of Nuclear Engineering
University of Arizona
Tucson, AZ 85721

Oak Ridge National Laboratory
P. O. Box Y
Oak Ridge, TN 37830
Attn: T. Kress

K. Holtzclaw
General Electric--San Jose
Mail Code 682
175 Kurtner Avenue
San Jose, CA 95125

Argonne National Laboratory
9700 S. Cass Avenue
Argonne, IL 60439
Attn: J. Rest

Cathy Anderson
Nuclear Safety Oversight Commission
1133 15th St., NW
Room 307
Washington, DC 20005

Battelle Columbus Laboratory (3)
505 King Avenue
Columbus, OH 43201
Attn: P. Cybulskis
R. Denning
J. Gieseke

J. E. Antill
Berkeley Nuclear Laboratory
Berkeley GL 139 PB
Gloucestershire
England, U.K.

W. G. Cunliffe
Bldg. 396
British Nuclear Fuels, Ltd.
Springfield Works
Salwick, Preston
Lancashire,
England, U.K.

UKAEA
Reactor Development Division (4)
Winfrith, Dorchester
Dorset DT2 8DH
England, U.K.
Attn: R. Potter

Nucleare e della Protezione Sanitaria (DISP) (2)
Ente Nazionnle Energie Alternative (ENEA)
Viale Regina Margherita, 125
Casella Postale M. 2358
I-00100 Roma A.D., Italy
Attn: Mr. Manilia
Mr. G. Petrangeli

Dr. K. J. Brinkman
Reactor Centrum Nederland
P. O. Box 1
1755 ZG Petten
THE NETHERLANDS

Kernforschungszentrum Karlsruhe
Postfach 3640
75 Karlsruhe
Federal Republic of Germany
Attn. H. Rininsland

Mr. H. Bairiot, Chief
Department LWR Fuel
Belgonucleaire
Rue de Champde Mars. 25
B-1050 BRUSSELS, BELGIUM

Japan Atomic Energy Research Institute
Tokai-Mura, Naka-Gun
Ibaraki-Ken 319-11
Japan
Attn: S. Saito

Wang Lu
TVA
400 Commerce, W9C157-CK
Knoxville, TN 37902

M. Fontana
Director, IDCOR Program
Technology for Energy, Inc.
P. O. Box 22996
10770 Dutchtown Rd.
Knoxville, TN 37922

H. J. Teague (3)
UKAEA
Safety and Reliability Directorate
Wigshaw Lane
Culcheth
Warrington, WA3 4NE
United Kingdom

Dr. Frau Reusenbach-Berger
Gesellschaft fur Reaktorsicherheit (GRS mbH)
Postfach 101650
Glockengasse 2
500 Koeln 1
Federal Republic of Germany

M. Jankowski
IAEA
Division of Nuclear Reactor Safety
Wagranerstrasse 5
P. O. Box 100
A/1400 Vienna, Austria

Statens Karnkraftinspektion
L. Hammer
P.O. Box 27106
S-10252 Stockholm, Sweden

Studsvik Energiteknik AB
K. Johansson
S-611 82 Nykoping, Sweden

Atomic Energy Canada Ltd.
M. Notley
Chalk River, Ontario
Canada K0J 1J0

Atomic Energy Canada Ltd.
H. Rosinger
Pinawa, Manitoba
Canada R0E 1L0

Korea Adv Energy Research Inst
H.R. Jun
P.O. Box 7
Daeduk-Danji
Choong-Nam, Korea

Institute of Nuclear Energy Res
Sen-I Chang
P.O. Box 3
Lungtan
Taiwan 325, Rep. of China

3141 S. A. Landenberger (5)
3151 W. L. Garner
5161 J. E. Gronager
6000 E. H. Beckner
6400 A. W. Snyder
6410 J. W. Hickman
6412 A. L. Camp
6420 J. V. Walker (2)
6421 P. S. Pickard
6422 D. A. Powers (10)
6422 J. E. Brockmann (3)
6422 R. M. Elrick
6422 E. R. Copus (5)
6422 W. W. Tarbell
6423 T. R. Schmidt
6425 B. R. Bradley (5)
6425 W. J. Camp
6425 M. Pilch
6427 M. Berman
6440 D. A. Dahlgren
6442 W. A. Von Riesemann
6449 K. D. Bergeron
6454 G. L. Cano
7530 T. B. Lane
7537 N. R. Keltner
8024 P. W. Dean

NRC FORM 335 (2 84) NRCM 1102, 3201, 3202

U.S. NUCLEAR REGULATORY COMMISSION

BIBLIOGRAPHIC DATA SHEET

SEE INSTRUCTIONS ON THE REVERSE

1 REPORT NUMBER (Assigned by TIDC and Vol. No., if any)

NUREC/CR-4420
SAND85-0707

2 TITLE AND SUBTITLE

TURC1: Large Scale Metallic Melt-Concrete Interaction Experiments and Analysis

3 LEAVE BLANK

4 DATE REPORT COMPLETED

MONTH	YEAR
October	1985

5 AUTHOR(S)

J.E. Gronager, A.J. Suo-Anttila, D.R. Bradley, J.E. Brockmann

6 DATE REPORT ISSUED

MONTH	YEAR
December	1985

7 PERFORMING ORGANIZATION NAME AND MAILING ADDRESS (Include Zip Code)

Severe Accident Source Terms Division 6422
Sandia National Laboratories
Albuquerque, NM 87185

8 PROJECT/TASK/WORK UNIT NUMBER

9 FIN OR GRANT NUMBER

Fin No. A1218

10 SPONSORING ORGANIZATION NAME AND MAILING ADDRESS (Include Zip Code)

Containment Systems Branch
Division of Accident Evaluation
U.S. Nuclear Regulatory Commission
Washington, DC 20555

11a TYPE OF REPORT

Topical

b PERIOD COVERED (Inclusive dates)

12 SUPPLEMENTARY NOTES

13 ABSTRACT (200 words or less)

Two large-scale molten debris-concrete experiments, TURCIT, a thermite-concrete interaction experiment, and TURC1SS, a stainless steel-concrete experiment, are reported here. The experiments consisted of teeming molten debris (>100 kg) onto limestone/common sand concrete. The molten debris was allowed to cool naturally. The concrete ablation rate, composition of evolved gases, and aerosol data are presented.

The experimental results have been compared to CORCON calculations in order to validate the code. This comparison showed that while some parts of the code performed well (chemical equilibrium model), other sections require further model development (melt-concrete heat transfer model).

An analysis of the two experiments was performed using a new analysis model. The results of the analysis seem to suggest that the heat transfer mechanism of concrete ablation is similar to nucleate boiling heat transfer, rather than gas film heat transfer.

14 DOCUMENT ANALYSIS - a KEYWORDS/DESCRIPTORS

Aerosol generation; Combustible Gas Production; Concrete Ablation; CORCORN comparison; Melt-concrete heat transfer; Molten core - concrete interaction

b IDENTIFIERS/OPEN ENDED TERMS

15 AVAILABILITY STATEMENT

NTIS
GPO Sales

16 SECURITY CLASSIFICATION

(This page)
Unclassified
(This report)
Unclassified

17 NUMBER OF PAGES

182

18 PRICE

☆ U.S. Government Printing Office 1985-676-049/21021

120555078877 1 1AN1R51R7
US NRC
ADM-DIV OF TIDC
POLICY & PUB MGT BR-PDR NUREG
W-501
WASHINGTON DC 20555